

UNCLASSIFIED

AD NUMBER
AD487449
NEW LIMITATION CHANGE
TO Approved for public release, distribution unlimited
FROM Distribution authorized to U.S. Gov't. agencies and their contractors; Critical Technology; JUL 1966. Other requests shall be referred to Air Force Materials Laboratory, Wright-Patterson AFB, OH 45433.
AUTHORITY
AFSC ltr dtd 2 Mar 1972

THIS PAGE IS UNCLASSIFIED

THE EVALUATION OF MATERIALS SYSTEMS FOR HIGH
TEMPERATURE AEROSPACE APPLICATIONS

PART 1

John C. Wurst
John A. Cherry
Dennis A. Gerdeman
Norman L. Hecht

University of Dayton Research Institute
Dayton, Ohio 45409

TECHNICAL REPORT AFML TR 65-339, Part I
July 1966

Qualified requestors may obtain
copies of this report from DDC

Air Force Materials Laboratory
Research and Technology Division
Air Force Systems Command
Wright-Patterson Air Force Base, Ohio 45433

NOTICES

When Government drawings, specifications, or other data are used for any purpose other than in connection with a definitely related Government procurement operation, the United States Government thereby incurs no responsibility nor any obligation whatsoever; and the fact that the Government may have formulated, furnished, or in any way supplied the said drawings, specifications, or other data, is not to be regarded by implication or otherwise as in any manner licensing the holder or any other person or corporation, or conveying any rights or permission to manufacture, use, or sell any patented invention that may in any way be related thereto.

Qualified requesters may obtain copies of this report from the Defense Documentation Center (DDC), (formerly ASTIA), Cameron Station, Bldg. 5, 5010 Duke Street, Alexandria, Virginia, 22314. The distribution of this report is limited because the report contains technology identifiable with items on the strategic embargo lists excluded from export or re-export under U. S. Export Control Act of 1949 (63 STAT. 7), as amended (50 U. S. A. App. 2020.2031), as implemented by AFR 400-10.

Copies of this report should not be returned to the Research and Technology Division unless return is required by security considerations, contractual obligations, or notice on a specific document.

**THE EVALUATION OF MATERIALS SYSTEMS FOR HIGH
TEMPERATURE AEROSPACE APPLICATIONS**

**John C. Wurst
John A. Cherry
Dennis A. Gerdeman
Norman L. Hecht**

**University of Dayton Research Institute
Dayton, Ohio 45409**

**Qualified requestors may obtain
copies of this report from DDC**

FOREWORD

This report covers work performed during the period from January 1964 to January 1965 on Air Force Contract AF 33(615)-1312. This contract was initiated under Project No. 7381, "Materials Application," and Task No. 738102, "Materials and Process Evaluation". The work was administered under the direction of the Applications Division, Air Force Materials Laboratory, Wright-Patterson Air Force Base, Ohio. Mr. L. N. Hjelm and Lt. D. R. James were Co-Project Monitors of this work.

University of Dayton personnel who made major contributions to the program include: J. C. Wurst, Project Leader; J. A. Cherry, coated refractory alloys evaluation; D. A. Gerdeman, arc-plasma-jet testing; N. L. Hecht plasma sprayed coating studies; and research technicians cooperating in this program, S. W. Brzezicki, D. C. Maxwell, T. L. Doane, and G. E. Stuber.

The manuscript was released by the authors October 1965 for publication as an RTD Technical Report.

This technical report has been reviewed and is approved.



A. OLEVITCH, Chief
Materials Engineering Branch
Materials Applications Division
Air Force Materials Laboratory

ABSTRACT

This report presents the evaluation of candidate materials for high temperature aerospace applications in three sections: the evaluation of refractory alloy coatings, the arc-plasma-jet evaluation of materials, and the evaluation of plasma sprayed coatings.

Section I describes the evaluation of two columbium base alloys, D43 (Cb-10W-1Zr) and C129Y (Cb-10W-10Hf-0.1Y), each with six different oxidation resistant coatings. The evaluation consisted of metallographic analyses, bend and tensile tests, cyclic oxidation tests from 1600° to 3000°F, and statistically designed creep rupture tests. The results of this evaluation are described in detail and the coated alloys ranked according to mechanical properties, oxidation resistance, and creep rupture behavior.

It should be noted that the majority of the coatings were semicommercial systems, still in the development stage. They were purchased on a best-effort basis and their performance was not necessarily representative of a fully optimized product.

Section II discusses the results of screening tests at cold wall heat flux levels from 100 to 1000 Btu/ft² sec of two resin impregnated zirconia foam materials, graphite cloth and high silica fabric laminates of phenolic resin, and a gelatin molding compound. In addition, this section contains a summary of preliminary screening tests of nine candidate materials for use as an external ablative coating for the Mach 8 version of the X-15 research aircraft. The results of these screening tests are presented as a tabulation of test conditions and their effect upon the specimens. Performance indices include weight loss, depth and volume of erosion, density change, and surface temperature behavior.

Section II also discusses the development of a plasma fired rocket exhaust simulator which employs subscale nozzles as test specimens and has provisions for simulation of high temperature rocket exhausts by controlled chemical additives to the plasma effluent. Preliminary data are presented for a series of tests of ATJ graphite nozzles in a nitrogen effluent seeded with additives of CO, CO₂, and H₂O vapor.

Section III describes the evaluation of factors which affect the bond strength and thermal cycling endurance of plasma sprayed ceramic coatings modified with metal additives. This evaluation includes the influence of the primer coating upon coating adherence and the relationship of particle size and ceramic/metal ratios upon the "as sprayed" characteristics of metal-graded ceramic coatings. Test results are presented for NiCr graded ZrO₂ and NiAl graded Al₂O₃ which illustrate the relative importance of the plasma spraying variables (input power, arc and carrier gas flow rate, and spray distance) and the physical characteristics of the spray powder (blend proportions and particle size) as they affect the quality of the sprayed coating.

TABLE OF CONTENTS

	Page
SECTION I THE EVALUATION OF COATINGS FOR REFRACTORY	
ALLOYS.	1
INTRODUCTION	1
EXPERIMENTAL METHODS	2
METALLOGRAPHIC ANALYSES.	2
BEND TRANSITION TEMPERATURE	3
TENSILE TESTING	3
CYCLIC OXIDATION TESTING.	4
CREEP RUPTURE TESTING	9
MATERIAL AND SPECIMEN PROCUREMENT	11
COATING SELECTION	13
D43 Coatings.	14
C129Y Coatings.	14
EXPERIMENTAL RESULTS	15
METALLOGRAPHIC ANALYSES.	15
D43 Columbium Alloy.	18
C129Y Columbium Alloy	25
BEND TRANSITION TEMPERATURE	26
D43 Columbium Alloy.	26
C129Y Columbium Alloy	26
TENSILE TESTING	28
D43 Columbium Alloy.	28
C129Y Columbium Alloy	28
CYCLIC OXIDATION TESTING.	34
D43 Columbium Alloy.	34
C129Y Columbium Alloy	48
CREEP RUPTURE TESTING	51
D43 Columbium Alloy.	58
C129Y Columbium Alloy	59
SUMMARY	59

	Page
D43 COLUMBIUM COATINGS	59
Sylcor Ag-Si-Al/D43	59
TRW Cr-Ti-Si/D43	60
Other D43 Coatings	61
C129Y COLUMBIUM COATINGS	61
Sylcor Ag-Si-Al/C129Y	61
TRW Cr-Ti-Si/C129Y	62
Other C129Y Coatings	63
DISCUSSION OF COATING RATINGS.	63
RECOMMENDATIONS.	67
 SECTION II ARC-PLASMA-JET TESTING.	 69
INTRODUCTION	69
EVALUATION PROCEDURES	69
TEST RESULTS.	71
IMPREGNATED POROUS CERAMICS	71
MANUFACTURER I	71
MANUFACTURER UT.	72
ABLATIVE COMPOSITES	76
MANUFACTURER ASD.	77
MANUFACTURER CT.	77
X-15 STUDIES.	82
MANUFACTURER AG.	84
MANUFACTURER A.	84
MANUFACTURER E.	85
MANUFACTURER EG.	85
MANUFACTURER GR.	85
MANUFACTURER CA.	85
MANUFACTURER M	86
MANUFACTURER MC	86
SUMMARY	86
SCREENING TEST FOR NOZZLE MATERIALS.	87

	Page
SECTION III PLASMA-SPRAYED COATING STUDIES	99
INTRODUCTION	99
BACKGROUND	99
COATING PROCEDURES.	100
TESTING PROCEDURES.	103
EXPERIMENTAL RESULTS.	103
METAL COATINGS	103
METAL-CERAMIC BLENDED COATINGS	109
MULTILAYER GRADED COATINGS	116
CONCLUSIONS AND RECOMMENDATIONS.	117
 APPENDIX I THEORETICAL DETERMINATION OF PARTICLE SIZE RATIOS FOR METAL-CERAMIC POWDER BLENDS.	 119
APPENDIX II THEORETICAL DETERMINATION OF VELOCITY-TIME RELATIONSHIP OF PARTICLES BEING ACCELERATED BY A MOVING GAS STREAM.	 125
APPENDIX III A SIMPLE THEORY FOR PREDICTION OF THE THERMAL EXPANSION OF COMPOSITE MATERIALS.	 128
APPENDIX IV EVALUATION OF CANDIDATE ABLATIVE MATERIALS DATA FOR X-15 APPLICATION.	 135
REFERENCES.	174

ILLUSTRATIONS

Figure		Page
1	Transition Temperature Fixture	4
2	Cyclic Oxidation Specimens Ready for Insertion into Furnace. . .	5
3	Testing Apparatus Consisting of a Standard Lever-Arm-Type Creep Testing Machine	10
4	Coating Test Specimens.	12
5	Photomicrograph of Uncoated D43.	16
6	Comparative Photomicrographs of Coated D43.	16
7	Comparative Photomicrographs of Coated D43.	17
8	Irregularity of Sylcor Coating on D43.	17
9	Sylcor D43 Creep Rupture Specimens.	18
10	Typical Photomicrographs of Coated D43.	19
11	Comparative Photomicrographs of TRW Cr -Ti-Si Coated C129Y. .	20
12	Comparative Photomicrographs of Sylcor Ag-Si-Al Coated C129Y	20
13	Typical Photomicrographs of Coated C129Y	21
14	Photomicrograph of Uncoated C129Y	22
15	Batch Comparison of TRW Cr-Ti-Si Coating on 20 mil C129Y . .	22
16	Typical Stress-Strain Diagrams for Coated D43 (Tested at Room Temperature)	31
17	Typical Stress-Strain Diagrams for Coated C129Y (Tested at Room Temperature)	32
18	Typical Stress-Strain Diagrams for Coated C129Y (Tested at Room Temperature)	33
19	Typical Stress-Strain Diagrams for Coated D43 (Tested at Room Temperature)	33
20	Weibull Plot of 2600° F Cyclic Oxidation Test Results; Sylcor Ag-Si-Al Coating on 20 mil D43	37
21	Weibull Plot of 2600° F Cyclic Oxidation Test Results; TRW Cr-Ti-Si Coating on 20 mil D43	38
22	Weibull Plot of 2600° F Cyclic Oxidation Test Results; Pfaudler PFR-32 Coating on 20 mil D43	38

Figure		Page
23	Weibull Plot of 2600° F Cyclic Oxidation Test Results; Boeing Disil Coating on 20 mil D43	39
24	Weibull Plot of 2600° F Cyclic Oxidation Test Results; LTV Two-Cycle Modified Silicide Coating on 20 mil D43	39
25	Weibull Plot of 2600° F Cyclic Oxidation Test Results; Sylcor Ag-Si-Al Coating on 20 mil C129Y.	40
26	Weibull Plot of Cyclic Oxidation Test Results; TRW Coating on 20 mil C129Y.	41
27	Weibull Plot of 2600° F Cyclic Oxidation Test Results; Boeing Disil Coating on 20 mil C129Y	42
28	Weibull Plot of 2600° F Cyclic Oxidation Test Results; LTV Two-Cycle Modified Silicide Coating on 20 mil C129Y.	42
29	Weibull Plot of 2600° F Cyclic Oxidation Test Results; Chromizing Durak KA Coating on 20 mil C129Y	43
30	Weibull Plot of 2400° F Cyclic Oxidation Test Results; Sylcor Ag-Si-Al Coating on 20 mil C129Y.	43
31	Weibull Plot of 2400° F Cyclic Oxidation Test Results; TRW Cr-Ti-Si Coating on 20 mil C129Y.	44
32	Weibull Plot of 2400° F Cyclic Oxidation Test Results; Boeing Disil Coating on 20 mil C129Y	44
33	Weibull Plot of 2400° F Cyclic Oxidation Test Results; Pfaudler PFR-32 Coating on 20 mil C129Y	45
34	Weibull Plot of 2400° F Cyclic Oxidation Test Results; LTV Cr-B-Silicide Coating on 20 mil C129Y	45
35	Weibull Plot of 2400° F Cyclic Oxidation Test Results; Chromizing Durak KA Coating on 20 mil C129Y	46
36	Creep-and Stress-Rupture Curves for Sylcor (Ag-Si-Al) Coated 20 mil D43	52
37	Creep-Rupture Curves for the Sylcor Ag-Si-Al Coating on 20 mil C129Y.	53
38	Creep-Rupture Curves for the TRW Cr-Ti-Si Coating on 20 mil C129Y.	53
39	Combined Calorimeter and Pitot Tube Assembly	70
40	Nozzle Test Chamber	87
41	Plasma-Fired Nozzle Materials Testing Facility.	88

Figure		Page
42	Nozzle Test Specimen (Type II)	89
43	Typical Pressure-Temperature-Time Histories of ATJ Graphite Type II Nozzle Specimens Exposed to an N_2-O_2 Effluent at Initial Temperatures of 2400°, 2700°, and 3500°F	93
44	Typical Pressure-Temperature-Time Histories of ATJ Graphite Type II Nozzle Specimens Exposed to an N_2-CO_2 Effluent at Initial Temperatures of 2400°, 2700°, and 3500°F	94
45	Typical Pressure-Temperature-Time Histories of ATJ Graphite Type II Nozzle Specimens Exposed to an N_2-H_2O Effluent at Initial Temperatures of 2400°, 2700°, and 3500°F	95
46	Average Weight Loss Rate Versus Nozzle Wall Temperature of ATJ Graphite Nozzles Exposed to Environments with Various Additives	97
47	Average Rate of Increase in Throat Area Versus Nozzle Wall Temperature of ATJ Graphite Nozzles Exposed to Environments with Various Additives	97
48	Shear Fracture of NiAl Coated 304 Stainless Steel	106
49	Bond Strength Failure by Coating Separation from Substrate (Mo Coated 304 Stainless Steel)	107
50	Bond Strength Failure by Coating Separation from Substrate (NiCr Coated 304 Stainless Steel)	108
51	Effect of Particle Size Ratio of Metal and Ceramic Powders. Photos of Coatings Prepared from Blends Containing 15% NiCr- 85% ZrO_2	109
52	NiAl Coating Compared to NiAl- Al_2O_3 Blended Coating	111
53	Influence of Particle Size Variation on Bond Strength and Thermal Shock Cycles to Failure.	111
54	Influence of Fine Ceramic Particles Dispersed in a Metal Matrix.	111
55	Effect of Molybdenum Flashing on Bond Strength	112
56	Effect of Distance from Gun. Photos of Coatings Prepared from a Blend Composed of 15% NiCr-85% ZrO_2	113
57	Effect of Spray Power. Photos of Coatings Prepared from a Blend Composed of 15% NiCr-85% ZrO_2	113
58	Bond Strength Versus Spray Power Setting	114
59	Bond Strength and Thermal Shock Resistance Versus % Ceramic Phase.	115

Figure		Page
60	Effect of Ceramic to Metal Ratio.	115
61	NiCr-ZrO ₂ Graded Coating	117
62	Thin Slice of Actual Composite.	128
63	Model Rigid-Block System Substitute.	128
64	Dimensions of Model.	129
65	Block System	129
66	Substrate Temperature-Time History of Various Materials Exposed to 15 Btu/ft ² sec Heat Flux Environment. Ablative Material Thickness Nominally 50 mils. Thermocouple Located Within Approximately 10 mils of Bondline, Unless Otherwise Noted.	136
67	Substrate Temperature-Time History of Various Materials Exposed to 40 Btu/ft ² sec Heat Flux Environment. Ablative Material Thickness Nominally 50 mils. Thermocouple Located Within Approximately 10 mils of Bondline.	137
68	Substrate Temperature-Time History of Various Materials Exposed to 40 Btu/ft ² sec Heat Flux Environment. Ablative Material Thickness Nominally 50 mils. Thermocouple Located Within Approximately 10 mils	138
69	Substrate Temperature-Time History of Various Materials Exposed to 40 Btu/ft ² sec Heat Flux Environment. Ablative Material Thickness Nominally 50 mil. Thermocouple Located Within Approximately 10 Mils of Bondline, Unless Otherwise Noted.	139
70	Substrate Temperature-Time History of Various Materials Exposed to 40 Btu/ft ² sec Heat Flux Environment. Ablative Material Thickness Nominally 1/4 Inch. Thermocouple Located on Back Surface of Substrate, Unless Otherwise Noted	140
71	Substrate Temperature-Time History of Various Materials Exposed to 40 Btu/ft ² sec Heat Flux Environment. Ablative Material Thickness Nominally 3/8 Inch. Thermocouple Located on Back Surface of Substrate	141
72	Substrate Temperature-Time History of Emerson Electric T-500 4-A Exposed to 150 Btu/ft ² sec Heat Flux Environment. Ablative Material Thickness Nominally 50 mils. Thermocouple Located Within Approximately 10 mils of Bondline.	142
73	Substrate Temperature-Time History of Various Materials Exposed to 150 Btu/ft ² sec Heat Flux Environment. Ablative Material Thickness Nominally 1/4 Inch. Thermocouple Located on Back Surface of Substrate	143

74	Substrate Temperature-Time History of Various Materials Exposed to 150 Btu/ft ² sec Heat Flux Environment. Ablative Material Thickness Nominally 1/4 Inch. Thermocouple Located Within Approximately 10 mils of Bondline, Unless Otherwise Noted.	144
75	Substrate Temperature-Time History of Various Materials Exposed to 150 Btu/ft ² sec Heat Flux Environment. Ablative Material Thickness Nominally 3/8 Inch. Thermocouple Located on Back of Substrate.	145
76	Substrate Temperature-Time History of Various Materials Exposed to 150 Btu/ft ² sec Heat Flux Environment. Ablative Material Thickness Nominally 3/8 Inch. Thermocouple Located on Back Surface of Substrate, Unless Otherwise Noted	146
77	Substrate Temperature-Time History of Various Materials Exposed to 150 Btu/ft ² sec Heat Flux Environment. Ablative Material Thickness Nominally 3/8 Inch. Thermocouple Located Within Approximately 10 mils of Bondline, Unless Otherwise Noted.	147

TABLES

Table	Page
1 Rank Tables for 5% and 95% Confidence Limits and Median Rank for Specimen Sizes 1 to 20	8
2 Composition and Property Data Furnished by the Alloy Vendors for D43 and C129 Columbium Alloys	11
3 Metallographic Data for Coated D43.	23
4 Metallographic Data for Coated C129Y, Phases I and II.	24
5 Bend Transition Temperature Measurements of Coated D43 and C129Y	27
6 Room Temperature Tensile Test Results for Coated D43 Columbium Alloy	29
7 Room Temperature Tensile Test Results for Coated C129Y Columbium Alloy	30
8 Cyclic Oxidation Data for Coated D43 Columbium.	35
9 Cyclic Oxidation Data for Coated C129Y Columbium.	36
10 Probable Cyclic Oxidation Life at 2600°F of Coated D43 for Various Levels of Reliability.	48
11 Probable Cyclic Oxidation Life at 2600°F of Coated C129Y for Various Levels of Reliability.	50
12 Probable Cyclic Oxidation Life at 2400°F of Coated C129Y for Various Levels of Reliability.	51
13 Stress-Rupture Data for 20 mil D43 Columbium Coated with Sylcor Ag-Si-Al Slurry Silicide.	54
14 Creep-Rupture Data for 20 mil C129Y Columbium Coated with Sylcor Ag-Si-Al Slurry Silicide.	55
15 Creep-Rupture Data for 20 mil C129Y Columbium Coated with TRW Cr-Ti-Si Coating	56
16 Analysis of Variance of Creep Rupture Data for Sylcor (Ag-Si-Al) Coated 12 mil D43	57
17 Analysis of Variance of Creep Rupture Data for Sylcor (Ag-Si-Al) Coated 20 mil C129Y.	57
18 Analysis of Variance of Creep Rupture Data for TRW (Cr-Ti-Si) Coated 20 mil C129Y.	57
19 Comparative Creep Rupture Data for TRW and Sylcor Coated C129Y	58

Table		Page
20	Coating Performance Ratings	64
21	Results of Step-Down Oxidation Tests on Coated B66 Columbium .	66
22	Test Conditions and Results for Manufacturer I Foamed ZrO_2 Specimens Impregnated with Phenolic Resin	73
23	Test Conditions and Results for Manufacturer I Foamed ZrO_2 Specimens.	74
24	Test Conditions and Results of Manufacturer UT Chemically Bonded ZrO_2 Specimens Impregnated with Phenolic Resin	75
25	Test Conditions and Results of Manufacturer ASD Gelatin Mold- ing Compound Specimens	78
26	Test Conditions and Results of Manufacturer CT Phenolic/Quartz Cloth Laminates.	79
27	Test Conditions and Results of Manufacturer CT Phenolic/Quartz Cloth Laminates.	80
28	Test Conditions and Results of Manufacturer CT Phenolic/Graphite Topped Phenolic/Quartz Laminates	81
29	Candidate X-15 Ablative Materials Tested and Heat Flux Levels to Which They Were Exposed	83
30	Results of ATJ Graphite Nozzles Exposed to Various Environ- ments in Exhaust Simulation Test	92
31	Power Settings for Metal Coatings.	101
32	Composition of 85% ZrO_2 - 15% NiCr Blends Prepared for Study of Particle Size Ratio Effects.	102
33	Composition of 75% Al_2O_3 - 25% NiAl Blends Prepared for Study of Particle Size Ratio Effects.	102
34	Composition of NiCr- ZrO_2 Blends.	102
35	Composition of NiAl- Al_2O_3 Blends.	102
36	Composition and Spray Settings for Graded Coatings.	104
37	Results of Bond Strength Tests for Metal Coatings.	105
38	Results of Bond Strength Tests for Graded Coatings.	116
39	Material Properties	120
40	Results of Manufacturer AG Filled Epoxy Formulation Exposed to Arc-Plasma-Jet Effluent	148
41	Results of Manufacturer A Fibrous Ablative Composite Exposed to Arc-Plasma-Jet Effluent	149

Table		Page
42	Results of Manufacturer A-1 Fibrous Ablative Composite Exposed to Arc-Plasma-Jet Effluent	150
43	Results of Manufacturer E Subliming Epoxy Exposed to Arc-Plasma-Jet Effluent	151
44	Results of Manufacturer E Subliming Epoxy Exposed to Arc-Plasma-Jet Effluent	152
45	Results of Manufacturer E Subliming Epoxy Fiber Reinforced Subliming Salt Composition Exposed to Arc-Plasma-Jet Effluent .	153
46	Results of Manufacturer EG Low Density Silicone Elastomer in Honeycomb Exposed to Arc-Plasma-Jet Effluent	154
47	Results of Manufacturer EG Low Density Silicone Elastomer in Honeycomb Exposed to Arc-Plasma-Jet Effluent	155
48	Results of Manufacturer EG Low Density Silicone Elastomer in Honeycomb Exposed to Arc-Plasma-Jet Effluent	156
49	Results of Manufacturer EG Low Density Silicone Elastomer Without Honeycomb Exposed to Arc-Plasma-Jet Effluent.	157
50	Results of Manufacturer EG Medium Density Silicone Elastomer in Honeycomb Exposed to Arc-Plasma-Jet Effluent	158
51	Results of Manufacturer EG Medium Density Silicone Elastomer in Honeycomb Exposed to Arc-Plasma-Jet Effluent	159
52	Results of Manufacturer EG High Density Silicone Elastomer in Honeycomb Exposed to Arc-Plasma-Jet Effluent	160
53	Results of Manufacturer EG High Density Silicone Elastomer in Honeycomb Exposed to Arc-Plasma-Jet Effluent	161
54	Results of Manufacturer EG High Density Silicone Elastomer Without Honeycomb Exposed to Arc-Plasma-Jet Effluent.	162
55	Results of Manufacturer GR Ablative Polymer X7 Exposed to Arc-Plasma-Jet Effluent	163
56	Results of Manufacturer GR Ablative Polymer Exposed to Arc-Plasma-Jet Effluent	164
57	Results of Manufacturer GA Ablative Composite Exposed to Arc-Plasma-Jet Effluent	165
58	Results of Manufacturer GA Ablative Composite Exposed to Arc-Plasma-Jet Effluent	166

Table		Page
59	Results of Manufacturer M Microballoon Filled Silicone Elastomer in Honeycomb Exposed to Arc-Plasma-Jet Effluent	167
60	Results of Manufacturer MC Silicone Elastomer in Honeycomb Exposed to Arc-Plasma-Jet Effluent	168
61	Results of Manufacturer MC Silicone Elastomer in Honeycomb Exposed to Arc-Plasma-Jet Effluent	169
62	Results of Manufacturer MC Silicone Elastomer Without Honeycomb Exposed to Arc-Plasma-Jet Effluent	170
63	Results of Manufacturer MC Modified Silicone Elastomer in Honeycomb Exposed to Arc-Plasma-Jet Effluent	171
64	Results of Manufacturer MC Modified Silicone Elastomer Without Honeycomb Exposed to Arc-Plasma-Jet Effluent	172
65	Results of Manufacturer MC Modified Silicone Elastomer in Honeycomb Exposed to Arc-Plasma-Jet Effluent	173

SUMMARY

Section I Evaluation of Coatings for Refractory Alloys

The objective of this program was to evaluate the relative potential of commercially available coatings for columbium base alloys. It was not intended that design data be generated, but rather that a range of capabilities be established for these coatings and any inherent deficiencies which could limit their use be identified and placed in proper perspective.

Three general areas were investigated: the effect of the coating and/or the coating process upon the physical and mechanical properties of the substrate, the oxidation protection provided by the coating, and the load-bearing capability of alloys for extended periods at elevated temperatures.

Methods of evaluation used included metallographic analyses of the "as received" coated alloys, room temperature tensile tests, bend transition temperature measurements, cyclic oxidation tests from 1600° to 3000°F, and creep-rupture testing at stress levels from 6000 to 9000 psi.

The metallographic evaluation and the tensile and bend tests provided the necessary base line information for assessing the effect of the coating and the application process upon the physical characteristics of the base metal.

The oxidation resistance of the coated alloys was determined through a series of furnace tests in still air in which specimens were cycled to room temperature at hourly intervals for inspection. The test was somewhat stringent for two reasons. First, coating life was undoubtedly shortened by the hourly air quench of the specimens. Secondly, specimens were retired from test at the first sign of substrate oxidation. Thus, the test was a measure of the relative incidence and severity of critical flaws in the coating under conditions of thermal cycling and high temperature air exposure.

Oxidation tests were conducted on four specimens per coating batch at 1600°, 2400°, and 3000°F for a qualitative definition of oxidation resistance at these temperatures. All 2600°F tests and a few at 2400°F were performed on a number of specimens sufficient to permit the data to be fitted to a Weibull cumulative failure frequency function. With these data, it was then possible to estimate the reliability of the coating (a frequently overlooked factor) and to evaluate the mode and manner by which coating failures occurred (something rarely considered even by the coating vendors).

In evaluating the high temperature load-bearing capability of these alloys, creep-rupture testing was chosen in preference to elevated temperature tensile tests. This was based upon the belief that, while most columbium base alloy

development was directed toward attainment of improved high temperature tensile properties, such tests (in reality, just accelerated creep tests) had led to unwarranted optimism regarding the high temperature structural capabilities of these alloys. It was felt that the useful upper limit of temperature for the columbium base alloys would be dictated by long term creep behavior rather than short term hot strength. For this reason, a simple creep-rupture experiment was included in the program.

The same six coatings (Pfaudler PFR-32, Boeing Disil, Chromizing Durak KA, LTV Cr-B-Si, TRW Cr-Ti-Si, and Sylcor Ag-Si-Al) were evaluated on two columbium base alloys, D43 (Cb-10W-1Zr) and C129Y (Cb-10W-10Hf-0.1Y). Five of these coatings were modified silicides; the sixth, Ag-Si-Al, was a slurry type coating.

While each of these systems was considered either a commercial or semicommercial coating, it became apparent during the evaluation that several coatings had hardly passed the advanced research stage. Some vendors were unable to process in a single coating operation the modestly sized lot of specimens used in this program. Where two coating batches were evaluated, significant differences between batches were often observed. This was also noted among specimens from a common batch. Batch-to-batch and specimen-to-specimen variations both suggested inadequate control of the coating processes.

Intimate bonding of the coating to the substrate was achieved with each of these systems by chemical diffusion which inevitably consumed a portion of the substrate. Decreases in substrate thickness from starting values of 20 mils ranged from 0.6 mil to 1.4 mils per side for the D43 and from 0.5 mil to 1.3 mils per side for C129Y. A decrease in apparent tensile strength of 6 to 14% could therefore be anticipated if such calculations were based upon substrate thickness prior to coating.

Four of the coated D43 systems showed an increase in ultimate strength after coating. The TRW Cr-Ti-Si coating produced a decrease of 20 to 25%, and a severe loss of strength (40%) was measured with the Disil coated D43. Boeing had reported serious problems with the processing of the D43 and had not anticipated good results.

Ductility of the D43 was adversely affected by all of the coatings. Decreases of ultimate elongation which ranged from 27 to 60% less than the uncoated values (19%) were measured.

The D43 alloy was purchased in the stress relieved condition and showed no further grain growth or recrystallization after coating. The C129Y alloy, on the other hand, was submitted for coating in the wrought condition. The different coating processes produced varying degrees of annealing and recrystallization of the substrate. This was reflected in the tensile test results which, in general, showed a decrease in ultimate strength to values near that for recrystallized C129Y

and an increase in ultimate elongation approaching that of the annealed alloy. With one exception, the changes in tensile properties correlated with the degree of substrate recrystallization after making allowance for the reduction in substrate thickness by the coating process. This exception was the Pfaudler PFR-32 coated C129Y which exhibited little change in strength and ductility despite nearly full recrystallization of the substrate. It is likely that base metal contamination was responsible since the bend transition temperature of this system was rather high (75° to 125°F), whereas the BTT of the other coated C129Y specimens was well below room temperature.

Exceptionally low bend transition temperatures were measured for both coated alloys. Other than the LTV and the Pfaudler specimens, which had BTT values of 0° to 25°F and 75° to 125°F respectively for both alloys, ductility was maintained to -50°F, the lowest temperature investigated. Since columbium alloys are easily embrittled by interstitials, the vendors' control over this aspect of the coating process appears to be unusually well regulated.

The cyclic oxidation tests yielded a familiar pattern of relatively low reliability and a predominance of edge failures. With silicides in particular, coatings tended to develop deep fissures which resulted in premature failures. In the cyclic oxidation tests of D43 and C129Y, 50% of the failures at 2400° and 2600°F occurred at an edge.

Inadequate edge coverage was evident at 1600°F where edge failures were observed with 4 of the 6 coatings on both alloys in short term exposures. Since lifetimes exceeding several hundred hours would be anticipated for these coatings at 1600°, it can only be concluded that severe edge defects which exposed the substrate or left only a very thin protective layer were present in the specimen prior to test.

Only one coating demonstrated protective capabilities at 3000°F. This was the Sylcor Ag-Si-Al system (a 5 to 10 mil non-silicide slurry coating) which protected C129Y for 3 to 8 hours and D43 for 11 to 17 hours.

The other coatings, all of them silicides, failed in less than two hours at 3000°F. However, these coatings should not be downgraded for this reason, since it is highly probable that interaction between the silicide coating and the alumina support medium caused accelerated failures of the specimens.

Based upon Weibull plots, the life expectancy of these coatings in cyclic oxidation at 2600°F ranged from 4 to 130 hours for coated D43*. At 2400° and 2600°F, the life expectancy ranges for coated C129Y were 9 to 100 hours and 1 to 130 hours respectively. Reliability estimates based upon a 90% probability of

* Life expectancy is defined as the time to failure for 50% of the specimen population.

survival also showed a wide range of lifetimes. For coated D43 at 2600°F the lifetimes associated with 90% survival ranged from 1 to 58 hours. Coated C129Y at 2400° ranged from 1 to 90 hours and at 2600°F from less than 1 hour to 110 hours.

The outstanding performance of the Sylcor Ag-Si-Al on both alloys at 2400° and 2600°F was not unexpected in view of the relative thickness and good edge coverage provided by this coating. Among the silicides, the TRW Cr-Ti-Si was clearly the most oxidation resistant and consistently outperformed the other coatings at every temperature level but 1600°F. One batch of four TRW coated C129Y specimens failed very early in the 1600°F test, while a second batch successfully completed 48 hours at this temperature without failure.

The program plan called for creep-rupture evaluations of two coating systems per alloy. An error by one of the vendors eliminated one set of D43 specimens, making a comparison of creep-rupture behavior for different coatings possible only with the C129Y alloy.

In all of the creep-rupture tests, extremely clean specimen breaks were obtained with very little oxidation along the fracture line. This indicated that rupture life was controlled by the creep characteristics and that catastrophic oxidation was not producing premature rupture failures by gross removal of substrate material. The appearance of the ruptured specimens indicated that the coatings protected the substrate through relatively large levels of creep, probably up to the initiation of third stage creep.

The Ag-Si-Al coated D43 had measurably greater creep resistance and rupture strength than C129Y with the same coating.

At 2400°F, rupture life of the Cr-Ti-Si coated C129Y was more than twice that of the Ag-Si-Al coated alloy. At 2600° and 2800°F, the difference in rupture lives diminished significantly and the TRW system was only slightly better at these two higher temperatures. Very little difference in creep resistance was observed between the two C129Y systems for creep levels up to 3%. Since structural applications of columbium alloys are creep-limited, the greater rupture life of the Cr-Ti-Si coating has little practical utility. In terms of creep resistance, the two C129Y coating systems were considered equal.

None of the coating systems could be singled out as being superior to the others in every area of evaluation. Each coating had one or more serious deficiencies which could restrict its use in certain applications. In the final analysis, any overall performance rating must be closely tailored to a specific end use and factors such as reliability, mechanical properties, and creep behavior weighed accordingly.

In general, it was noted that these coatings are not really commercial systems, but are actually in an advanced development stage. Consequently,

problems with scale-up and reproducibility must be resolved before production hardware can be routinely processed.

Users of coated refractory metals must recognize that with diffusion type coatings a reduction in substrate cross sectional area and a corresponding reduction in "apparent" tensile strength is almost a certainty. Contamination by interstitial elements during the coating process will affect the strength, ductility, and bend transition temperature, if not well controlled.

Most of the coatings are processed at time-temperature levels sufficient to cause annealing of the substrate. Alloys which rely upon special heat treatment for their optimum properties are likely to be severely affected by the coating process. In cases such as this, postcoating heat treatment might be necessary to restore the substrate to its optimum condition.

Most of the coatings exhibited potential for fairly long high temperature service but were compromised by a propensity for early failures. If absolute perfection is demanded of these coatings, their reliability is extremely low. If, on the other hand, through proper design, an occasional slow-growing edge failure or pinhole defect in a coated component can be tolerated, the situation appears much improved.

The creep tests revealed that a coating can affect the rupture life of a columbium alloy. Such information, however, has little utility in evaluating the potential of systems for creep-limited structural applications.

The creep-rupture tested specimens in this program were well protected for the duration of the testing and showed no evidence of premature failure due to catastrophic oxidation. It would appear, therefore, for short term applications, that any coating which is reasonably nonreactive with the substrate and which provides protection to the substrate into secondary stages of creep will give satisfactory service.

Section II Arc-Plasma-Jet Testing

Arc plasma screening tests performed on two 2" x 2" x 1/2" resin impregnated foam systems and a gelatin molding compound were conducted in a 120 KW arc-plasma-jet in a simulated air effluent. In general, the test procedures followed the recommendations of the Refractory Composites Working Group.

One of the foamed zirconia systems, a Manufacturer I material, had exceptional thermal endurance. Unfilled specimens survived a full 300-second exposure at 275 Btu/ft² sec at equilibrium surface temperatures exceeding 4000 °F with only minor thermal stress cracking. This was in marked contrast to

previously evaluated unfilled foams which shattered in similar tests. With approximately 30 to 40 w/o phenolic resin impregnant, this material underwent no measurable erosion during test, provided good back surface thermal protection during resin ablation, and experienced no difficulties with thermal stress cracking.

In contrast to the Manufacturer I material, a phenolic impregnated foamed zirconia from Manufacturer UT was severely eroded, with burnthrough occurring in 120 seconds. In subsequent furnace tests, it was shown that the structure of the ceramic was not continuous and the foam would collapse after slow burn-out of the resin. It was concluded that, in this foam composite, the resin acted as a binder and, upon ablative decomposition of this resin, the ceramic would be washed away.

From tests of a gelatin molding compound at 100, 500, and 1000 Btu/ft² sec, it was concluded that this material offered little potential as a thermally protective ablator at these heat flux levels.

Tests of several phenolic/quartz laminates, including one with a top layer of 1/16" phenolic/graphite cloth, were conducted at several heat flux levels from 40 to 1000 Btu/ft² sec. No particular advantage over a phenolic/quartz laminate was noted with the two-layer system. Oxidation of the phenolic/graphite top layer resulted in rapid exposure of the phenolic/quartz substrate at all heat flux levels. The phenolic/quartz laminates exhibited typical ablative behavior for the class of materials, with perhaps somewhat less thermal insulating ability than had previously been observed.

The regular test procedure was modified for a screening evaluation of candidate ablative coatings for the Mach 8 version of the X-15 research aircraft. Coatings of nine different materials in several thicknesses were bonded to Inconel plates fitted with thermocouples to monitor bondline temperature. Tests were conducted at heat flux levels of 15, 40, and 150 Btu/ft² sec. These levels were representative of heating rates encountered at various regions of the aircraft during flight.

Two silicone elastomers from Manufacturers EG and MC were identified as having a potential for the X-15 application. Advanced plasma testing and a flight evaluation were recommended for these systems.

A technique for evaluating candidate nozzle materials in a simulated propellant combustion environment was also investigated. The experimental apparatus consisted of a 50 KW arc-plasma-jet equipped with a mixing chamber for controlled addition of liquids and gases to the plasma effluent, a fixture for coupling subscale test nozzles to the plasma jet discharge orifice, a test chamber, and a wet wash scrubber assembly for cleaning and disposing of the test products.

Initial tests were conducted on ATJ graphite nozzle test specimens approximately 1-3/4" long with a 1/2" diameter base which converged to a 1/8" diameter throat. The effects of additives of CO, CO₂, and H₂O were evaluated at specimen wall temperatures ranging from 2400° to 3500°F and peak pressures of approximately 50 psia.

Test results indicated that specimen erosion measured in terms of weight loss and throat area increase was a direct function of additive reactivity, pressure, and temperature. It was recommended that the study be continued with various materials, such as coated refractory metals, metal-ceramic composites, and reinforced plastics, and that experimental procedures be developed for simulation of multicomponent exhaust chemistries which, with suitable analysis, would identify reactive species and combinations thereof.

Section III Plasma-Sprayed Coating Studies

This phase of the program was directed toward the evaluation of metal-ceramic coatings deposited from premixed powder blends. The goal of the investigation was the development of techniques for the plasma spraying of metal-ceramic coatings of specific microstructure and composition for the purpose of developing tailored properties in the resulting composite material.

Coatings were prepared from a number of metal-ceramic blends. The influence of blend composition, particle size ratio, and the plasma spraying process variables were evaluated in terms of their effect upon bond strength and thermal shock endurance.

Metallic coatings of NiCr, Mo, NiAl, blends of NiCr-ZrO₂ and NiAl-Al₂O₃, and multilayer graded coatings of these materials were sprayed and tested.

This study demonstrated that composite coatings tailored for specific requirements could be prepared by plasma spraying. Predetermined volumetric proportions and microstructures in a binary coating could be obtained, and coating properties such as bond strength and thermal shock resistance could be modified. Fabricating the desired composite required control of the interdependent critical process variables (powder particle size ratio, spray power, and spray distance) to achieve proper thermal conditioning of the composite constituents.

Metallic coatings were found to be more dense and to have higher bond strength and thermal shock resistance than either the ceramic or composite coatings. The composite coatings of metal and ceramic exhibited significantly better thermal shock resistance than the pure ceramic coatings. The addition of coarse ceramic particles dispersed in the matrix of a metallic coating

improved bond strength by better than 1000 psi. This improvement was believed to be due to an annealing effect induced by heat retention of ceramic particles which reduced the cooling rate of the sprayed coating during deposition.

The importance of proper thermal conditioning in this spraying of materials emphasized the desirability of a better understanding of this phenomenon.

SECTION I THE EVALUATION OF COATINGS FOR REFRACTORY ALLOYS

INTRODUCTION

Interest in the refractory metal alloys as high temperature structural materials has fostered a substantial number of research efforts directed toward the development of effective coatings for the oxidation protection of these alloys.

Initially, the testing and evaluation associated with the development of these coatings was conducted independently by the research laboratories. This testing generally consisted of simple oxidation tests and limited mechanical property determinations. Several government agencies sponsored programs for the comparative evaluations of protective coating systems from several sources. Because these programs were oriented toward specific applications, they were sufficiently different in technique, scope, and emphasis that inter-laboratory comparison of test results was virtually impossible.

There was clearly a need for standardized tests designed to identify the more promising coatings from among the many under development. Three years ago, the University of Dayton received an Air Force contract to develop an evaluation program which was simple and readily standardized. This program was to be used to generate performance data for coatings of current interest. The objective was not to produce design data, but rather to assemble a body of information describing the effect of the coating process on the base metal and the relative response of coating-alloy combinations to specific environmental inputs. Emphasis was directed primarily, but not exclusively, toward sheet metal structural applications.

This program included a continuous re-evaluation of testing procedures with revision, where necessary, to increase the yield of information. Efforts of the Materials Advisory Board (Refs. 1 and 3) and the American Society for Testing and Materials in the area of standardized testing were continually reviewed, and their recommendations, where appropriate, were incorporated into the program.

The preliminary efforts of the University of Dayton in the development of a coatings evaluation program, as well as in the evaluation of TZM molybdenum and B66 columbium coating systems, are described in a report entitled, "The Evaluation of High Temperature Materials, Parts I and II" issued as ML-TDR-64-62 (Ref. 2). This work was performed under USAF Contract AF 33(616)-7838.

A continuation of this effort, covering the evaluation of D43 and C129Y columbium coating systems, is described in this report.

EXPERIMENTAL METHODS

The evaluation was intended to explore three areas: (1) the oxidation resistance of the coating; (2) the effects of the coating and/or coating process upon the mechanical and physical properties of the substrate alloy; and (3) the load-bearing capability of the coated alloy at elevated temperatures. This was accomplished by:

- metallographic analyses
- bend transition temperature measurement
- tensile tests
- cyclic oxidation tests at 1600° to 3000°F
with a failure rate analysis at 2600°F
- creep rupture tests in a full factorial experiment

METALLOGRAPHIC ANALYSES

Metallographic specimens of each coating system were prepared to study the effects of the coating process on the substrate and to evaluate the overall quality of the coating. Magnified visual inspection of substrate microstructure and of the coating itself permitted an evaluation of coating uniformity and integrity along with any changes in the substrate microstructure, such as grain growth and reactions between coating and substrate. Microhardness measurements of all zones were also conducted to supplement the visual analyses.

Coated specimens were prepared in the following manner:

- (1) sectioned with a fourteen inch diameter, high speed, SiC cutoff wheel and mounted in bakelite (processed at 4200 psi and 140 °C);
- (2) hand lapped to a flat surface for approximately two to three minutes on a cast-iron lapping wheel with 400 mesh SiC abrasive;
- (3) lead lapped for five minutes with 800 mesh emery abrasive to remove most of the coating cracks resulting from the cutting and prior lapping operation;
- (4) hand polished on a silk wheel using $1 \mu \text{ Al}_2 \text{ O}_3$ until all lead lap marks were removed;
- (5) further hand polished on a silk wheel with $3 \mu \text{ Al}_2 \text{ O}_3$;
- (6) final polished for approximately one hour in a vibratory polisher using $0.05 \mu \text{ Al}_2 \text{ O}_3$ on felt cloth.

During these first finishing operations, no special precautions were taken to avoid rounding of the specimen surfaces and a few coating cracks were usually present. Finishing to a flat, crack-free metallographic surface was achieved by repeating the sequence from lead lapping through vibratory polishing. The finishing time on the vibratory polisher for the second polishing cycle was reduced to forty-five minutes and then extended in fifteen-minute increments thereafter, as necessary. Occasionally, persistent cracks in the coating required that the lead lap through vibratory polish sequence be repeated two or three times before a satisfactory specimen was obtained.

Since the etchant for both alloys was reactive with the coatings, photomicrographs were prepared for each specimen in the unetched condition to show details of the coating and substrate diffusion regions. The specimens were then etched in a solution of 50 ml H_2O , 25 ml HF , and 25 ml HNO_3 for examination of the substrate microstructure.

BEND TRANSITION TEMPERATURE

Bend transition temperature tests were conducted to evaluate ductility changes in the coated substrate as a result of contamination and/or recrystallization produced by the coating process.

Bend transition temperature as defined by Ref. 3 is the lowest temperature at which a 90° free bend can be formed about a radius four times the thickness of a rectangular 1-1/4" x 1/2" test tab. A bend test fixture, shown in Figure 1, was placed in a controlled temperature chamber (-50 to 500°F) and linked to a universal testing machine. The fixture was designed for testing twenty-mil sheet stock and consisted of a rectangular female die which placed the specimen in three-point loading at the center by a male punch 0.08 inch in radius (four times the uncoated specimen thickness) and at each end by 0.08 inch radius support rollers with a center line spacing of 0.32 inch. A punch speed of 0.016 inch per minute was used. At this rate of bend, the operator had good control of the test and could easily detect brittle specimen failure.

A sufficient number of specimens were tested to bracket the transition temperature within a 25°F interval.

TENSILE TESTING

Room temperature tensile tests were conducted on coated specimens to measure changes in strength or ductility resulting from the coating process. Tests were conducted in triplicate using sheet specimens measuring 1" x 5-5/8" with a 1/2" wide gage section 2" in length.

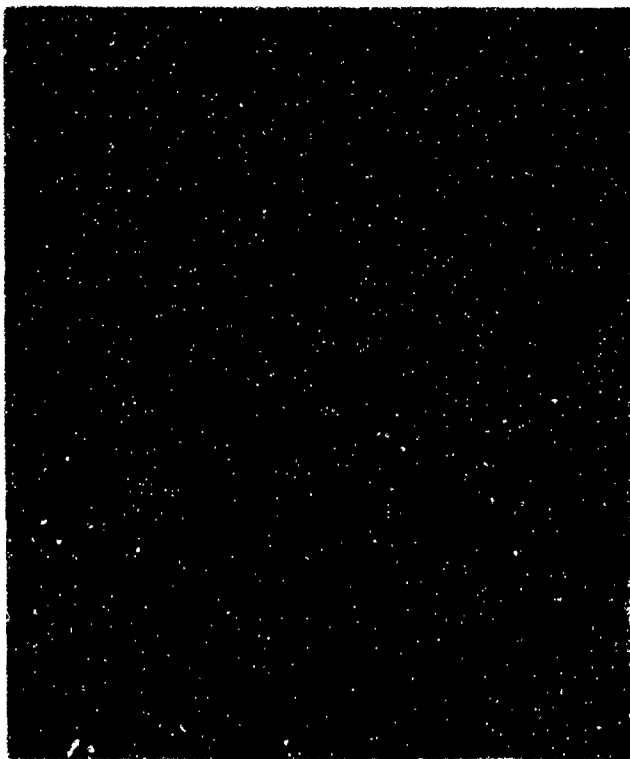


Figure 1. Transition Temperature
Fixture

A standard hydraulic universal test machine was employed for the tests. Strain measurements were recorded with a breakaway extensometer and converted to stress-strain diagrams for comparison with the uncoated alloy. Ultimate elongation was measured by placing the fractured specimens together and measuring the elongation within the gage length.

Ultimate and 0.1% offset yield strengths were compared before and after coating using the original specimen dimensions to calculate stress values for the coated specimens. Ultimate elongations were also compared before and after processing to determine any change in ductility.

CYCLIC OXIDATION TESTING

Since the value of a coating is measured largely by its ability to protect a substrate from oxidation, it follows that the type of oxidation test employed and the subsequent analysis of results are most important in a comparative screening of candidate coatings.

Furnace oxidation tests are the most widely used method for measuring the relative oxidation resistance of coatings. Its popularity stems from the inherent simplicity, low cost, and relative ease of testing large batches of specimens.

In this test, small coated tabs are furnace heated in air at specific temperature levels. At regular intervals the specimens are removed from the furnace, cooled to room temperature, weighed, and visually inspected. Specimens are retired from test at the first indication of substrate oxidation. Testing continues until all of the specimens have failed. The relative oxidation resistance of the coating is then rated as a function of the number of thermal cycles to failure.

Such testing was conducted in this program at four temperatures: 1600°, 2400°, 2600°, and 3000°F. Sheet specimens measuring 1-1/4" x 1/2" x 0.020" were exposed to these temperatures in resistance heated box furnaces. No special

provisions were made for air circulation or the measurement of oxygen content; normal leakage and the draft produced by periodic opening of the furnace door were considered sufficient to provide an adequate oxygen supply for testing. Except for the 1600°F tests, specimens were cycled to room temperature at one-hour intervals for weighing and inspection.

Figure 2 shows a group of specimens supported on high purity alumina boats (Norton RH3084) ready for insertion in a furnace. Because of possible interactions between oxidation products, different coating systems were never tested together.



Figure 2. Cyclic Oxidation Specimens Ready for Insertion into Furnace

The 1600°F tests served as a check for low temperature sensitivity. Four specimens were tested at this temperature for a 48-hour exposure with twice daily inspections at four-hour intervals and sixteen-hour overnight soaks.

In most of the 2400° and 3000°F tests, only four specimens of each coating system were tested. This provided a qualitative evaluation of performance at these temperatures. At 2600°F, at least ten specimens of each coating batch were tested and the data used to estimate coating reliability, to identify multiple failure modes, and to estimate the maximum cyclic life of the coating.

The Weibull distribution function was employed in the analysis of the 2600°F data. It is generally recognized that cyclic oxidation tests measure the

relative incidence and severity of critical coating flaws. Specimen failures should, therefore, follow a pattern of failure analogous to the failures of the weakest link of a chain. The Weibull function was considered appropriate since it describes this type of failure distribution.

In fitting empirical data to any statistical distribution, hundreds or even thousands of data points are required for absolute identification of the exact mathematical relationship of failure frequency. However, it is possible to estimate these failure distributions and place confidence limits upon such an estimate. The risk lies in assuming that estimates from a small number of samples are truly representative and can be used to make sweeping generalizations about the behavior of a coating system. It is also hazardous to use such data to extrapolate beyond the experimentally defined regions in an effort to predict reliability. Recognizing the limitations of empirical statistics derived from relatively few data points, less emphasis was placed upon "statistical constants," and the Weibull analysis was used primarily as a graphical display of failure data. Its secondary function was to identify multiple failure modes, to make gross estimates of reliability, and to determine the maximum probable coating life.

The Weibull cumulative frequency function is expressed by the mathematical relationship:

$$F(t) = 1 - e^{-\left(\frac{t-\alpha}{\theta}\right)^\beta}$$

where

- $F(t)$ = the cumulative failures expressed as a fraction of the original sample lot;
- t = time;
- α = the threshold or location parameter (normally equal to zero);
- θ = the time to failure of 63.2% of the sample population;
- β = the shape parameter ($\beta > 0$). *

Weibull probability paper, in which the log-log of the cumulative frequency function $F(t)$ is the ordinate and the log-time the abscissa, is available for graphical display of empirical data and evaluation of the various distribution parameters.

Since only ten to twenty specimens per coating were tested, it was necessary to approximate the time failure distribution through the use of ranking tables which have been developed for small tests (numerically less than 50) to estimate the most likely distribution curve as a function of the number of specimens tested and to generate a 90% confidence interval about this approximation (Ref. 4, Table 1).

* For $\beta = 1.0$ the distribution is exponential, for $\beta = 3.6$, the normal distribution is approximated

The purpose of these ranking tables is to estimate the validity of a numerically small-sized experiment with respect to the total sample population by generating upper and lower limits on the data which provide statistical assurance that true values lie within the interval formed by these limits. In describing the distribution of component failures by a graphical display on Weibull probability paper, cumulative failure percentages are plotted against time to failure. The ranking tables are employed to locate the interval in which the true cumulative failure percentage lies (with a specified level of probability) and the most likely position of this value.

The ranking levels of interest in this study were the median or 50% rank and the 95% and 5% ranks. The median rank represents that cumulative failure fraction which has an equal probability of being higher or lower than the true value. The 95% rank represents that value which has a 5% probability of being lower than the true value, a 95% probability of being higher. Conversely, the 5% rank has a 95% probability of being lower than the true value, a 5% probability of being higher.

Thus, the 95% and 5% rank levels establish an interval which has a 90% probability of containing the true cumulative failure fraction. The median rank locates the most likely position of that value.

A straight line fit of the median rank points is a good indication that a failure distribution can be represented by a Weibull function. It should be noted that assuming the location parameter (α) to be zero may not result in a straight line, and it may be necessary to assign a positive value to this parameter to obtain a linear fit (Ref. 5). Occasionally, the data are better fitted with two or more straight line segments. This is generally an indication that two or more failure modes are active. Multisegmented distribution curves often can be correlated with the physical characteristics of different failure modes.

On a Weibull plot of failure data, the physical slope of the line segment measured directly from the curve will provide information regarding the nature of the failure process. Defective components, improperly prepared or damaged in pretest handling, will form a distribution line of slope less than one (a so-called "infant mortality" distribution), while failures representing general wearout will assume a distribution having a slope greater than one. As the slope of the distribution increases, the dispersion of life test data diminishes and failures become more uniform.

Weibull plots also can be used to estimate the reliability of a system, i. e., its probability of survival for any given lifetime, provided no attempts are made to extrapolate beyond the experimental confines of the data. For tests involving ten to twenty samples, it would be unwise to project such an analysis beyond reliability levels of 0.90 to 0.95.

Table I.
Rank Tables for 5% and 95% Confidence Limits
and Median Rank for Specimen Sizes 1 to 20

		No. of Specimens															
		1			2			3			4				5		
		5%	50%	95%	5%	50%	95%	5%	50%	95%	5%	50%	95%		5%	50%	95%
No. of Cumulative Failures	1	5	50	95	2.3	29	78	1.7	21	63	1.3	16	53	1.0	13	45	1
	2				22	71	97	14	50	83	10	39	75	7.6	31	66	2
	3							37	79	98	25	61	90	19	50	81	3
	4										47	84	99	34	68	92	4
	5													55	87	99	5
		No. of Specimens															
		6			7			8			9				10		
		5%	50%	95%	5%	50%	95%	5%	50%	95%	5%	50%	95%		5%	50%	95%
No. of Cumulative Failures	1	.8	11	39	.7	9.4	35	.6	8.3	31	.6	7.4	28	.5	6.7	26	1
	2	6.3	26	58	5.3	23	52	4.7	20	47	4.1	18	43	3.7	16	39	2
	3	15	42	73	13	36	66	11	32	60	9.8	29	55	8.7	26	51	3
	4	27	58	85	22	50	77	19	44	71	17	39	65	15	35	61	4
	5	42	73	94	34	63	87	29	56	81	25	50	75	22	45	70	5
	6	61	89	99	48	77	95	40	68	89	34	61	83	30	55	78	6
	7				65	90	99	53	80	93	45	71	90	39	64	85	7
	8							69	92	99	57	82	96	49	74	91	8
	9										72	93	99	60	84	96	9
	10													74	93	99	10
		No. of Specimens															
		11			12			13			14				15		
		5%	50%	95%	5%	50%	95%	5%	50%	95%	5%	50%	95%		5%	50%	95%
No. of Cumulative Failures	1	.5	6.1	24	.4	5.6	22	.4	5.2	20	.4	4.8	19	.3	4.5	19	1
	2	3.3	15	36	3.1	14	34	2.8	13	32	2.6	12	30	2.4	11	27	2
	3	8	24	47	7.2	22	44	6.6	20	41	6.1	19	38	5.7	17	36	3
	4	14	32	56	12	30	53	11	28	49	10	26	46	9.7	24	44	4
	5	20	41	65	18	38	61	17	35	57	15	33	54	14	30	51	5
	6	27	50	73	24	46	68	22	42	64	21	39	61	19	37	58	6
	7	35	59	80	31	54	75	29	50	71	26	46	67	24	43	64	7
	8	43	67	86	39	62	82	35	57	77	33	53	73	30	50	70	8
	9	53	76	92	47	70	88	43	65	83	39	60	79	36	56	75	9
	10	63	85	97	56	78	93	50	72	89	46	67	85	42	63	81	10
	11	76	94	99	66	86	97	59	80	93	53	74	89	49	69	86	11
	12				78	94	99	68	87	97	61	81	94	56	76	90	12
	13							79	95	100	70	88	97	64	82	94	13
	14										81	95	100	72	89	96	14
	15													82	95	100	15
		No. of Specimens															
		16			17			18			19				20		
		5%	50%	95%	5%	50%	95%	5%	50%	95%	5%	50%	95%		5%	50%	95%
No. of Cumulative Failures	1	3	4.2	17	.3	4	16	.3	3.8	15	.3	3.6	15	.3	3.4	14	1
	2	2.3	10	26	2.2	9.7	25	2	9.2	24	1.9	8.7	23	1.8	8.3	22	2
	3	5.4	16	34	5	15	33	4.8	15	31	4.5	14	30	4.3	13	28	3
	4	9.1	22	42	8.5	21	39	8	20	38	7.6	19	36	7.2	18	35	4
	5	13	29	48	12	27	46	12	25	44	11	24	42	10	23	40	5
	6	18	35	55	17	33	52	16	31	50	15	29	47	14	28	45	6
	7	23	41	61	21	38	58	20	36	55	19	34	53	18	33	51	7
	8	28	47	66	26	44	64	24	42	61	23	40	58	22	38	56	8
	9	33	53	72	31	50	68	29	47	64	27	45	63	26	43	60	9
	10	39	59	77	35	56	74	34	53	71	32	50	68	30	47	65	10
	11	45	65	82	42	61	79	39	58	75	37	55	72	35	52	70	11
	12	51	71	87	48	67	83	45	63	80	42	60	77	39	57	74	12
	13	58	77	91	54	73	87	50	69	84	47	65	81	44	62	79	13
	14	66	83	95	60	79	91	56	74	88	52	71	85	49	67	82	14
	15	74	90	98	67	84	95	62	80	92	58	76	89	54	72	86	15
	16	83	96	100	75	90	98	69	85	95	64	81	92	60	77	88	16
	17				83	96	100	76	91	97	70	86	85	65	82	93	17
	18							84	96	100	77	91	99	71	87	96	18
	19										85	96	100	78	92	98	19
	20													86	96	100	20

CREEP RUPTURE TESTING

In order to gain insight into the high temperature structural capability of candidate coating systems, creep rupture tests were conducted at three levels of temperature (2400°, 2600°, and 2800°F) and three levels of stress (6000, 7500, and 9000 psi).

The problems of inconsistency and scatter of data associated with normal creep testing are compounded in testing coated refractory alloys by variations in the coating oxidation resistance from batch to batch and from specimen to specimen. Specimens with severe coating defects may fail prematurely by catastrophic oxidation, while "identical" specimens lacking critical flaws may survive much longer exposures. Another factor which must be considered is the effect of subtle, but significant differences among the testing machines employed which can affect the test results. To monitor the effect of any uncontrolled test variables, such as specimen and testing machine variability, creep rupture tests were performed in a full factorial experiment which was statistically evaluated to determine the relative effect of all test variables and their interactions.

In the evaluation of coated D43 columbium alloy, thirty-six tests were required to evaluate the relative effects of temperature (three levels), stress (three levels), and to assess the effect of the two coating batches and the two machines which were involved in these tests.

The experimental design was modified in subsequent tests of coated C129Y columbium alloy. Thirty-two tests were performed on two coating batches at two stress levels (6000 and 9000 psi) and two temperatures (2400° and 2800°F), using four creep testing machines.

The resulting data were treated with a standard analysis of variance to determine the relative significance of the input variables and their interactions. To do this, a comparison of the expected mean square of each source of known input variance was made with the error term to determine which made a statistically significant contribution to the output (time to rupture).

To provide intermediate data points for the creep rupture plots prepared from the test data, supplemental tests of the C129 creep rupture plots were conducted at 2600°F on specimens from each coating batch at stress levels of 6000, 7500, and 9000 psi as well as at 2400° and 2800°F at 7500 psi.

The testing apparatus shown in Figure 3 consisted of standard lever-arm-type creep testing machines with a 20:1 load ratio and induction heated specimen furnaces.

The 1-1/2" x 6" rectangular test specimen was slipped through the induction furnace susceptor element (modified JTA graphite composite) and heated at the center over a 1-3/4" span. Temperature measurements were taken with

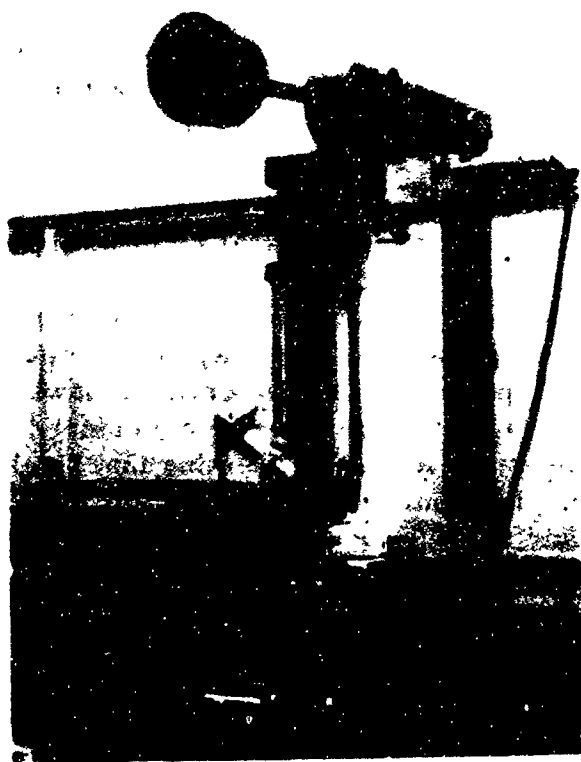


Figure 3. Testing Apparatus Consisting of a Standard Lever-Arm-Type Creep Testing Machine

an optical (disappearing filament type) pyrometer by sighting on the specimen through a hole in the side of the susceptor. A total radiation (thermopile type) pyrometer mounted above and focused on the susceptor was used to control the induction heater power supply.

Because of the extreme temperatures in the specimen hot zone and problems with coating compatibility, extensometer measurement of elongation was not attempted. Since practically all elongation occurred over a 1.75 inch long section of the specimen, elongation was measured as a function of lever-arm displacement and converted to percentage creep on the assumption that all elongation was confined to a gage length of 1.75 inches. Lever-arm displacement was measured with a linear differential transformer and recorded for a permanent record of creep extension.

The test procedures were as follows: with the susceptor at room temperature, a specimen was slipped through and pinned at either end in TD nickel grips. A one-pound weight was added to the back of the creep-frame lever arm to load the specimen lightly and draw the connecting linkage taut. The specimen was then centered in the susceptor and the extensometer zeroed. The one-pound load was removed and the specimen heated to test temperature. When the

susceptor stabilized at temperature, the control setting of the total radiation pyrometer was adjusted to maintain this temperature and the test load slowly applied by an elevator mechanism. Temperature and load were maintained until specimen rupture.

MATERIAL AND SPECIMEN PROCUREMENT

The two columbium alloys evaluated in this program were D43 (Cb-10W-1Zr) and C129Y (Cb-10W-10HF-0.1Y). The D43 was obtained from E. I. DuPont de Nemours and Company in 12 and 20 mil thicknesses, the C129Y from Wah Chang Corporation in 20 mil sheet only. The composition and mechanical property data supplied by the vendors of these alloys are summarized in Table 2.

Table 2. Compositional and Property Data Furnished by the Alloy Vendors for D43 and C129 Columbium Alloys

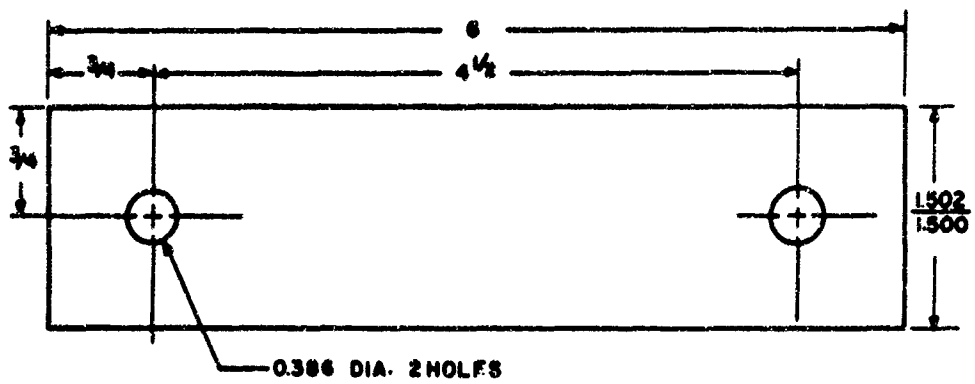
Alloy-Heat and/or Heat No.	Alloying Elements -%					Impurities-PPM				Tensile Strength - KSI				Elong. (%)		Condition
	Zn	W	Hf	Y	Cb	C	N	O	H	Ultimate		0.27 Yield		Trans.	Long	
										Trans.	Long	Trans.	Long			
D43 (0.012") 43-396-13	0.96	9.6	--	--	Bal.	985	46	244	3	85.6	82.7	61.7	66.7	15.5	20.0	Annealed
D43 (0.020") 43-283	0.95	9.8	--	--	Bal.	920	33	93	1	86.9	83.8	60.6	60.5	20.0	22.0	Stress Relieved
C129Y (0.020") 46-70613	--	10.3	8.9	0.07	Bal.	100	50	90	2.6	--	89.8	--	75.7	--	25.0	Not Stated*

* Mechanical data for 30 mil C129Y sheet which has been recrystallized 1 hour at 2200°F.

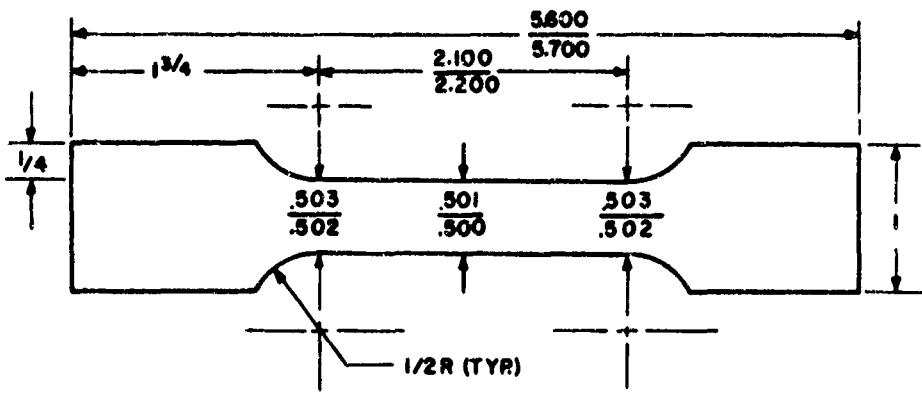
The three types of specimens used in this program are shown in Figure 4. All C129Y specimens were of 20 mil thickness; the D43 creep-rupture specimens were fabricated from the 12 mil sheet, the remainder from 20 mil stock.

Specimens from both alloys were fabricated by shearing oversize and milling to final dimensions with a high speed end mill. All specimens were prepared with their major axis parallel to sheet rolling direction.

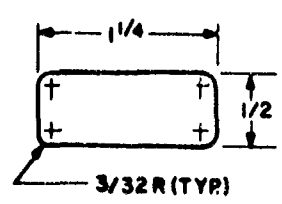
The edges of the specimens were rounded to a radius of 5 to 7 mils in a SWECO vibrating finishing mill. The abrasive medium was a mixture of two parts number 1-1/2A and one part number 5A Norton Alundum stones. A small amount of low sudsing powdered detergent was added to the mix along with just enough water to keep the stones wet.



TENSILE FATIGUE, STRESS RUPTURE
AND THERMAL STRESS SPECIMEN



TENSILE SPECIMEN



BEND & OXIDATION SPECIMEN

Figure 4. Coating Test Specimens

COATING SELECTION

So that a maximum number of coating-alloy combinations would be represented in the program, the evaluation procedure was divided into two phases. The first was essentially a screening phase consisting of complete metallographic analyses of the "as coated" alloy, tensile strength and bend transition temperature measurements, and cyclic oxidation tests; all Phase I specimens tested were to represent a single coating process run. Based on the results of the screening phase, two coatings per alloy were selected for Phase II testing which included the full factorial creep-rupture test and a replication of the screening tests. The Phase II specimens were to be coated in two batches either sequentially in the same retort or in two different retorts. Half the creep-rupture specimens were to be coated in one batch, and the other half (plus the second set of screening specimens) were to be coated in the other batch. Any short term process variability could thereby be measured in the evaluation.

With the concurrence of the AFML Project Engineer, the same six vendors coated both D43 and C129Y alloys for Phase I testing. They were: Thompson-Ramo-Wooldridge (TRW), Sylcor Division of Sylvania Electric Products Corporation, the Pfaudler Company, LTV Corporation, the Boeing Company, and Chromizing Corporation. On the basis of performance of these screening tests (primarily in cyclic oxidation), TRW and Sylcor were selected to coat specimens of both alloys for Phase II tests.

The TRW Cr-Ti-Si coating is a titanium and chromium modified silicide applied in two consecutive vacuum pack cycles. The first cycle consists of an eight-hour treatment at 2250 °F in a 50 Cr-50 Ti prealloyed pack with a KF activator. The second is a three-hour cycle at 2050 °F in a silicon pack also with a KF activator.

The Sylcor coating is a silver-aluminum modified silicide (R 508) applied as a sprayed slurry and fired at 2300 ° to 2500 °F. In an effort to improve the coating and reduce firing temperature, Sylcor has slightly changed the composition of the slurry from time to time, using three different designations (A, B, and C) to describe their 508 series coatings.

The Pfaudler coating is a modified silicide of proprietary composition designated as PFR-32.

The LTV coating is a Cr-B modified silicide with silicon deposited in the first cycle and chromium and boron codeposited in the second cycle. A slip pack cementation process is employed in both cycles, which are approximately eight hours in duration at a process temperature of 2000 °F.

The Boeing Disil coating is a modified silicide produced in a fluidized bed process.

D43 Coatings

TRW gave no indication of difficulty in coating the Phase I specimens. However, contrary to instructions, all of the creep-rupture Phase II specimens were coated in one batch and the remainder of the specimens in another. Thus, a batch-to-batch comparison of creep-rupture behavior was impossible. Furthermore, none of the creep-rupture specimens received a proper chromium precoat because of a processing accident, and the resultant coating was unacceptable. It was necessary, therefore, to eliminate creep-rupture tests in the evaluation of this coating.

Sylcor reported that the Phase I specimens were coated in two batches: the tensile specimens in one and the bend and static oxidation specimens in another. The resulting weight gain of the tensile specimens was 20% less than the other specimens, indicating that the former received a thinner coating. In processing the Phase II specimens, Sylcor encountered difficulties in coating the specimens in two batches. In processing the first batch of creep-rupture specimens, proper separation of individual specimens was not maintained. A number of specimens stuck together and had to be reprocessed. The second batch of creep-rupture specimens was subdivided into two batches to prevent the reoccurrence of this problem. All Phase I and Phase II specimens were coated using Sylcor's R 508B process.

Boeing encountered difficulty in applying the Disil coating and found it necessary to pickle the specimens to achieve a proper surface finish. The pickling treatment removed approximately 1.0 mil of material from each side of the specimens. Despite this surface treatment, nine specimens were judged to contain defects and were not returned. Boeing did not anticipate good performance of their coating on those specimens which were returned.

LTV, Chromizing, and Pfaudler presumably had no difficulty in coating this alloy.

C129Y Coatings

Sylcor employed their R 508B process in coating the Phase I specimens and reported some difficulties with "blobbing" of the coating during a diffusion treatment, resulting in considerable nonuniformity in coating thickness. Prior to the processing of the Phase II specimens, Sylcor modified their coating procedure to permit lower processing temperatures and, consequently, less effect upon mechanical properties of the substrate. This modified process, designated as R 508C, was employed in coating all of the Phase II specimens for which no difficulties were reported.

None of the other five vendors reported any difficulties in coating the C129Y specimens.

EXPERIMENTAL RESULTS

METALLOGRAPHIC ANALYSES

Photomicrographs of all the D43 and C129Y coating systems, as well as those of the uncoated alloys, are shown in Figures 5 through 15. Note that the photomicrographs consist of two separate photographs: one of the coating and unetched substrate, and another of an etched section from the center of the substrate. This technique was utilized because of reactivity of the coating and intermediate zones with the columbium etchant. Microhardness and coating thickness data are summarized in Tables 3 and 4.

D43 Columbium Alloy

In general, all of the Phase I coatings on this alloy, except the Sylcor system, exhibited good substrate coverage, and all were fairly uniform in thickness. The Sylcor coating consisted of a two mil thick uniform zone adjacent to the substrate and a very porous and irregular two-phase outer layer, which varied from approximately 5 to 11 mils (see Figure 8). This outer zone was essentially very soft (57 DPH), with small hard (2290 DPH) isolated zones scattered within it. The other five coatings ranged in average thickness from 1.2 mils (Chromizing) to 3.6 mils (LTV). The Pfaudler, Chromizing, LTV, and Boeing coatings all were slightly thicker at specimen edges, which previous experience has shown to be characteristic of silicide coatings.

The Pfaudler, Chromizing, and Boeing coatings showed no evidence from visual examination or microhardness measurements of any diffusional reactions between coating and substrate. The LTV coating had three distinct zones. The TRW coating had a broad diffusion zone approximately 1-1/2 mils thick which contained many "islands" much harder than the surrounding matrix.

Each coating process produced some reduction in substrate thickness ranging from 0.6 mil/side for the PFR-32 coating to a maximum of 1.9 mils/side for the LTV two-cycle silicide. None of the specimens showed any evidence from visual examination or microhardness measurements of a change in substrate microstructure as a result of the coating process.

Comparative photomicrographs of the TRW Phase I and II specimens are presented in Figure 6. These specimens were slightly different with respect to average coating thickness (2.0 and 1.6 mils) and loss of substrate thickness after coating (.82 and .62 mil/side respectively). Both coatings were similar in appearance, and microhardness measurements within the various zones were not appreciably different.



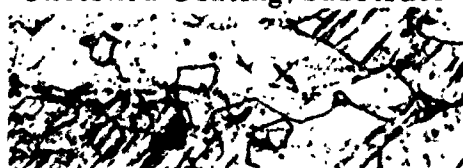
(250x)

Figure 5. Photomicrograph of Uncoated D43

Phase I



Unetched Coating/Substrate



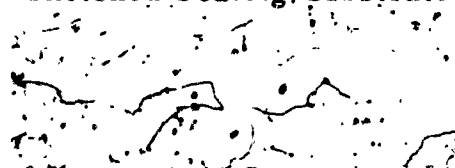
Etched Substrate

(250x)

Phase II



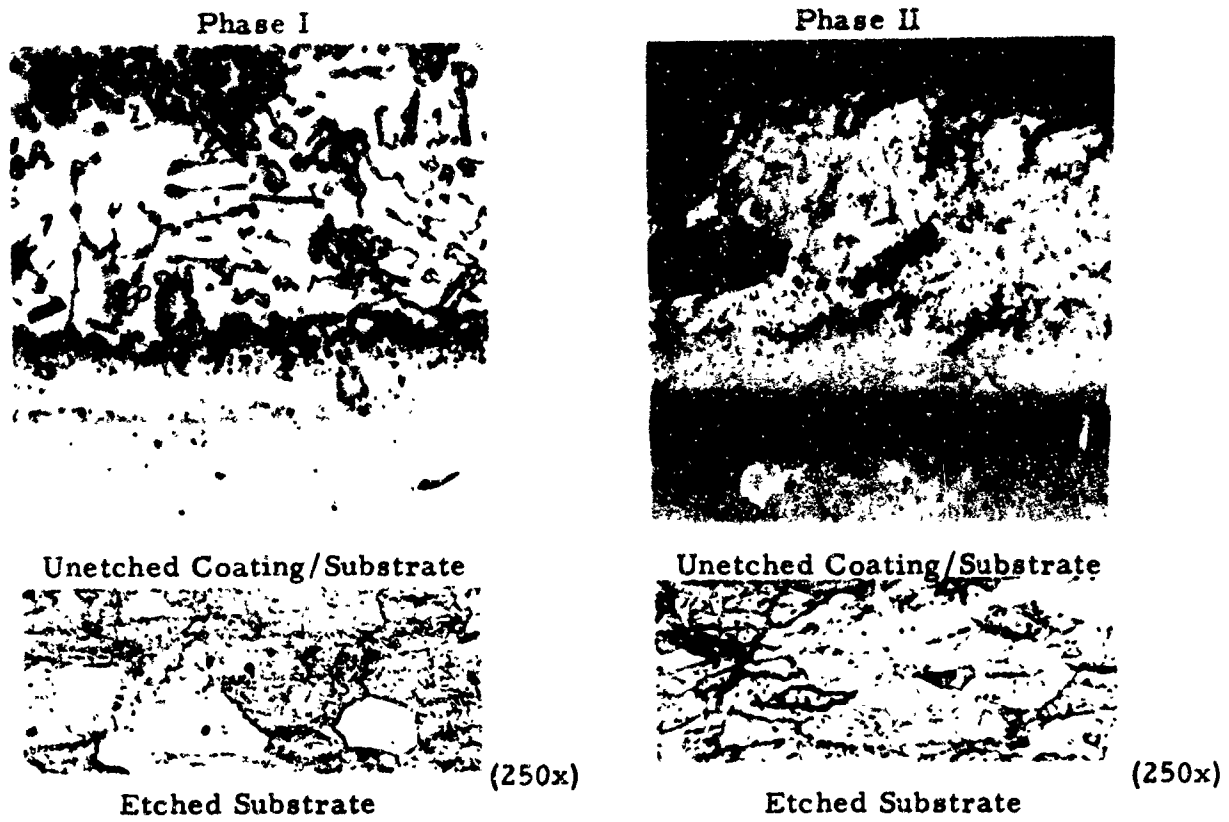
Unetched Coating/Substrate



Etched Substrate

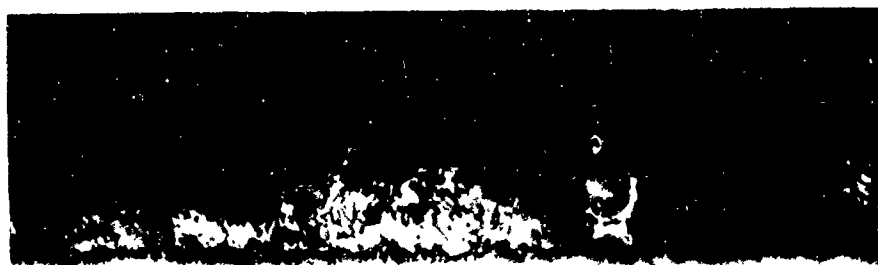
(250x)

Figure 6. Comparative Photomicrographs of Coated D43



Sylcor Ag-Si-Al

Figure 7. Comparative Photomicrographs of Coated D43



(100x)

Figure 8. Irregularity of Sylcor Coating on D43

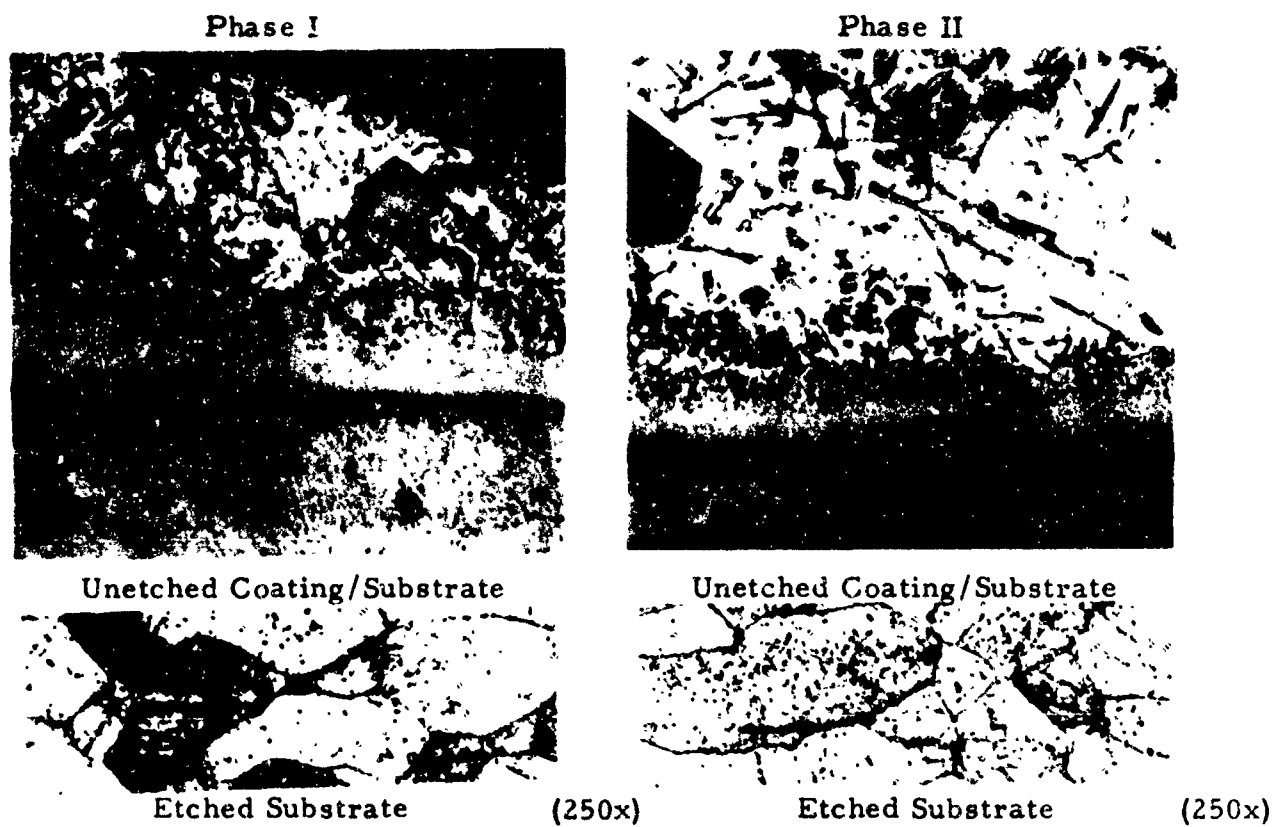
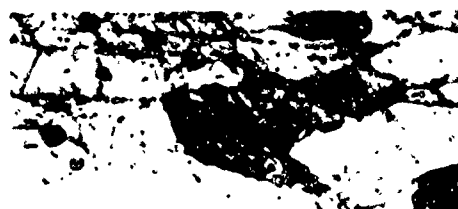


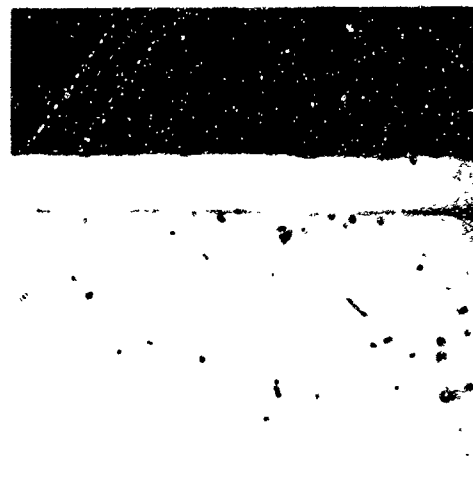
Figure 9. Sylcor D43 Creep Rupture Specimens



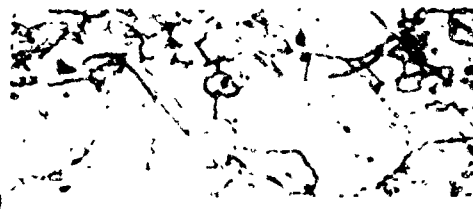
Unetched Coating/Substrate



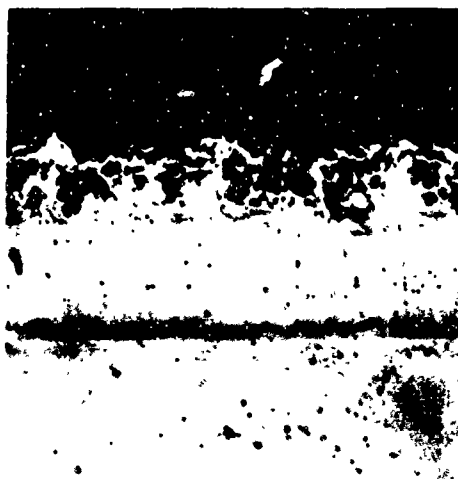
Etched Substrate
Boeing Disil



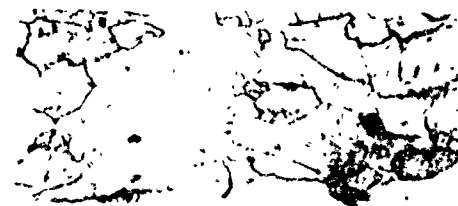
Unetched Coating/Substrate



Etched Substrate
Chromizing Durak KA



Unetched Coating/Substrate



Etched Substrate
LTV Modified Two-Cycle
Silicide



Unetched Coating/Substrate



Etched Substrate
Pfaudler PFR-32

Figure 10. Typical Photomicrographs of Coated D43

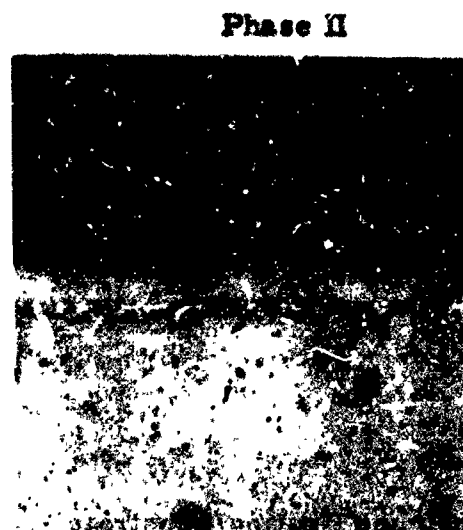


Unetched Coating/Substrate



Etched Substrate

(250x)



Unetched Coating/Substrate



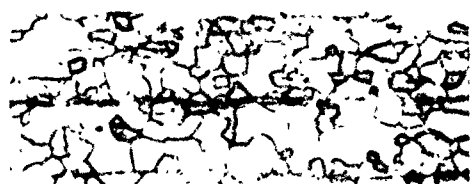
Etched Substrate

(250x)

Figure 11. Comparative Photomicrographs of TRW Cr-Ti-Si Coated C129Y



Unetched Coating/Substrate

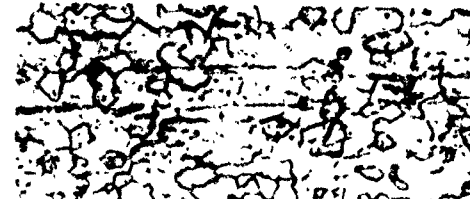


Etched Substrate

(250x)



Unetched Coating/Substrate



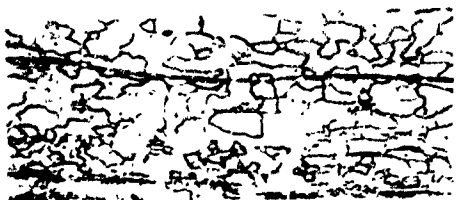
Etched Substrate

(250x)

Figure 12 Comparative Photomicrographs of Sylcor Ag-Si-Al Coated C129Y



Unetched Coating/Substrate



(250x)

Etched Substrate
LTV Cr-B Modified Silicide

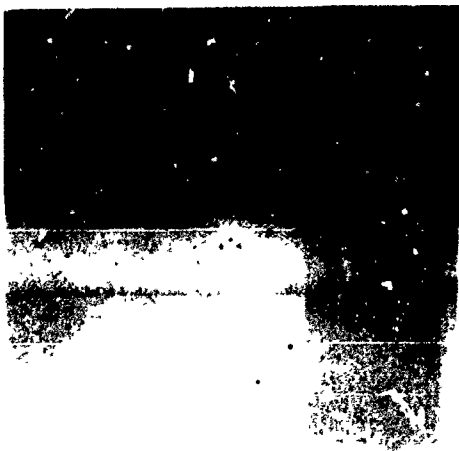


Unetched Coating/Substrate



(250x)

Etched Substrate
Pfaudler PFR-32



Unetched Coating/Substrate



(250x)

Etched Substrate
Boeing Disil



Unetched Coating/Substrate



(250x)

Etched Substrate
Chromizing Durak KA

Figure 13. Typical Photomicrographs of Coated C129Y

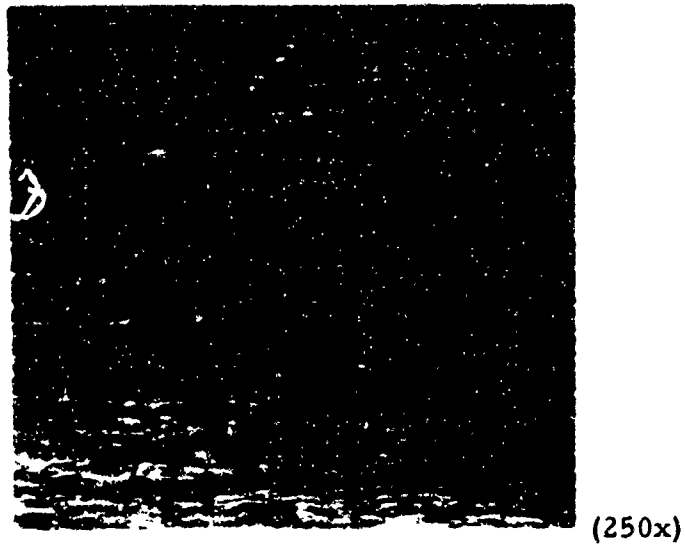


Figure 14. Photomicrograph of Uncoated C129Y



Phase i



Phase II (1x)

Figure 15. Phase Comparison of TRW Cr-Ti-Si Coating on 20 mil C129Y

Table 3. Metallographic Data for Coated D43, Phases I and II

Coating	DPH HARDNESS						Substrate Thickness (mils) Before After
	Phase	Coating	Outer Intermediate Zone	Center Zone	Inner Zone	Nominal Coating Thickness (mils)	
Chromizing (Durak KA)	I	1855/2900*	- -	- -	- -	1.2	20.1 18.65
Pfudler (PFR-32)	I	1534/1855*	- -	- -	- -	1.8	19.7 18.40
LTV (Cr-B Modified Two Cycle Silicide)	I	2900	2900	2290	1855	3.6	19.8 16.0
Boeing (Disil)	I	1855	- -	- -	- -	2.4	19.3 17.2
TRW (Cr-Ti-Si)	I	3790/1097*	572/946**	- -	237	2.0	19.8 18.15
	II	2290/1288*	514/1207**	- -	- -	1.6	20.1 18.85
Sylcor (Ag-Si-Al)	I	57/2290**	1033	- -	1033	7.2 - 13.6	19.7 18.00
	II	116/946**	1097/1288**	- -	- -	2.4 - 7.6	20.4 16.60
Sylcor (Ag-Si-Al)**	I	116/1097**	1097	- -	- -	2.0 - 12.0	- - 10.40
	II	88/1097**	1097	- -	- -	2.0 - 16.0	- - 10.95
Uncoated	I	- -	- -	- -	- -	- -	- - - -

* Inner boundary/outer boundary

** Zone/"islands" within zone

*** Creep-rupture specimens

Table 4. Metallographic Data for Coated C129Y, Phases I and II

Coating	DPH HARDNESS						Nominal Coating Thickness (mils)	Substrate Thickness (mils)	
	Phase	Coating	Outer Intermediate Zone	Center Zone	Inner Zone	Substrate			
Chromizing (Durak KA)	I	2290	- -	- -	- -	274	1.4	20.8	19.40
Pfadtler (PFR-32)	I	2290/1855*	- -	- -	- -	262	2.0	19.8	18.40
LTV (Cr-B Modified Two Cycle Silicide)	I	2290	- -	1246	1132	262	2.6	20.0	17.75
Boeing (Disil)	I	1855	- -	- -	- -	206	2.1	20.6	18.35
FRW (Cr-Ti-Si)	I	2290	1534	- -	- -	262	2.1	20.3	19.20
	II	1855/1097*	- -	- -	- -	274	1.6	21.4	20.40

Sylcor (Ag-Si-Al)	I	96/1855**	2290/1534*	- -	- -	297	4.8 - 10.6	20.7	18.45
	II	110/1288**	1097	- -	- -	215	5.76-8.56	19.9	17.75
Uncoated	I	- -	- -	- -	- -	297	- -	20.8	- -

* Inner boundary/outer boundary

** Zone/"island" within zone

*** Numerous "islands" within substrate too small for hardness measurements

The Sylcor Phase I and II specimens, shown in Figure 7, were somewhat different. Both exhibited similar diffusion zones of uniform thickness (approximately 2 mils); however, the outer zone of the Phase II specimen was absent in spots and as thick as 5.2 mils in other areas. Average thickness was less than the Phase I coating, but was also more irregular. Substrate losses, as a result of the coating process, were also different, being approximately one mil/side for the Phase I specimen and 2 mils/side for Phase II. Micro-hardness measurements were similar for the various diffusion zones, except for the "islands" in the coating which were much harder in the Phase I coating (2290 DPH as compared to 946 DPH).

In a further study of the Sylcor coating, one specimen from each of the creep-rupture specimen batches was prepared. It was felt that these specimens, fabricated from thinner sheet than the rest of the specimens (0.012 inches instead of 0.020), might provide an interesting comparison with the 20 mil specimens. These specimens, shown in Figure 9, were quite similar, exhibiting virtually the same hardness measurements and inner zone thicknesses. Coverage by the outer zone was somewhat erratic. It was missing in some areas and up to 16 mils in thickness in others.

The most appreciable difference among the four specimens was the range of outer zone thickness. This was probably not a batch difference, but rather a specimen-to-specimen difference. A spot check of some of the other specimens from common batches also showed a large variability of overall coating thickness. All prepared specimens seemed to have approximately the same 2 mil inner zone thickness, however.

C129Y Columbium Alloy

All six coating systems evaluated in the screening phase of the program were very similar to the D43 specimens. All exhibited void-free substrate coverage with reasonably uniform coating thickness, except for the Sylcor specimens which varied from 4.8 to 10.6 mils. The five other coatings were much thinner, averaging 1.4 mils (Chromizing) to 2.6 mils (LTV), with a slight thickening at the edges.

As with the D43 coatings, there was no evidence of a diffusional reaction between the coating with substrate of the Boeing, Pfaudler, or Chromizing specimens, but the Sylcor, LTV, and TRW systems each contained intermediate zones. The Sylcor system was very similar to the D43 coating, containing one intermediate zone and numerous hard "islands" in the porous outer layer. The LTV system, like the D43 coating, contained three distinct zones. The TRW Phase II coating differed from the D43 coating in that no hard "islands" were found within the diffusion zone.

In every instance, there was some reduction in substrate thickness after coating. Approximately one-half mil/side was observed with the TRW, Chromizing, and Pfudler coatings and approximately one mil/side with the Sylcor, LTV, and Boeing coatings. Substrate recrystallization was observed in five of the six coatings, particularly in the TRW, Sylcor, and LTV systems. Only the Chromizing process failed to alter the substrate microstructure.

Comparative photomicrographs for the TRW and Sylcor Phase I and II specimens are presented in Figures 11 and 12.

The Sylcor specimens were quite similar in appearance. Both coatings were comparable in thickness (7.7 and 7.2 mils, respectively) and experienced approximately the same loss of substrate thickness as a result of the coating application (1.12 and 1.07 mils respectively). The only notable difference was the higher hardness values within the various zones of the Phase I specimen (see Table 4).

The two TRW coating batches were quite different. The surface of the Phase II coating was much darker in appearance than the Phase I coating, as shown in Figure 15. In cross section, the Phase I coating had an intermediate layer which was not visible in the Phase II system. Furthermore, at the coating-substrate interface of the Phase II coating, irregularly spaced fingers extended from the base of the coating into the substrate. Nominal coating thickness was one-half mil less in the Phase II specimen. With respect to microhardness and loss of substrate thickness, the two coating batches were not appreciably different.

BEND TRANSITION TEMPERATURE

Bend transition data are summarized for both alloys in Table 5. Included with these data are test results for uncoated D43 and C129Y, both of which were ductile at -50 °F (the lowest temperature at which tests were conducted).

D43 Columbium Alloy

The Sylcor and TRW coatings, both evaluated in two batches, exhibited no loss of ductility in this test. Ductile 90° bends were formed in specimens from both batches of each coating at -50 °F.

Of the other four coatings tested in a single batch, the Chromizing and Boeing coatings maintained a BTT below -50 °F, while the BTT of the LTV specimens increased to between 125° and 150 °F, and that of the Pfudler samples increased to between 125° and 150 °F.

C129Y Columbium Alloy

These six coating systems behaved very similarly to the D43 coatings. Among the coatings tested in one batch, only the Chromizing and Boeing coatings

Table 5. Bend Transition Temperature Measurements
of Coated D43 and C129Y

<u>D43</u>		
<u>Coating Vendor</u>	<u>Coating Designation</u>	<u>Bend Transition Temperature (t) - °F</u>
TRW (Two Phases)	Cr-Ti-Si	-50 > t
Chromizing	Durak KA	-50 > t
Pfautler	PFR-32	75 < t < 125
Sylcor (Two Phases)	R508	-50 > t
LTV	Cr-B Modified Two-Cycle Silicide	0 < t < 25
Boeing	Disil	-50 > t
<u>C129Y</u>		
<u>Coating Vendor</u>	<u>Coating Designation</u>	<u>Bend Transition Temperature (t) - °F</u>
TRW (Two Phases)	Cr-Ti-Si	-50 > t
Chromizing	Durak KA	-50 > t
Pfautler	PFR-32	125 < t < 150
Sylcor (Two Phases)	R508	-50 > t
LTV	Cr-B Modified Two-Cycle Silicide	0 < t < 25
Boeing	Disil	-50 > t

maintained a BTT below -50°F , the Pfaudler coating showed an increase in BTT to between 125° and 150°F , and the LTV system increased to a value between 0° and 25°F . The TRW and Sylcor coatings, both tested in two batches, were ductile at -50°F .

TENSILE TESTING

Room temperature tensile test results are summarized in Table 6 for D43 and in Table 7 for C129Y. Supplementing the tabular data are typical stress-strain diagrams for each coating system (Figures 16 through 19).

D43 Columbium Alloy

In Phase I testing, the Pfaudler, LTV, and Sylcor coatings had virtually no effect on the yield or ultimate strengths of the alloy. The LTV specimens actually showed a 9% average increase in yield strength. All three coating systems exhibited significant loss in ductility as evidenced by their ultimate strain. The LTV specimens had an average ultimate strain of 10.7%, 56% less than the average of the uncoated specimens, whereas the Pfaudler and Chromizing specimens had respective average ultimate strains of 12.3% and 12.7%, approximately 34% less than the uncoated alloy.

The Boeing coating produced the most severe loss of strength. Both yield and ultimate strength decreased by 40%. This was based on one test alone, since the other two specimens were not returned by the vendor. The ultimate strain of this specimen was reduced by only 22% which was less than any of the other five coating systems.

The Sylcor Phase I specimens had a 9% average reduction in yield strength and a 6% reduction in ultimate strength. Average ultimate strain was 11.8%, 38% less than the uncoated alloy. The Phase II specimens yielded similar data, with yield and ultimate strength reductions of 8% and an average ultimate strain of 12.7%.

The TRW coating displayed a definite batch difference. The Phase I specimens showed average reductions in yield strength of 24% and a reduction in ultimate strength of 26%, whereas the Phase II specimens exhibited an average reduction in both yield strength and ultimate strength of 19%. The Phase II samples were also more ductile, averaging an ultimate strain of 16.3% as compared to only 9.5% for the Phase I specimens.

C129Y Columbium Alloy

Unlike the D43 alloy, which was stress relieved, the C129Y alloy was submitted for coating in the wrought condition. The resulting tensile property changes were partially the result of stress relief and recrystallization produced

**Table 6. Room Temperature Tensile Test Results
for Coated D43 Columbium Alloy**

<u>Coating</u>	<u>Phase</u>	<u>Tensile Strength (ksi)</u>		<u>Ultimate Elongation (%)</u>
		<u>Yield*</u>	<u>Ultimate</u>	
TRW (Cr-Ti-Si)	I	45.0(.77)	62.5(.75)	10.5(.55)
		44.0(.75)	58.0(.70)	7.6(.40)
	II	45.6(.78)	66.3(.80)	15.1(.79)
		47.5(.81)	68.2(.82)	16.3(.85)
		50.0(.85)	68.2(.82)	16.7(.87)
Sylcor (Ag-Si-Al)	I	54.0(.92)	77.0(.93)	10.7(.56)**
		55.5(.95)	78.0(.94)	10.7(.56)
		50.0(.85)	78.5(.94)	14.0(.74)
	II	47.0(.80)	76.4(.92)	12.1(.63)
		57.5(.98)	76.7(.92)	13.9(.73)
		58.8(1.00)	76.1(.91)	12.9(.67)
Pfaudler-PFR-32	I	59.0(.99)	85.5(1.03)	10.7(.56)
		60.0(1.02)	86.5(1.04)	13.1(.69)
		55.0(.94)	84.0(1.01)	13.2(.70)
Chromizing -Durak KA	I	57.5(.98)	81.5(.98)	12.7(.67)
		58.5(1.0)	82.5(.99)	12.7(.67)
		57.5(.98)	79.0(.95)	12.7(.67)
LTV -Cr-B Modified Silicide	I	60.0(1.02)	85.5(1.02)	11.4(.60)
		66.3(1.13)	84.0(1.01)	10.4(.55)
		66.0(1.13)	80.0(.96)	10.3(.54)
Boeing -Disil	I	35.0(.60)	49.4(.59)	14.8(.78)
Uncoated		57.5	83.3	20.3
		56.8	83.2	18.3
		61.2	83.2	18.6

* 0.1% offset

** Broke outside gage length.

NOTE: All stress values were based upon original substrate dimensions. Tests were conducted at a strain rate of 0.05 in/in/min. The numbers in parentheses represent the ratio of coated to average uncoated values.

**Table 7. Room Temperature Tensile Test Results
for Coated C129Y Columbium Alloy**

<u>Coating</u>	<u>Phase</u>	<u>Tensile Strength (ksi)</u>		<u>Ultimate Elongation (%)</u>
		<u>Yield*</u>	<u>Ultimate</u>	
TRW (Cr-Ti-Si)	I	76.0(.78)	90.0(.80)	20.9(1.60)
		75.0(.77)	87.6(.78)	20.3(1.55)
		72.0(.75)	83.0(.73)	20.9(1.60)
	II	72.5(.75)	86.9(.77)	22.5(1.72)
		78.0(.80)	90.8(.80)	18.15(1.39)
		68.5(.71)	85.5(.76)	19.55(.149)
Sylcor (Ag-Si-Al)	I	78.0(.80)	87.2(.77)	16.2(1.24)
		79.0(.81)	90.6(.80)	16.2(1.24)
		73.0(.75)	86.0(.76)	15.5(1.18)
	II	58.0(.60)	82.6(.73)	14.7(1.12)
		70.0(.72)	86.0(.76)	14.8(1.13)
		61.5(.63)	83.0(.73)	16.0(1.22)
Pfaudler -PFR-32	I	91.0(.94)	111.0(.98)	13.5(1.03)
		87.0(.90)	95.6(.85)	8.5(.65)**
		88.0(.91)	99.0(.88)	11.0(.84)
Chromizing - Durak KA	I	96.0(.99)	106.0(.94)	15.4(1.18)
		103.0(1.06)	110.0(.97)	12.8(.98)
		97.0(1.00)	103.2(.91)	14.8(1.13)
LTV -Cr-B Modified Silicide	I	78.0(.80)	90.8(.80)	13.8(1.05)
		80.5(.83)	85.7(.76)	15.3(1.17)
		--	90.8(.80)	14.9(1.14)
Boeing - Disil	I	77.5(.80)	88.0(.78)	19.0(1.45)
		71.5(.74)	87.0(.77)	18.9(1.44)
		74.0(.76)	85.2(.75)	18.9(1.44)
Uncoated		92.5	109.0	11.8
		100.0	114.0	13.8
		98.6	116.2	13.8

* 0.1% offset

** Broke outside gage length

NOTE: All stress values were based upon original substrate dimensions. Tests were conducted at a strain rate of 0.05 in/in/min. The numbers in parentheses represent the ratio of coated to average uncoated values.

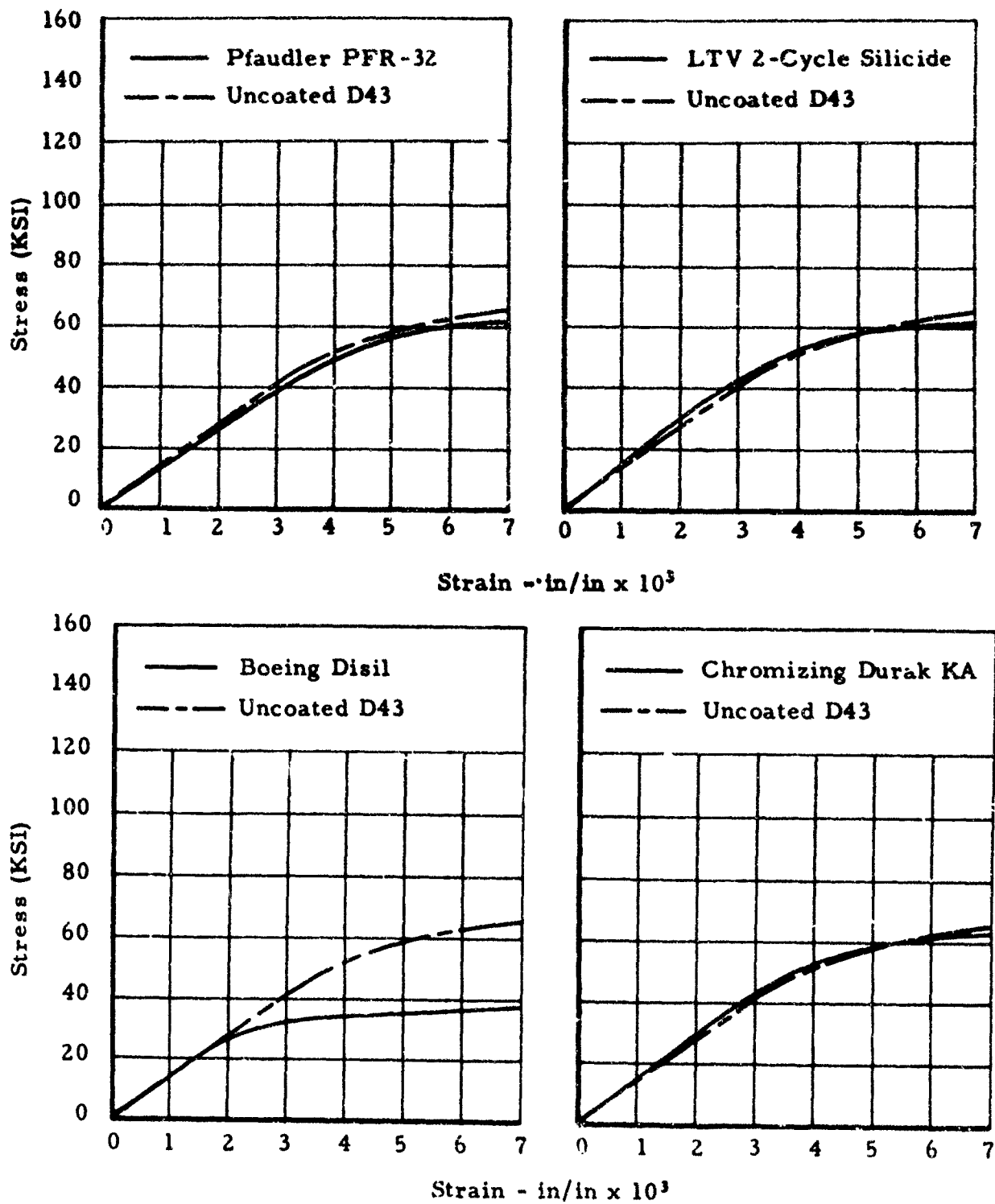


Figure 1c. Typical Stress-Strain Diagrams for Coated D43 (Tested at Room Temperature)

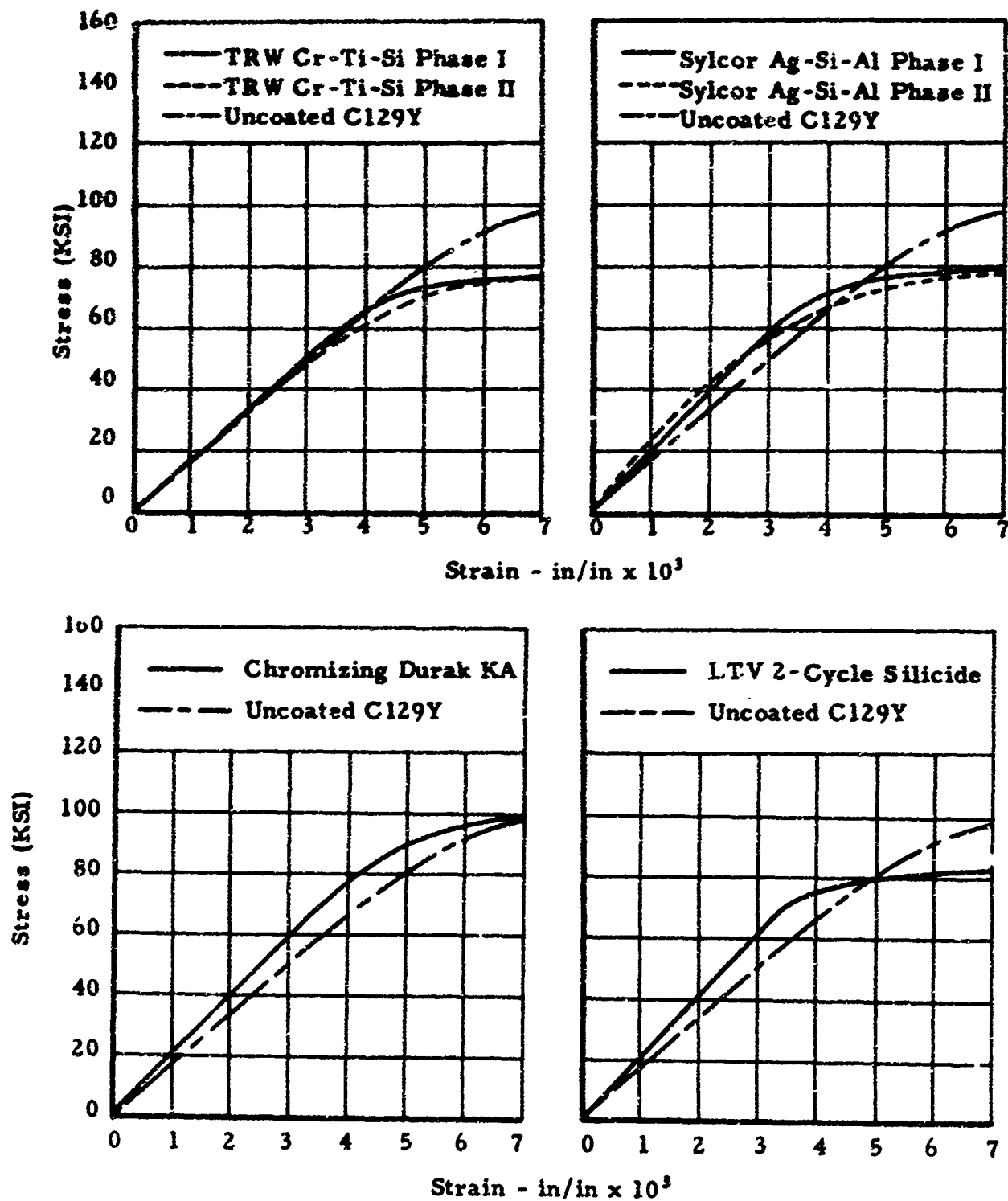


Figure 17. Typical Stress-Strain Diagrams for Coated C129Y (Tested at Room Temperature)

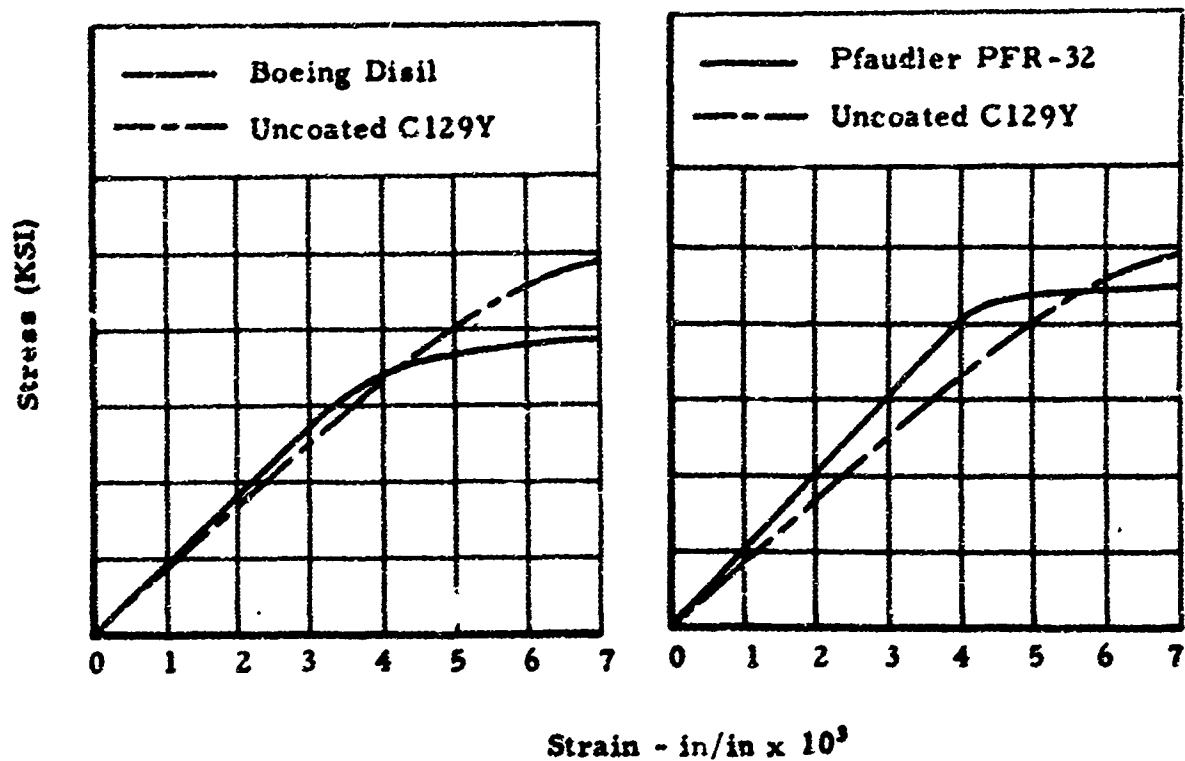


Figure 18. Typical Stress-Strain Diagrams for Coated C129Y (Tested at Room Temperature)

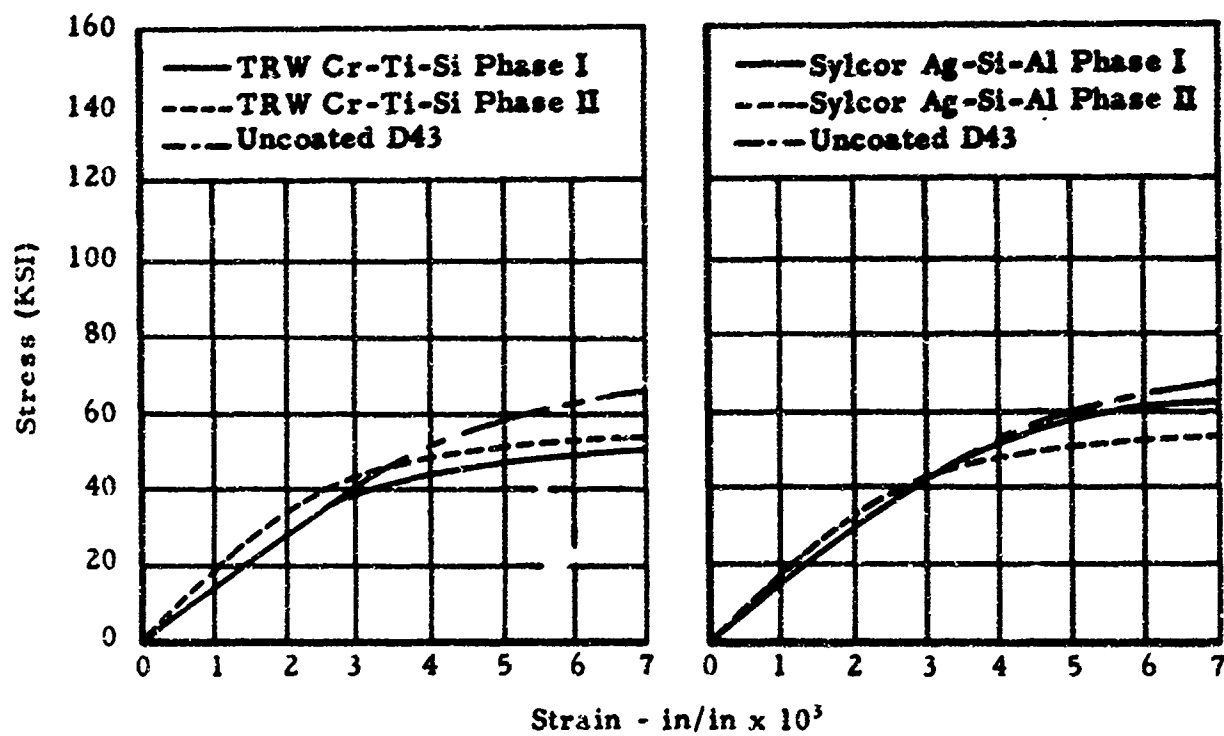


Figure 19. Typical Stress-Strain Diagrams for Coated D43 (Tested at Room Temperature)

by heating during coating application. This was borne out by the observed microstructure changes in the coated substrate. For example, the Chromizing specimens displayed very little difference in yield and ultimate strengths or ultimate strain, and no changes occurred in the substrate microstructure. On the other hand, the Phase I TRW specimens, which experienced the greatest degree of recrystallization, exhibited a 23% loss in both yield and ultimate strength as well as a 58% increase in ultimate strain. With one exception, the other Phase I coating systems exhibited strength and ductility consistent with their microstructures. The single exception was the Pfaudler specimens which revealed an average reduction in ultimate strain of 26%, despite significant recrystallization of the substrate. However, a pronounced increase in the bend transition temperature of this coating system, noted previously in this report, suggested significant embrittlement of the substrate by the coating process.

The Phase II tensile tests conducted on the Sylcor and TRW coatings are also presented in Table 7. Very little difference was noted for the two TRW specimen batches. The two Sylcor batches yielded similar ultimate strength and elongation values; however, the average yield strength of the Phase I specimens was approximately 12% greater than that of the Phase II specimens. This was contrary to expectations, since it was felt that the lower temperature used in processing the Phase II specimens would have produced a smaller change of tensile properties.

CYCLIC OXIDATION TESTING

Results of the cyclic oxidation tests are presented in Table 8 for coated D43 and in Table 9 for coated C129Y. The Sylcor and TRW coatings which had exhibited the best oxidation protection in Phase I tests of both alloys were selected for Phase II testing and were tested in two batches at each temperature.

Weibull plots for all 2600°F tests of both alloys and at 2400°F for coated C129Y are shown in Figures 20 through 35. In constructing the 2600°F plots for the Sylcor and TRW coatings, the data were analyzed for statistically significant differences between the two batches. If no batch differences were detected, the data were pooled. However, where significant batch differences were present, two separate curves were plotted.

D43 Columbium Alloy

Because of difficulties encountered in testing the Chromizing Durak KA coating at 2600°F (see below), no specimens were available for testing at the other temperatures. At 1600°F, only the TRW and Sylcor coatings exhibited good oxidation protection. The TRW specimens, run in two batches, had only one edge failure in the last 16-hour cycle, and the Sylcor coating, tested in only one batch because of insufficient specimens from the Phase II group, showed no

Table 8. Cyclic Oxidation Data for Coated D43 Columbium

Coating	Temp. °F	Hours to Failure	
		Phase I	Phase II
TRW (Cr-Ti-Si)	1600	48*, 48*, 48*, 48(e)	48*, 48*, 48*, 48*
	2400	101(e), 115(e), 139(e), 153(e)	48(e), 76(e), 78(e), 94(e)
	2600	6(e), 7(e), 9(e), 25(e), 26(e), 29(e), 33(e), 36(e), 46(e), 61(e)	2(e), 23(e), 36(e), 36(e), 36(e), 36(e), 37(e), 37(e), 37(e), 39(c)**
	3000	1(c), 1(c), 1(c), 1(c)	1(c), 1(c), 1(c), 1(c)
Sycor (Ag-Si-Al)	1600	48*, 48*, 48*, 48*	Not conducted - insufficient specimens
	2400	90(e), 103(e), 113(e), 122(e)	87(e), 93(e), 97(e), 98(e)
	2600	63(e), 63(c), 110(e), 112(e), 117(c), 138(e), 144(e-s), 153(c), 153(c), 155(c)	52(c), 59(e), 79(e), 79(e), 84(c), 89(e), 91(e), 114(e), 117(e-s), 117(e-e)
	3000	11(c), 11(c), 12(c), 13(e)	15(c), 16(e), 17(c)
Pfandler (PFR-32)	1600	24(e), 24(e), 24(e), 24(e)	
	2400	10(e, s), 10(e), 11(e), 11(e), 12(e), 12(e), 13(e), 15(e), 19(e), 20(e)	
	2600	2(e), 2(e), 3(e), 3(e, s), 3(e), 5(e), 5(e), 6(e), 6(e), 8(e)	
	3000	1(c), 1(c), 1(c), 1(c)	
LTV (Cr-B Modified Silicide)	1600	8(e), 8(e), 8(e), 48*	
	2400	21(e), 28(e), 47(e), 49(e)	
	2600	2(e), 9(e), 13(e), 15(e), 24(c), 28(e), 30(e), 31(e), 34(e), 35(e)	
	3000	1(c), 1(c), 1(c), 1(c)	
Boeing (Disil)	1600	4(c), 8(c), 8(c)	
	2400	6(s), 10(s), 22(c), 30(c)	
	2600	4(s), 9(s), 9(s), 9(s), 9(s), 9(s), 9(s), 10(c), 12(s), 13(e)	
	3000	1(c), 1(c), 1(c), 1(c)	
Chromizing (Durak KA)	2600	2(s), 2(s), 6(e, s), 5(s), 6(e, s), 6(e), 6(e, s), 6(e, s)	

(Other Tests Not Conducted - Insufficient Specimens)

*Did not fail

** The furnace became inoperative during the 35th cycle, reducing the temperature to 2200°F before it was discovered.

NOTE: Letters in parentheses refer to failure location; i. e., s = edge, s = surface, c = catastrophic

Table 9. Cyclic Oxidation Data for Coated C129Y Columbium

Coating	Temp. °F	Hours to Failure	
		Phase I	Phase II
TRW (Cr-Ti-Si)	1600	8(s), 8(s), 8(s), 8(s, e)	48*, 48*, 48*, 48*
	2400	27(s), 42(s), 36(s), 65(s), 67(s), 69(s), 72(s), 75(s), 81(s), 81(s)	70(s), 70(s), 91(s, e), 103(s) *
	2600	25(s), 37(s), 31(s), 37(s), 37(s), 37(s), 55(s), 69(s, e), 89(s), 92(s)	26(s), 27(s), 29(s), 30(s), 31(s), 35(c), 42(s), 42(s), 46(c), 53(c)
	3000	1(c), 1(c), 1(c), 1(c)	1(c), 1(c), 1(c), 1(c)
Sylcor (Ag-Si-Al)	1600	48*, 48*, 48*, 48*	48*, 48*, 48*, 48*
	2400	28(s), 95(s), 95(s), 97(s), 97(s), 97(s), 99(s), 100(s), 105(s), 107(s)	43(s), 64(s), 67(s), 78(s)
	2600	68(s), 106(s), 108(s), 112(s), 115(c), 116(c), 120(s), 127(s), 129(s), 129(s)	29(s), 32(c), 32(c), 33(c), 36(c), 36(c), 37(s), 38(s), 43(c), 78(c)
	3000	3(c), 3(c), 3(c), 7(c)	7(c), 8(c), 8(s), 8(s)
Pfaudler (PFR-32)	1600	28(s), 48*, 48*, 48*	
	2400	14(c), 17(s), 17(s), 20(s), 21(s), 21(s), 21(s, e), 25(s), 27(s), 29(s)	
	2600	6(s) - all ten specimens	
	3000	1(c), 1(c), 1(c), 2(c)	
LTV (Cr-B Modified Silicide)	1600	4(s), 24(s), 48*, 48*	
	2400	5(s), 5(s), 6(s), 5(s), 6(s), 7(s), 7(s), 7(s), 25(s), 37(s)	
	2600	2(c), 2(c), 2(c), 2(s), 2(c), 2(s, e), 3(s), 4(c), 6(s), 15(s)	
	3000	1(c), 1(c), 1(c), 1(c)	
Boeing (Disil)	1600	4(s), 48*, 48*, 48*	
	2400	19(s), 24(s), 24(s), 28(s), 29(s), 30(s), 30(s), 33(s), 35(s), 36(s)	
	2600	2(s), 2(s), 2(s), 4(s), 4(s), 17(s), 18(s), 23(s), 25(s, e), 27(s)	
	3000	1(c), 1(c), 2(c)	
Chromizing (Durak KA)	1600	48*, 48*, 48*, 48*	
	2400	14(s), 14(s), 16(s), 16(s), 17(s), 17(s), 19(s), 21(s), 21(s), 25(s)	
	2600	3(s), 8(s, e), 8(s), 8(s), 8(s), 8(s), 8(s), 9(s), 9(s), 11(s)	
	3000	2(c), 2(c), 2(c)	

* Did Not Fail

NOTE: Letters in parentheses refer to failure location; i. e., s = edge,
e = surface, c = catastrophic

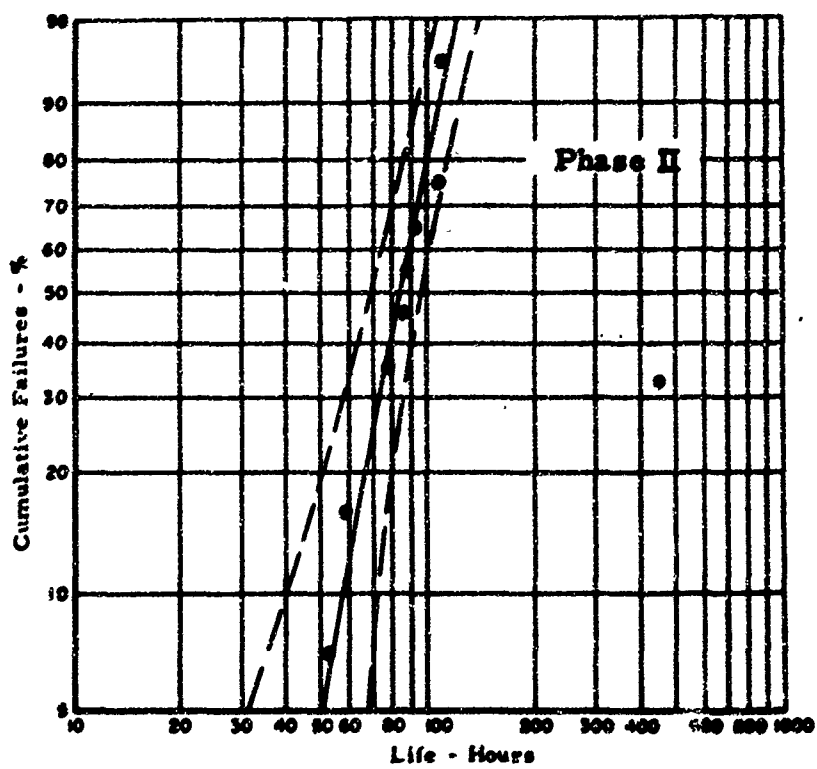
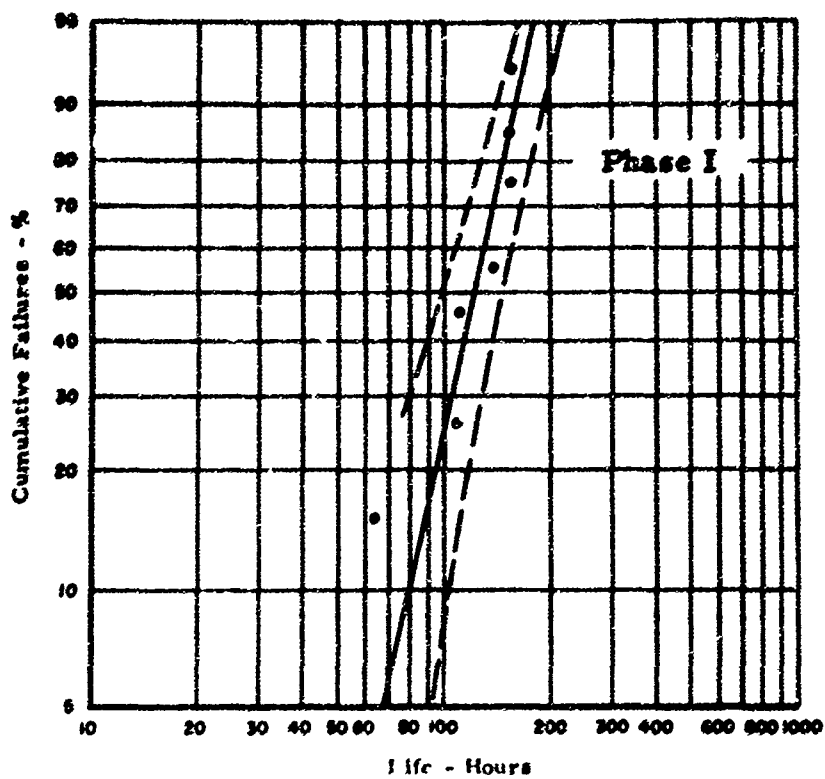


Figure 20. Weibull Plot of 2600°F Cyclic Oxidation Test Results;
Sylcor Ag-Si-Al Coating on 20 mil D43

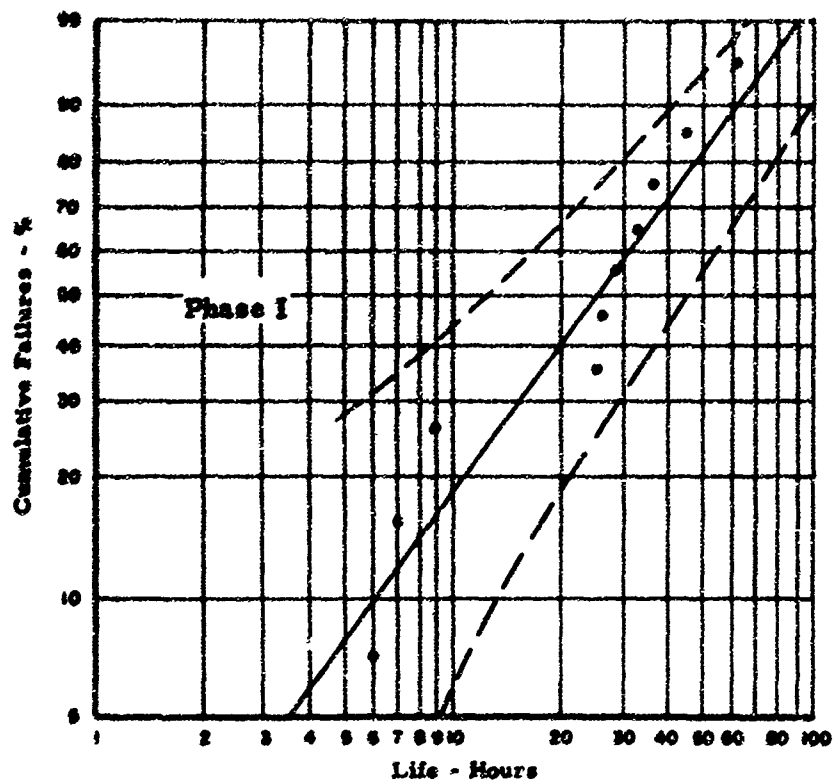


Figure 21. Weibull Plot of 2600°F Cyclic Oxidation Test Results;
TRW Cr-Ti-Si Coating on 20 mil D43

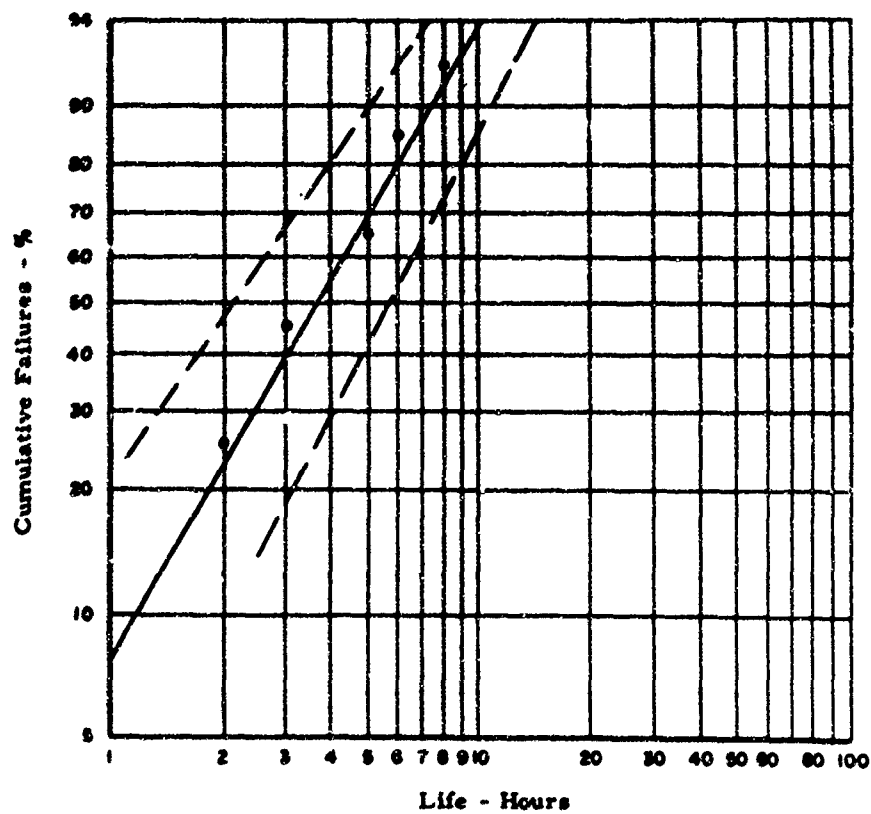


Figure 22. Weibull Plot of 2600°F Cyclic Oxidation Test Results;
Pfaudler PFR-32 Coating on 20 mil D43

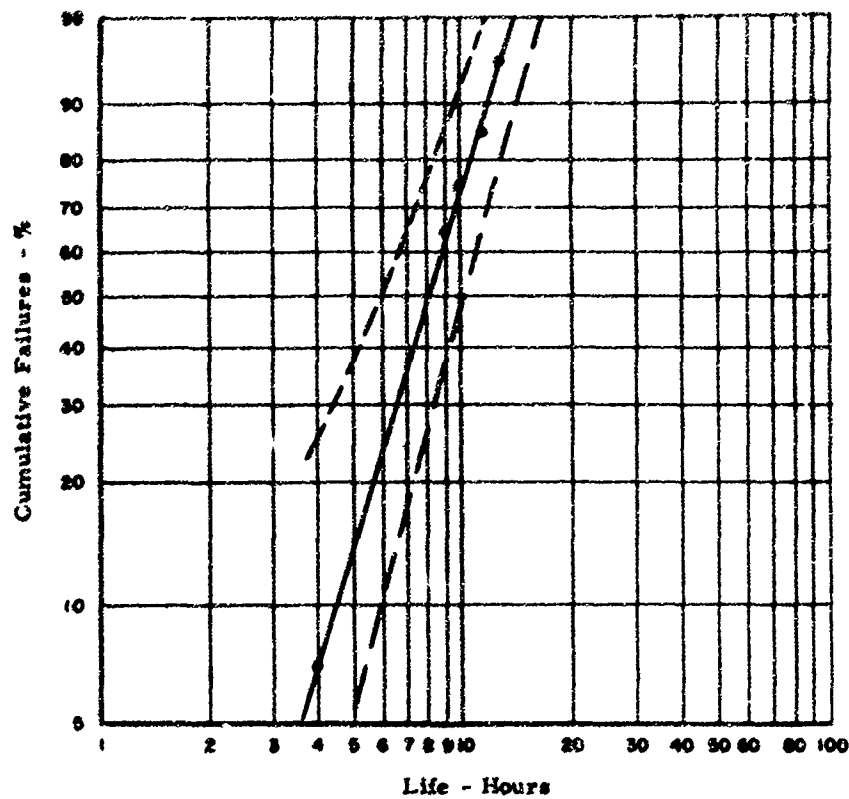


Figure 23. Weibull Plot of 2600°F Cyclic Oxidation Test Results;
Boeing Disil Coating on 20 mil D43

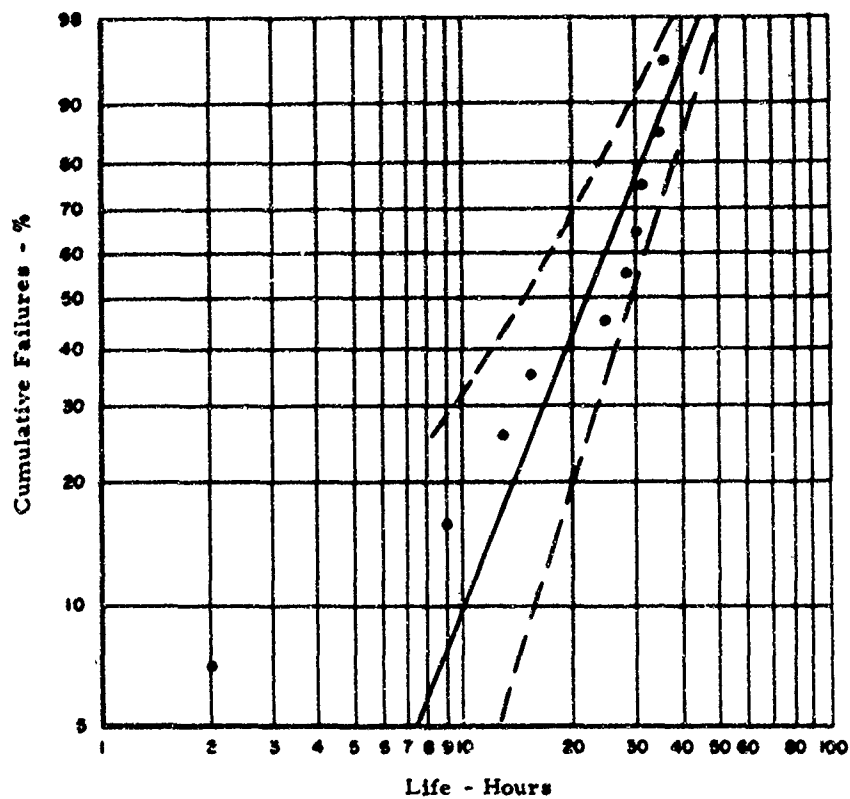


Figure 24. Weibull Plot of 2600°F Cyclic Oxidation Test Results;
LTV Two-Cycle Modified Silicide Coating on 20 mil D43

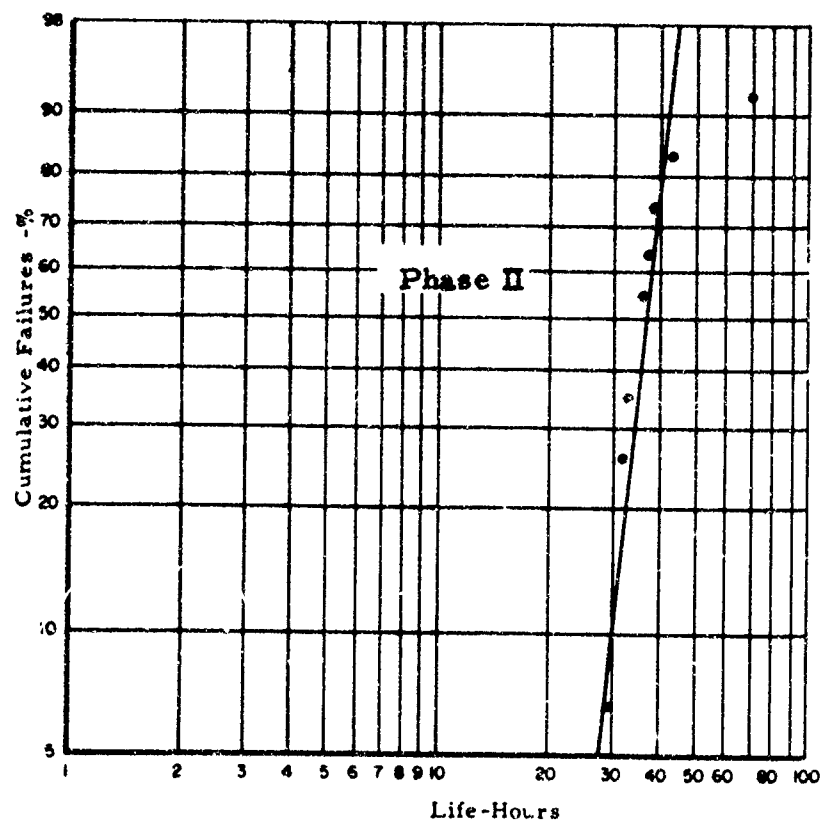
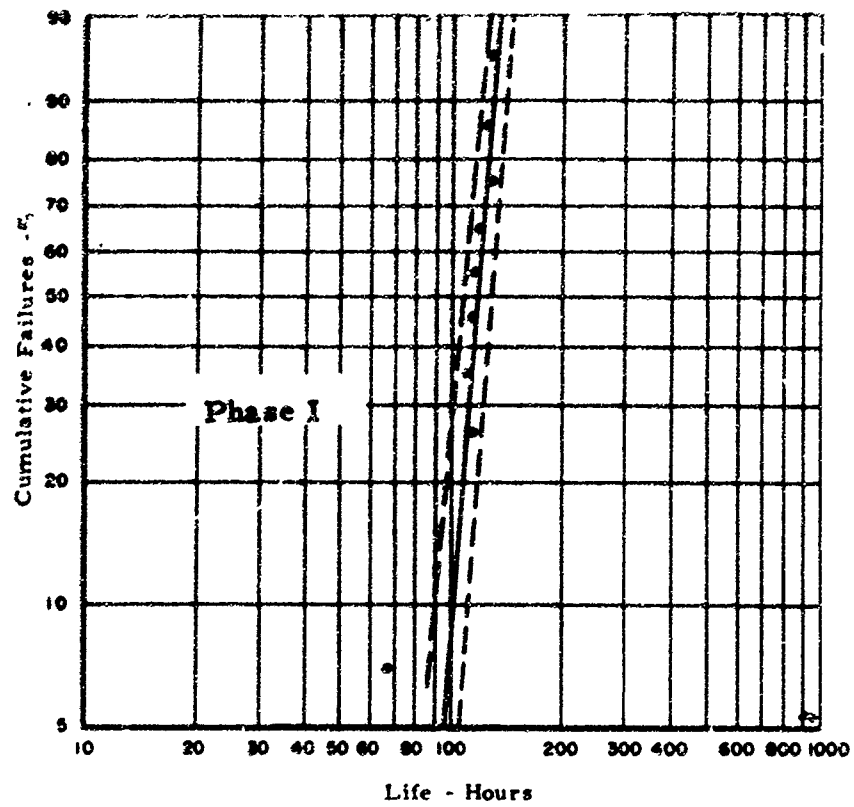


Figure 25. Weibull Plot of 2600°F Cyclic Oxidation Test Results;
Sylcor Ag-Si-Al Coating on 20 mil C129Y

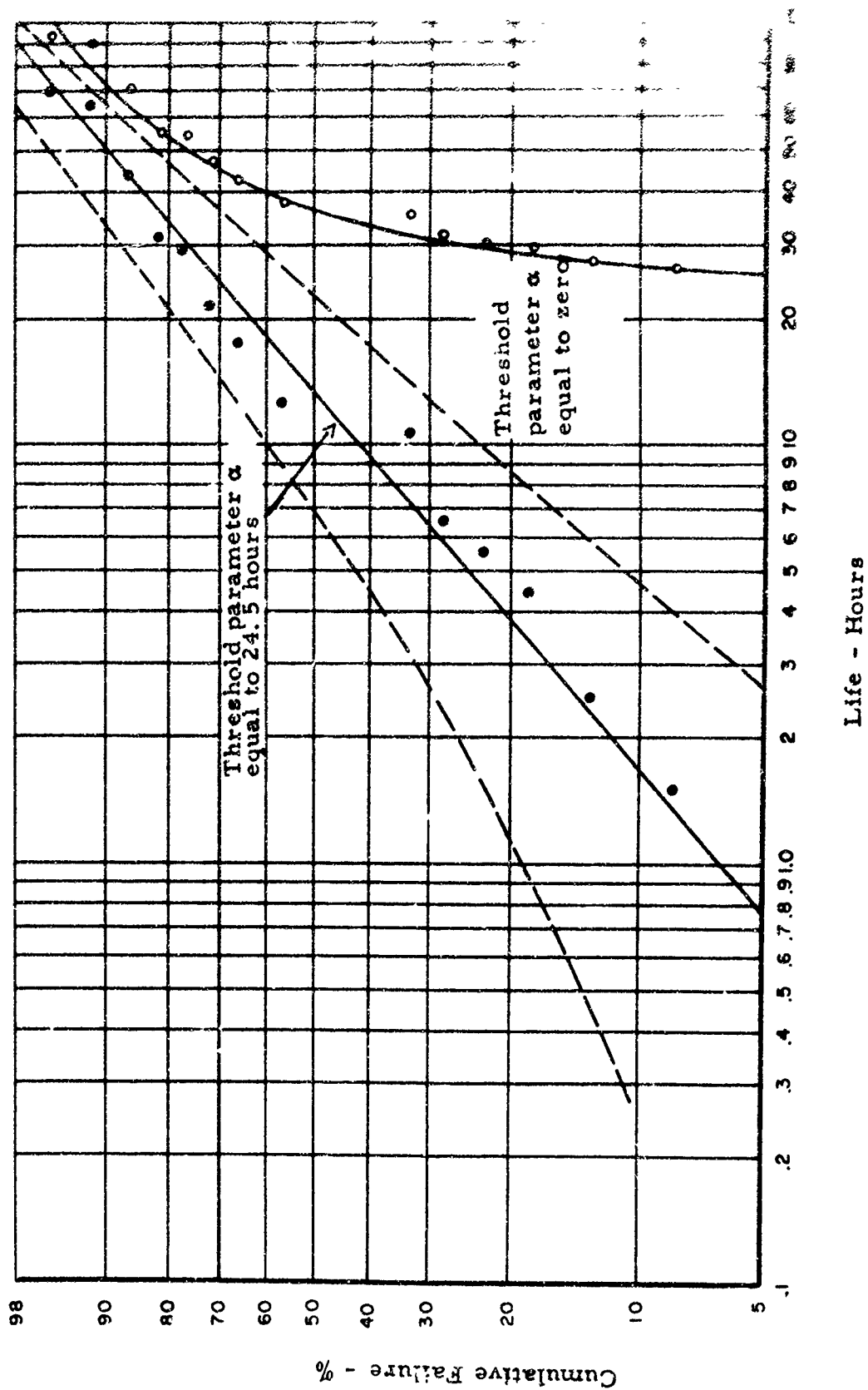


Figure 26. Weibull Plot of 2600°F Cyclic Oxidation Test Results; TRW Cr-Ti-Si Coating on 20 mil C129Y

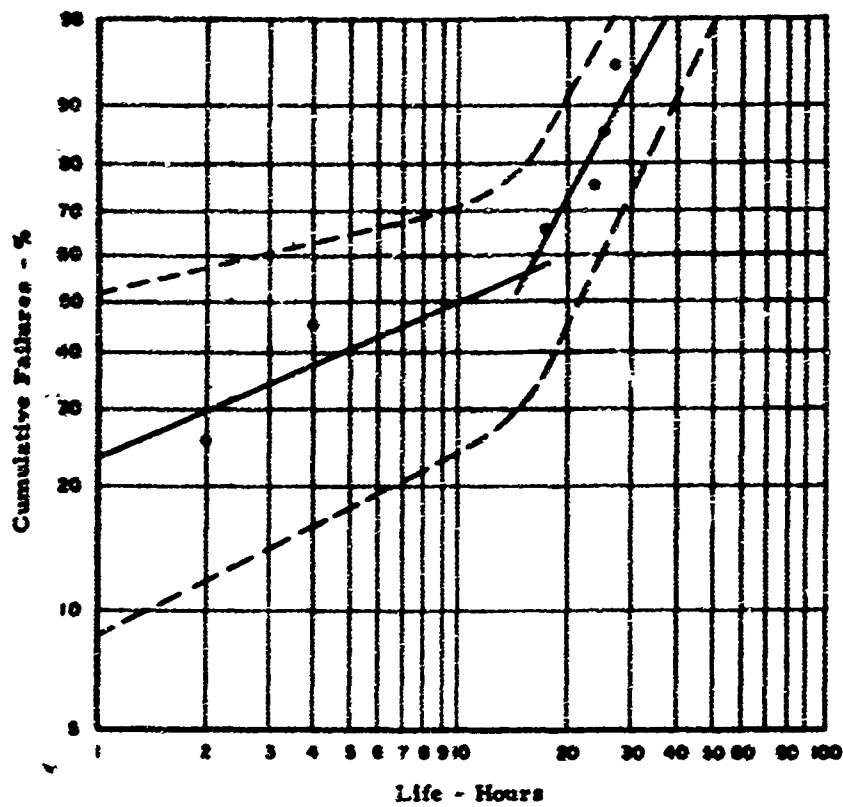


Figure 27. Weibull Plot of 2600°F Cyclic Oxidation Test Results; Boeing Disil Coating on 20 mil C129Y

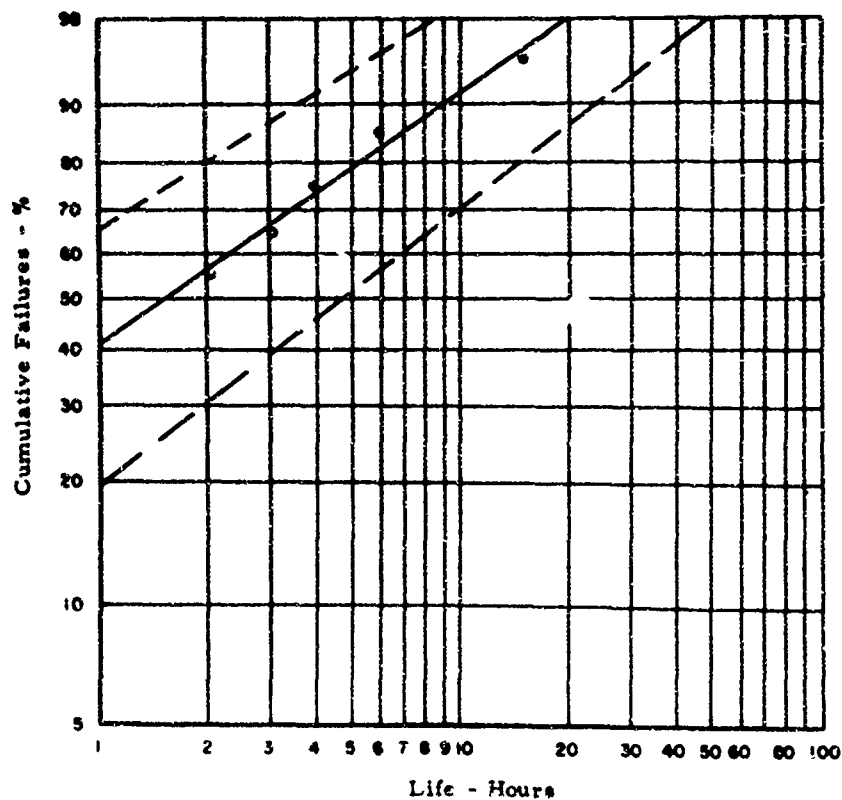


Figure 28. Weibull Plot of 2600°F Cyclic Oxidation Test Results; LTV Two-Cycle Modified Silicide Coating on 20 mil C129Y

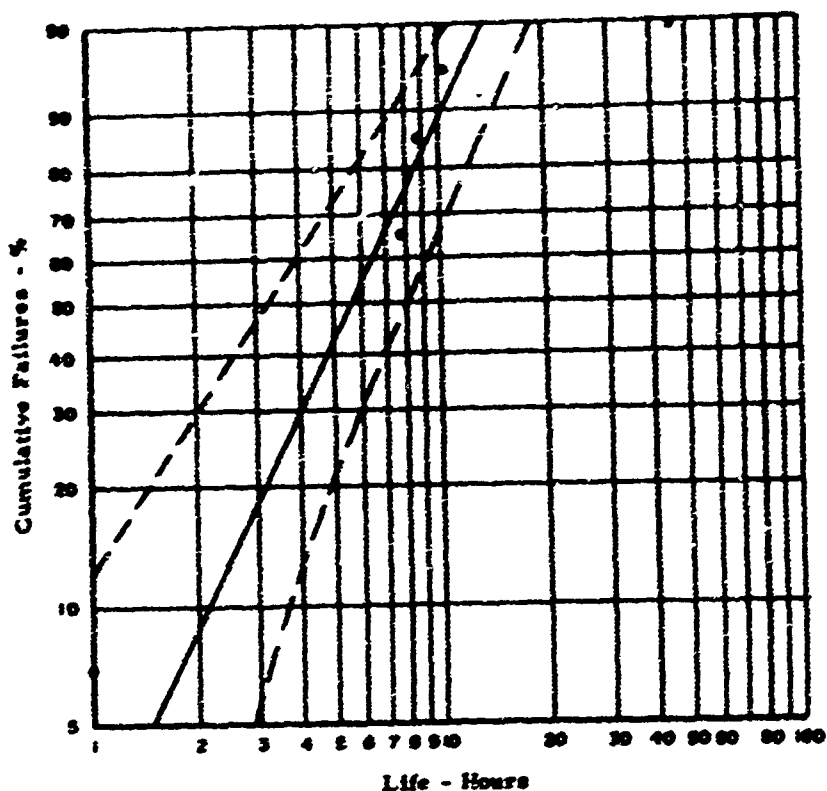


Figure 29. Weibull Plot of 2600°F Cyclic Oxidation Test Results; Chromizing Durak KA Coating on 20 mil C129Y

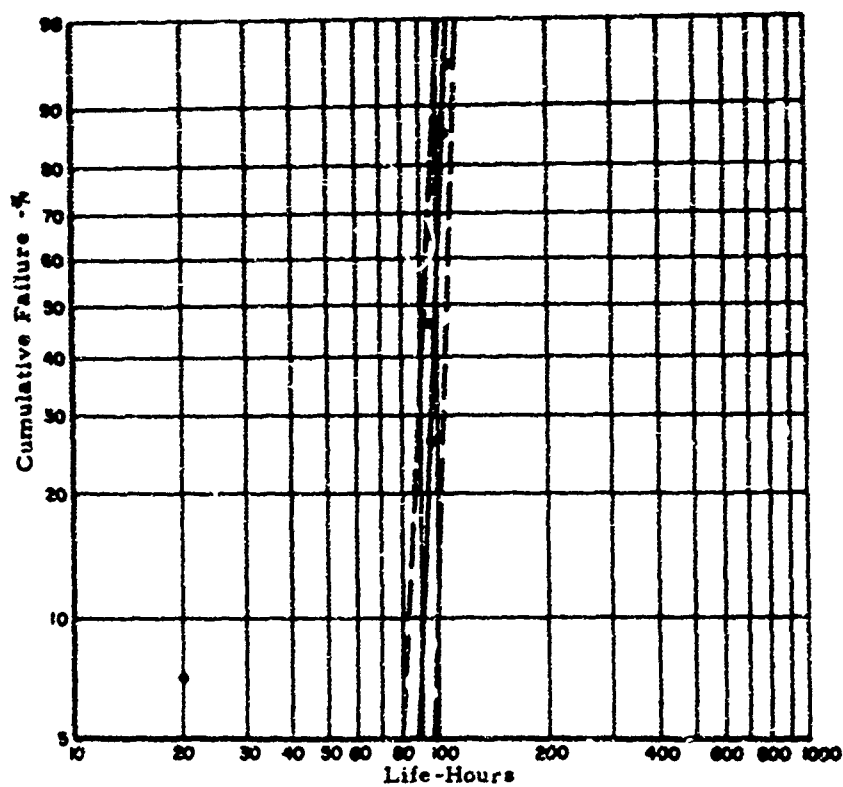


Figure 30. Weibull Plot of 2400°F Cyclic Oxidation Test Results; Sylcor Ag-Si-Al Coating on 20 mil C129Y

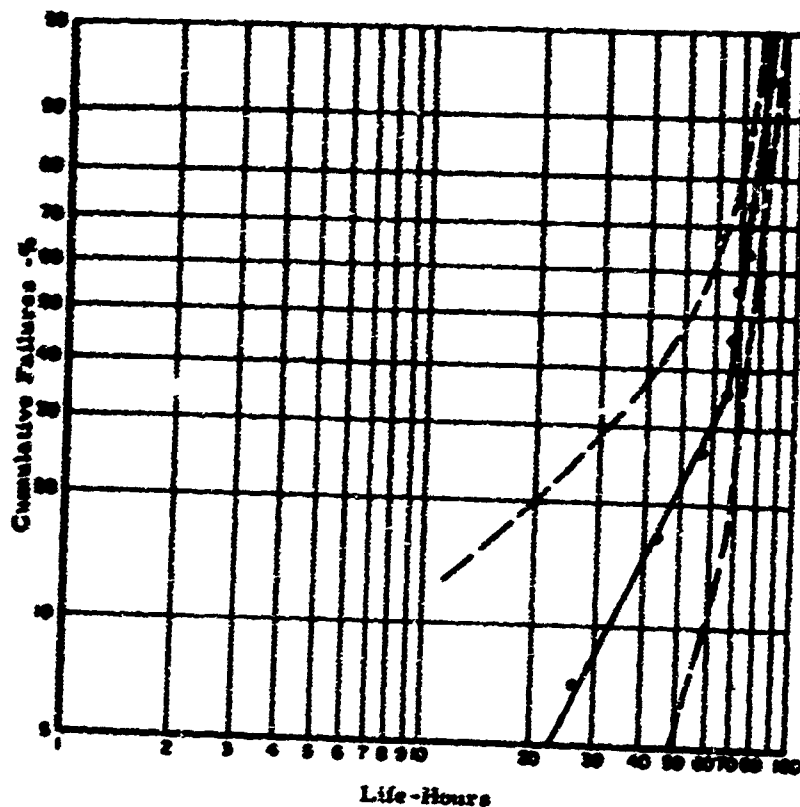


Figure 31. Weibull Plot of 2400°F Cyclic Oxidation Test Results; TRW Cr-Ti-Si Coating on 20 mil C129Y

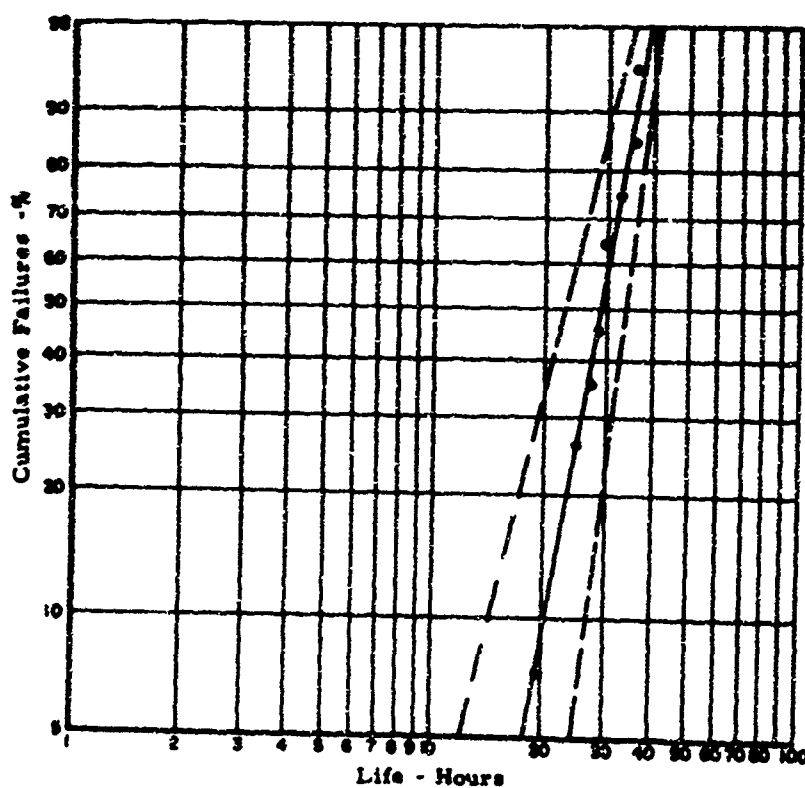


Figure 32. Weibull Plot of 2400°F Cyclic Oxidation Test Results; Boeing Disil Coating on 20 mil C129Y

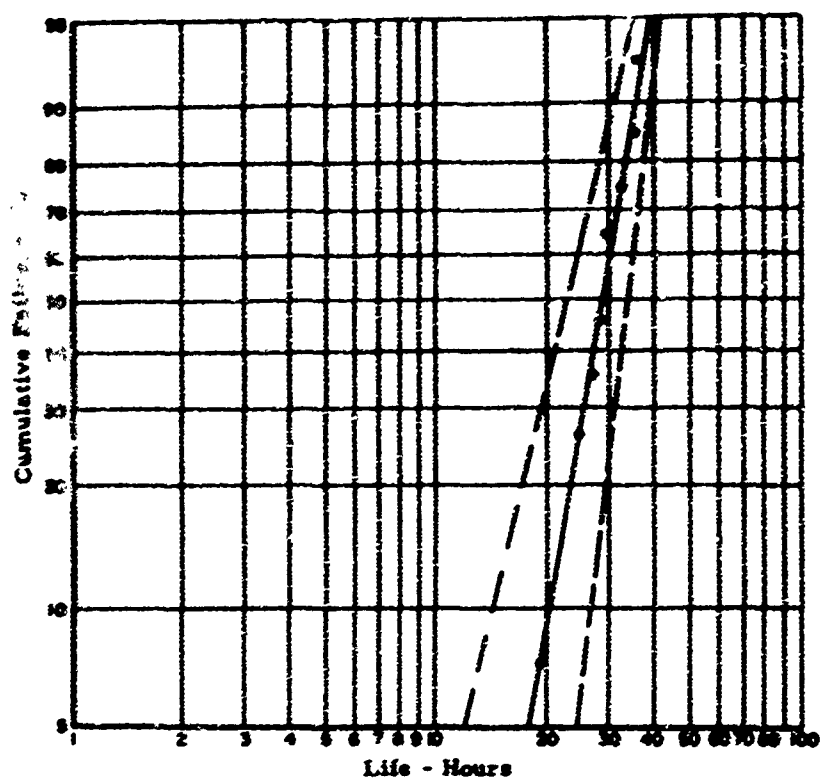


Figure 33. Weibull plot of 2400°F Cyclic Oxidation Test Results; Pfadler PFR-32 Coating on 20 mil C129Y

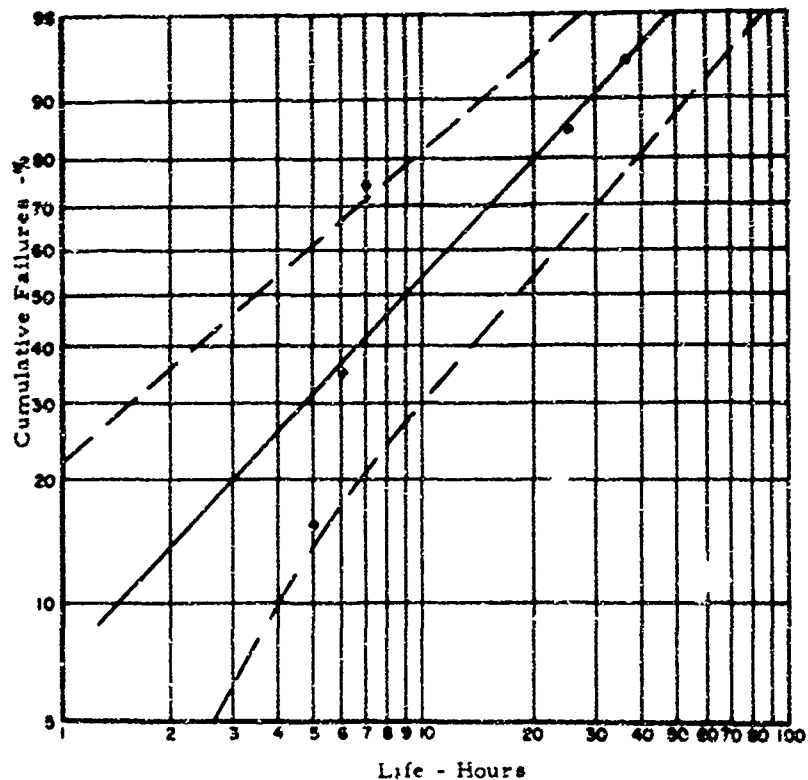


Figure 34. Weibull plot of 2400°F Cyclic Oxidation Test Results; LTV Cr-B-Silicide Coating on 20 mil C129Y

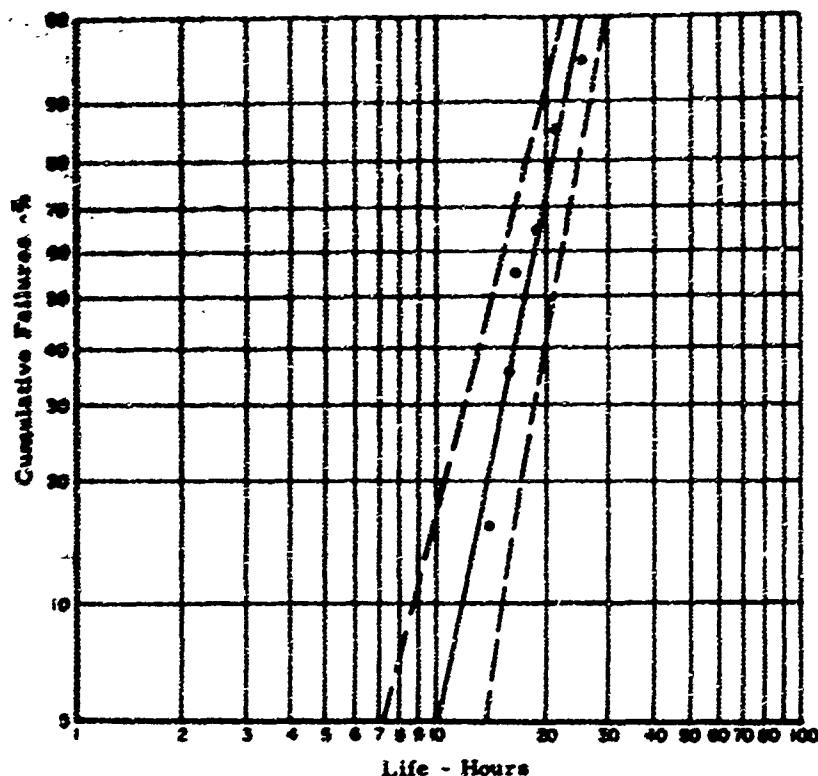


Figure 35. Weibull Plot of 2400°F Cyclic Oxidation Test Results; Chromizing Durak KA Coating on 20 mil C129Y

failures. In general, the Pfadler, LTV, and Boeing coatings showed very poor low temperature protection, and all but one LTV specimen failed to survive the 48-hour test period.

Of those tested at 3000°F, only the Sylcor Ag-Si-Al coating provided any measure of oxidation protection; all others failed catastrophically during the first thermal cycle. The Sylcor coating, tested in two batches, was surprisingly effective at this temperature, with coating lifetime ranging from 11 to 17 hours.

At 2600°F, the Sylcor Ag-Si-Al coating was clearly the best of the six systems tested. This was not unexpected in view of the relative thickness of the coating. In the Phase I group of ten specimens, the first failures occurred at 63 hours, a value which exceeded the longest time to failure of any other coated D43 specimen. The Weibull distribution slope of these data was 4.3 (indicative of a nearly normal distribution) with a maximum probable life of 180 hours (see Figure 20). The Phase II group behaved somewhat differently; a standard statistical comparison (the Wilcoxon Rank Test) revealed that the batches did not represent the same population, and, therefore, a separate Weibull distribution was plotted (see Figure 20). The resulting slope was very close to the Phase I

plot, but the extrapolated maximum life was 120 hours. This batch difference did not seem unusual since the coating on the Phase I specimens (7.2 - 13.6 mils) was much thicker than that on the Phase II specimens (2.4 - 7.6 mils).

The Phase I batch of the TRW Cr-Ti-Si coating followed a nearly exponential Weibull slope of 1.3 with a maximum expected life of 90 hours (see Figure 21). In testing the Phase II specimens, the furnace failed during the thirty-fifth cycle and cooled from 2600° to 2200°F before discovery. When testing was resumed, the remaining specimens failed within the next four cycles. The Phase II data were, therefore, considered compromised and unsuitable for analysis or comparison.

The Pfaudler and Boeing coated D43 specimens exhibited relatively poor oxidation resistance. The Pfaudler specimens formed a Weibull failure distribution slope of 1.7 and a maximum probable life of ten hours (see Figure 22). The Boeing samples exhibited a 3.1 Weibull slope and a maximum probable life of fourteen hours (see Figure 23).

The Chromizing specimens showed a tendency to react with the alumina boats during test. The first two batches of ten specimens reacted rather severely within the first three cycles of test. A third batch of eight specimens was ultimately tested by supporting the specimens on platinum wire. Although no reactions were noted, the third set failed in less than six hours, and, because of the limited amount of data, no attempt was made to plot a Weibull representation of the failure distribution.

The LTV specimens failed along a Weibull slope of 2.4 with a maximum probable life of 44 hours (see Figure 24).

Estimates of reliability at 70%, 90%, and 95% probabilities of survival as determined from the Weibull plots, are shown in Table 10. The Sylcor coating was clearly the most reliable of the group at the 95% level, followed by two systems of nearly equal reliability, the LTV and TRW coatings. It is interesting to note that the positions of these latter two systems were interchanged at the 90% and 70% levels.

In the Phase I tests at 2400°F, the TRW Cr-Ti-Si coating exhibited substantially longer life than the Sylcor Ag-Si-Al system, with a mean life of 127 hours as compared to 107 hours. This was a reversal of the 2600°F results, where the Sylcor coating was clearly the better of the two. Both coating systems exhibited apparent batch differences in these tests at 2400°F. The Phase II TRW specimens had a mean life of 74 hours, while the Phase I coating mean was 127 hours. The Phase II Sylcor coating exhibited an average oxidation life of 94 hours as compared to 107 hours for the Phase I specimens. Because of the extremely limited number of specimens run, it was not possible to substantiate these apparent batch differences by statistical analyses. It is quite possible that the results were

**Table 10. Probable Cyclic Oxidation Life at 2600°F of
Coated D43 for Various Levels of Reliability**

<u>Coating</u>	<u>Coating Life (Hours) at Specified Levels of Reliability</u>		
	<u>70%</u>	<u>90%</u>	<u>95%</u>
TRW Cr-Ti-Si	16	6	3 - 4
Pfudler PFR-32	2-3	1	<1
Chromizing Durak KA	2-3	1-2	1 - 2
LTV -Cr-B Modified Two-Cycle Silicide	17	10	7 - 8
GT&E Ag-Si-Al (I)	110	80	68
(II)	73	58	50
Boeing Disil	6-7	4-5	3 - 4

coincidental and the specimens actually represented the same population. However, the Sylcor batch difference seems to be borne out in the statistical comparison of the 2600°F results. The existence of a real batch difference with the TRW coating must be left to conjecture, although the difference in nominal coating thickness between the batches (2.1 for Phase I compared to 1.6 for Phase II) could have produced this effect.

At 2400°F, the LTV, Pfudler, and Boeing coatings were of nearly equal rank. As in the 2600°F tests, the LTV specimens demonstrated better oxidation resistance than either the Boeing or Pfudler coatings, and the latter two were approximately equal.

C129Y Columbium Alloy

At 1600°F, most of the six coatings demonstrated better low temperature oxidation protection on this alloy than on D43. A notable exception was the TRW Phase I specimens. All four samples with this coating failed within the first eight hours. In contrast, none of the Phase II specimens from TRW failed in 48 hours at 1600°F. Single specimens from Pfudler and Boeing and two LTV specimens failed within the 48-hour test period. These were all edge failures, not the catastrophic failures usually associated with low temperature protection problems. None of the Chromizing or Sylcor specimens failed in this test.

Most of the coatings were nonprotective at 3000°F, all specimens failing within two cycles. The only exception was the Sylcor Ag-Si-Al coating which protected specimens from three to eight hours at this temperature.

As in the D43 cyclic oxidation tests, the Sylcor coating again exhibited the best oxidation resistance at 2600°F. The Weibull distribution slope from Phase I tests of this coating was 12.7, and the extrapolated maximum life was 132 hours (see Figure 25). A statistical comparison of Phase I and Phase II groups again showed batch difference, so a separate plot was constructed for the Phase II data. This group had a Weibull slope of 9.4 and a maximum life of 45 hours, considerably less than the Phase I batch. Although one of the Phase II specimens lasted through 70 hours, it did not appear that this specimen followed the failure trend for this batch, thus the conservative extrapolation of maximum life.

The Wilcoxon Rank Test revealed that the two TRW batches at 2600°F represented the same population, and the data were pooled in plotting the Weibull distribution. With a threshold parameter (α) equal to zero, the resulting plot as shown in Figure 26 was not a straight line. By successive approximations it was finally determined that with an α equal to 24.5 hours, a straight line plot could be made. The resulting distribution had a slope of 0.9 (approximately exponential) and a maximum expected life of 114 hours.

The Boeing group exhibited the only bimodal failure distribution at 2600°F. The initial failure distribution followed a 0.7 distribution slope to 17 hours and a slope of 1.7 thereafter (see Figure 27). Maximum probable life of this coating was 39 hours.

The other three coatings demonstrated rather poor oxidation protection at 2600°F compared to the TRW and Sylcor coatings. The Pfadler PFR-32 coating exhibited rather unusual behavior. From the first cycle of test, an oxide film formed over the surface of all the specimens. This film was brushed away at each hourly cycle, but continued to reform. At the sixth cycle, the entire lot of specimens was removed from test and judged to be failed because of this oxide layer formation. These data were not treated by the Weibull analysis. The LTV specimens formed a Weibull slope of 0.7 for a maximum expected life of 20 hours (see Figure 28), and the Chromizing samples followed a slope of 2.0 with a maximum probable life of 13 hours (see Figure 29).

Estimates of reliability from the Weibull curves are summarized in Table 11. The relative positions of all of the coatings were identical at the 70, 90, and 95% levels of reliability and ranked as follows: Sylcor Phase I, Sylcor Phase II, TRW (pooled), Chromizing, Boeing, and LTV. The Pfadler was not ranked because of its erratic behavior.

Weibull plots for the 2400°F tests were presented in Figures 30 through 35. In the TRW and Sylcor Phase II tests, only four specimens per coating were tested, so the distribution plots represent only Phase I tests.

The oxidation behavior of the Sylcor Phase I coating at 2400°F was rather unusual inasmuch as specimen life was shorter than at 2600°F. The data were

**Table 11. Probable Cyclic Oxidation Life at 2400°F of
Coated C129Y for Various Levels of Reliability**

Coating	Coating Life (Hours) at Specified Levels of Reliability		
	70%	90%	95%
TRW Cr-Ti-Si	31	26	25
Pfudler PFR-32	(All Specimens Tested Failed After 6 Hours)		
Chromizing Durak KA	4	2	1-2
LTV Cr-B Modified Two-Cycle Silicide	<1	<1	<1
Sylcor Ag-Si-Al (I)	115-120	110	95
(II)	35	30	28
Boeing Disil	2	<1	<1

very tightly grouped as the Weibull slope (21.0) would indicate, and maximum expected life was 107 hours (see Figure 30). The mean life for the Phase I set was 90 hours, as compared to an average life of 64 hours for the Phase I group. This confirmed the 2600°F test results, which indicated a batch difference. Tests of the Phase II specimens of this coating followed expectations, showing longer life at 2400°F than at 2600°F.

A bimodal failure distribution was observed at 2400°F with the TRW Phase I coating. Initial failures followed a slope of 1.9 to 65 hours. The distribution broke sharply at this point and followed a slope of 7.7 to a maximum probable life of 85 hours (see Figure 31). A comparison of average failure times for the specimens of Phase I and Phase II (64 and 83 hours) suggested a batch difference not resolved in the 2600°F statistical comparison.

The other four systems behaved as follows at 2400°F:

- The Boeing coating failures followed a Weibull slope of 5.5 with a maximum coating life of 40 hours (see Figure 32);
- The Pfudler failure distribution formed a slope of 5.25 to a maximum expected life of 30 hours (see Figure 33);
- The LTV coating followed a random failure distribution (Weibull slope equal to 1.0) to a life of 50 hours (see Figure 34);
- The Chromizing coating exhibited a slope of 4.75 to a maximum life of 25 hours (see Figure 35).

The relative order of reliability for the six coatings at 2400°F (Table 12) was as follows: Sylcor, TRW, Boeing, Pfaudler, Chromizing, and LTV. It should be noted that the Boeing coating ranked much better at 2400°F than it had at 2600°F.

Table 12. Probable Cyclic Oxidation Life at 2400°F of Coated C129Y for Various Levels of Reliability

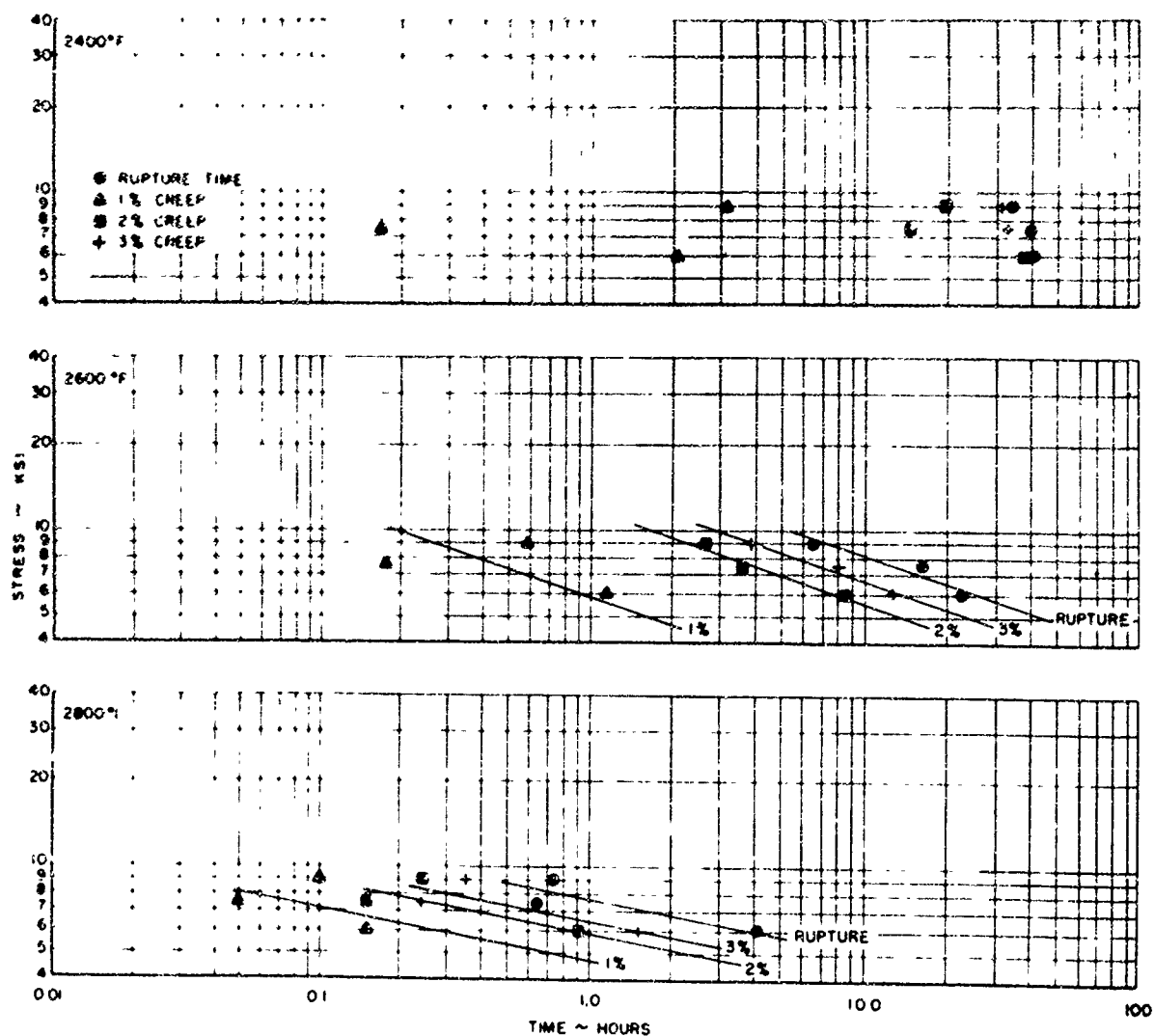
Coating	Coating Life (Hours) at Specified Levels of Reliability		
	70%	90%	95%
TRW - Cr-Ti-Si	60	32	23
Pfaudler -PFR-32	19	16	14
Chromizing - Durak KA	16	13	10
LTV -Cr-B Modified Two-Cycle Silicide	5	1	<1
Sylcor - Ag-Si-Al	96	90	82
Boeing - Disil	26	21	18

CREEP RUPTURE TESTING

The results of the creep rupture tests of the Sylcor Ag-Si-Al coating on D43 and C129Y and the TRW Cr-Ti-Si coating on C129Y are summarized in Figures 36 through 38 and Tables 13 through 19. The data include the times to 1%, 2%, and 3% creep and the time to rupture. The indicated percentages refer to the specimen elongation in excess of that produced by initial loading and thermal expansion. These creep levels are used merely to describe the behavior of the coating systems and are in excess of normal design limits.

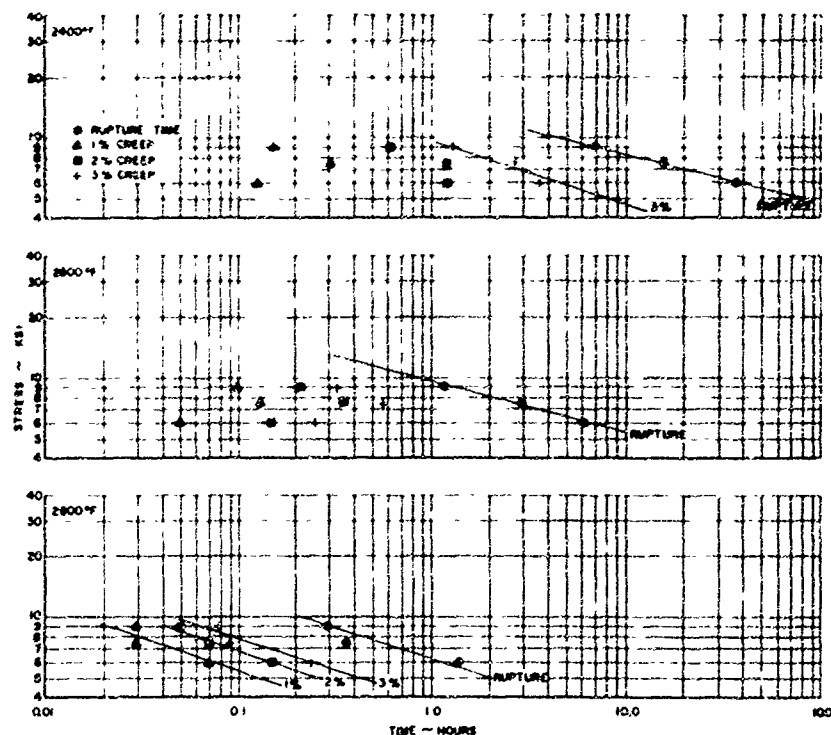
The analysis of variance applied to the data of these tests was to evaluate the quality of the experiment with respect to the overall effect of uncontrolled factors (the so-called "error term"), such as specimen or machine variability, and to estimate the effect of batch or testing machine differences.

Each point on the creep-rupture diagrams represents an average of the several tests at that particular stress-temperature combination. Where the scatter of data was not excessive, a regression line was fitted through the points by visual inspection.



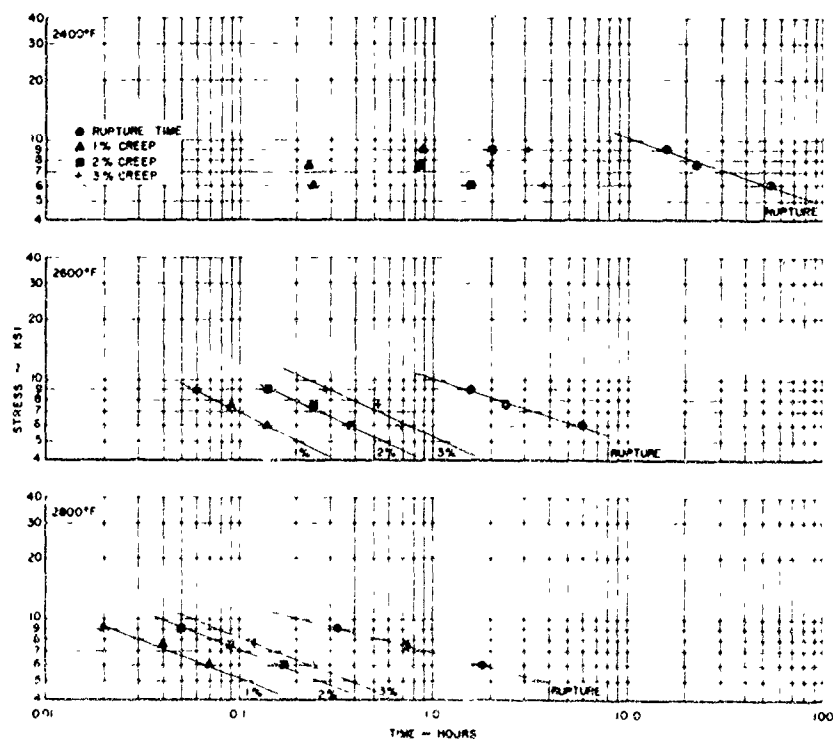
NOTE EACH POINT REPRESENTS AN AVERAGE OF FOUR VALUES CREEP DATA ARE BASED UPON A 175" GAGE LENGTH, ARE CORRECTED FOR THERMAL EXPANSION AND EXCLUDE THE INITIAL LOADING ELONGATION

Figure 36. Creep- and Stress-Rupture Curves for Sylcor (Ag-Si-Al) Coated 20 mil D43



NOTE EACH POINT REPRESENTS AN AVERAGE OF FOUR VALUES CREEP DATA ARE BASED UPON A 1.75" GAGE LENGTH, ARE CORRECTED FOR THERMAL EXPANSION AND EXCLUDE THE INITIAL LOADING ELONGATION

Figure 37. Creep-Rupture Curves for the Sylcor Ag-Si-Al Coating on 20 mil C129Y



NOTE EACH POINT REPRESENTS AN AVERAGE OF FOUR VALUES CREEP DATA ARE BASED UPON A 1.75" GAGE LENGTH, ARE CORRECTED FOR THERMAL EXPANSION AND EXCLUDE THE INITIAL LOADING ELONGATION

Figure 38. Creep-Rupture Curves for the TRW Cr-Ti-Si Coating on 20 mil C129Y

**Table 13. Stress-Rupture Data for 20 Mil D43 Columbian
Coated with Sylcor -Si-Al Slurry Silicide**

Temp. (°F)	Stress (psi)	Batch No.	Machine No.	Time (Hours) to Specific Creep Level			
				1%	2%	3%	Rupture
2400	6000	1	1	0.25	56.12	---	57.70
		1	2	7.92	46.45	51.55	52.23
		2	1	0.12	---	---	26.07
		2	2	0.17	---	---	26.95
2400	7500	1	1	0.11	2.70	40.02	62.52
		1	2	0.23	33.92	43.43	43.80
		2	1	0.26	20.15	23.60	27.25
		2	2	0.07	1.93	---	28.25
2400	9000	1	1	5.90	24.78	34.70	38.45
		1	2	6.65	34.00	47.00	53.62
		2	1	0.12	14.21	18.65	20.05
		2	2	0.09	7.16	28.32	28.32
2600	6000	1	1	0.27	5.37	9.53	23.08
		1	2	3.72	13.88	17.47	38.46
		2	1	0.42	8.68	17.60	23.46
		2	2	0.23	6.94	7.50	7.90
2600	7500	1	1	0.12	0.83	4.04	13.02
		1	2	0.13	2.45	4.91	15.03
		2	1	0.13	3.49	8.66	19.35
		2	2	0.34	7.73	11.46	18.70
2600	9000	1	1	0.16	1.17	2.25	6.55
		1	2	0.59	1.38	2.10	4.25
		2	1	1.19	3.76	5.10	6.66
		2	2	0.10	4.55	6.41	8.80
2800	6000	1	1	0.10	0.28	0.54	3.28
		1	2	0.09	0.29	0.64	2.65
		2	1	0.13	1.93	3.07	6.11
		2	2	0.26	1.10	1.72	4.18
2800	7500	1	1	0.05	0.14	0.27	0.93
		1	2	0.05	0.15	0.26	0.90
		2	1	0.07	0.17	0.26	0.56
		2	2	0.06	0.13	0.17	0.24
2800	9000	1	1	0.05	0.09	0.15	0.59
		1	2	0.05	0.14	0.21	0.75
		2	1	0.13	0.34	0.53	0.70
		2	2	0.16	0.38	0.52	0.87

NOTE: Stress values are based upon original substrate thickness.

Percent elongation values are based upon a 1-3/4" gage length. They are corrected for thermal expansion and exclude the initial elongation.

Table 14. Creep-Rupture Data for 28 Mil C129Y Columbian
Coated with Sylcor Ag-Si-Al Slurry Silicide

Temp. (°F)	Stress (psi)	Batch No.	Machine No.	Time (Hours) to Specific Creep Level			
				1%	2%	3%	Rupture
2400	6000	1	1	0.07	0.49	2.58	38.99
		1	2	8.20	1.86	4.14	32.66
		1	3	0.12	0.55	2.14	36.19
		1	4	0.10	0.47	3.21	47.21
		2	1	0.05	0.46	2.10	37.77
		2	2	0.13	2.92	7.75	34.97
		2	3	0.23	1.75	3.45	33.46
		2	4	0.16	1.52	4.15	40.01
2400	7500	1	4	0.27	1.55	4.00	17.84
		2	4	0.35	0.93	1.53	14.02
2400	9000	1	1	0.35	1.14	2.00	8.72
		1	2	0.15	0.85	1.86	7.61
		1	3	0.18	0.64	1.45	5.96
		1	4	0.17	0.81	1.65	6.68
		2	1	0.06	0.25	0.78	6.64
		2	2	0.12	0.42	0.82	3.80
		2	3	0.16	0.62	1.17	5.29
		2	4	0.08	0.35	0.92	4.46
2600	6000	1	3	0.07	0.24	0.47	6.22
		2	3	0.03	0.07	0.10	6.03
2600	7500	1	3	0.15	0.41	0.63	2.65
		2	4	0.11	0.30	0.50	3.18
2600	9000	1	4	0.09	0.19	0.29	1.91
		2	4	0.12	0.23	0.35	1.33
2800	6000	1	1	0.05	0.12	0.19	1.68
		1	2	0.09	0.19	0.30	1.54
		1	3	0.07	0.15	0.23	1.36
		1	4	0.05	0.16	0.26	1.70
		2	1	0.06	0.13	0.20	1.25
		2	2	0.04	0.15	0.23	1.27
		2	3	0.07	0.14	0.22	1.30
		2	4	0.07	0.18	0.29	0.92
2800	7500	1	3	0.03	0.07	0.10	0.41
		2	3	0.03	0.07	0.09	0.31
2800	9000	1	1	0.03	0.07	0.09	0.41
		1	2	0.03	0.07	0.09	0.22
		1	3	0.02	0.04	0.06	0.16
		1	4	0.03	0.05	0.08	0.32
		2	1	0.03	0.05	0.07	0.31
		2	2	0.03	0.06	0.10	0.30
		2	3	0.02	0.05	0.07	0.37
		2	4	0.02	0.05	0.08	0.22

NOTE: Stress values are based upon original substrate thickness.

Percent elongation values are based upon a 1-3/4" gage length. They are corrected for thermal expansion and exclude the initial elongation.

**TABLE 25. Creep Rupture Data for 20 M21 C12V Columbium
Coated With TRW Cr-Ti-Si Coating**

Temp. (°F)	Stress (psi)	Batch No.	Machine No.	Time (Hours) to Specific Creep Level			Rupture
				1%	2%	3%	
2400	6000	1	1	0.12	1.23	3.42	53.45
		1	2	0.26	2.13	4.15	46.19
		1	3	0.13	0.46	1.40	47.52
		1	4	0.47	2.41	4.42	74.81
		2	1	0.24	2.15	3.75	50.70
		2	2	0.14	1.56	3.92	42.20
		2	3	0.20	1.08	2.66	45.50
		2	4	0.30	1.42	5.79	71.39
2400	7500	1	2	0.15	0.78	2.19	24.55
		2	1	0.30	0.93	1.72	20.47
2400	9000	1	1	2.33	4.34	5.80	18.80
		1	2	1.40	2.23	3.18	12.83
		1	3	1.66	4.35	6.73	35.56
		1	4	0.09	0.38	0.98	14.09
		2	1	0.83	2.45	3.72	15.67
		2	2	0.28	0.80	1.21	4.85
		2	3	0.23	0.64	1.55	11.40
		2	4	0.19	0.87	1.64	12.69
2600	6000	1	2	0.12	0.30	0.55	5.45
		2	1	0.15	0.45	0.80	6.15
2600	7500	1	1	0.10	0.23	0.37	2.19
		2	2	0.08	0.25	0.43	2.53
2600	9000	1	2	0.04	0.09	0.15	1.25
		2	1	0.08	0.19	0.30	1.82
2800	6000	1	1	0.10	0.20	0.30	1.82
		1	2	0.70	0.17	0.26	1.66
		1	3	0.07	0.15	0.25	1.76
		1	4	0.06	0.13	0.21	1.76
		2	1	0.08	0.11	0.17	1.28
		2	2	0.05	0.12	0.18	1.69
		2	3	0.05	0.14	0.23	2.19
		2	4	0.08	0.18	0.29	1.99
2800	7500	1	1	0.05	0.11	0.17	1.06
		2	2	0.03	0.05	0.07	0.37
2800	9000	1	1	0.02	0.05	0.08	0.29
		1	2	0.02	0.03	0.04	0.30
		1	3	0.02	0.05	0.07	0.35
		1	4	0.03	0.09	0.13	0.56
		2	1	0.03	0.06	0.08	0.35
		2	2	0.02	0.06	0.09	0.40
		2	3	0.03	0.05	0.08	0.27
		2	4	0.02	0.04	0.06	0.31

NOTE: Stress values are based upon original substrate thickness.

Percent elongation values are based upon a 1-3/4" gage length. They are corrected for thermal expansion and exclude the initial elongation.

Table 16. Analysis of Variance of Creep Rupture
Data for Sylcor (Ag-Si-Al) Coated 12 Mil D43

Significant Inputs	Level of Significance	% Contribution to Variance of Failure Time
Temperature	99%+	65.08
Stress	99%+	2.86
Batch	99%+	7.33
Temperature x Batch	99%+	17.45
Error	--	7.27

Table 17. Analysis of Variance of Creep Rupture
Data For Sylcor (Ag-Si-Al) Coated 20 Mil C129Y

Significant Inputs	Level of Significance	% Contribution to Variance of Failure Time
Temperature	99%+	37.13
Stress	99%+	22.19
Batch	95%+	0.09
Machine	95%+	0.18
Temperature x Stress	99%+	38.63
Temperature x Machine	95%+	0.36
Temperature x Stress x Machine	95%+	0.68
Stress x Machine	95%+	0.33
Error	--	0.41

Table 18. Analysis of Variance of Creep Rupture
Data for TRW (Cr-Ti-Si) Coated 20 Mil C129Y.

Significant Inputs	Level of Significance	% Contribution Variance of Failure Time
Temperature	99%+	45.84
Stress	99%+	15.65
Batch	95%+	0.41
Machine	99%+	0.78
Temperature x Stress	99%+	26.92
Temperature x Batch	95%+	0.82
Temperature x Machine	99%+	1.48
Stress x Machine	99%+	2.31
Temperature x Stress x Machine	99%+	4.71
Error	--	1.08

**Table 19. Comparative Creep Rupture Data for TRW
and Sylcor Coated C129Y**

Temp (°F)	Stress (psi)	Average Time (hrs) to Specific Creep Levels							
		1%		2%		3%		Rupture	
		TRW	Sylcor	TRW	Sylcor	TRW	Sylcor	TRW	Sylcor
2400	6000	0.24	0.13	1.55	1.25	3.69	3.70	53.72	37.58
	7500	0.23	0.31	0.86	1.24	1.96	2.77	22.51	15.93
	9000	0.88	0.16	2.03	0.64	3.10	1.33	15.74	6.15
2600	6000	0.14	0.05	0.38	0.16	0.68	0.26	5.80	6.13
	7500	0.09	0.13	0.24	0.36	0.40	0.56	2.36	2.92
	9000	0.06	0.11	0.14	0.21	0.23	0.32	1.56	1.18
2800	6000	0.07	0.06	0.17	0.15	0.24	0.24	1.77	1.38
	7500	0.04	0.03	0.08	0.07	0.12	0.10	0.72	0.46
	9000	0.02	0.03	0.05	0.06	0.08	0.08	0.34	0.29

Rather dramatic differences were noted in the creep-rupture behavior of the two alloys. The coated D43 was definitely superior to both C129Y coating systems in creep resistance and rupture life at all stress levels and temperatures. Although no data for the uncoated alloys were available for comparison, it would seem unlikely that the difference in behavior between the two Sylcor systems (both with the same basic coating) could be attributed entirely to coating effects. It is more probable that these data reflect inherent differences in the creep-rupture properties of the two alloys.

The error term in each analysis, which in effect represented the combined influence of all uncontrolled variables, was relatively low. Since this term includes the effect of specimen-to-specimen variability, it can be concluded that specimen reproducibility was fairly good with both alloys.

D43 Columbium Alloy

The creep-rupture behavior of the Sylcor coating system was fairly uniform at 2600°F and 2800°F, and regression lines were fitted to the data. However, no attempt was made to fit curves to the 2400°F data because of the wide scatter.

As was expected, the analysis of variance revealed temperature, stress, and the temperature x stress interaction to be the dominant factors in the experiment. However, batch difference, not expected to be important, was also significant, appearing as a main effect and a batch x temperature interaction. There is little doubt that the batch variations of the Sylcor Ag-Si-Al coating significantly affected the creep-rupture behavior of D43 columbium.

Analyzing for machine difference revealed that the two creep frames were identical and in no way exerted any influences upon the creep-rupture evaluation.

C129 Columbium Alloy

Both the TRW and the Sylcor coating systems exhibited rather uniform creep-rupture curves at 2800°F. A smooth curve was also developed for the TRW coating at 2600°F, whereas the Sylcor data at 2600°F were very erratic except at rupture. However, the fact that only two tests rather than eight were performed at each stress level could be partially responsible. At 2400°F, the Sylcor test data were fairly uniform at 3% creep and rupture, but somewhat scattered at the two lower creep levels. The TRW system at 2400°F demonstrated widely scattered results at all creep levels.

In comparing the performances of both coatings, inconsistencies in the averaged data were noted (see Table 19, previous page). However, most of this was confined to the 2600°F tests at all stress levels and the 7500 psi tests at the other temperatures. These were the levels at which only two tests were performed at each stress-temperature combination. The other averages, based upon eight tests, indicated that the TRW coated C129Y consistently outperformed the Sylcor system with respect to creep-rupture life.

Analyses of variance for their rupture behavior, presented in Tables 17 and 18, showed both coating systems to be significantly affected by temperature, stress, and the temperature x stress interaction. These three factors accounted for a total of 97.95% of the total variance in the TRW analysis and 88.41% of the total variance in the Sylcor analysis. Unlike the coated D43 tests, however, these analyses both showed statistically significant machine and batch differences as well as interactions of the two with other factors. However, in each case, the total contribution of these factors to the overall variance was very small, and it is reasonable to assume that their effect on the evaluation was negligible.

SUMMARY

D43 COLUMBIUM COATINGS

Sylcor Ag-Si-Al/D43

The Sylcor Ag-Si-Al slurry coating proved to be extremely oxidation resistant at all test temperatures and was the only one which provided protection at 3000°F. It was a very thick and nonuniform coating, not typical of the others evaluated in this program. However, this particular system could present a problem in applications requiring close tolerances on mating parts such as threaded fasteners, faying surfaces, etc.

Metallographic analyses, conducted on one specimen from each of the two 12 mil creep-rupture batches and one specimen from each of the two 20 mil batches, revealed some interesting differences. All four specimens contained similar 2 mil inner coating zones, but the outer zone coverage was very irregular. Thickness measurements of other specimens not metallographically analyzed revealed a wide range of coating thicknesses within batches. Therefore, it is suspected that coating thickness differences were a specimen-to-specimen rather than a batch-to-batch phenomenon.

In oxidation testing, specimen lives appeared to correlate directly with average thickness at most test temperatures. For instance, at 2600°F, where ten specimens from each batch were tested, the Phase I group demonstrated a life ranging from 63 to 155 hours, whereas the thinner Phase II set ranged from 52 to 117 hours.

There was no apparent batch effect with regard to the measured mechanical properties of this coating system. Both batches exhibited similar mechanical properties, maintaining a BTT below -50°F and similar losses in tensile strength and ductility, none severe compared to the other coatings tested.

Creep-rupture tests of this coating on D43 revealed statistically significant batch differences. Batch I specimens in several tests exhibited creep and rupture times twice those of Batch II specimens tested under the same conditions.

With respect to the other coatings, this system possessed the best oxidation resistance at all temperatures but was rather poor with respect to reproducibility of coating coverage and thickness control. In mechanical properties, it ranked among the best.

TRW Cr-Ti-Si/D43

This coating, although not demonstrating the degree of protectiveness of the Sylcor Ag-Si-Al system, performed quite well when compared to the other coatings tested in this program. Furthermore, it was much thinner and more uniform than the Sylcor coating, which could be a distinct advantage in certain applications. One liability of this coating was its poor batch-to-batch reproducibility.

In metallographic analyses, batches were similar in appearance and hardness measurements, but differed slightly in thickness (2.0 to 1.6 mils). This thickness difference apparently affected room temperature mechanical properties as well as the oxidation performance of the system.

Both batches maintained a BTT below -50°F, but the thinner coating demonstrated approximately 10% greater strength and 75% greater ductility (as shown by ultimate tensile elongation).

As expected, the thicker coating performed better in cyclic oxidation tests. At 2400°F, the only temperature where comparison could be made, the thicker coating showed a mean life of 127 hours as compared to 74 hours for the thinner one.

It is apparent that this coating provided good oxidation protection and was quite uniform and reproducible from specimen to specimen within the same batch. However, it did demonstrate rather severe batch-to-batch differences which grossly affected the characteristics of the coated alloy.

Other D43 Coatings

Among the other four coatings evaluated in Phase I tests (Pfaudler PFR-32, LTV Cr-B Silicide, Boeing Disil, and Chromizing Durak KA), the Chromizing and Pfaudler coatings demonstrated the best overall mechanical properties of the six D43 coating systems evaluated, but both ranked last in oxidation resistance.

The LTV coating ranked last in retention of mechanical properties, but ranked below only the Sylcor and TRW systems in oxidation protection (considering all test temperatures) and was quite superior to these other three coatings.

The Boeing Disil system ranked fifth in oxidation resistance and sixth in overall mechanical properties along with the TRW Phase I coating system.

C129Y COLUMBIUM COATINGS

Wrought rather than fully annealed sheet was used in the evaluation of coatings for C129Y. Several of the coating processes produced partial or full annealing of the base metal which was quite evident in both "as coated" metallography and in tensile testing. This presented an interesting, but quite unintentional opportunity to observe how each of the coating processes affected the heat treatment of the alloy. Since high temperature applications of this alloy would most probably involve fully recrystallized sheet, no attempt was made to rate the six C129Y coating systems with respect to tensile properties after coating. With only one exception (PFR-32), changes in tensile properties after coating were directly related to the degree of substrate recrystallization. The PFR-32 coating system was apparently embrittled during coating application.

Sylcor Ag-Si-Al/C129Y

This slurry coating on C129Y performed similarly to the same system on D43. It provided good protection at all test temperatures, including 3000°F. While not as thick or as nonuniform as the D43 coating, in comparison with the five silicides, it would hardly be called a thin coating.

Metallographic analyses of "as received" specimens of the two batches showed them to be very similar both in appearance and in average coating thickness, but of slightly different hardness values.

In oxidation testing, the Phase I batch outperformed the Phase II set at 2400°F (average failure times were 91 and 64 hours respectively). At 2600°F, the Phase I batch averaged 113 hours to failure, the Phase II batch 39 hours. It should be noted that the Phase I average failure time was greater at 2600°F than at 2400°F.

The two batches revealed similar mechanical properties. Both maintained a BTT below -50°F, as the uncoated C129Y had done. While the ultimate strength and elongation values were not appreciably different, the average yield strength of the Phase I batch was approximately 12% greater than the Phase II specimens.

Creep-rupture testing revealed statistically significant batch differences on the creep resistance and rupture life of this coating. However, these differences were very slight and, for all practical purposes, could be neglected.

The Sylcor Ag-Si-Al slurry coating demonstrated very good oxidation protection compared to most of the other coatings, although its oxidation resistance varied greatly from batch to batch. This coating did not appear to appreciably affect the mechanical properties of the substrate. The main deficiencies of this coating are its thickness and irregularity of coverage, as well as the aforementioned batch variation in oxidation resistance.

TRW Cr-Ti-Si/C129Y

This coating was very similar to the TRW coating on D43. While not protective at 3000°F, it demonstrated good oxidation protection at all other test temperatures and ranked close to the Sylcor coating in this respect, while being much thinner and more uniform. Furthermore, it showed more batch consistency in performance even though the physical appearance of the two batches suggested significant batch differences.

In metallographic analyses, the two batches were similar with respect to microhardness, but exhibited some difference in coating thickness (2.1 and 1.6 mils), just as the TRW/D43 coating had shown. The two batches were quite different in appearance, the Phase II coating was much darker and contained only one distinct layer, whereas the Phase I coating contained two visible layers.

The two TRW batches yielded similar mechanical property data. Both exhibited a BTT below -50°F and had similar strength and ultimate elongation values.

In oxidation testing at 2600°F, where sufficient specimens were tested to make a statistical comparison, both batches were found to represent the same population.

The TRW coating demonstrated better creep resistance and rupture life than the Sylcor system, with lives averaging about 1-1/2 times that of the slurry coating. Some small statistical batch variations were noted in creep and rupture performance, but the magnitude of these variations was small.

The TRW coating on C129Y proved to be a fairly reproducible and uniform coating which provided good oxidation protection.

Other C129Y Coatings

As in the D43 coatings' evaluation, the other four coatings evaluated in Phase I tests only were: Pfudler PFR-32, LTV Cr-B Silicide, Boeing Disil, and Chromizing Durak KA.

Like the D43 coatings, the Pfudler and Chromizing coatings demonstrated some substrate embrittlement through an increase in bend transition temperature, but the remaining two (LTV and Boeing) retained their ductility to -50°F.

In overall oxidation resistance, the LTV coating ranked last, whereas, in the D43 evaluation, it had ranked just behind the Sylcor and TRW systems. The Chromizing coating demonstrated much better oxidation protection on C129Y than on D43 and ranked third in this test series.

DISCUSSION OF COATING RATINGS

Table 20 lists the relative order of performance for the best effort coatings evaluated in this program. Ratings were established for the three major areas investigated: retained mechanical properties, oxidation resistance, and creep-rupture behavior. These ratings are based upon simple tests and should not be considered absolute for any refractory metal applications. They reflect the personal judgement of the authors and are presented only as a guide for selection of candidate coatings.

Since the performance of individual coatings has been summarized elsewhere, this section will be devoted to a general discussion of testing methods and an interpretation of test results.

Since cyclic oxidation testing was emphasized in this program, it is appropriate to devote a major portion of this discussion to the advantages and disadvantages of this test. It is recognized that the cyclic oxidation test as performed in this program is not perfect and that there are other effective approaches to measuring the oxidation protection of coatings.

Table 20. Coating Performance Ratings

Mechanical Properties

<u>Rank</u>	<u>D43 Columbium</u>
1	Pfautler PFR-32
1	Chromizing Durak KA
3	Sylcor Ag-Si-Al Phase I
3	Sylcor Ag-Si-Al Phase II
5	LTV Cr-B Modified Silicide
6	TRW Cr-Ti-Si Phase II
7	TRW Cr-Ti-Si Phase I
7	Boeing Disil

Oxidation Resistance

<u>Rank</u>	<u>D43 Columbium</u>	<u>Rank</u>	<u>C129Y Columbium</u>
1	Sylcor Ag-Si-Al Phase I	1	Sylcor Ag-Si-Al Phase I
2	Sylcor Ag-Si-Al Phase II	2	Sylcor Ag-Si-Al Phase II
3	TRW Cr-Ti-Si Phase I	3	TRW Cr-Ti-Si Phase II
4	TRW Cr-Ti-Si Phase II	4	TRW Cr-Ti-Si Phase I
5	LTV Cr-B Modified Silicide	5	Chromizing Durak KA
6	Boeing Disil	6	Pfautler PFR-32
7	Pfautler PFR-32	7	Boeing Disil ¹
8	Chromizing Durak KA	8	LTV Cr-B Modified Silicide

Creep Resistance
(C129Y Columbium)

<u>Rank</u>	<u>2400°F</u>	<u>2800°F</u>
1	TRW Cr-Ti-Si	TRW Cr-Ti-Si
2	Sylcor Ag-Si-Al	Sylcor Ag-Si-Al

Creep Rupture Life
(C129Y Columbium)

<u>Rank</u>	<u>2400°F</u>	<u>2800°F</u>
1	TRW Cr-Ti-Si	TRW Cr-Ti-Si
2	Sylcor Ag-Si-Al	Sylcor Ag-Si-Al

The use of Weibull analysis in the treatment of cyclic oxidation test data provided a better understanding of the coating failure processes. However, with only ten to twenty tests per coating system, the overall sensitivity of the experiment was low. It would seem that an increase in the minimum number of specimens to twenty-five would provide a much more reliable analysis.

The coated columbium specimens were considered failed in cyclic oxidation when a major coating rupture became evident from an accumulation of oxide on the specimen surface. It is possible that, in some cases, diffusion of oxygen through the coating and into the base metal occurred before there was visual evidence of substrate oxidation. Leakage of oxygen and the extreme embrittlement and loss of strength which accompany such oxygen contamination could seriously compromise the structural capability of a columbium alloy.

If the visual inspection of cyclic oxidation specimens had been augmented with bend testing and metallographic examination, a drastic revision in the relative order in which these systems were rated could have resulted. Present systems for evaluating oxygen contamination by these two methods necessarily involve destruction of the specimens and do not lend themselves readily to the present scheme of testing. Future coating evaluations should probably include a series of expendable specimens to be tested concurrently with the cyclic oxidation tabs. These expendable specimens would be removed from test at specified intervals, bend-tested, and metallographically examined to measure any time-dependent changes in the coating and base metal.

The step-down oxidation test proposed by the Materials Advisory Board (Reference 1) can provide useful information regarding the sensitivity of coatings to slow thermal cycling. To illustrate this, tests were conducted on a group of B66 columbium coatings including: Boeing Disil, Pfaudler PFR-32, Sylcor Cr-Ti-Si, and Chromizing Durak KA. They consisted of a series of cyclic exposures in three decreasing temperature steps with examination of specimens at the end of each three-temperature cycle. Three furnaces operating at 2600°, 2200°, and 1400°F were employed. Starting at 2600°F, specimens were subjected to 30-minute exposures at decreasing increments of temperature by quickly transferring specimens from one furnace to another at the end of each 30-minute period. Specimens were subjected to a maximum of five cycles, with visual examination and weighings between cycles.

The results, summarized in Table 21, were rather interesting. Varying degrees of performance were observed among the four coating systems, and only the Boeing Disil survived five full thermal cycles. Three of the coatings demonstrated very poor resistance to this type of thermal cycling, including the Sylcor system, which had exhibited outstanding protection in conventional cyclic oxidation tests (Reference 2). It appears that further evaluation of this technique should continue with similar testing of other coated columbium base alloys.

**Table 21. Results of Step-Down Oxidation Tests
on Coated B66 Columbium**

<u>Coating</u>	<u>No.</u>	<u>Cycles</u>	<u>Remarks</u>
Boeing (Disil)	1	5 (No Failure)	First cycle crazing with formation of a buff oxide in the cracks
	2	5 (No Failure)	
	3	5 (No Failure)	
Pfaudler (PFR-32)	1	1(c)	Crazing and spotty oxide which spalled, exposing the substrate
	2	3(e)	
	3	2(e)	
Sylcor (Ti-Cr-Si)	1	2(e)	Green after first cycle
	2	2(e)	
	3	4(e)	
Chromizing	1	2(c)	75% coverage with buff oxide after first cycle
	2	1(c)	
	3	2(c)	

NOTE: Letters in parentheses refer to failure location; i. e., e = edge, s = surface, c = catastrophic.

The addition of a low pressure oxidation testing capability also appears to be desirable for a balanced program which can provide basic information necessary to select candidate coatings for a variety of applications. Such a furnace, capable of rapidly processing large groups of specimens, is presently being constructed.

To obtain performance data on a maximum number of coatings within the time allotted for this program, the practice of testing in two separate phases was followed. It was intended that two coatings from an initial group of six would be selected from Phase I screening tests for a more comprehensive evaluation in the second phase of the program. This selection was to be based upon retained mechanical properties and demonstrated oxidation resistance. In reality, retained mechanical properties played a minor role in coating selection, and primary emphasis centered about oxidation behavior.

Since the oxidation test was an arbitrarily defined procedure, it is conceivable that coatings' systems of potential merit with superior batch-to-batch reproducibility and creep-rupture properties were screened from the program. It would have been very desirable to carry every coating through the entire evaluation; however, as was previously noted, this was not possible due to time limitations.

The hazard of using only one performance criterion, such as cyclic oxidation life, for the screening of coatings was illustrated by the results obtained in creep-rupture tests of the systems rated first and second in the Phase I evaluation. The Sylcor Ag-Si-Al coated C129Y was definitely superior to the TRW Cr-Ti-Si coated C129Y in cyclic oxidation resistance, and yet the TRW system was noticeably better in creep resistance and rupture life. In the creep-rupture tests, very clean specimen breaks were obtained with both coating systems, and there was a minimum of oxidation in these regions. This would suggest that factors other than pure oxidation resistance (such as reactivity between the coating and the base metal at elevated temperatures and substrate changes produced by the coating process) controlled the creep-rupture behavior of these two systems.

Another example of conflicting test results was observed between cyclic oxidation and step-down oxidation test results. In this case, the Sylcor Ti-Cr-Si coating on B66 averaged 88 hours to failure in 2600°F cyclic oxidation tests. This same system failed in 2 to 4 cycles of a step-down oxidation test where the total exposure time in each cycle was 1-1/2 hours divided equally among three temperatures, 1400°, 2200°, and 2600°F.

The different ordering of results for creep-rupture, cyclic oxidation, and step-down oxidation tests illustrates an important consideration that must be foremost in the minds of those who interpret laboratories' evaluation data to select candidate coatings for a specific application. No coating system presently available excels in all categories of performance, and, therefore, the environmental parameters associated with the ultimate use of such coatings must be considered in weighing the relative importance of performance indices measured in these tests. Furthermore, since many of these tests were arbitrarily defined, there may not be close similarity between the test environment and the ultimate use environment. When this is the case, extreme caution must be exercised in the analysis of screening data, and final coating selection should be based upon tests which specifically simulate the final application.

RECOMMENDATIONS

The following recommendations seem appropriate for the continuation of this effort in a balanced program which provides basic information necessary for the selection of candidate coatings for current and advanced refractory metal applications.

1. The step-down oxidation test recommended by the Materials Advisory Board has merit and should be included, in addition to conventional cyclic oxidation testing. Furthermore, a continued close cooperation with the MAB should be maintained in adding new tests or changing current techniques.

2. Low pressure oxidation testing should be added to the program as quickly as possible.

3. No candidate coating should be omitted from Phase II testing unless Phase I tests reveal it to be grossly inadequate. If reasonable performance is obtained in preliminary tests, a full evaluation should follow.

4. The Weibull analysis of cyclic oxidation tests should be continued, but the number of specimens per batch should be increased to improve the sensitivity of the test. Furthermore, improved techniques for identification of oxidation failures should be devised.

5. In creep-rupture testing, tests at mid-level stress and temperature combinations should be conducted only in sufficient quantity to provide intermediate points for the preparation of creep-rupture diagrams. The full factorial testing should concentrate on replicated experiments at two levels of temperature and stress.

6. Emphasis should be shifted from sheet metal structural applications to other refractory metal uses, including propulsion systems. Tests should be added and modified as necessary to reflect any such change in emphasis.

SECTION II ARC-PLASMA-JET TESTING

INTRODUCTION

In May, 1959, a subcommittee of the Refractory Composites Working Group issued a tentative screening test procedure for the preliminary evaluation of high temperature materials (Ref. 6). This proposed test was intended to serve as a standard screening criterion and was designed for simplicity and economy. A nitrogen stabilized arc plasma jet modified to deliver a 1/2" diameter effluent of high-temperature simulated air was proposed as the testing device. Environmental levels were to be controlled as a function of cold wall heat flux measured by a standard 1/2" diameter flat face water-cooled copper calorimeter. Standard test conditions were 100, 300, and 500 Btu/ft² sec with exposure times adjusted such that the product of heat flux and exposure time always equalled a total heat pulse of 12,000 Btu/ft² sec. The test specimen was a 2" x 2" x 1/2" flat plate, oriented at a 45° angle to the subsonic discharge of the plasma stream.

Arc-plasma-jet screening tests performed by the University of Dayton were patterned after the procedures recommended by the Working Group. Minor changes were made where it was believed such changes would result in more meaningful test data.

EVALUATION PROCEDURES

In routine arc-plasma evaluations, test conditions are specified in terms of cold wall heat flux and stagnation pressure. These effluent properties are measured at the specimen location with a combined pitot tube-calorimeter probe (Figure 39). In this instrument, the calorimeter portion is a 1/2" diameter copper tube sealed at one end by a flat disc. Heat flux to this calorimeter is measured as a function of the rate of heat energy transfer through this disc to water circulating through the calorimeter body. The pitot tube orifice is located in the water-cooled guard ring of the probe, directly below the centerline orifice of the calorimeter face. To obtain a pressure measurement, the calorimeter portion of the probe assembly is centered in the flow and then the entire probe lifted a preset distance by a mechanical lever to position the pitot tube orifice in the center of the plasma discharge.

The procedure for performing these screening tests was as follows: prior to exposure of a test specimen, test conditions were determined from measurements of

- (a) nitrogen and oxygen flow rate,
- (b) input power to the plasma jet,
- (c) power losses to the coolant,
- (d) heat flux at the sample location,
- (e) stagnation pressure at the sample location.

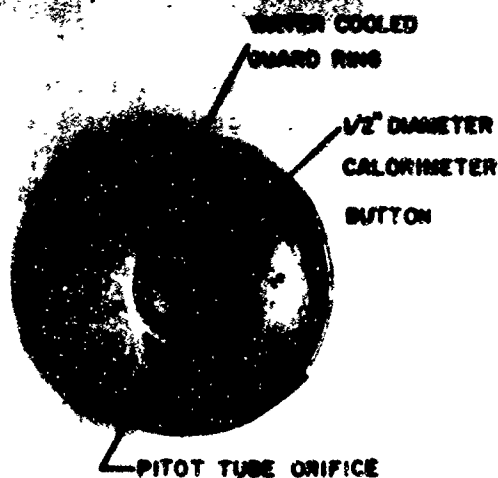


Figure 39. Combined Calorimeter and Pitot Tube Assembly

From these measured values were calculated:

- (a) effluent velocity at the sample,
- (b) effluent enthalpy at the exit plane of the plasma-jet,
- (c) effluent temperature at the exit plane of the plasma-jet.

Following the calibration procedure, the specimens which had previously been weighed and measured were inserted into the plasma stream for test. During exposure, front and back surface temperatures were continuously recorded as a function of time. Front surface temperature was also monitored periodically with an optical pyrometer.

Immediately after test, the calibration procedure was repeated as a recheck of the initial test conditions. Samples were photographed and the following physical measurements taken: depth and volume of erosion, density, and weight. Details of the calibration, test and sample measurement procedures are described in Refs. 7, 8, and 9.

Several special tests which depart from the "standard" procedure described above have evolved to meet the requirements of different specimen geometry or when a more sophisticated evaluation is desired. Two such tests are described in subsequent sections of this report.

TEST RESULTS

The results of "standard" screening tests are described for several classes of materials and include a brief discussion of the test method employed. For those materials which were proprietary, only a general description of the material will be presented, and any reference to their manufacturer will be by code letter only.

The majority of test data is tabulated in a standard form describing test conditions and their effects upon the sample. Supplementing these data are front and back surface temperature-time histories for each specimen. The final front surface temperature reported in the tables will be optical pyrometer temperature and will generally not correspond with the recorded total radiation temperature because of emittance effects.

Unless otherwise noted, all tests were conducted in a simulated air environment at a mass flow rate of 0.0082 lb/sec.

IMPREGNATED POROUS CERAMICS

Resin-impregnated porous ceramics have been proposed for use in certain high temperature applications where, in addition to being insulative and capable of providing thermal protection, the material must have a high strength to weight ratio and be resistant to erosion and thermal shock. Composites of this type include the resin-impregnated open-cell foamed refractory ceramics.

A number of foamed ceramics were evaluated in the arc-plasma facility. These tests were conducted at a heat flux level of 275 Btu/ft² sec for a scheduled 300-second exposure. Tests were terminated earlier only if erosion proceeded to the extent that back surface temperatures reached excessive values (2000° to 2800°F). The heat flux level for these tests was selected so that the equilibrium temperature of the ceramic would not exceed the melting point of the ceramic matrix but would impose a thermal loading sufficient to decompose the ablative impregnant and damage any system sensitive to thermal shock.

In analyzing these test data, the significant parameters were test duration, erosion depth, and back surface temperature. Weight and volume loss measurements were useful only if no erosion of the ceramic occurred, and then only to estimate the amount of impregnant lost during test. Since some of these specimens did experience erosion, the performance indices of erosion volume and weight loss should be treated in a very qualitative sense in this evaluation.

MANUFACTURER I

Twelve specimens of foamed zirconia and three densities (1.0, 1.1, and 1.24 gm/cc) were evaluated at 275 Btu/ft² sec for 300-second exposures according

to the general procedures described in the preceding section. Half of the specimens (two of each density) were phenolic resin-impregnated with approximately 30 to 40 w/o resin. Duplicate tests were then performed on each foam density, two unfilled and two with phenolic resin impregnant.

The ceramics were resin-impregnated in a bell jar apparatus by immersing the specimen in SC1008 phenolic resin and then evacuating the bell jar to force the resin into the pores of the ceramic. When air bubbles ceased to issue from the specimen, it was removed from the chamber, cured for 16 hours at 165°F, followed by 4 hours at 200°F, and then machined to size.

The results of these tests and the corresponding temperature-time histories are summarized in Tables 22 and 23.

The performance of the unfilled foams was rather impressive. Unlike previously evaluated unfilled foamed zirconia specimens which failed in thermal shock after a few seconds of heating (Ref. 14) these specimens all survived a full 300-second exposure. Thermal stress cracking was observed with both of the two low density specimens and one each of the medium and high density specimens. These failures were evident from the back surface temperature behavior which either stabilized at a higher level or increased abruptly at the time of thermal stress cracking as the result of hot gas flow through the specimen. Despite these cracking failures, attrition of material was only minor and in no instance did weight loss exceed 2%. Front surface temperatures of the unfilled foams stabilized at approximately 4200°F. Back surface temperature levels were inversely proportional to foam density and ranged from 1000°F to 2360°F.

The phenolic resin-impregnated specimens experienced no measurable erosion, nor was there any evidence of thermal stress cracking. Back surface temperatures remained at room temperature for the first 75 seconds of test, and then began to rise slowly. After 125 seconds, when resin ablation was nearing completion, the influence of density upon thermal insulating ability was discernible. The low and medium density foams followed nearly the same back surface temperature profile. The high density foam remained at a lower back surface temperature throughout each test.

Final specimen temperatures of the impregnated samples, both front and back surface, followed the same relative order, with the low density foam the highest and the high density foam the lowest.

MANUFACTURER UT

Two samples of a chemically bonded zirconia foam which had been phenolic resin-impregnated by the manufacturer were also evaluated at a 275 Btu/ft² sec heat flux. The results of these tests are presented in Table 24 along with their corresponding temperature-time histories.

Material		Low Density Foam		Medium Density Foam		High Density Foam	
Heat Flux (BTU/ft ² -sec)		275		275		275	
Gas Evolveloz (BTU/lb)		25500		25500		25500	
Total Porosity (cc)		300		300		300	
Magnesium Pressure (psi)		0.577		0.570		0.577	
Gas Temperature (°F)		5910		5920		5910	
Gas Velocity (ft/sec)		890		880		890	
Decrease in Gas Weight %		16.54		15.82		17.15	
Density Before (gm/cc)		34.2		34.1		37.3	
Density After (gm/cc)		1.95		1.93		2.11	
Depth of Erosion (in.)		-0.018		-0.013		-0.018	
Volume of Erosion (in. ³)		0.025		0.022		0.046	
Final Back Face Temp (°F)		1660		1650		1300	
Final Front Face Temp (°F)		630		640		300	
Remarks		94.6 w/o Phenolic Resin 94.3 w/o Phenolic Resin		94.1 w/o Phenolic Resin 94.3 w/o Phenolic Resin		94.6 w/o Phenolic Resin 94.3 w/o Phenolic Resin	



Low Density



Medium Density



High Density

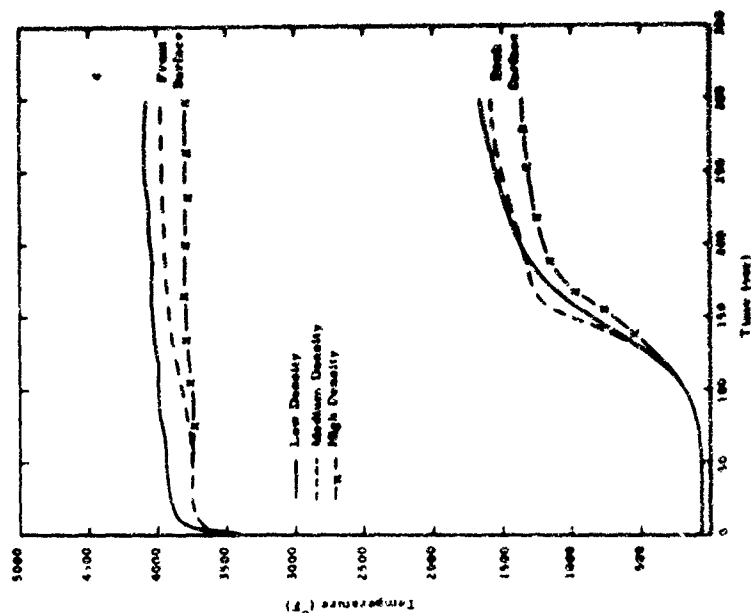


Table 22. Test Conditions and Results for Manufacturer 1 Foamed ZrO_2 Specimens Impregnated with Phenolic Resin

Material		Phenolic Impregnated Chem Bonded ZrO ₂ Form	
Heat Flux (BTU/ft ² - sec)		275	275
Gas Enthalpy (BTU/lb)		2219	2219
Test Duration (sec)		120	87
Stagnation Pressure (psig)		0.560	0.560
Gas Temperature (°F)		5620	5620
Gas Velocity (ft/sec)		862	862
Decrease in Weight		24.970	19.926
		45.0	38.3
Density (gm/cc)		1.593	1.578
		1.309	1.305
Depth of Erosion (in.)		Burn Through	Burn Through
Volume of Erosion (in. ³)		0.703	0.510
Final Back Face Temp °F		1650	2780
Final Front Face Temp °F		3650	3685
Remarks		Specimen No. UT-IF-1	Specimen No. UC-IF-2



UC-IF-1



UC-IF-2

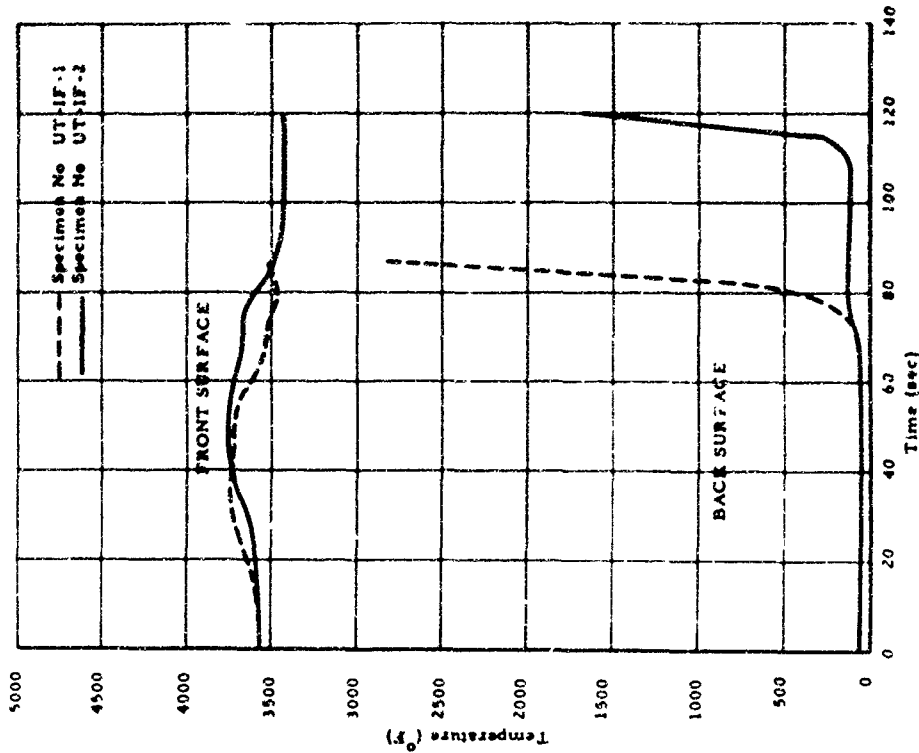


Table 24. Test Conditions and Results of Manufacturer UT Chemically Bonded ZrO₂ Specimens Impregnated with Phenolic Resin

The pattern of erosion of these samples differed greatly from that of other impregnated ceramic foams. Normally, materials of this type experience thermal decomposition of the impregnant, often with no erosion of the ceramic matrix. However, the UT materials sustained severe erosion with burnthrough occurring in less than 120 seconds. Unlike other foamed materials which "burn clean," leaving a structurally intact ceramic, these specimens were heavily charred and quite friable after exposure.

Beneath the char layer (which was approximately 1/4" thick), the material was virtually unaffected, the only physical change being a slight discoloration of the resin impregnant.

Because of the unusual behavior of these materials, static furnace tests at several temperatures ranging from 550°F to 2900°F were conducted on small samples of this foam in an attempt to identify the mode of thermal degradation.

In these furnace tests, severe swelling of the specimens was noted at all temperatures, and at 2900°F, where complete pyrolysis of the phenolic resin and subsequent oxidation of the char occurred, the zirconia foam structure was completely destroyed. At the lower temperatures, exposure times were not sufficient to cause a complete removal of the resin, and, while these specimens were in various stages of degradation, in every instance there was structural damage in the outer regions of the foam matrix.

Long term furnace tests were then conducted at 1000°F and 2000°F. At both temperature levels, the ceramic matrix structure was completely destroyed. The only notable difference in the results of the 1000°F and 2000°F tests was the color of the remaining ceramic. At 2000°F, the residual ceramic had the characteristic buff color of zirconia, while the ceramic residue from the 1000°F test was grey in color. No attempt was made to identify the exact composition of the remaining ceramic from either test.

It was tentatively concluded that the zirconia foam was structurally damaged either during the filling and curing of the specimens or during thermal decomposition of the resin. In either case, the foam was unable to maintain its integrity at elevated temperatures. This would explain the unusually poor performance of this composite in the arc-plasma-jet tests.

ABLATIVE COMPOSITES

The standard screening test proposed by the Refractory Composites Working Group is well suited for the evaluation of ablative materials. It affords an excellent opportunity to evaluate thermomechanical stability, erosion resistance, and thermal insulating ability. It should be noted, however, that small arc-plasma-jets such as employed in the program do not produce the high mass

flows and stagnation pressures associated with most ablative material applications. It is likely, therefore, that some materials that would be acceptable because of a marginally weak char structure or a tendency to form a low viscosity surface-melt could demonstrate good performance in the less severe environment produced in the plasma-jet facility.

MANUFACTURER ASD

Samples of a gelatin molding compound supplied by the AF Materials Laboratory were exposed at three heat flux levels, 100, 500, and 1000 Btu/ft² sec, for the times sufficient to produce complete specimen penetration.

This material eroded rapidly, forming a thin, soft char at all three heat flux levels, although the front surface temperatures remained below the lower limit of the total radiation pyrometers (1360 °F). Burnthrough occurred in 56, 27, and 20 seconds at the respective heat fluxes of 100, 500, and 1000 Btu/ft² sec (Table 25).

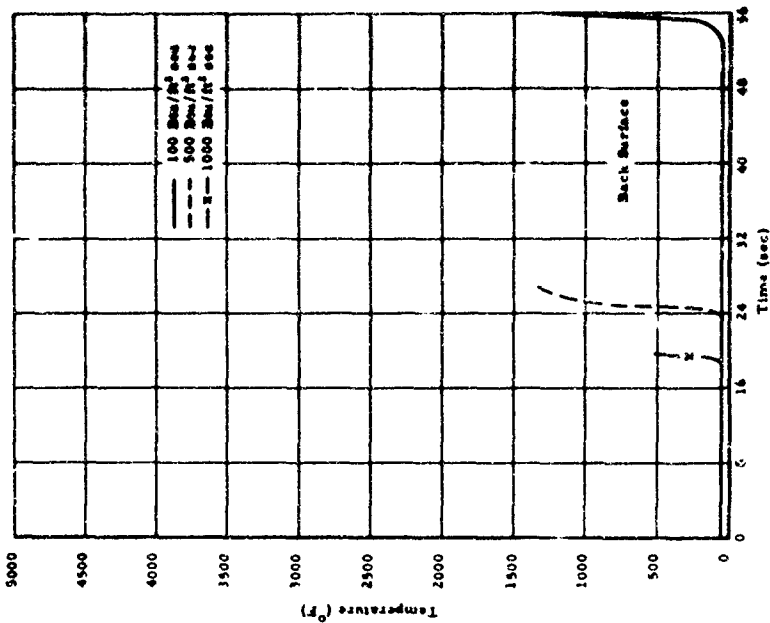
Although the erosion rate was very high, these samples experienced virtually no back surface temperature rise until immediately prior to specimen burnthrough.

MANUFACTURER CT

Four samples of a phenolic/quartz cloth laminate were submitted for evaluation at 40, 150, 500, and 1000 Btu/ft² sec. The samples tested at 40 and 150 Btu/ft² sec were approximately 50 mils thick, while those evaluated at 500 and 1000 Btu/ft² sec were 3/8" thick. In addition to these, two 1/4" thick samples, consisting of a 3/16" phenolic/quartz cloth laminate topped with a 1/16" layer of phenolic/graphite cloth, were evaluated at 100 and 1000 Btu/ft² sec. All six specimens were bonded to 1/8" Inconel X plates. The results of these tests are summarized in Tables 26, 27, and 28.

The 50 mil phenolic/quartz cloth laminates experienced no appreciable linear erosion at the two lower heat flux levels (40 and 150 Btu/ft² sec). However, there was substantial pyrolysis of the resin, and, as a result, the samples were very susceptible to handling damage after test. The back surface temperature of both specimens began to increase immediately upon exposure and stabilized after approximately 150 seconds.

The response of this laminate to more severe thermal test conditions (heat fluxes of 500 and 1000 Btu/ft² sec) was markedly different. Front surface temperatures exceeded 3500 °F, and the quartz cloth reinforcement melted (Table 27). After approximately 30 seconds, back surface temperatures increased rapidly and were still rising at the end of each exposure.







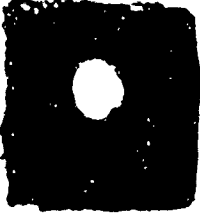

Material		Gelatin Molding Compound	
Heat Flux (B.T.U./ft ² -sec)	100	500	1000
Gas Velocity (B.T.U./lb)	1010	3424	5585
Test Duration (sec)	56	27	20
Sequestration Pressure (psi)	2.249	0.758	1.159
Gas Temperature (°F)	3200	6880	9910
Gas Velocity (ft/sec)	381	1167	1784
Decrease in Gaseous Weight	23.29	24.03	23.67
Density	31.87	56.98	59.96
Before	1.305	1.320	1.308
After			
Depth of Erosion (in.)	Burnthrough	Burnthrough	Burnthrough
Volume of Erosion (in ³)			
Final Back Face Temp °F	1250	1340	800
Final Front Face Temp °F	--	--	--
Remarks			
			

Table 25. Test Conditions and Results of Manufacturer ASD Gelatin Molding Compound Specimens

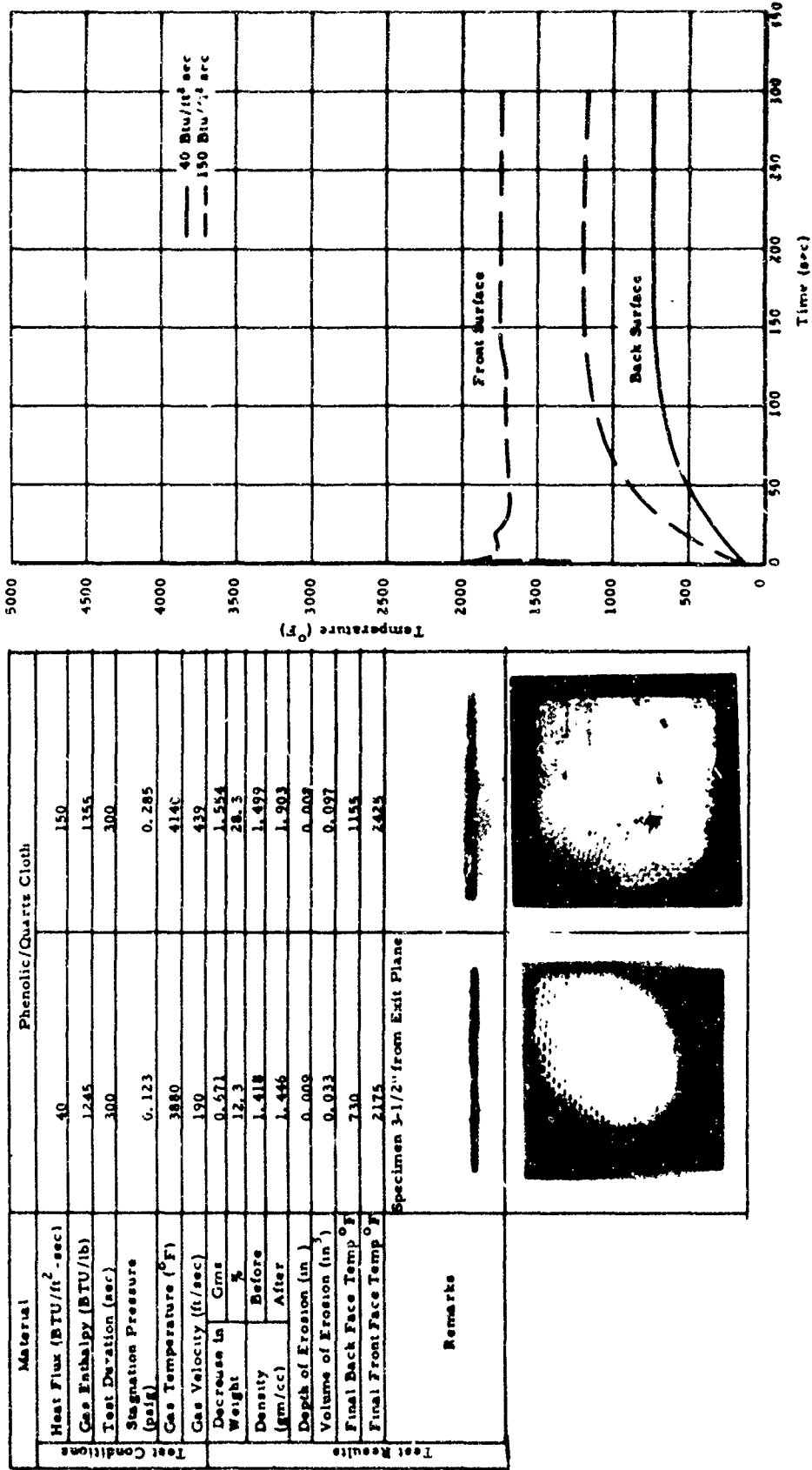
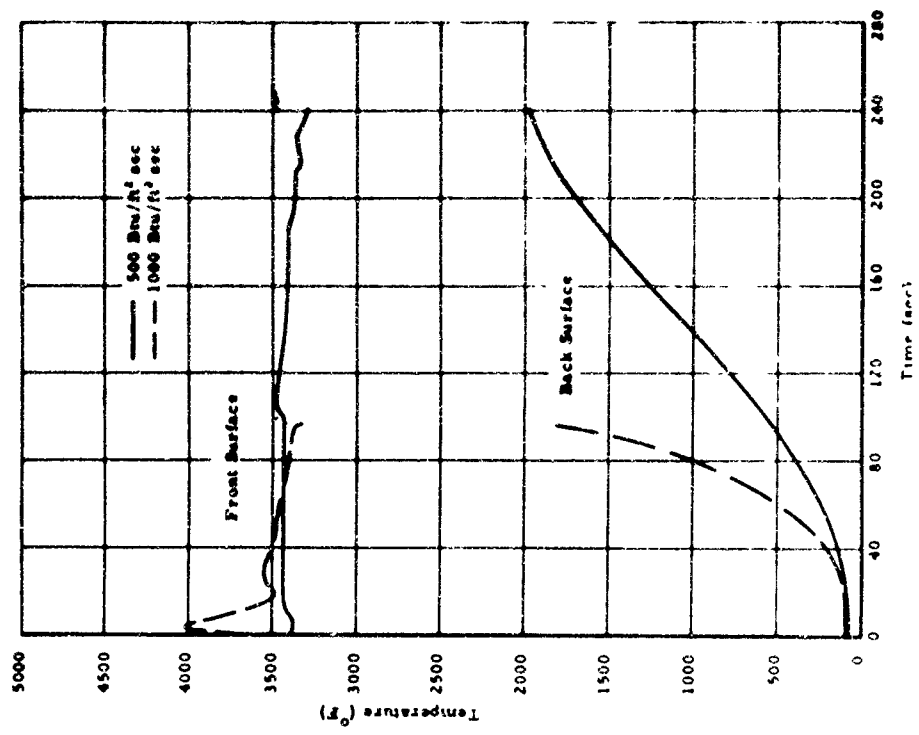


Table 26. Test Conditions and Results of Manufacture: CT Phenolic/Quartz Cloth Laminates



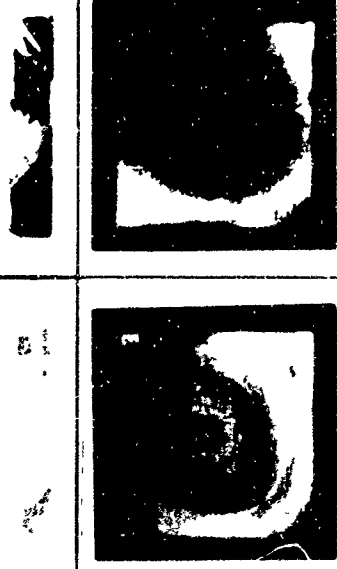
Material		Phenolic/Quartz Cloth	
Heat Flux (BTU/ft²-sec)		500	1000
Gas Enthalpy (BTU/lb)		3340	5525
Test Duration (sec)		240	97
Stagnation Pressure (psig)		0.747	1.224
Gas Temperature (°F)		6760	9655
Gas Velocity (ft/sec)		1150	1885
Decrease in Weight %		10.238	13.750
Density Before		26.7	35.8
Density After		1.555	1.561
(gm/cc)		1.582	1.535
Depth of Erosion (in.)		Burnthrough	Burnthrough
Volume of Erosion (in³)		0.421	0.522
Final Back Face Temp °F		1980	1800
Final Front Face Temp °F		3540	4120
Test Results			

Table 27. Test Conditions and Results of Manufacturer CT Phenolic/Quartz Cloth Laminates

Material		Phenolic/Graphite Topped Phenolic/Quartz Cloth	Phenolic/Graphite Topped Phenolic/Quartz Cloth
Heat Flux (BTU/ft ² sec)		100	1000
Gas Enthalpy (BTU/lb)		1025	5525
Test Duration (sec)		300	68
Stagnation Pressure (psig)		0.148	1.224
Gas Temperature (°F)		3240	9655
Gas Velocity (ft/sec)		228	1895
Decrease in Gms		5.923	13.284
Weight %		22.3	50.6
Density		Before	After
(gm/cc)		--	--
Depth of Erosion (in.)		0.085	Burnthrough
Volume of Erosion (in ³)		0.276	0.579
Final Back Face Temp °F		705	2280
Final Front Face Temp °F		2255	3850

18

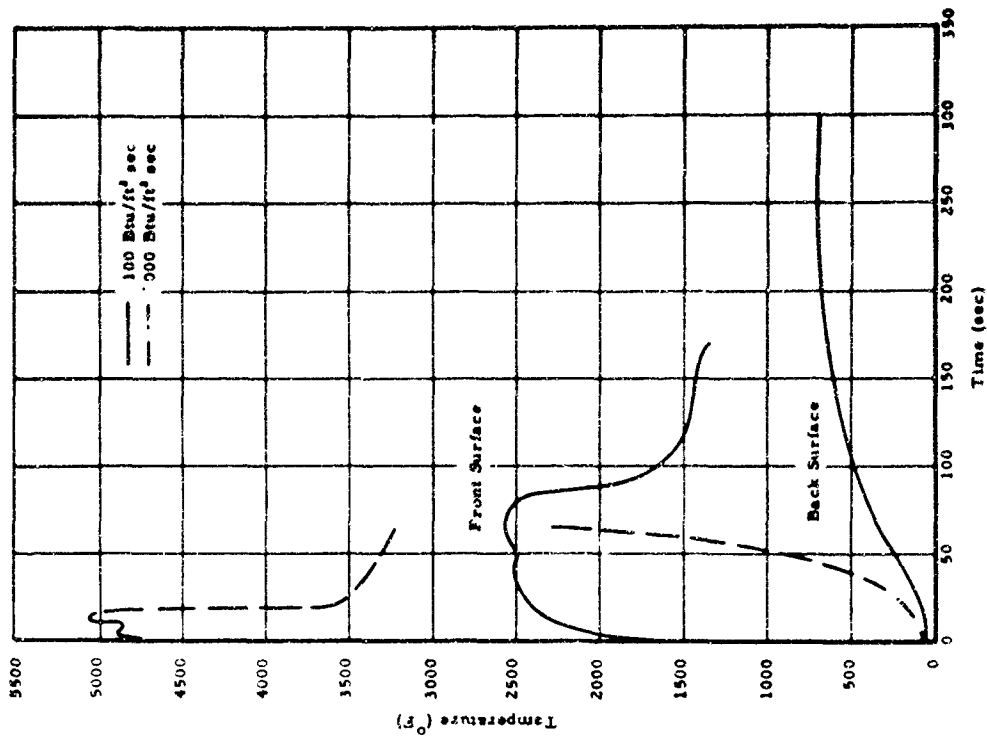


Table 28. Test Conditions and Results of Manufacturer CT Phenolic/Graphite Topped Phenolic/Quartz Laminates

The two-layer laminates of phenolic/quartz cloth and phenolic/graphite cloth experienced rapid oxidation of the top layer. This layer was penetrated after approximately 80 seconds at 100 Btu/ft² sec, exposing the underlying phenolic/quartz. The phenolic/quartz was virtually unaffected at this heat flux level and remained intact throughout the remaining 220 seconds of test.

At 1000 Btu/ft² sec, the phenolic/graphite portion of the specimen was penetrated in less than 20 seconds and melting of the newly exposed surface of quartz cloth was initiated and sustained throughout the remainder of the 68-second exposure.

Back surface temperatures of the two-layer composites at both heat flux levels rose to relatively high levels. At 100 Btu/ft² sec, it stabilized at approximately 750°F. At 1000 Btu/ft² sec, back surface temperature reached 2300°F and was still increasing rapidly at the termination of the test.

The phenolic/quartz cloth laminates performed as a typical high silica laminate; that is, specimen erosion occurred only at the higher heat flux levels. However, with respect to thermal insulating ability, these laminates were not nearly as effective as others of this general class. In all tests, the back surface temperature began to rise rather sharply after only a short exposure time.

X-15 STUDIES

Preliminary screening tests were conducted on nine candidate ablative coatings for the advanced Mach 8 version of the X-15 research aircraft. A complete listing of the materials and the heat flux levels of test is shown in Table 29.

Three heat flux levels, 15, 40, and 150 Btu/ft² sec, were selected as being representative of heating rates encountered at various regions of the craft during flight. It was expected that nonstagnation areas would be subjected to relatively low level heating, approximately 15 Btu/ft² sec, whereas leading edges would experience short-duration peak heating of 150 Btu/ft² sec. During the major portion of flight, heat inputs of approximately 40 Btu/ft² sec were expected. This evaluation, therefore, emphasized behavior of the 40 Btu/ft² sec heat flux level. Additional testing at 15 and 150 Btu/ft² sec was performed on selected ablative coatings.

All the specimens were bonded to or applied directly on 2" x 2" x 1/8" Inconel X plates. Nominal ablative material thicknesses were 3/8", 1/4", and 0.050".

After normal pretest calibration of the plasma jet, specimens were inserted into the plasma effluent. Tests were terminated when the temperature

Table 29. Candidate X-15 Ablative Materials Tested and Heat Flux Levels to Which They Were Exposed

Manufacturer	Material	Nominal Density (gm/cc)	Material Thickness	Heat Flux (Btu/ft ² sec)
AG	Filled Epoxy Formulation	1.0	1/4 in.	1 @ 150
			3/4 in.	1 @ 40
				1 @ 150
A	Fibrous Ablative Composite	0.6	50 mil	1 @ 15
				2 @ 40
			3/8 in.	2 @ 150
E	Subliming Epoxy	1.4	50 mil	1 @ 15
				3 @ 40
			1/4 in.	1 @ 150
E	Fiber Reinforced Subliming Epoxy	1.4	50 mil	1 @ 40
			1/4 in.	1 @ 150
EG	Low Density Silicone Elastomer in Honeycomb	0.8	50 mil	2 @ 40
			1/4 in.	1 @ 40
				1 @ 150
			3/8 in.	2 @ 150
EG	Low Density Silicone Elastomer Without Honeycomb	0.7	50 mil	1 @ 40
EG	Medium Density Silicone Elastomer in Honeycomb	0.9	1/4 in.	1 @ 40
				1 @ 150
			3/8 in.	1 @ 40
EG	High Density Silicone Elastomer in Honeycomb	1.1	1/4 in.	1 @ 40
				1 @ 150
			3/8 in.	1 @ 40
				1 @ 150
EG	High Density Silicone Elastomer Without Honeycomb	1.0	50 mil	1 @ 40
GR	Ablative Polymer	1.3	50 mil	2 @ 40
			1/4 in.	2 @ 40
			3/8 in.	2 @ 150
GA	Ablative Composite	1.4	1/4 in.	1 @ 40
				1 @ 150
			3/8 in.	1 @ 40
				1 @ 150
M	Microballoon Filled Silicone Elastomer in Honeycomb	0.6	1/8 in.	2 @ 40
MC	Silicone Elastomer in Honeycomb	0.9	1/4 in.	1 @ 40
				2 @ 150
			3/8 in.	1 @ 150
MC	Silicone Elastomer Without Honeycomb	0.7	50 mil	2 @ 15
MC	Modified Silicone Elastomer in Honeycomb	0.8	1/4 in.	1 @ 40
				2 @ 150
			3/8 in.	1 @ 150
MC	Modified Silicone Elastomer Without Honeycomb	0.7	50 mil	1 @ 15
				2 @ 40

of the Inconel X substrate plate reached 500°F. In some low heat flux level tests and in the test of thicker materials, this back surface temperature was not attained, and tests were terminated after 15 minutes of exposure.

Nominal test conditions at the three heat flux levels were:

Heat Flux (Btu/ft ² sec)	15	40	150
Specimen Distance From Exit Plane (in)	6.25	3.5	1.125
Gas Enthalpy (Btu/lb)*	1150	1263	1568
Stagnation Pressure (psig)	0.055	0.145	0.365
Gas Temperature (°F)*	3618	3917	4590
Gas Velocity (ft/sec)	84	223	562

* Conditions at the exit plane of plasma-jet

The test results of Appendix 4 include substrate temperature-time histories (Figures 66 through 77), ablative material weight loss, depth of erosion, final front and back surface temperatures, and post-test photographs of the specimens (Tables 40 through 65).

Most of the materials evaluated in these screening tests were not developed for use as an ablative coating. Consequently, poor performance in these tests should not be construed as indicative of a material's capability in those applications for which it was originally intended.

MANUFACTURER AG

This material, a filled epoxy formulation of 1.0 gm/cc density, performed extremely poorly at both 40 and 150 Btu/ft² sec. It exhibited a very high rate of erosion and was a relatively ineffective ablative system, as indicated by its rapid increase of back surface temperature (Tables 40 and 41).

MANUFACTURER A

The composition of this material, a fibrous composite of 0.6 gm/cc density, was not specified. The erosion rate of this system was high at all levels of test. The 3/8" thick samples exposed at 150 Btu/ft² sec reached a substrate plate temperature of 500°F in approximately 100 seconds, indicating poor insulating characteristics for this material. A 50 mil specimen tested at 15 Btu/ft² sec stabilized at an Inconel plate temperature approximately 100°F higher than most other candidate materials (Figure 48), even though no appreciable erosion occurred.

MANUFACTURER E

Tests were performed on two versions of a subliming salt-epoxy composite, with and without fiber reinforcement. The nonreinforced material performed well at the 150 Btu/ft² sec heat flux level, but at 40 Btu/ft² sec it formed deep surface fissures which adversely affected the thermally protective function of this system.

The erosion resistance of the fiber-reinforced materials was superior to that of unreinforced T-500, but no significant improvement in insulating ability was noted (Tables 43, 44, and 45).

MANUFACTURER EG

These materials were all variations of one basic formulation, designated by the vendor as a silicone elastomer. A low, medium, and high density elastomer (0.8, 0.9, and 1.1 gm/cc) in a honeycomb reinforcement and low and high density materials without honeycomb (densities of 0.7 gm/cc and 1.0 gm/cc) were evaluated.

The lower and medium density elastomers appeared to perform more effectively as thermal insulators than the high density material. It was also noted that the thin (50 mil) specimens had a lower insulation efficiency, probably due to the air-foamed characteristics of the material. In a thick sample, the open surface pores represented a negligible fraction of the total sample thickness, whereas, in the thin samples, these open pores represented a rather large percentage of the total sample thickness and thus reduced the effective ablative material thickness (Tables 46 through 54).

MANUFACTURER GR

These samples (designated as an ablative polymer, a bright green homogeneous plastic of 1.3 gm/cc density) performed very poorly at all levels of exposure and for all sample thicknesses. The material melted profusely immediately upon exposure and was a very ineffective thermal insulator (Tables 45 and 56).

MANUFACTURER GA

These ablative composites of unspecified composition (density ~1.4 gm/cc) performed very well at the 40 Btu/ft² sec heat flux level, their insulating ability being comparable to that of the EG silicone elastomers. At this heat flux, there was no surface erosion. However, at 150 Btu/ft² sec, the GA material eroded severely and was completely penetrated in a relatively short period of time (Tables 57 and 58).

MANUFACTURER M

Several honeycomb-reinforced specimens of a silicone elastomer filled with microballoons were evaluated.

Because thin (50 mil) samples were not evaluated, it was impossible to completely evaluate this material; however, in most instances, the performance of this system compared favorably to that of the EG elastomers (Table 59).

MANUFACTURER MC

Two materials were submitted: a silicone elastomer and a second generation modification of it, developed for improved char surface characteristics. These materials were of nearly equal density (~ 0.7 gm/cc). Both were available in a slightly higher density honeycomb configuration for improved erosion resistance.

Both materials, with and without honeycomb, performed very well at 15 and 40 Btu/ft² sec, and, in fact, maintained a consistently lower back face temperature than any other material evaluated in these tests.

Only honeycomb samples were exposed to 150 Btu/ft² sec. In general, their performance was very poor because the filler material tended to separate from the honeycomb and expose the Inconel substrate plate to hot gas impingement. As a result of this separation, relatively high back surface temperatures were recorded in this test series. The separation failure was apparently initiated at some critical heat flux level between 40 and 150 Btu/ft² sec.

No appreciable difference was apparent between the regular and the modified elastomers with respect to their thermal protective ability. As was expected, however, the surface of the honeycomb reinforced modified system was noticeably smoother after test (Tables 60 through 75).

SUMMARY

It was obvious from these tests that many of the candidate materials would not satisfy the basic performance criterion of the X-15 application, namely to provide short-term ablative protection. A few systems, including those from manufacturers EG and MC, appeared to be satisfactory in this respect.

It should be recognized that elementary screening tests such as this should not constitute the only basis for acceptance of a candidate material. It was, therefore, recommended that advanced plasma testing and actual flight tests be performed upon those systems which performed well in these tests and which satisfied other design criteria not considered in this study (method of application, weight factors, curing requirements, etc.).

SCREENING TESTS FOR NOZZLE MATERIALS

Efforts have been directed toward the development and refinement of a plasma-fired materials testing facility designed for the screening of potential nozzle materials in chemical and thermal environments simulating rocket exhausts.

The apparatus (Figures 40 and 41) consists of four major components:

- (1) a 50 KW arc-plasma-jet as a source of high temperature gas
- (2) a mixing chamber for the injection of gaseous and liquid additives to simulate components of actual rocket exhausts
- (3) a test chamber in which subscale nozzles are evaluated
- (4) a wet-wash scrubber system to contain the test products as they leave the test chamber, cool them to room conditions and render them physiologically and corrosively harmless so that they may be discharged into the atmosphere or a liquid drainage system.

Details of these components have been discussed in previous reports (Refs. 10, 11, and 13).

This facility was designed for rapid, inexpensive testing of proposed nozzle materials to determine their compatibility with the corrosive products of rocket fuel combustion. The high temperatures associated with rocket exhausts are easily achieved with the plasma-jet, and, although the chamber pressures are low (up to approximately 75 psig with the present arrangement), they are representative of small liquid-fueled motors used for attitude control.

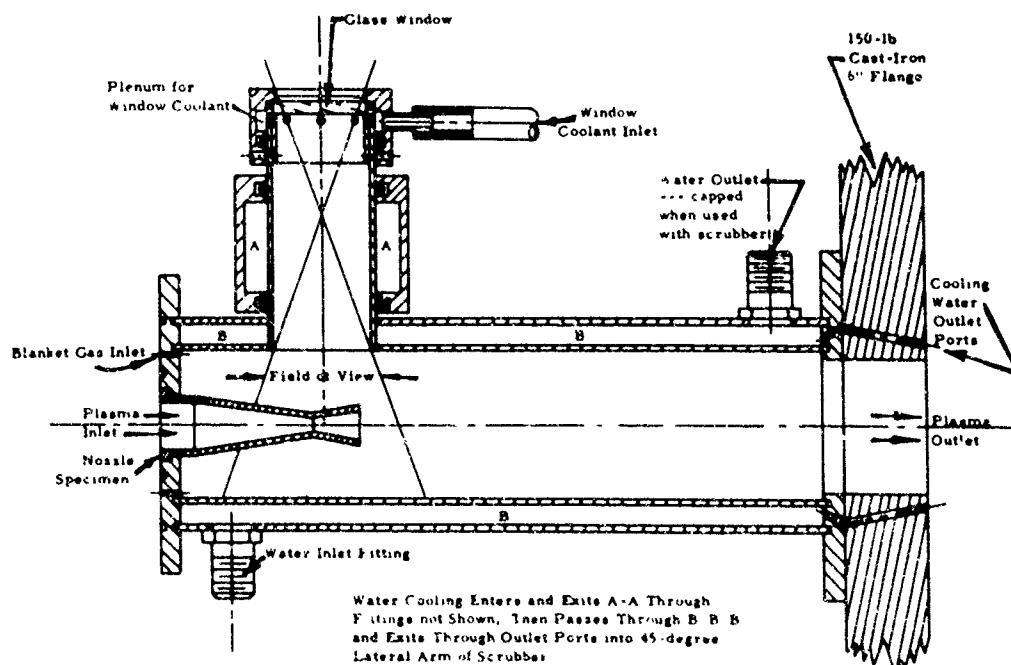


Figure 40. Nozzle Test Chamber

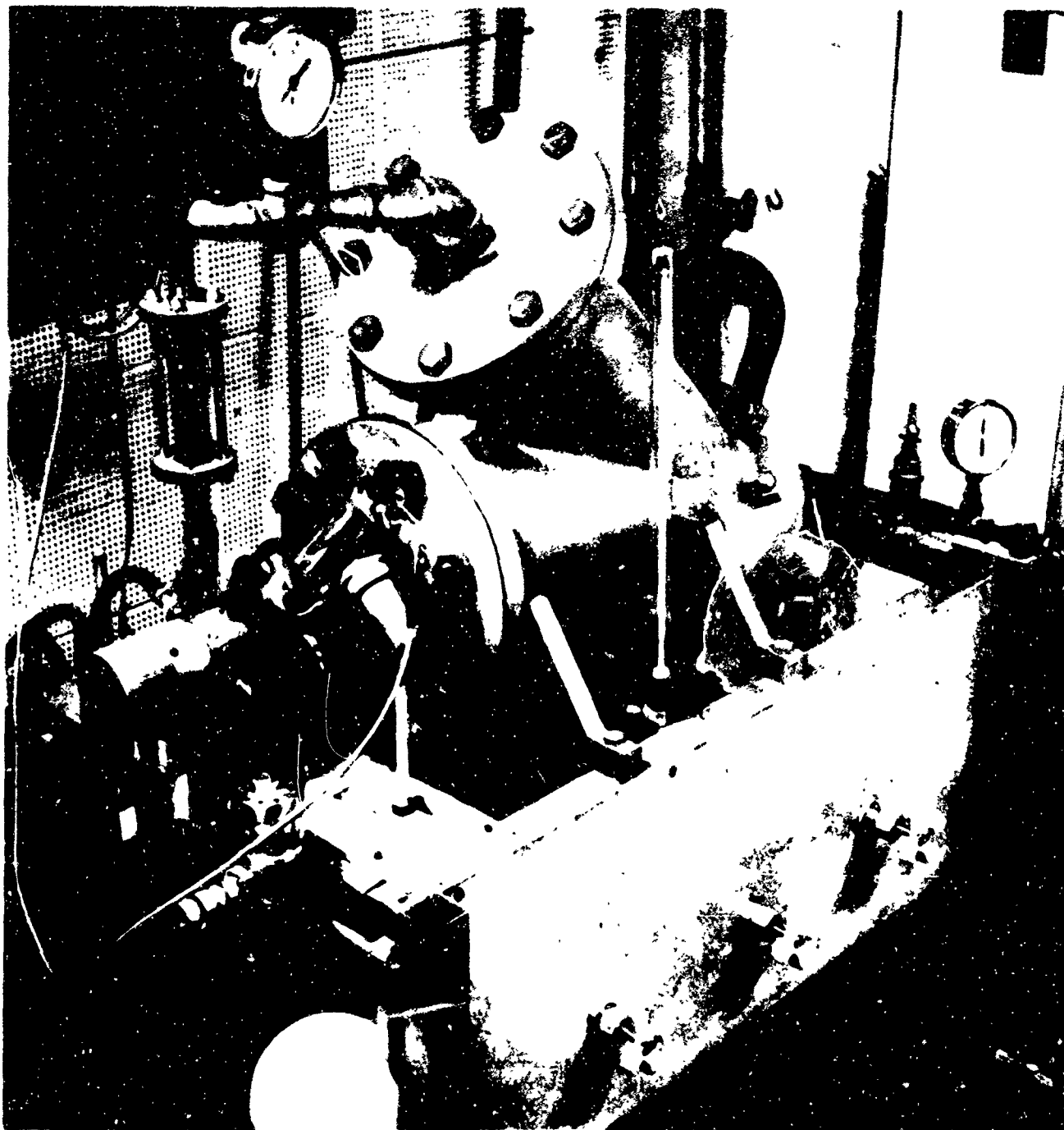
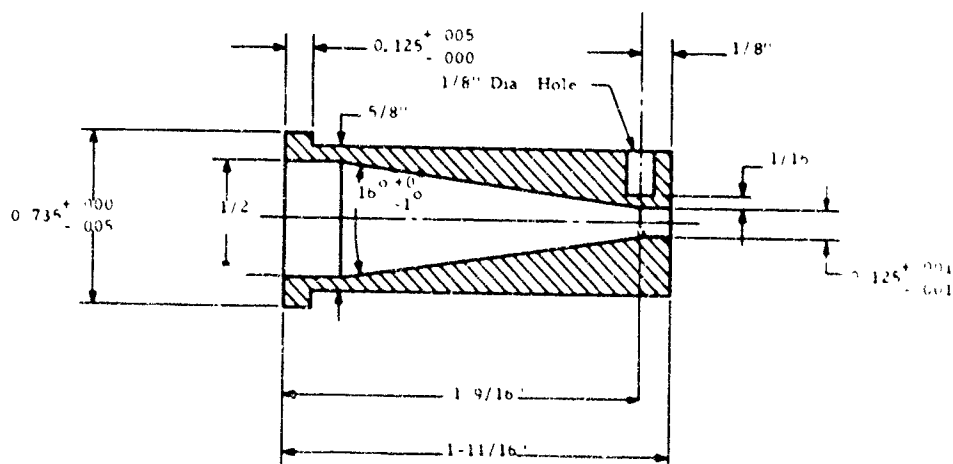


Figure 41. Plasma-Fired Nozzle Materials Testing Facility

Instrumentation for the measurement of test conditions and specimen behavior during test includes rotameter type flow meters for the measurement and control of gaseous or liquid additives to the plasma stream, a "100" series Ircon Automatic Optical Pyrometer for continuous recording of nozzle specimen wall temperatures, and a Teledyne pressure transducer (range 0 to 100 psig) for continuous recording of pressures. A direct reading bourdon tube pressure gage was installed for cross-check measurements of chamber pressure.

As a first step in simulating rocket exhaust constituents, a series of tests were performed on ATJ graphite nozzles. These nozzles were of a simple converging shape (see Figure 42) designed primarily for ease of fabrication.

The nozzle specimens were tested with a nitrogen stabilized plasma-jet effluent with additives of O_2 , CO_2 , or H_2O in proportions which produced an equal weight percentage (4.37 w/o) of oxygen in each case. A total of thirty specimens were tested (ten with each additive) at a nozzle wall temperature of $2700^\circ F$. Limited testing was also performed with each of these additives at nozzle wall temperatures of $2400^\circ F$ and $3500^\circ F$.



89

In conducting these tests, nozzle specimens (which had been weighed in air and in water to determine their weight, volume, and density) were clamped in place at the discharge of the plasma-jet. An argon cover gas was passed over the exterior surface of the specimen and the nitrogen arc gas introduced through the system. After a four-minute purge of the entire system, the plasma torch was fired and input power adjusted to produce the desired nozzle wall temperature. When equilibrium conditions were established, the additive was introduced and the test begun. Tests were terminated after a predetermined time of exposure (earlier if a catastrophic failure occurred) and the nozzle test specimen allowed to cool in an inert atmosphere of N_2 on the interior, Ar on the exterior.

Post-test measurements included the specimen weight in air and in water to facilitate computation of weight loss, volume loss, and change in density.

Direct measurement of the nozzle throat area was found to be quite difficult because the erosion pattern was often quite irregular. An alternate method of determining effective throat area change based on the relationship between chamber pressure and throat area was employed.

To calculate throat area change as a function of chamber pressure requires that either choked flow (sonic flow at the throat) or nonchoked flow (subsonic flow at the throat) be maintained throughout the test exposure. Since the initial chamber pressure was never low enough to produce nonchoked flow, it was determined that all tests be run under choked flow conditions. For these conditions to be met, the ratio of the pressure at the throat (in a simple converging nozzle, the exit) to the chamber pressure must never exceed 0.53.

Therefore, the chamber pressure in these tests was never permitted to drop below:

$$\frac{15}{0.53} = 28.3 \text{ PSIA} \approx 14.0 \text{ PSIG}$$

Since the test was conducted under choked flow conditions, the ratio of initial absolute chamber pressure to final absolute chamber pressure was inversely proportional to the ratio of initial throat area to final throat area:

$$\frac{P_i}{P_f} = \frac{A_f}{A_i} *$$

The initial throat area in all tests was known and the initial and final chamber pressures were obtained from the test records. The final throat areas

* This is derived by assuming perfect gas laws and using elementary compressible fluid flow relationships.

obtained by this technique compared favorably with those obtained by actual measurement on test nozzles which exhibited circular throat cross sections after exposure.

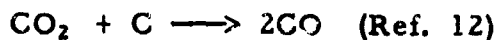
Preliminary test data are summarized in Table 30 in terms of weight loss, volume of erosion, and increase in throat area, each expressed as a rate to normalize differences in exposure time. Also presented are typical time histories of chamber pressure and nozzle wall temperature (Figures 43, 44, and 45).

As was expected, the corrosive effect of O_2 was the most severe in these tests. The primary reaction normally assumed to occur is



from which it is evident that all the oxygen present in the effluent is available to react with the graphite.

In the tests with CO_2 , this was not true. The primary reaction is



and, thus, only one-half of the oxygen in the effluent is available to react with the graphite. The specimen erosion should, therefore, be correspondingly less severe, and this was supported by the data, which exhibited approximately 70% less weight loss with the CO_2 additive.

The expected water-gas reaction of water vapor with graphite,



would suggest that all the added oxygen is available for reaction with the graphite and that the erosion produced in these tests should be equal to that observed in the O_2 tests. However, in the water vapor tests, the graphite nozzle specimens experienced only 75% of the total weight loss of the O_2 tests.

This is believed to be the result of a difference in chemical reaction rates for the two additives. The reaction of H_2O and graphite is endothermic and should proceed at a slower rate than the exothermic O_2 -graphite reaction. It is possible that the residence time of the H_2O in the graphite nozzle may not have been sufficient to allow total consumption of the available oxygen.

The temperature-pressure-time histories for these tests show a slight increase in nozzle temperature the first few seconds after injection of O_2 to the plasma effluent (Figure 43). This is believed to be the result of heat liberated by the exothermic O_2 -graphite reaction. The opposite effect (a decrease in nozzle temperature) was noted in the CO_2 tests (Figure 44). This was expected

Table 30. Results of ATJ Graphite Nozzles Exposed to Various Environments in Exhaust Simulation Test

Additive Injected Into N ₂ Arc Gas	Initial Nozzle Wall Temp. (°F)	Erosion Rates			Comments	
		Weight Loss (gms/sec)	Volume Loss (cc/sec)	Throat Area Increase (in ² /sec)		
O ₂	2400	Average	0.0119	0.0076	0.000106	Average of 3 Tests
	2700	Average s	0.0114 0.000265	0.0065 0.00053	0.000104 0.00000922	Average of 6 Tests Sample Deviation
	3500	Average	0.0221	0.0129	0.000177	Average of 4 Tests
	2400	Average	0.0032	0.0022	0.000033	Average of 5 Tests
CO ₂	2700	Average s	0.0039 0.00056	0.0029 0.00058	0.000052 0.000010	Average of 10 Tests Sample Deviation
	3500	Average	0.0125	0.0079	0.000099	Average of 2 Tests
	2400	Average	0.0076	0.0045	0.000033	Average of 4 Tests
H ₂ O	2700	Average s	0.0100 0.00091	0.0055 0.00052	0.000070 0.000012	Average of 10 Tests Sample Deviation
	3500	Average	0.0154	0.0097	0.000113	Average of 2 Tests

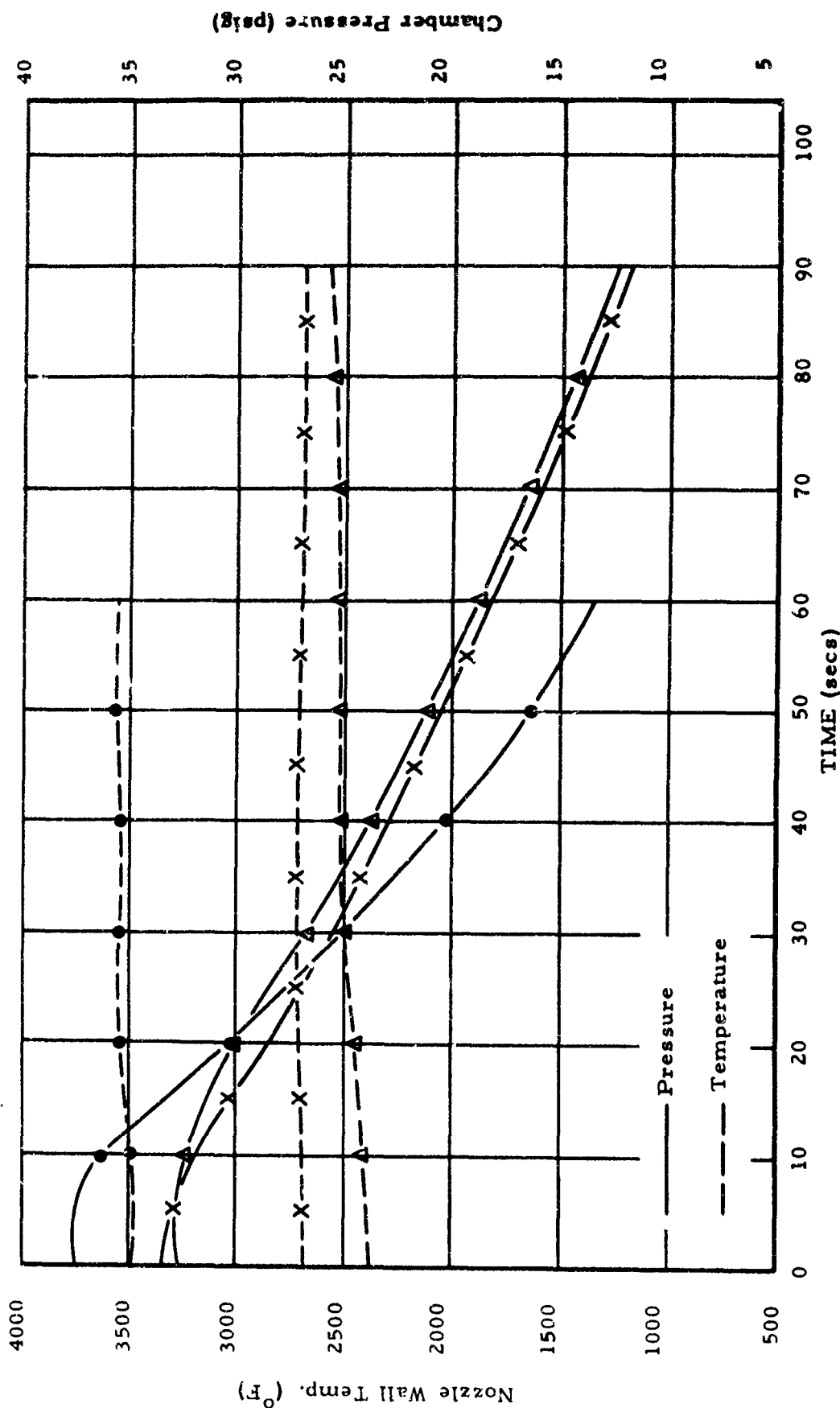


Figure 43. Typical Pressure-Temperature-Time Histories of ATJ Graphite Type II Nozzle Specimens Exposed to an N_2-O_2 Effluent at Initial Temperatures of 2400°, 2700°, and 3500° F

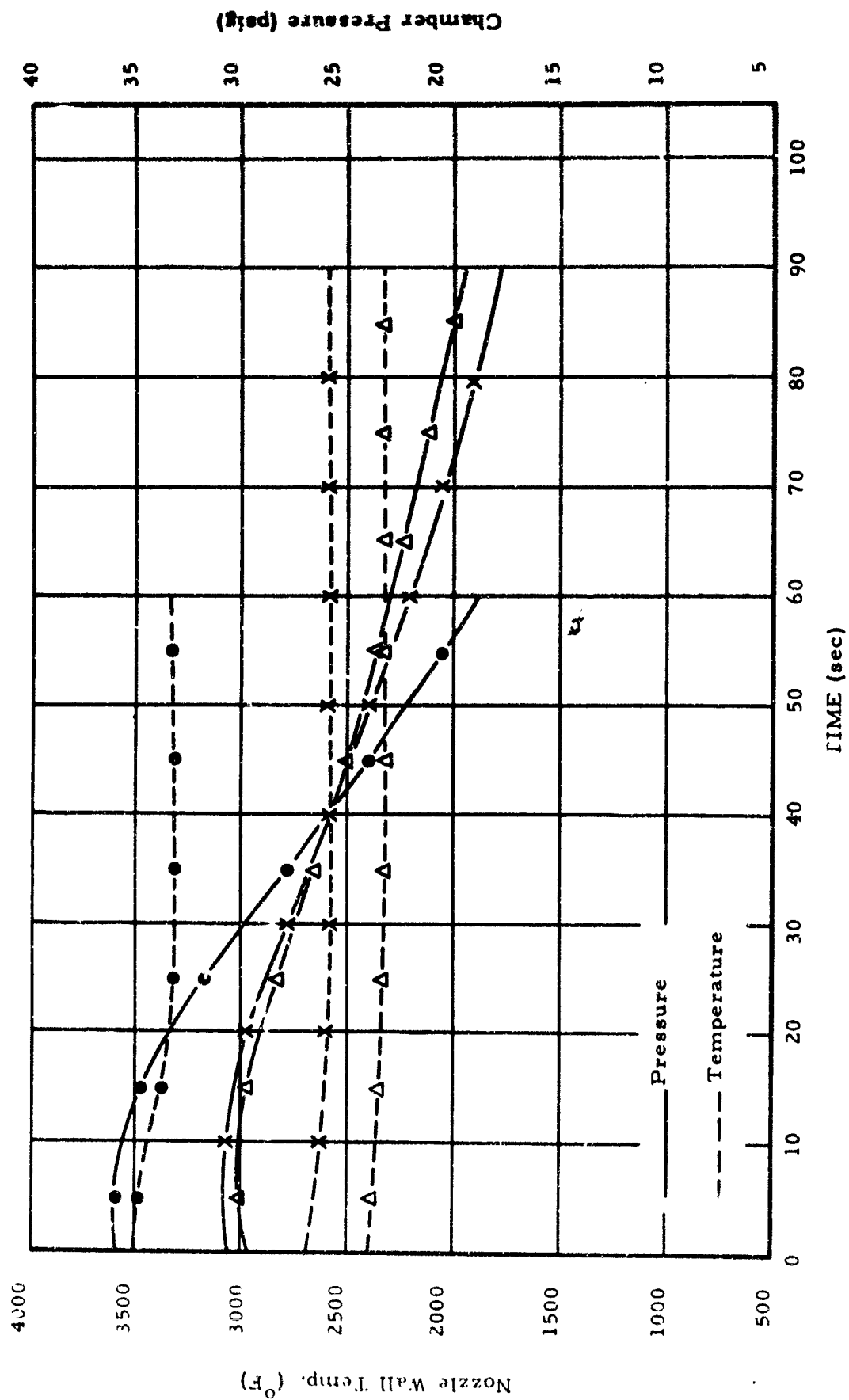


Figure 44. Typical Pressure-Temperature-Time Histories of ATJ Graphite Type II Nozzle Specimens Exposed to an N_2 - CO_2 Effluent at Initial Temperatures of 2400°, 2700°, and 3500°F

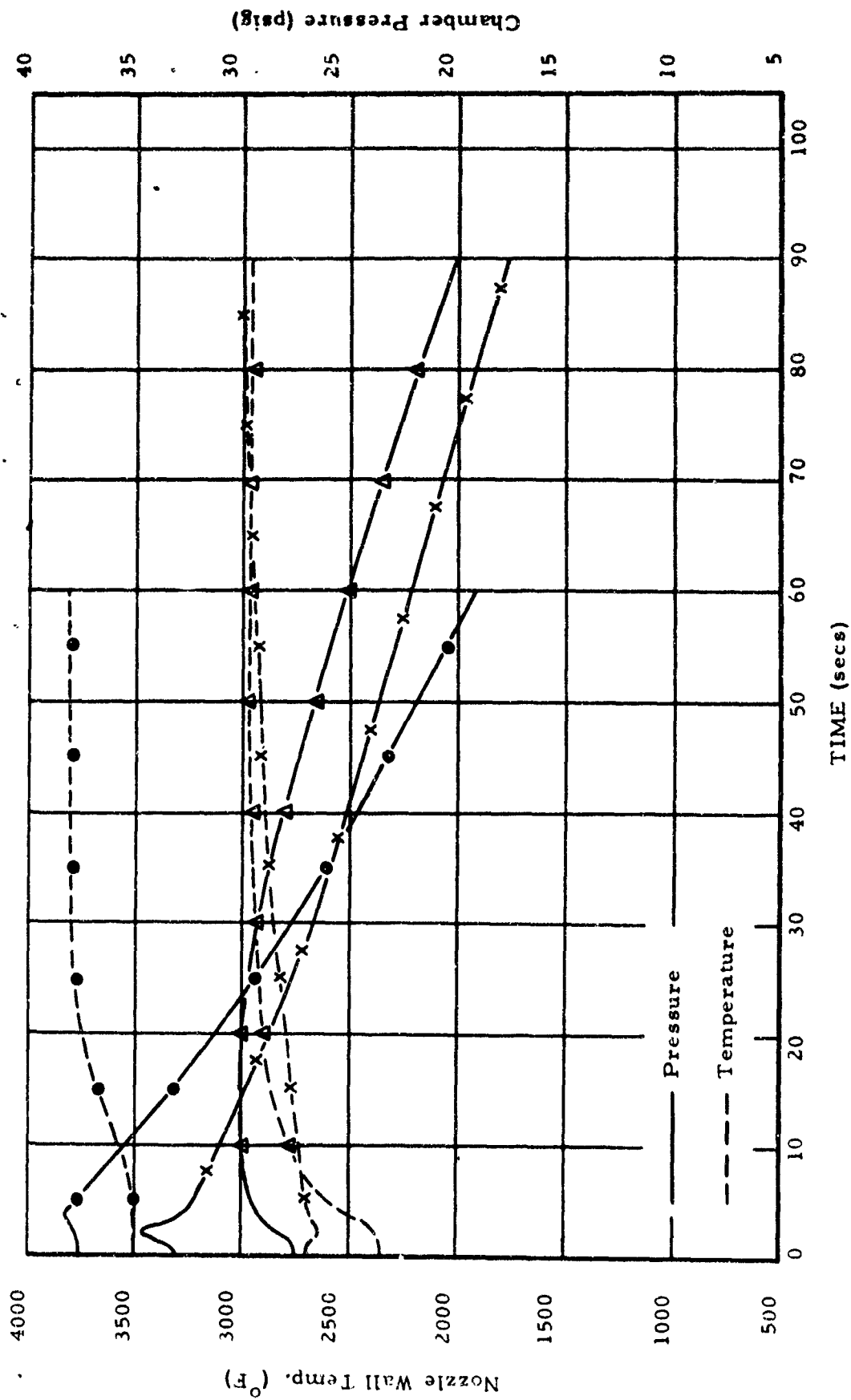


Figure 45. Typical Pressure-Temperature-Time Histories of ATJ Graphite Type II Nozzle Specimens Exposed to an N_2-H_2O Effluent at Initial Temperatures of 2400° , 2700° , and $3500^\circ F$

since the carbon dioxide-graphite reaction is endothermic. It is possible, however, that the observed decrease in wall temperature was not entirely due to the thermodynamics of the reaction. Expansion of the CO_2 from the high pressure storage bottle to the relatively low pressure of the mixing chamber and the corresponding drop in temperature very likely could have had a cooling effect upon the plasma effluent. It is believed that the decrease of specimen temperature reflected the combined effects of gas cooling and heat absorption in the CO_2 -C reaction.

The temperature-time history of the H_2O tests (Figure 45) revealed a slight drop in temperature (and corresponding increase in chamber pressure) after approximately one second of test, followed by a steady increase in wall temperature to the end of the exposure. The drop in temperature was a result of cooling by the initial pulse of injected liquid H_2O . After this initial pulse, the temperature of the test nozzle would be expected to decrease as a result of the reaction of H_2O with graphite (which is endothermic). However, another phenomenon occurs. The principal mode of heat transfer is conduction from a transparent gas to an opaque nozzle. However, when water vapor is present in the heating effluent, the gas becomes translucent (or even opaque with sufficient quantities of vapor) in the infrared wave length range, even though it remains transparent in the visible range. Thus, there is additional heating of the nozzle specimen by radiation. The quantity of radiative heat absorbed by the specimen far outweighs the losses due to the endothermic reaction, and the result is a net increase of nozzle wall temperature.

The results of these tests were essentially as expected, with the corrosive effect of gaseous O_2 being most severe, followed in decreasing order of severity by H_2O and CO_2 . This is readily apparent in Figures 46 and 47, which show weight loss and throat area increase ratio as a function of specimen wall temperature. Note that sample deviation bands were fitted to the data at 2700°F , but not at the other two temperatures because of an insufficient number of tests.

Although only a limited number of tests were conducted at the lower (2400°F) and the higher (3500°F) temperatures, the results indicated that the specimen erosion increases appreciably at the higher temperature (and the corresponding higher pressure).

The sample deviation bands plotted for two erosion rate parameters (weight loss and throat area increase) indicate that the weight loss rate is the more reproducible. This parameter will probably be the primary measure of nozzle erosion in subsequent tests.

Results to date have shown this test to be responsive to variations in specimen chamber pressure and temperature and effluent chemistry. Major problems with the operation of the plasma-jet, mixing chamber scrubber, and associated instrumentation have been resolved. A complete evaluation of the full potential of this approach to materials evaluation has just begun. The

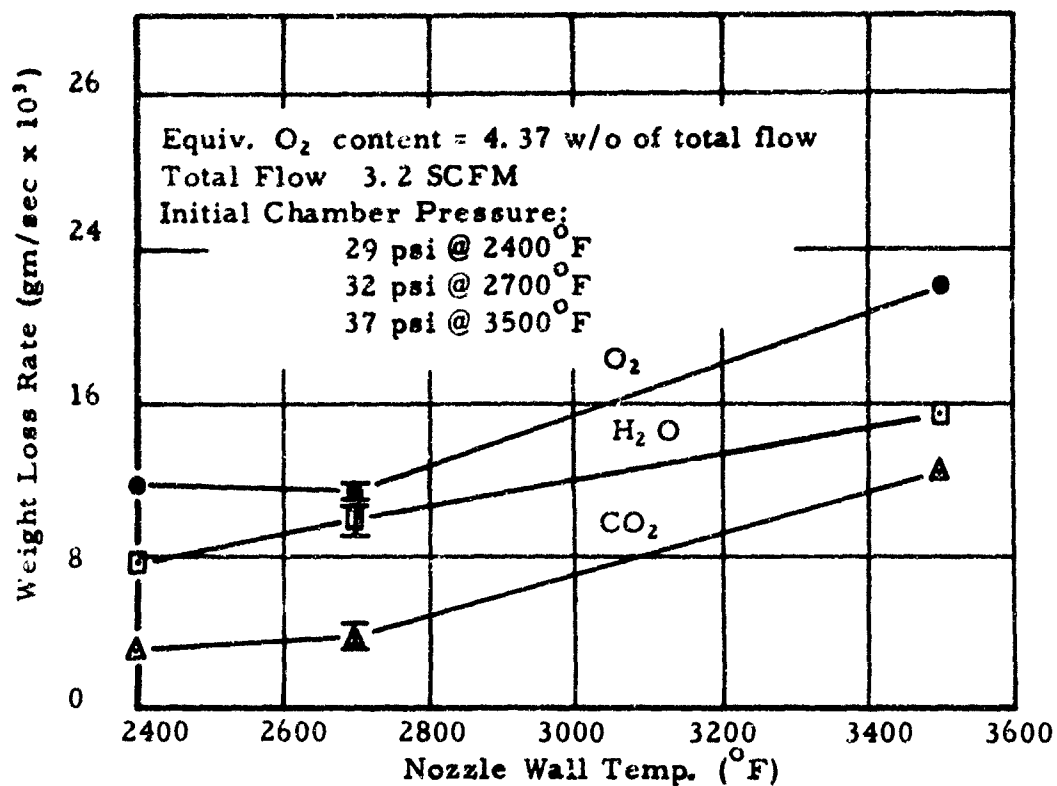


Figure 46. Average Weight Loss Rate Versus Nozzle Wall Temperature of ATJ Graphite Nozzles Exposed to Environments with Various Additives

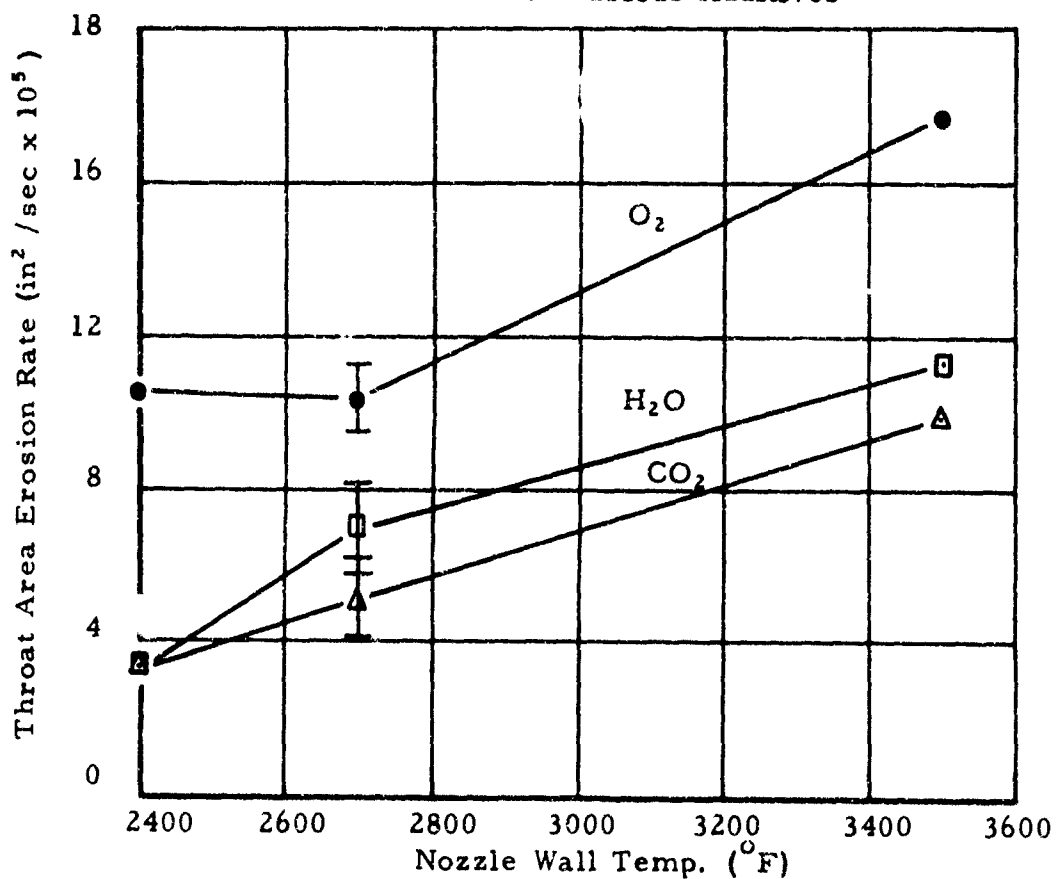


Figure 47. Average Rate of Increase in Throat Area Versus Nozzle Wall Temperature of ATJ Graphite Nozzles Exposed to Environments with Various Additives

facility was designed for testing a variety of materials, including refractory metals, metal-ceramic composites, and reinforced plastics. An investigation of the problems specific to the evaluation of these various materials should be pursued. Studies of chemical efforts should be expanded into simulation of multicomponent exhaust chemistry in carefully controlled experiments designed to identify the relative influence of individual exhaust species and interaction of two or more chemical components.

SECTION III PLASMA-SPRAYED COATING STUDIES

INTRODUCTION

Unique coating systems, fabricated by plasma spraying, have been the subject of an intensive twelve-month investigation. This study centered about the evaluation of metal-modified ceramic coatings deposited from premixed power blends. The objective of the program was the development of techniques for the plasma deposition of metal ceramic coatings of specific microstructures and composition for the purpose of developing tailored properties in the resulting composite material.

BACKGROUND

In either flame or plasma spraying, it is necessary to properly condition the spray material in transit from the spray torch to the surface being coated. With powdered materials, this conditioning consists of increasing the thermal and kinetic energy of each particle so that adequate deformation, conducive to proper coating build-up, is achieved upon impact with the substrate surface.

In plasma spraying, the energy transfer to a particle is related to the composition, enthalpy, static pressure and velocity of the plasma stream, physical and thermal properties of the spray powder, particle size, shape and density, melting point, thermal conductivity, heat capacity, heat of fusion, and emittance. Thermal conditioning is also affected by the energy distribution across the plasma stream, the rate of powder addition to the plasma stream, and the distribution of particles within the stream.

Since particle size is a physical factor which influences both the velocity and heat transfer to a spray powder, thermal conditioning can be controlled by adjustments of this parameter. When spraying blends of metal and ceramic with greatly different thermal properties, size control may offer the only means of properly conditioning both materials for successful codeposition under fixed operating conditions of the spraying equipment.

A study of the effects of the particle size ratio and determination of an optimum ratio between two spray materials can be approached theoretically or empirically. A theoretical approach requires the development of equations describing the velocity and heating rate of a particle as a function of its size. Models for determining particle heating rates as related to required thermal energy for melting are reviewed in Appendix I. An equation for determining particle velocity has been developed and is outlined in Appendix II.

An empirical study can be accomplished by preparing coatings from a number of metal-ceramic blends of varying particle size ratios and evaluating

their characteristics. A study of this type was pursued to determine the effect of process variables, blend compositions, and powder size ratios upon the thermal and physical properties of the composite coatings. The program was oriented towards the development of high bond-strength coatings with good thermal shock resistance. In conjunction with this program, an analysis of the thermal expansion behavior of metal-ceramic composites and the internal thermal stresses developed from thermal expansion mismatch was conducted. This study is also detailed in Appendix III of this report.

COATING PROCEDURES

Three types of plasma-sprayed coatings on 304 stainless steel were studied: pure metal, single layer metal-ceramic mixture, and multilayer systems consisting of a metal flashing, several layers of metal-ceramic mixture, and a ceramic surface layer.

Metallic coatings of NiCr, Mo, and NiAl were prepared in a study of processing variables. Metal-ceramic coatings of NiCr-ZrO₂ and NiAl-Al₂O₃ were prepared for a study of metal to ceramic particle size ratio, volumetric ratio, and the principal process variables of arc input power, spray distance, and arc gas flow rate. In the later phase of the program, multilayer graded ceramic coatings were also prepared for evaluation. Bond strength, thermal shock behavior, and microstructural analysis provided guidelines in the evaluation of these coatings.

The coatings were sprayed with a Plasmadyne SG-1 plasma torch using argon as the arc stabilizing gas. Spray powder was delivered to the torch by a screw feed hopper system designed by Research Institute personnel. One-eighth inch, 304 stainless steel was the substrate material used for all coated specimens. Prior to coating, these specimen blanks were grit blasted using 40 mesh SiC at 150 psig, cleaned in trichlorethylene, and desiccated until sprayed. Bond strength determinations were made on 1" x 1" plates, and thermal shock testing was conducted on 2" x 2" plates. Microstructure of the coating was determined from photomicrographs of representative bond strength specimens.

The ZrO₂ powder was purchased from Zircoa, Solon, Ohio, and the Al₂O₃ powder was purchased from Norton Company, Worcester, Mass. All of the other powders used in this study were purchased from Atlantic Equipment Engineers, Bergenfield, N. J.

Ten mil coatings of NiCr, Mo, and NiAl were prepared for bond strength and thermal shock testing. The spray conditions for each of the metals were determined by the slide-distance technique developed by Moore (Ref. 17). The average particle size of all the metal powders was 50 μ . For this particle size, the following spray parameters were fixed:

1. arc gas (argon) flow rate - 88 SCFH
2. powder carrier gas (nitrogen) flow rate - 15 SCFH
3. volumetric feed rate for spray powder - 550 ml/hr
4. spray distance - 4".

The input power to the torch was varied from 14-17 KW as a function of the metal being sprayed. Specific power settings are given in Table 31.

Table 31. Power Settings for Metal Coatings

<u>Material</u>	<u>Power Setting (K W)</u>
NiAl	16.3
NiCr	15.2
Mo	15.0

The influence of the particle size ratio of the metal and ceramic powder was determined from an analysis of coatings prepared from six 15% NiCr-85% ZrO₂ blends of different ratios (see Table 32). Four blends of 25% NiAl and 75% Al₂O₃ were also prepared, as shown in Table 33. To study the effect of metal content, blends of 90μ metal and 50μ ceramic were prepared from five mixtures of NiCr-ZrO₂, ranging in metal content from 35% to 5% (by volume) as shown in Table 34.

Similar mixtures of NiAl-Al₂O₃ in four blends ranging from 60% metal to 10% metal were also prepared (Table 35).

Five bond strength test specimens and three thermal shock specimens of each of the different particle size and volumetric ratio blends were sprayed at a power level of 16 KW, 3 inches from the torch, using an argon arc gas flow rate of 110 SCFH, a powder feed rate of 550 milliliters per hour, and an argon carrier gas flow rate of 15 SCFH. Prior to coating, all of the substrates were flashed with a 1-2 mil coating of coarse Mo (80μ) to promote substrate bonding.

The influence of input power and spray distance was studied on pre-blended mixtures of 15% NiCr-85% ZrO₂ and 25% NiAl-75% Al₂O₃. Specimens were coated at 2, 3, 4, and 5 inches from the torch and at input power levels ranging from 11 to 22 KW. Five samples were sprayed at each of several selected spray distances and power level combinations for bond strength testing and metallographic analyses. Except for the selected spray distances and power levels, all of the other spray conditions were as described above.

Five additional bond strength specimens of both the 15% NiCr-85% ZrO₂ and the 25% NiAl-75% Al₂O₃ mixtures were sprayed directly on the steel plates

Table 32. Composition of 85% ZrO₂ -15% NiCr Blends Prepared for Study of Particle Size Ratio Effects

<u>Blend</u>	<u>NiCr Particle Size Range</u>	<u>ZrO₂ Particle Size Range</u>
NZ 1	43-38 μ	93-87 μ
NZ 2	74-57 μ	74-57 μ
NZ 3	93-87 μ	43-38 μ
NZ 4	93-87 μ	57-43 μ
NZ 5	87-74 μ	43-38 μ
NZ 6	87-74 μ	57-43 μ

Table 33. Composition of 75% Al₂O₃ -25% NiAl Blends Prepared for Study of Particle Size Ratio Effects

<u>Blend</u>	<u>NiAl Particle Size Range</u>	<u>Al₂O₃ Particle Size Range</u>
NA 1	43-38 μ	93-87 μ
NA 2	47-57 μ	74-57 μ
NA 3	93-87 μ	57-43 μ
NA 4	93-87 μ	43-38 μ

Table 34. Composition of NiCr-ZrO₂ Blends

<u>Blend</u>	<u>% NiCr</u>	<u>% ZrO₂</u>
NZ 7	35	65
NZ 8	25	75
NZ 9	15	85
NZ 10	10	90
NZ 11	5	95

Table 35. Composition of NiAl-Al₂O₃ Blends

<u>Blend</u>	<u>% NiAl</u>	<u>% Al₂O₃</u>
NA 5	60	40
NA 6	40	60
NA 7	20	80
NA 8	10	90

to evaluate the influence of the molybdenum flash coat. These coatings were also sprayed at 16 KW, 3 inches from the torch.

Metallographic specimens were prepared for several NiCr-ZrO₂ and NiAl-Al₂O₃ coatings which had been sprayed at selected arc gas flow rates in the range of 70 SCFH-130 SCFH, holding all other spray conditions at the previously described levels.

Graded composite coatings of NiCr-ZrO₂ and NiAl-Al₂O₃ were also prepared. For the NiCr-ZrO₂ system, a 2 mil coating of Mo was applied to the substrate followed by three NiCr-ZrO₂ graded layers, each approximately 3 mils thick, and a top coating of approximately 4 mils of ZrO₂. For the NiAl-Al₂O₃ system, a 2 mil coating of NiAl was applied to the substrate, followed by three NiAl-Al₂O₃ graded layers, each 3 mils thick, and 4-5 mil top coat of Al₂O₃. The blend compositions and spray settings are described in Table 36.

TESTING PROCEDURES

To determine bond strength, the coated specimens were epoxy bonded between two aluminum test blocks and then loaded with a universal testing machine in a direction normal to the plane of the coating. The load was slowly increased until coating failure occurred. Bond strength was defined as the breaking load divided by the surface area.

Representative samples from each group of specimens were selected for metallographic analyses. These samples were prepared by standard metallographic procedures and photomicrographs were taken at 250x.

Thermal shock resistance of the metal-ceramic blended coatings was evaluated with a 100 KW plasma-jet. The 2" x 2" test specimens were attached to a water-cooled copper holder that permitted the cooling water to be in direct contact with the back surface of the sample. An "O" ring seal around the outer periphery of the specimen provided a watertight joint between the copper holder and back surface of the specimen. The specimens were subjected to a series of thermal cycles consisting of 10 seconds in the hot plasma effluent and 10 seconds in a cooling stream of ambient air until coating failure. Power input to the plasma-jet was increased after every 10 cycles of test from a starting heat flux of 560 Btu/ft² sec to a final value of 1560 Btu/ft² sec for a total of 90 accumulated cycles. Failure was determined by visual inspection of the coating during the cooling cycle.

EXPERIMENTAL RESULTS

METAL COATINGS

The results of the bond strength tests for the metal coatings are summarized in Table 37.

Table 36. Composition and Spray Settings for Graded Coatings

<u>System NiCr-ZrO₂</u>										
Layer	Blend %	Average Particle Size (μ)	Approx. Thickness (mils)	Spray Distance (in.)	Spray Power (KW)	Arc Gas Flow Rate (scfh)	Carrier Gas Flow Rate (scfh)	Feed Rate (ml/hr)		
1 Mo	100	80	2.5	4	15	110	15	550		
2 NiCr	75	40	3	3	16	110	15	550		
2 ZrO ₂	25	80								
3 NiCr	25	90	2.5	3	16	110	15	550		
3 ZrO ₂	75	50								
4 NiCr	5	80	3.5	3	16	110	15	550		
4 ZrO ₂	95	50								
5 ZrO ₂	100	50	5	3	16.5	110	15	550		
<u>System NiAl-Al₂O₃</u>										
1 NiAl	100	90	2.0	4	15.2	110	15	550		
2 NiAl	75	50	2.7	3	17	110	15	550		
2 Al ₂ O ₃	25	90								
3 NiAl	25	90	3	3	17	110	15	550		
3 Al ₂ O ₃	75	50								
4 NiAl	5	90	3	3	17	110	15	550		
4 Al ₂ O ₃	95	50								
5 Al ₂ O ₃	100	50	4	3	17	90	15	550		

Table 37. Results of Bond Strength Tests for Metal Coatings

<u>Material</u>	<u>Sample No.</u>	<u>Bond Strength</u>	<u>Mode of Failure</u>
NiAl	A-1	3070	Coating separation was a complex failure starting at the epoxy-coating interface, extending partially across the face of the coating, following a shear path at approximately 45° through the coating to the substrate, and then continuing along the substrate coating interface.
	2	3475	
	3	3555	
	4	3870	
	5	3200	
	6	2870	
	7	3570	
	8	5070	
	9	4300	
	10	<u>3370</u>	
	Av.	3635	
Mo	11	1975	Coating separated from substrate at interface.
	12	2870	
	13	2370	
	14	2905	
	15	<u>3480</u>	
	Av.	2720	
NiCr	16	2970	Coating separated from substrate at interface. (Except as noted)
	17	4210	
	18	3730	
	19	3560	
	20	3420	
	21	3240	
	22	3600	
	23	3860	
	24	3765*	Epoxy failure. " "
	25	<u>4110*</u>	
	Av.	3646	

* Failure of test block epoxy adhesive

The bond strength values measured for the ten NiAl coated specimens averaged 3635 psi, somewhat higher than generally reported for this material (Ref. 18). Separation of the test specimens started at the epoxy coating interface, extended partially across the face of the coating, and then followed a shear path at approximately 45° through the coating to the substrate. The separation then continued along the substrate-coating interface. This fracture pattern was consistently observed with all the NiAl specimens (see Figure 48). The two NiAl specimens exposed to thermal shock testing failed after 15 and 13 cycles respectively.

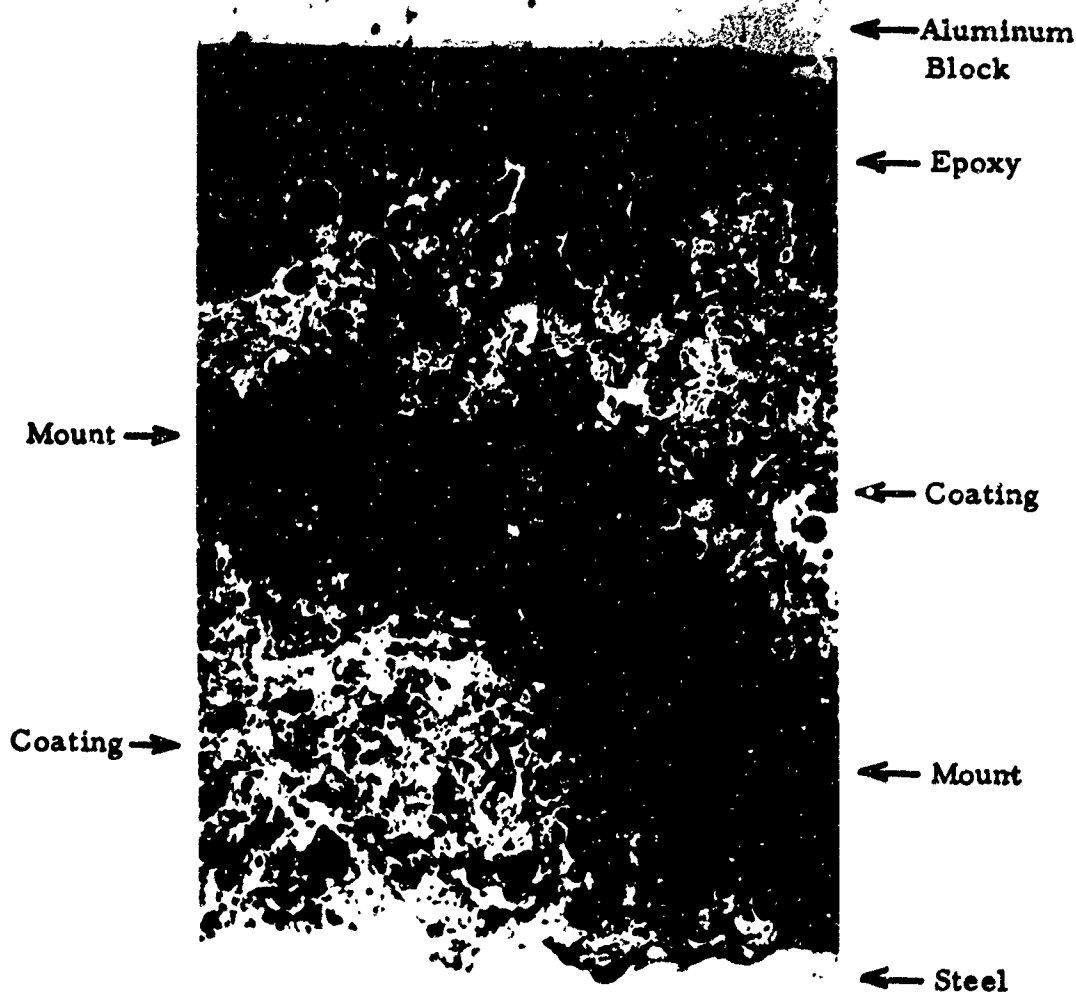
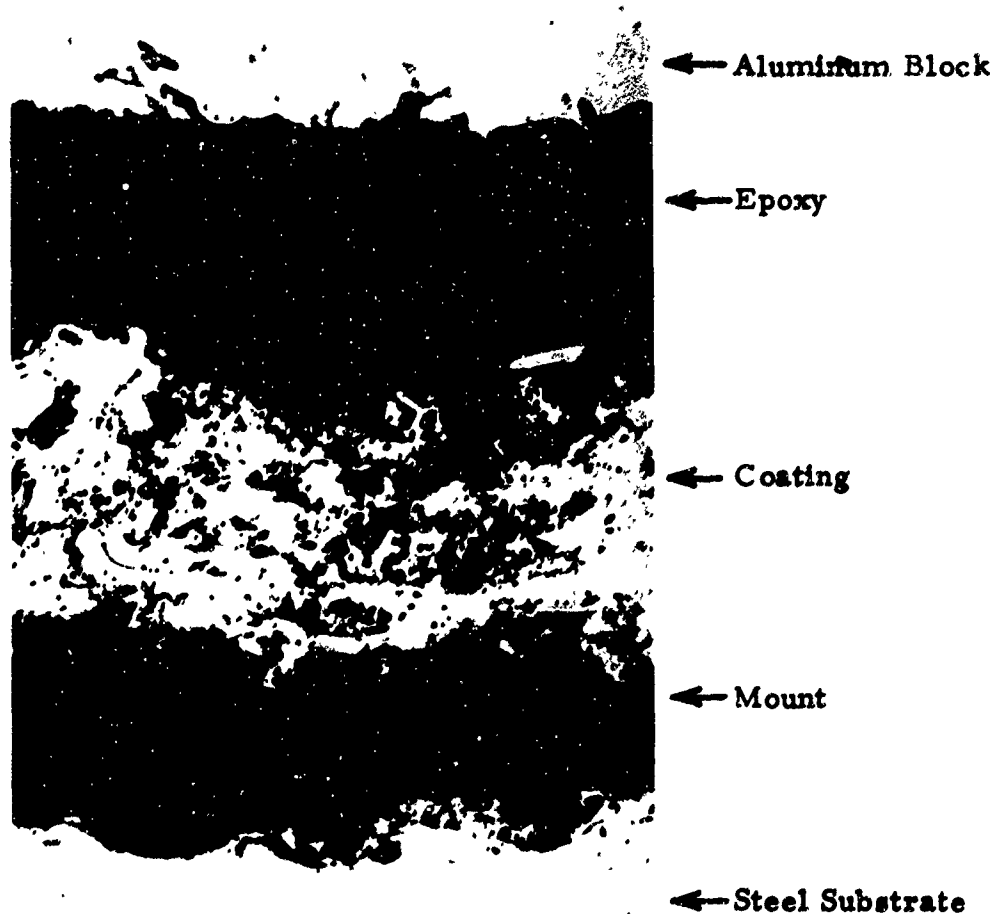


Figure 48. Shear Fracture of NiAl Coated 304 Stainless Steel

The average bond strength measured for the Mo coated specimens was 2720 psi, and failure was due to the separation of the coating from the substrate (see Figure 49). The bond strength values measured were somewhat lower than those usually reported for Mo coatings. Photomicrographs showed that the microstructure of the Mo coatings was more porous than is generally desirable.



250x

Figure 49. Bond Strength Failure by Coating Separation from Substrate (Mo Coated 304 Stainless Steel).

The average bond strength measured for 10 NiCr specimens was 3646 psi, and failure was predominately due to separation between coating and substrate (see Figure 50). Two specimens failed in the epoxy steel interface at 3765 and 4110 psi respectively. Similar failures in four other NiCr samples had been observed earlier in the program. Both thermal shock test specimens failed on the 40th test cycle.

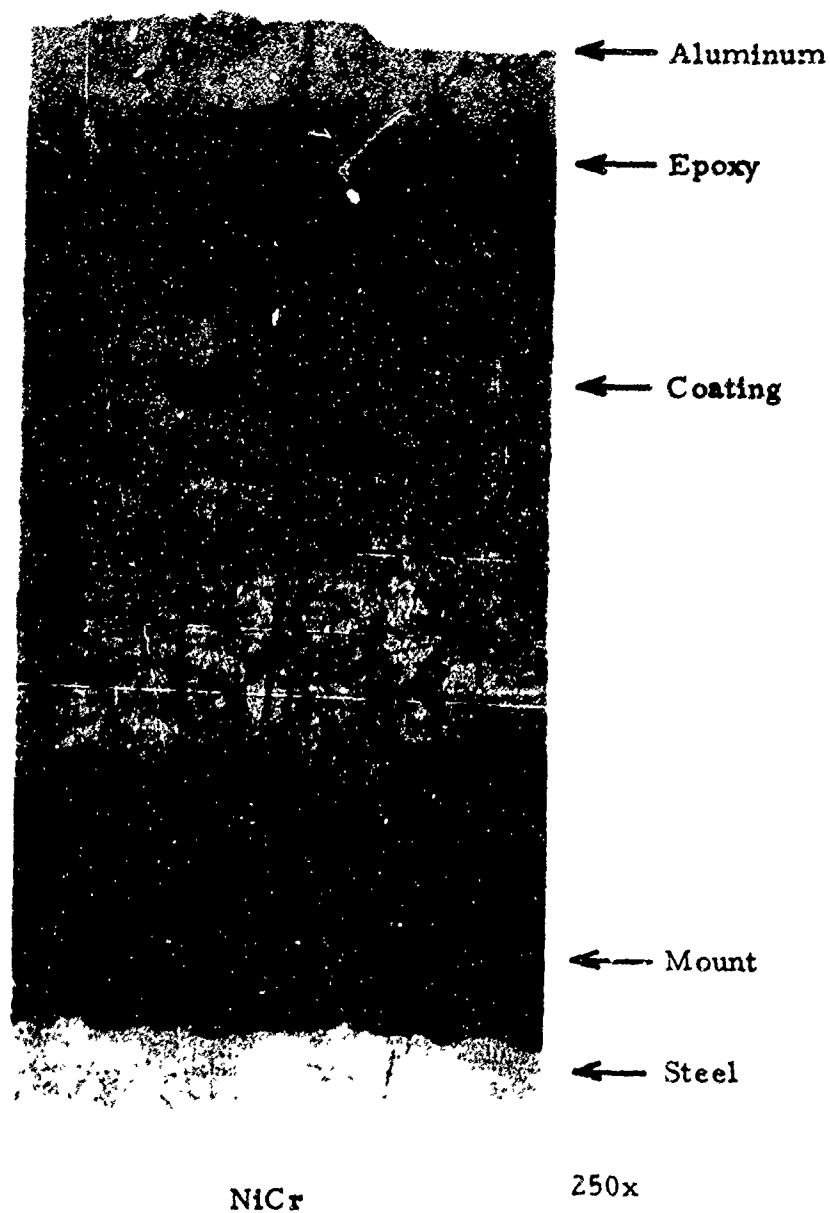
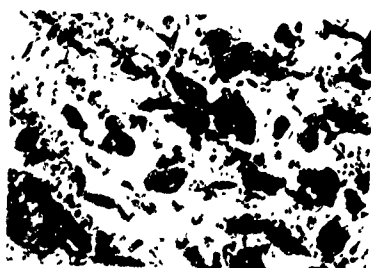


Figure 50. Bond Strength Failure by Coating Separation from Substrate (NiCr Coated 304 Stainless Steel)

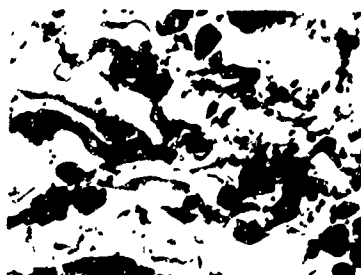
METAL-CERAMIC BLENDED COATINGS

The effect of the particle size ratios on the coating microstructure of the five NiCr-ZrO₂ blends is shown in Figure 51. The first photomicrograph shows a coating prepared from a blend using a fine metal particle (av. 40 μ) and a coarse ceramic particle (av. 90 μ). Very little of the ceramic phase was melted and retained in the coating. Most of the ceramic phase appears as irregular particles in a metallic matrix. The second photomicrograph shows a coating prepared from a blend using medium-sized (av. 65 μ) metal and ceramic particles. This coating is very similar to the first coating with only a slightly more melted ceramic phase.

The third photomicrograph shows a coating prepared from a blend using a coarse metal particle (av. 90 μ) and a fine ceramic particle (av. 40 μ). The ceramic phase in this coating was much more lamellar, and a greater amount was retained. The fourth photomicrograph shows a coating prepared from a coarse metal particle (av. 90 μ) and a moderately fine ceramic particle (av. 50 μ). The ceramic phase is retained to a greater degree, and the particles appear to be completely deformed. The ceramic phase now is the matrix for the lamellar metallic phase.



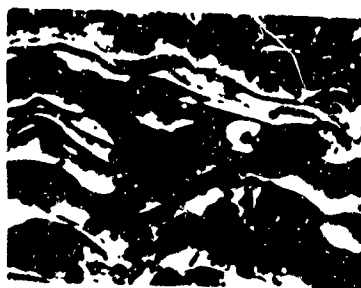
Coarse ZrO₂ (av. 90 μ)
Fine NiCr (Av. 40 μ)



Medium ZrO₂ (Av. 65 μ)
Medium NiCr (Av. 65 μ)



Fine ZrO₂ (Av. 40 μ)
Coarse NiCr (Av. 90 μ)



Moderately Fine ZrO₂ (Av. 50 μ)
Coarse NiCr (Av. 90 μ)

Figure 51. Effect of Particle Size Ratio of Metal and Ceramic Powders.
Photos of Coatings Prepared from Blends Containing 15%
NiCr-85% ZrO₂ (250 \times)

The porosity of the coatings increased with increasing ceramic phase. Much of this porosity, however, was due to ceramic particles pulled out during metallographic preparation. Although these pull-outs do not represent true porosity, they are areas of poor bonding.

Analysis of the NiAl-Al₂O₃ coating from the photomicrographs was exceptionally difficult due to the presence of five different phases. The presence of the different Ni and Al phases obscured the Al₂O₃ phases. An X-ray analysis of a nickel coated aluminum coating showed that nickel, aluminum, NiAl and Ni₃Al₂ were present as major phases. The difficulties of interpretation can be seen from Figure 52. Although photomicrographs were not extremely helpful, apparent coating microstructure and the trends in bond strength and thermal shock resistance were in general agreement with those observed for NiCr-ZrO₂ coatings.

The influence of particle size ratio on bond strength and thermal shock can be seen in Figure 53. The coatings prepared from the blends with a coarse ceramic particle (av. 90 μ) and a fine metal particle (av. 40 μ) had the highest bond strength and thermal shock resistance, while the coatings prepared from the blends with the coarse metal particle and fine ceramic particle had the poorest bond strength and thermal shock resistance. The average bond strengths for the NiCr-ZrO₂ coatings ranged from 2400 psi to 5100 psi and from 3100 to 4400 psi for the NiAl-Al₂O₃ coatings. It is interesting to note that the coatings prepared from the coarse ceramic particles and fine metal particles had bond strengths almost 1000 psi in excess of the pure metallic coatings. From the graph of Figure 54 it can be seen that the bond strength increased from 3600 for pure NiCr to 5100 psi for the selected NiCr-ZrO₂ blend and from 3600 for NiAl to 4400 psi for the selected NiAl-Al₂O₃ blend. It appears that the addition of irregular coarse grain ceramic particles in the matrix of the metal coating can improve bond strength.

The thermal shock resistance followed the same pattern as bond strength (Figure 53). Thermal shock resistance improved with increasing ceramic particle size. Failures of the NiCr-ZrO₂ coatings ranged from 22 cycles to 60 cycles, while the NiAl-Al₂O₃ coatings ranged from 3 to 40 cycles. It is interesting to note that the failure of the pure NiCr coating occurred at 40 cycles, whereas the pure NiAl coating failed at 14 cycles.

In general, bond strength and thermal shock resistance measurements were in good agreement and quite reproducible. This was especially true for the thermal shock measurements where, in all cases, the individual values were very close to their group average.

It was not surprising that the thermal shock resistance and bond strength of coatings which were metal-rich and retained only a small amount of ceramic phase were so high. With the metallic phase more closely approximating the thermal properties of the substrate, the possible stress-relieving effect of the substrate, and the possible stress relieving effect of the irregular ceramic particles dispersed through the metal, it is not difficult to predict the trends observed.

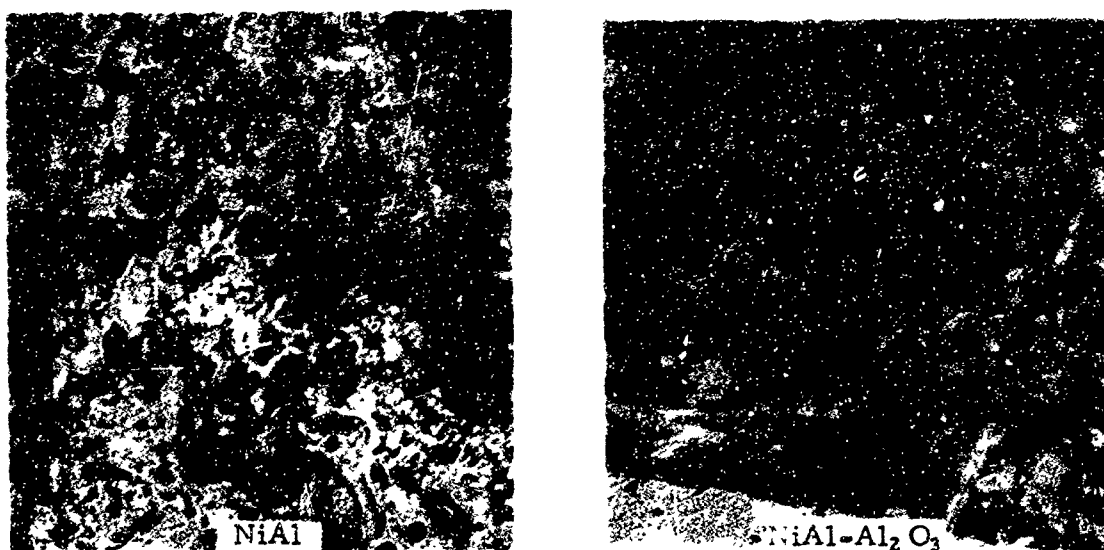


Figure 52. NiAl Coating Compared to NiAl-Al₂O₃ Blended Coating (250x)

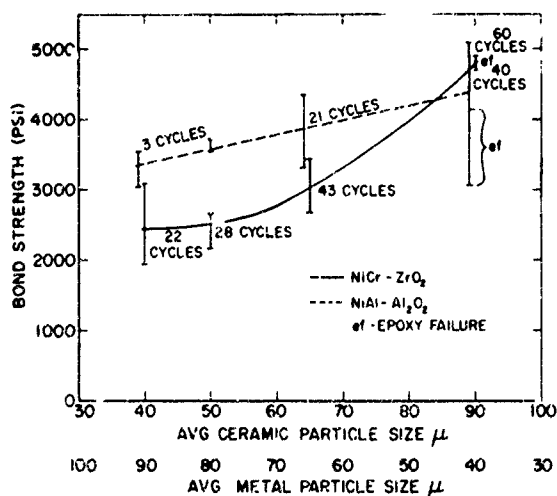


Figure 53. Influence of Particle Size Variation on Bond Strength and Thermal Shock Cycles to Failure

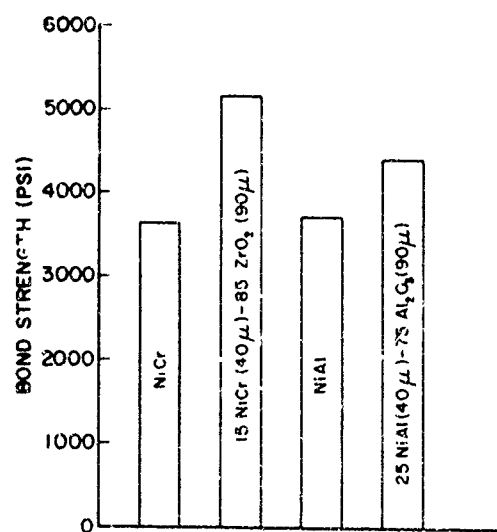


Figure 54. Influence of Fine Ceramic Particles Dispersed in a Metal Matrix

Bond strength specimens prepared on substrates without a molybdenum flashing are compared to identical coatings on molybdenum flashed substrates in Figure 55. The molybdenum flashing improved bond strength NiCr-ZrO₂ coatings (2000 psi to 2600 psi) but had no effect on the NiAl-Al₂O₃ coatings. It appeared that the molybdenum flashing acts as a better bonding agent than the steel for the NiCr-ZrO₂ coating, but it was not effective with the NiAl-Al₂O₃ coating. This was apparent from the location of bond failures: the NiCr-ZrO₂ coatings always failed at the Mo-NiCr-ZrO₂ interface, while failure of the NiAl-Al₂O₃ coatings was in the molybdenum or at the Mo-steel interface.

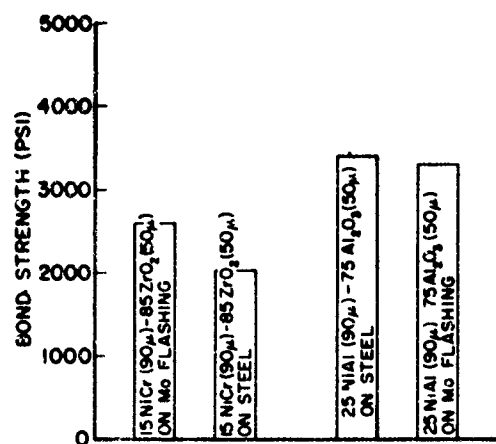


Figure 55. Effect of Molybdenum Flashing on Bond Strength

The effect of spray distance from the substrate upon coating microstructure is shown in Figure 56. The most significant effect was the increase in ceramic phase retained in the coating with decreasing spray distance. Comparing the third photomicrograph to the first and second photomicrographs, it is apparent that the shorter spray distances produce a coating in which the metal and ceramic particles are more lamellar. A relation between spray distance and bond strength could not be clearly established.

The effect of the input power level in plasma-spraying a ceramic-metal composite is shown in Figure 57. From a comparison of the four photomicrographs, it is apparent that as power level increases from 11 KW to 21 KW, the amount of ceramic in the coating increases, and more lamellar structure is formed (a direct indication of greater melting of the ceramic particles). As shown in Figure 58, when input power was increased, the bond strengths of the NiCr-ZrO₂ coatings decreased from 3400 psi to 2500 psi. This was not unexpected after observing the high metallic content and the dispersion of irregularly shaped ceramic particles in the microstructure of the coatings sprayed at the lower power settings. The NiAl-Al₂O₃ coatings did not follow this pattern. Although there was an initial drop in bond strength from 3000 psi to 2600 psi, the bond strength then increased to a final value of 3600 psi at the higher power settings. The photomicrographs of these coatings did not indicate any reason for this unpredictable behavior.

The influence of the arc gas flow rate on the blended coatings was unclear. In general, photomicrographs of the same blends sprayed at arc gas flow rates of 70, 90, 110, and 130 SCFH were very similar. The microstructure of the coatings did not appear to be affected by varying arc gas flow rate. There appeared to be some influence on deposition rate, but a definite trend could not be established. In the case of the pure oxide coatings, however, there was a definite increase in the deposition rate as the arc gas flow rate was decreased.

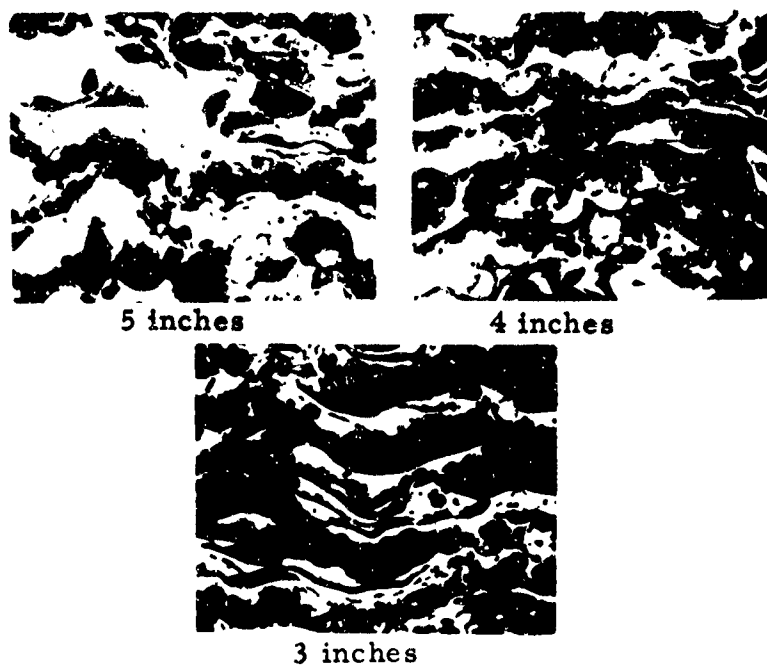


Figure 56. Effect of Distance from Gun. Photos of Coatings Prepared from a Blend Composed of 15% NiCr-85% ZrO₂ (250x)

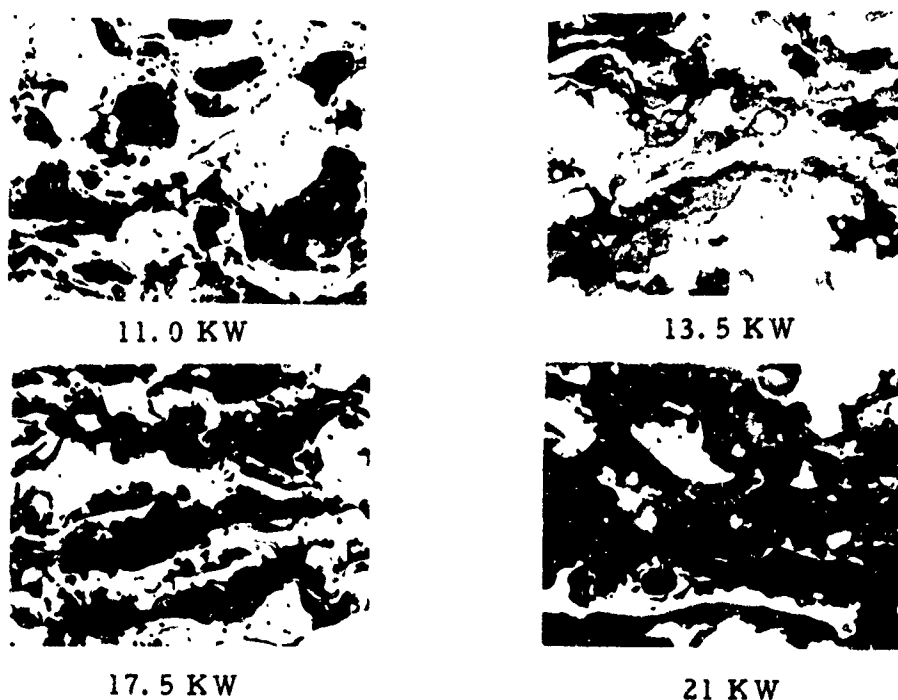


Figure 57. Effect of Spray Power. Photos of Coatings Prepared from a Blend Composed of 15% NiCr-85% ZrO₂ (250x)

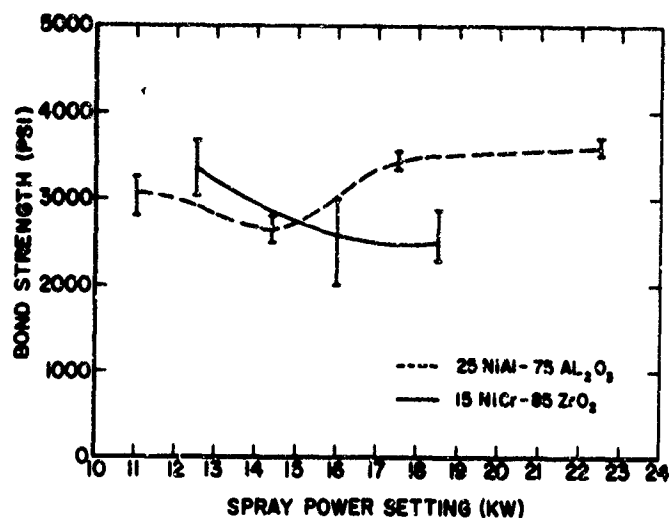


Figure 58. Bond Strength Versus Spray Power Setting

As expected, increasing the percent of ceramic to metal in the presprayed blend decreased the bond strength and thermal shock resistance of the coating. As shown in Figure 59, bond strength decreased from 2900 to 1800 psi and thermal shock resistance from 45 to 2 cycles with an increase in the preblend proportion from 65% to 95%. The bond strength of the NiAl-Al₂O₃ coatings dropped from 3400 to 2800 psi as the percentage of Al₂O₃ was increased from 50% to 80%. The 90% Al₂O₃ blend departed from expectations, with bond strength increasing to 3500 psi; photomicrographs did not reveal any reason for this. The thermal shock resistance was fairly consistent going from 10 to 4 cycles with increasing percentages of Al₂O₃. It was interesting to note that only in those blends containing over 90% ceramic did the sprayed coating closely approximate the metal-ceramic ratio of the presprayed mixture. Photomicrographs of the changing coating microstructure with change in volumetric ratio are shown in Figure 60.

Investigating the loss of ceramic phase for several blends sprayed under carefully selected conditions, it was found that particle segregation was occurring when the mixture entered the plasma stream. A well-blended mixture of 75% ceramic and 25% metal remained completely homogeneous until entering the plasma effluent. Selected blends were carried into the arc gas stream and sprayed into a silicone-coated beaker with the arc turned off. No segregation of phases was observed. However, when the same powder blends were carried into the arc gas stream with the arc on and sprayed on a glass plate, a segregated pattern was observed. It is interesting to note that on one occasion, powder segregation did not occur. This was observed with a worn set of electrodes. When these were replaced, the segregated pattern was again observed. Electrode geometry was one variable not under complete control. This single observation of the effect of electrode geometry would suggest it could be a significant variable.

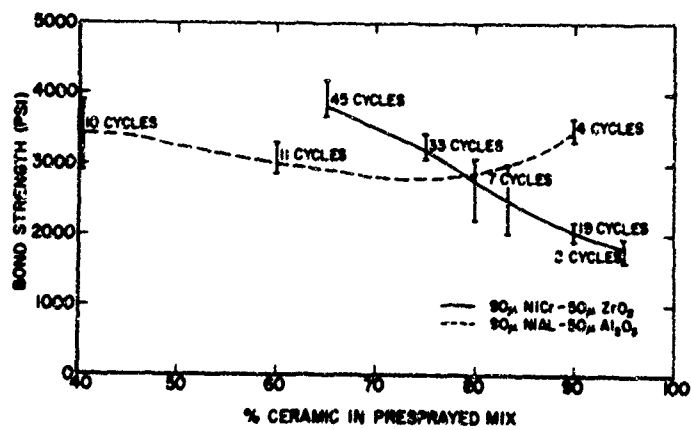
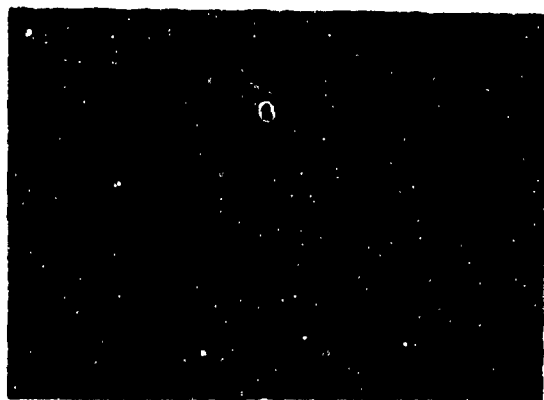
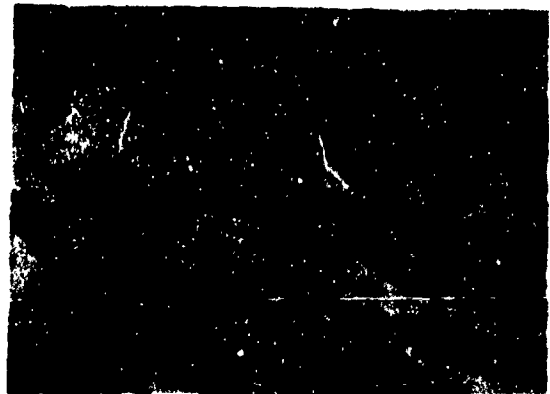


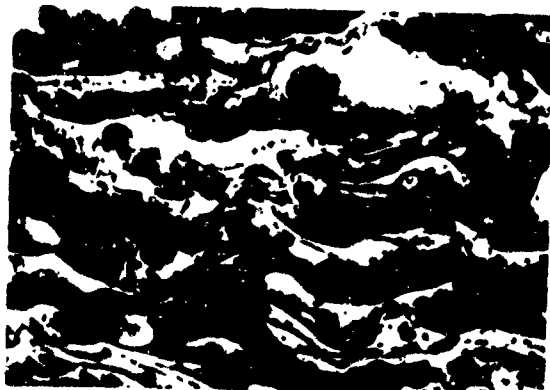
Figure 59. Bond Strength and Thermal Shock Resistance Versus % Ceramic Phase



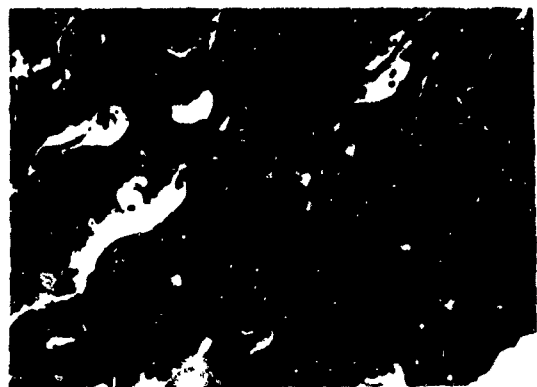
35 NiCr - 65 ZrO₂



25 NiCr - 75 ZrO₂



15% NiCr - 85% ZrO₂



5% NiCr - 95% ZrO₂

Figure 60. Effect of Ceramic to Metal Ratio (250x)

Obtaining a desired microstructure requires the proper selection of particle size ratio. The selection of a fine ceramic particle and coarse metal particle gave a coating with lamellar microstructure closely approximating the presprayed proportions, but with relatively low bond strength and thermal shock resistance. The selection of a coarse ceramic particle and a fine metal particle produced a coating with a high bond strength and thermal shock resistance, but lacking a microstructure conducive to high temperature resistance and insulation. Moreover, it was shown that coating quality depends upon proper selection of spray settings. It is also important to note that there is an interdependency between all three of the spray variables studied: distance, power level, and powder size ratio.

MULTILAYER GRADED COATINGS

Bond strength test results are summarized in Table 38 for specimens of two multilayer graded coatings, a NiCr-ZrO₂ and a NiAl-Al₂O₃ system.

Table 38. Results of Bond Strength Tests for Graded Coatings			
Material System	Sample No.	Bond Strength (psi)	Mode of Failure
NiCr-ZrO ₂	B-1	2580	In graded zone
	2	2540	
	3	2480	
	4	2635	
	5	2545	
	Avg.	2560	
NiAl-Al ₂ O ₃	6	2495	At Al ₂ O ₃ graded zone interface
	7	2345	
	8	1935	
	9	2500	
	10	2075	
	Avg.	2270	

The NiCr-ZrO₂ graded coatings had an average bond strength of 2560 psi. Coating separation occurred as an irregular shear line which passed through the second and third graded zones. This bond strength level was in close agreement with previously measured values for a blended NiCr-ZrO₂ layer (see Figure 53). A photomicrograph of a typical graded NiCr-ZrO₂ coating evaluated for bond strength is shown in Figure 61.

The NiAl-Al₂O₃ graded coatings had an average bond strength of 2270 psi, and failure occurred at the Al₂O₃ graded zone interface. The three NiAl-Al₂O₃

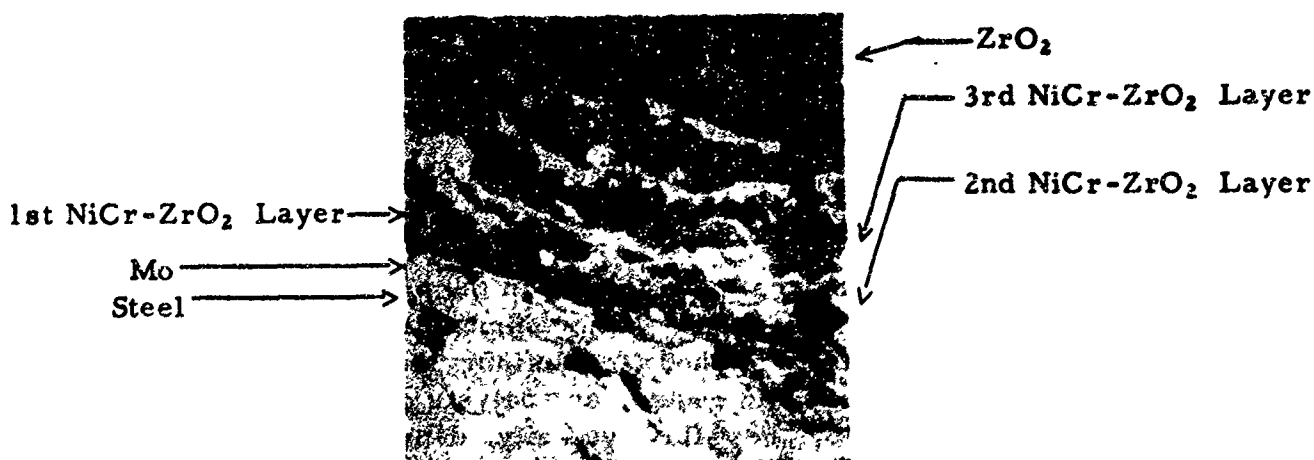


Figure 61. NiCr-ZrO₂ Graded Coating

coatings subjected to thermal cycling consistently failed on the 15th cycle. These results correlated closely with the thermal shock data for blended layers as shown in Figure 53.

The thermal shock resistance of the NiCr-ZrO₂ coatings was disappointing. Failure occurred during the fourth cycle of exposure at the initial heat flux of 560 Btu/ft² sec.

Analysis of the test specimens showed that, in all cases, failure was due to spalling of the top ZrO₂ layer. One of the test specimens was re-exposed to thermal shock cycling to determine the extent of the failure. Although some further spalling of the ZrO₂ layer occurred, the graded underlayers did not appear to be affected. This would suggest that the thermal shock resistance of ZrO₂ was not significantly improved by the graded underlayers. However, it is interesting to note the improved thermal shock resistance of a ZrO₂ layer with small additions of metal particles (15% NiCr-85% ZrO₂ withstood 22 thermal shock cycles).

CONCLUSIONS AND RECOMMENDATIONS

These studies have shown that composite coatings tailored for specific requirements can be prepared by plasma spraying. Predetermined volumetric proportions and microstructures in a binary coating can be obtained, and coating properties such as bond strength and thermal shock resistance can be modified. Fabricating the desired composite requires control of the critical process variables: powder particle size ratio, spray power, and spray distance. It is important to recognize the interdependency between these process variables. Heat transfer from the plasma effluent to the particle appears to have the most critical relationship to the thermal and physical properties of the materials and it is directly affected by the selection of the particle size ratio.

The metallic coatings were generally more dense and had higher bond strength and thermal shock resistance than the ceramic and composite coatings. The addition of coarse ceramic particles dispersed in the matrix of a metal coating improved bond strength by better than 1000 psi. This improvement may be due to an annealing effect induced by heat retention of ceramic particles which reduced the cooling rate of the sprayed coating.

The importance of the thermal conditioning in the plasma effluent suggests the need for further studies in this area. Major emphasis should be placed on the development of more accurate methods for defining the heat transfer phenomenon. A detailed study of this would require an analysis of the plasma effluent and characterization of enthalpy, heat flux, velocity, density, and temperature profiles. The nonuniform nature of the gas stream introduces complications which will require the establishment of "effective" numerical values for gas stream properties. It will also be important to determine accurately the distance the particle must travel in the effluent to become completely molten.

Calculations of particle velocities in the effluent also will be required for a more complete study of the thermal conditioning process. Laboratory verification of velocity calculations will be needed prior to extensive utilization of the relationships derived in Appendix II.

In addition to the proposed theoretical studies, a program to develop tailored composite coatings and components for current aerospace requirements should be initiated based upon knowledge generated from the present research efforts.

Current and expected material requirements for turbine engine and rocket motor applications offer interesting possibilities for composite coatings and plasma-sprayed free standing bodies. Developmental studies directed toward these and other aerospace applications could lead to the development of a family of plasma-sprayed composites tailored for specific thermal, chemical, and mechanical properties.

APPENDIX I

THEORETICAL DETERMINATION OF PARTICLE SIZE RATIOS FOR METAL-CERAMIC POWDER BLENDS

A review of the photomicrographs of the blended coatings prepared from mixtures of NiCr and ZrO_2 with selected particle size ratios indicated that the coarse NiCr (90μ) and fine ZrO_2 (50μ) particles produced the most desirable microstructures. The question then arose as to the possibilities of selecting optimum particle size ratios by theoretical analysis rather than by experimentation. A determination of optimum particle size ratios would have to be based upon an analysis and comparison of the thermal and physical properties of the blend materials.

An initial step in the analysis would be the compilation of the material properties. Properties for NiCr and ZrO_2 are shown in Table 39. From the data, it is apparent that NiCr is more dense, has a lower melting point and a higher thermal conductivity than ZrO_2 . From the nature of the spray process, it would be reasonable to assume that the melting energy is one of the more significant factors for comparison. Using the data of Table 39, the thermal energy required to melt a particle (L_m) can be calculated according to:

$$L_m = \frac{\rho \pi D^3}{6} (C_p \times T_m + H_f) \quad (1)$$

where

- L_m = Thermal energy required for melting (Btu)
- ρ = Material density (lb/ft³)
- D = Particle diameter (cm)
- T_m = Melting temperature ($^{\circ}F$)
- C_p = Specific heat (Btu/lb)
- H_f = Heat of fusion (Btu/lb)

Comparing the thermal energy requirements as a function of particle diameter for NiCr and ZrO_2 , the following ratio is observed:

$$L_n = \frac{8.4\pi}{6(454)} (0.13 \times 2600 + 125) D_n^3 \quad (2a)$$

$$L_z = \frac{5.6\pi}{6(454)} (0.15 \times 4700 + 304) D_z^3 \quad (2b)$$

where

L_n = Thermal energy required to melt NiCr

L_z = Thermal energy required to melt ZrO_2

$$\frac{L_n}{L_z} = \frac{0.69 (D_n)^3}{(D_z)^3} \quad (2c)$$

Table 39. Material Properties

Material	Density g/cc	Melting Point °F	Specific Heat Btu/lb. °F	Thermal Expansion in/in °F
Steel	7.9	2650	0.13	$8.5 - 10 \times 10^{-6}$
Molybdenum	10.2	4700	0.08	$3-4.5 \times 10^{-6}$
NiCr	8.36	2600	0.13	$6.5 \times 9.5 \times 10^{-6}$
ZrO_2	5.6	4700 to 5010	0.15	6.5×10^{-6}

Material	Thermal Conductivity Btu/hr ft °F	Emittance	Heat of Fusion cal/g mole	Elastic Modulus psi
Steel	8-14	--	Approx. 4000	$30-20 \times 10^6$
Molybdenum	90-40	0.2	6,660	45×10^6
NiCr	8-18	0.4	Approx. 4000	$35-25 \times 10^6$
ZrO_2	1.2	0.28	20,800	20×10^6

For particles of equal diameter, the ZrO_2 would require greater thermal energy for melting. Furthermore, the ZrO_2 would travel through the plasma effluent with a higher velocity than NiCr because of its lower density. Thus, for a NiCr- ZrO_2 blend of equal particle sizes, it can be assumed that the NiCr would melt in a shorter spray distance than the ZrO_2 since it travels at a lower velocity and requires less thermal energy.

If a particle is injected into the plasma effluent at a point, P_1 , and is carried a distance (S) to point P_2 , where it impinges on a substrate in a completely molten state, the thermal energy (Q) absorbed by the particle is equal to the average rate of heat transfer (q) multiplied by the residence time (t_r). If no ablation occurs, and the particle has just reached the molten state on substrate impact, the total thermal energy (Q) absorbed by the particle is equal to the melting energy (L), thus

$$Q = qt_r = Lm \quad (3)$$

$$t_r = \frac{S}{V_p} \quad (4)$$

$$q \frac{S}{V_p} = Lm \quad (5)$$

$$S = \frac{L_m V_p}{q} \quad (6)$$

where

- Q = Total thermal energy absorbed (Btu)
- t_r = Residence time (sec)
- S = Spray distance (ft)
- V = Average particle velocity (ft/sec)
- q = Heat transfer rate (Btu/sec)

For spraying a mixture of two materials (M_1 and M_2), selection of particle sizes would be based upon the requirement that both materials be molten at point P_2 . Since spray distance (S) would be the same for both materials:

$$\frac{Lm_1 V_{p1}}{q_1} = S = \frac{Lm_2 V_{p2}}{q_2} \quad (7)$$

A rough approximation describing the relationship of particle velocity as a function of particle diameter (D) and particle density (ρ) is given in equation (8).

$$\frac{V_{P_1}}{V_{P_2}} \propto \frac{\rho_2 D_2}{\rho_1 D_1} \quad (8)$$

where

ρ = Density
D = Particle diameter

The substitution of equation (8) into equation (7) and the rearrangement of the equation results in the following:

$$\frac{V_{P_1}}{V_{P_2}} = \frac{q_1 L m_2}{q_2 L M_1} = \frac{\rho_2 D_2}{\rho_1 D_1} \quad (9)$$

Combining equations (9) and (2c) and substituting density values of 8.4 and 5.6 gm/cc for NiCr and ZrO₂ yields the following:

$$\frac{D_n}{D_z} = 1.46 \sqrt{\frac{q_n}{q_z}} \quad (10)$$

If the rate of heat transfer to particles of NiCr and ZrO₂ is assumed to be the same, then the optimum diameter of the NiCr particle will be 1.46 times larger than the diameter of the ZrO₂ particle. Thus, if a diameter of 50 μ is selected for the ZrO₂ particle, a diameter of 73 μ would be required for the NiCr particle. An empirical analysis of NiCr-ZrO₂ blend indicated that for a 50 μ diameter ZrO₂ particle the optimum diameter for a NiCr particle was 90 μ . This results in a particle size ratio of 1:1.8. The discrepancy between the calculated and observed ratios probably arises from the simplifications employed in the velocity approximations and in the assumptions employed in the heat transfer analysis. A more accurate determination of an optimum particle size ratio would require a more precise evaluation of particle velocity and the rates of heat transfer. Models for calculating particle velocity have been developed by Keith, as given in Appendix 2, and by Engelke (Ref. 15). According to Keith:

$$V_p = V_g - \frac{1}{\frac{1}{V_g} + \frac{0.33 \rho_{gt}}{D_p \rho_p}} \quad (11)$$

where

- V_p = Particle velocity (ft/sec)
- V_g = Effluent velocity (ft/sec)
- ρ_g = Effluent density (lb/ft³)
- t = Time (sec)
- ρ_p = Density of the particle (lb/ft³)

As derived by Engelke

$$V_p = -V_g \exp(-18ut/D^2 \rho) \quad (12)$$

where

- u = Effluent viscosity (lb/ft sec)

Models for calculating rates of heat transfer have been developed by Engelke and Smith (Refs. 15 and 16). As with the velocity calculations, considerable data defining the condition of the plasma effluent are required. Obtaining these data would require an involved empirical analysis of the plasma effluent.

As derived by Engelke (Ref. 15), the rate of heat transfer designated by $(\lambda \Delta T)$ is:

$$(\lambda \Delta T) = \sqrt{\frac{u V_g}{16S}} \frac{LmD}{\sqrt{\rho}} \quad (13)$$

where

- λ = Coefficient of heat transfer (Btu/ft hr °F)
- S = Distance particle must travel to reach the molten state (ft)
- ΔT = Temperature difference between the gas and the particle (°F)

The most critical empirical determination in the equation is S , the distance the particle must travel to reach the molten state.

Another approach for determining the rate of heat transfer would lie in the assumption that the principal mode of heat transfer is convection and therefore:

$$q = h \Delta T A \quad (14)$$

where

h = Film coefficient (Btu/ft² sec °F)

A = Particle surface area (ft²)

q = Rate of heat transfer (Btu/sec)

The film coefficient (h) would be the most difficult factor to determine since it is a function of particle shape, size, roughness, and viscosity, as well as of the gas properties of temperature, velocity, viscosity, and density. The determination of the rate of heat transfer (q) is further complicated by the fact that the properties of the plasma effluent vary both with distance from the torch exit plane and with position in the effluent cross section.

APPENDIX II

THEORETICAL DETERMINATION OF THE VELOCITY-TIME RELATIONSHIP OF PARTICLES BEING ACCELERATED BY A MOVING GAS STREAM

ROGER KEITH*

In the course of arc-plasma-jet flame spray operations, a stream of powdered material is injected into a jet of moving gas and is accelerated by it. It is often desirable to calculate the resulting velocities of the particles at various distances from the point of injection, and the formulas given here will describe the motion of the particles with sufficient accuracy for practical purposes.

The drag force on a particle is given by

$$F_d = C A_p \rho u^2 / 2 g_c \quad (1)$$

where C = drag coefficient, dimensionless; A_p = projected area of particle in the direction of motion, sq. ft.; ρ = density of surrounding fluid, lb./cu. ft.; u = relative velocity between particle and fluid, ft./sec.; and g_c = dimensional constant, 32.17 lb. mass - ft./lb. force-sec².

The inertial force on a particle is given by

$$F_i = W a / g_c \quad (2)$$

where F_i = the inertial force tending to accelerate the particle, lb. force; w = the weight of the particle, lb. mass; and a = the acceleration of the particle, ft./sec².

In the case of a horizontally-accelerated particle, the vertical component of motion is usually negligible and of little or no interest. In this case, the drag and inertial forces are equal in magnitude, and from equations (1) and (2):

$$C A_p \rho u^2 / 2 = W a \quad (3)$$

Since the plasma-jet is highly turbulent, it can be assumed that the Reynolds number for the fluid is in the Newton's law regime, which covers values from 1000 to 200,000. In this region, the drag coefficient has a fairly constant value for spheres. This is:

$$C = 0.44 \quad (4)$$

* Associate Research Engineer

Noting also the dimensional relationships for the spherical particle

$$A_p = \pi D^2/4 \quad (5)$$

and
$$W = \rho_p \pi D^3/6 \quad (6)$$

where D = the diameter of the particle, ft.; and ρ_p is the density of the particle, lbs. -mass/ft³, and the relationship

$$u = U_f - U \quad (7)$$

where U_f = the velocity of the fluid, ft. /sec.; and U = the velocity of the particle, ft. / sec., then equation (3) can be modified to yield:

$$0.33 \rho_p dt/D\rho_p = dU/(U_f - U)^2 \quad (8)$$

by setting $a = dU/dt$, where t = time, in seconds.

Integrating this expression with respect to time yields

$$C_1 + 0.33 \rho_p t/D\rho_p = 1/(U_f - U) \quad (9)$$

and noting that when $t = 0$ then $U = 0$, thus $C_1 = 1/U_f$ and

$$1/U_f + 0.33 \rho_p t/D\rho_p = 1/(U_f - U) \quad (10)$$

which relates the velocity of the particle and time.

Rearranging equation (10), the following expression is obtained

$$dS = U_f dt - dt/(1/U_f + 0.33 \rho_p t/D\rho_p) \quad (11)$$

by setting $U = dS/dt$, where S = the distance traveled by the particle from rest, feet.

Integrating equation (11) with respect to time yields

$$S = U_f t - (3.0 D\rho_p/\rho) \ln (1/U_f + 0.33 \rho t/D\rho_p) + C_2 \quad (12)$$

Defining $S = 0$ at $t = 0$, then

$$C_2 = (3.0 D\rho_p/\rho) \ln (1/U_f) \quad (13)$$

and

$$S = U_f t + (3.0 D\rho_p/\rho) [\ln(1/U_f) - \ln(1/U_f + 0.33 \rho t/D\rho_p)] \quad (14)$$

which is the desired equation relating position of the particle and time.

BIBLIOGRAPHY

Boucher, D. and Alves, G. "Particle Dynamics," in Perry, et al, Chemical Engineers' Handbook, pp. 5-59 ff, 4th ed, McGraw-Hill, 1963.

APPENDIX III

A SIMPLE THEORY FOR PREDICTION OF THE THERMAL EXPANSION OF COMPOSITE MATERIALS

ROGER KEITH*

For a composite material, a thin cross section may be taken in which the configuration of material is essentially constant throughout the small dimension of the slice; in other words, both faces of the disc are identical in their mapping of the two components, and further sectioning of the slice would reveal only further duplication of this mapping. If it is assumed that only longitudinal forces need be considered, neglecting radial and tangential forces, stresses, strains, and so forth, then the slice of the actual material shown in Figure 62 can be replaced by the model rigid-block system of Figure 63:



Figure 62. Thin Slice of Actual Composite

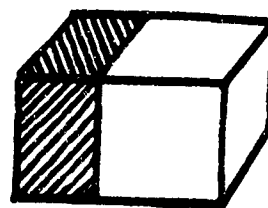


Figure 63. Model Rigid-Block System Substitute

where the relative cross-sectional areas, and thus the masses, of the two components are present in the same ratio in each model, and relative rotation of the piece shown in Figure 63 (as in a bimetal strip) is forbidden.

For a material having a fractional composition of N of component one by volume, this volume may be represented as:

$$V_1 = A_1 L \quad (1)$$

at the original temperature of the system (see Figure 64). Similarly, considering the volume of component two and adding the two values, the total volume of the system at the original temperature is:

$$V_1 + V_2 = (A_1 + A_2) L \quad (2)$$

and the fractional volume of component one is defined as:

$$N = \frac{V_1}{V_1 + V_2} = \frac{A_1 L}{(A_1 + A_2) L} = \frac{A_1}{A_1 + A_2} \quad (3)$$

* Associate Research Engineer

Similarly,

$$1-N = \frac{A_2}{A_1 + A_2} \quad (4)$$

and

$$\frac{A_1}{A_2} = \frac{N}{1-N} \quad (5)$$

If the temperature is increased by ΔT , then the pieces will increase in length by amounts ΔX_1 and ΔX_2 where:

$$\Delta X_1 = \alpha_1 L \Delta T \quad (6)$$

and

$$\Delta X_2 = \alpha_2 L \Delta T \quad (7)$$

where α_1 and α_2 are the coefficients of linear thermal expansion for the two materials. Assigning the designations of "component one" and "component two" to the two materials comprising the sample such that

$$\alpha_1 > \alpha_2 \quad (8)$$

is true, then it follows that $\Delta X_1 > \Delta X_2$. (9)

However, if the pieces are bonded together so that no shear is permitted along the juncture of the two pieces, and they behave as if rigidly capped with bending forbidden, as shown in Figure 65, then their behavior will more closely approximate that of the original material depicted in Figure 62.

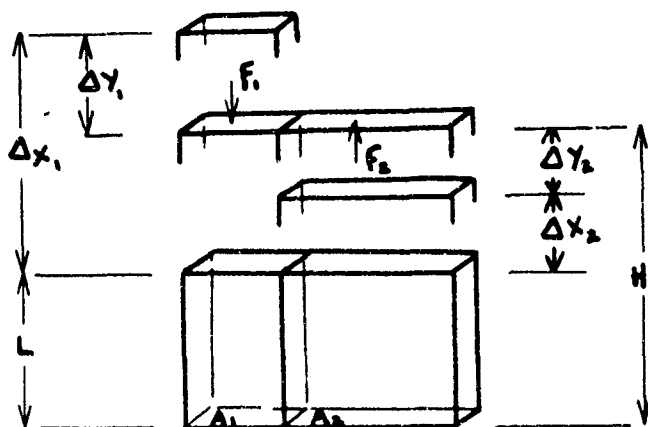


Figure 64. Dimensions of Model

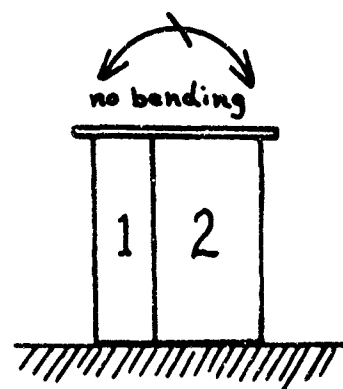


Figure 65. Block System

Note that the two component materials of the pieces shown in Figures 62 and 63 are forced to expand equally as the temperature is changed and that the force to compress the more rapidly expanding material is supplied by the tension of the less rapidly expanding one. Referring once more to Figure 64, application of the compressive force F_1 to material one will achieve a new height (H) which is defined as the new dimension of the composite produced by the action of temperature and interior stresses, and is also equal to the new height achieved by material two under the action of the tensile force F_2 :

$$H = L + \Delta X_1 - \Delta Y_1 = \Delta X_2 + \Delta Y_2 \quad (10)$$

An apparent coefficient of linear thermal expansion for the material (α_3) may be defined as:

$$H = L + \alpha_3 L \Delta T = L(1 + \alpha_3 \Delta T) \quad (11)$$

Note that from a force balance about the upper plane of the specimen, since the system is at rest,

$$\Sigma F = 0 \quad (12)$$

Therefore,

$$F_1 = F_2 \quad (13)$$

Assuming that these materials are within the Hooke's law region of linear stress-strain relationships, considering the strain to be Δ/H , where H is the gage length, and that the modulus of rigidity for the components is constant with temperature, then

$$E_1 = \frac{F_1/A_1}{\Delta Y_1/H} \quad (14)$$

and

$$E_2 = \frac{F_2/A_2}{\Delta Y_2/H} \quad (15)$$

where E_1 and E_2 are the moduli of elasticity for the two components.

Combining with equations (13), (14), and (15):

$$\frac{E_1 A_1 \Delta Y_1}{H} = \frac{E_2 A_2 \Delta Y_2}{H} \quad (16)$$

Cancelling H's and combining with equation (10):

$$E_1 A_1 (L + \Delta X_1 - H) = E_2 A_2 (H - L - \Delta X_2) \quad (17)$$

and combining with equations (6) and (7):

$$E_1 A_1 (L + \alpha_1 L \Delta T - H) = E_2 A_2 (H - L - \alpha_2 L \Delta T) \quad (18)$$

Substituting equation (11) to give a function of α_3 in place of H:

$$E_1 A_1 (L + \alpha_1 L \Delta T - L - \alpha_3 L \Delta T) = E_2 A_2 (L + \alpha_3 L \Delta T - L - \alpha_2 L \Delta T) \quad (19)$$

Combining L's and multiplying throughout by $L \Delta T$:

$$E_1 A_1 = (\alpha_1 - \alpha_3) = E_2 A_2 (\alpha_3 - \alpha_2) \quad (19a)$$

and rearranging:

$$E_1 A_1 \alpha_1 - E_1 A_1 \alpha_3 = E_2 A_2 \alpha_3 - E_2 A_2 \alpha_2 \quad (19b)$$

$$E_1 A_1 \alpha_1 + E_2 A_2 \alpha_2 = E_1 A_1 \alpha_3 + E_2 A_2 \alpha_3 \quad (19c)$$

$$\alpha_3 = \frac{E_1 A_1 \alpha_1 + E_2 A_2 \alpha_2}{E_1 A_1 + E_2 A_2} \quad (19d)$$

Dividing through by $(A_1 - A_2)$ and applying equations (3) and (4):

$$\alpha_3 = \frac{E_1 N \alpha_1 + E_2 (1 - N) \alpha_2}{E_1 N + E_2 (1 - N)} \quad (20)$$

Equation (20) can also be solved for N by the following manipulations:

$$E_1 N \alpha_3 + E_2 (1 - N) \alpha_3 = E_1 N \alpha_1 + E_2 (1 - N) \alpha_2 \quad (20a)$$

$$E_1 N \alpha_1 = E_1 N \alpha_3 = E_2 (1 - N) \alpha_2 \quad (20b)$$

$$E_1 N (\alpha_1 - \alpha_3) = E_2 (1 - N) (\alpha_3 - \alpha_2) \quad (20c)$$

$$E_1 N (\alpha_1 - \alpha_3) + N E_2 (\alpha_3 - \alpha_2) = E_2 (\alpha_3 - \alpha_2) \quad (20d)$$

$$N [E_1 (\alpha_1 - \alpha_3) + E_2 (\alpha_3 - \alpha_2)] = E_2 (\alpha_3 - \alpha_2) \quad (20e)$$

$$N = \frac{E_2 (\alpha_3 - \alpha_2)}{E_1 (\alpha_1 - \alpha_3) + E_2 (\alpha_3 - \alpha_2)} \quad (20f)$$

Note that, although the equations are derived assuming that a linear stress-strain relationship is present for each of the composite components, the derivation may be applicable to materials which do not exhibit such properties. For example, a brittle material which possesses compressive strength but little or no tensile strength (a typical vitreous substance) will perform according to the assumptions of the model if it may be considered to be component one of the

derivation, that is, if its coefficient of linear thermal expansion is greater than the other component, and will, therefore, be placed in compression by the action of temperature increase.

In most cases where two materials are being employed with differing thermal expansion coefficients, the glassy material has a lower thermal expansion coefficient than the plastic or metallic companion material, glasses having typically low expansion coefficients. Fortunately, in the application of this model, the same situation which makes the assumptions inept, often also makes the material itself inept: When the ceramic is placed in tension it fails when the Hooke's law region is exceeded, so that materials which might not fit the previous assumptions might also be poor materials of construction.

Prestressing has been used to eliminate this objection, recently by application of external mechanical stresses and, from antiquity, through the application of the natural stresses which occur as the composite pieces cool after firing. This process imposes thermal contractile forces which shrink the first component more than the glassy second component, placing the glassy substance in mechanical compression and the other component in tension. The effect of this prestress is to keep the vitreous substance in compression so that it can exhibit strength, until the forming temperature is exceeded. (Usually this is also the sintering temperature and an upper limit on the strength of the piece due to viscous-flow failure, so the lack of strength above the forming temperature is not a handicap.)

For purposes of checking the derived equations, three composite samples of selected proportions were prepared from E glass fiber and an epoxy resin. Samples were prepared from 1.94, 31.85, and 28.03 weight percent glass fiber for thermal expansion measurements. The results of these measurements were as follows:

1.94% fiber - 73.20×10^{-6} in/in/°C
 31.85% fiber - 11.10×10^{-6} in/in/°C
 28.03% fiber - 10.50×10^{-6} in/in/°C

The thermal expansion coefficient of the glass is 5.9×10^{-6} in/in/°C and 105×10^{-6} in/in/°C for the resin system (Genamide 2000 and Epon 815). The density is 2.55 g/cc for the glass and 1.2 g/cc for the resin system. Young's modulus is 10.5×10^6 psi for E glass and 0.35×10^6 psi for the resin system.

Substituting the above values into the equation derived the coefficients of expansion for composites containing 1.94, 31.85, and 28.03% fiber as follows:

$$\alpha_c = \frac{E_g N \alpha_g + E_r (1-N) \alpha_r}{E_g N + E_r (1-N)} \quad (21)$$

where α_c = the coefficient of thermal expansion of the composite, α_g and α_r = the coefficient of thermal expansion for constituents g and r (where g is the E glass and r is the resin), E = Young's modulus, N = volume percent of glass.

1) for 1.94 weight percent fiber

$$N = 0.01 \quad 1-N = .99$$

$$\alpha_g = 5.9 \times 10^{-6} \text{ in/in/}^\circ\text{C} \quad \alpha_r = 105 \times 10^{-6} \text{ in/in/}^\circ\text{C}$$

$$E_g = 10.5 \times 10^6 \text{ psi} \quad E_r = .35 \times 10^6 \text{ psi}$$

$$\begin{aligned} \alpha_c &= \frac{(10.5 \times 10^6)(.01)(5.9 \times 10^{-6}) + (.35 \times 10^6)(.99)(105 \times 10^{-6})}{(10.5 \times 10^6)(.01) + (.99)(.35 \times 10^6)} \\ &= \frac{.105 \times (5.9 \times 10^{-6}) + .3465(105 \times 10^{-6})}{.105 \times 3465} \\ &= \frac{.62 \times 10^{-6} + 36.4 \times 10^{-6}}{.4515} \end{aligned}$$

$$\alpha_c = \frac{37.02 \times 10^{-6}}{.4518} = 82 \times 10^{-6} \text{ in/in/}^\circ\text{C} \quad (22)$$

The experimentally measured value was $73 \times 10^{-6} \text{ in/in/}^\circ\text{C}$.

2) for 28.03 weight percent

$$N = .155 \quad 1-N = .845$$

$$\alpha_c = \frac{(10.5 \times 10^6)(5.9 \times 10^{-6})(.155) + (.35 \times 10^6)(105 \times 10^{-6})(.845)}{(10.5 \times 10^6)(.15) + (.35 \times 10^6)(.845)}$$

$$\alpha_c = \frac{62 \times 10^{-6} (.155) + 36.7 \times 10^{-6} (.845)}{1.58 + .296}$$

$$\alpha_c = \frac{9.6 \times 10^{-6} + 31 \times 10^{-6}}{1.876} = \frac{40.6 \times 10^{-6}}{1.876}$$

$$\alpha_c = 21.6 \times 10^{-6} \text{ in/in/}^\circ\text{C} \quad (23)$$

The experimentally measured value was $15.5 \times 10^{-6} \text{ in/in/}^\circ\text{C}$.

3) for 31.85 weight percent fiber

$$N = .18 \quad 1-N = .82$$

$$\alpha_c = \frac{(10.5 \times 10^6)(5.9 \times 10^{-6})(.18) + (.35 \times 10^6)(105 \times 10^{-6})(.82)}{(10.5 \times 10^6)(.18) + (.82)(.35 \times 10^6)}$$

$$\alpha_c = \frac{(62 \times 10^{-6})(.18) + (36.7 \times 10^{-6})(.82)}{1.89 + 2.86}$$

$$\alpha_c = \frac{11.13 \times 10^{-6} + 30 \times 10^{-6}}{2.176} = \frac{41.13 \times 10^{-6}}{2.176}$$

$$\alpha_c = 19 \times 10^{-6} \text{ in/in/}^\circ\text{C.} \quad (24)$$

The experimentally measured value was $11 \times 10^{-6} \text{ in/in/}^\circ\text{C.}$

The thermal expansion coefficient values calculated for the glass resin composites were consistently higher than the measured values by approximately $7.5 \times 10^{-6} \text{ in/in/}^\circ\text{C.}$ The nature of the discrepancy between the calculated and measured values would suggest that this difference is due to an error in the experimental method employed in the expansion determinations. This could not be verified due to the subsequent disassembly of the equipment. However, it does appear that the equations derived for the expansion coefficient provide reasonable working approximations.

APPENDIX IV
EVALUATION OF CANDIDATE ABLATIVE MATERIALS DATA
FOR X-15 APPLICATION

Included in this appendix are the data from the evaluation of candidate ablative materials for X-15 application in the arc-plasma-jet. These data consist of: test duration, decrease in specimen weight, depth of erosion, and final front and back surface temperatures, as well as substrate temperature-time histories for each test. Post-test specimen photographs are also included.

A discussion of these test results is included in the text of this report (pages 82 to 86).

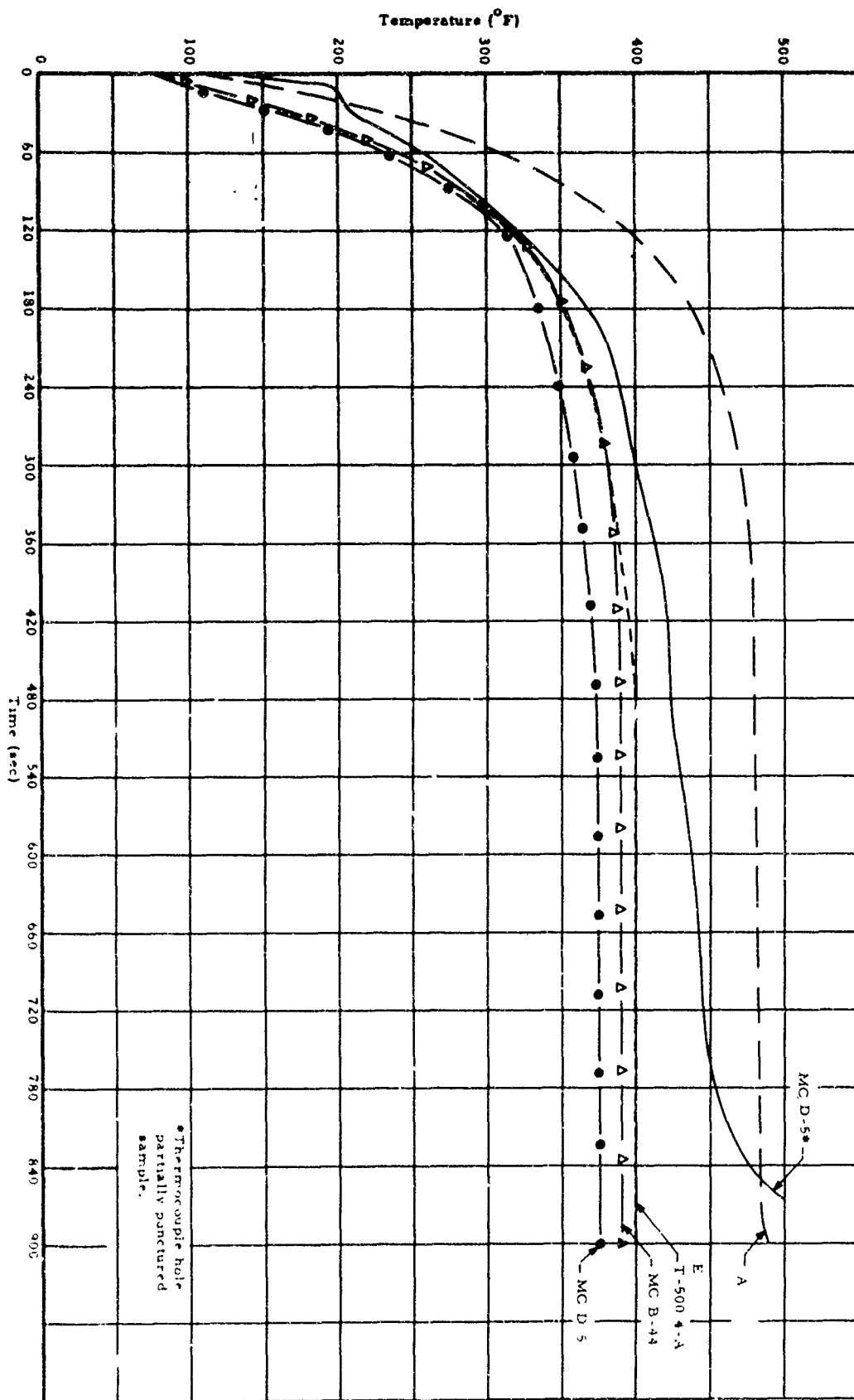


Figure 66. Substrate Temperature-Time History of Various Materials Exposed to 15 Btu/ft² sec Heat Flux Environment. Ablative Material Thickness Nominally 50 mils. Thermocouple Located Within Approximately 10 mils of Bondline, Unless Otherwise Noted

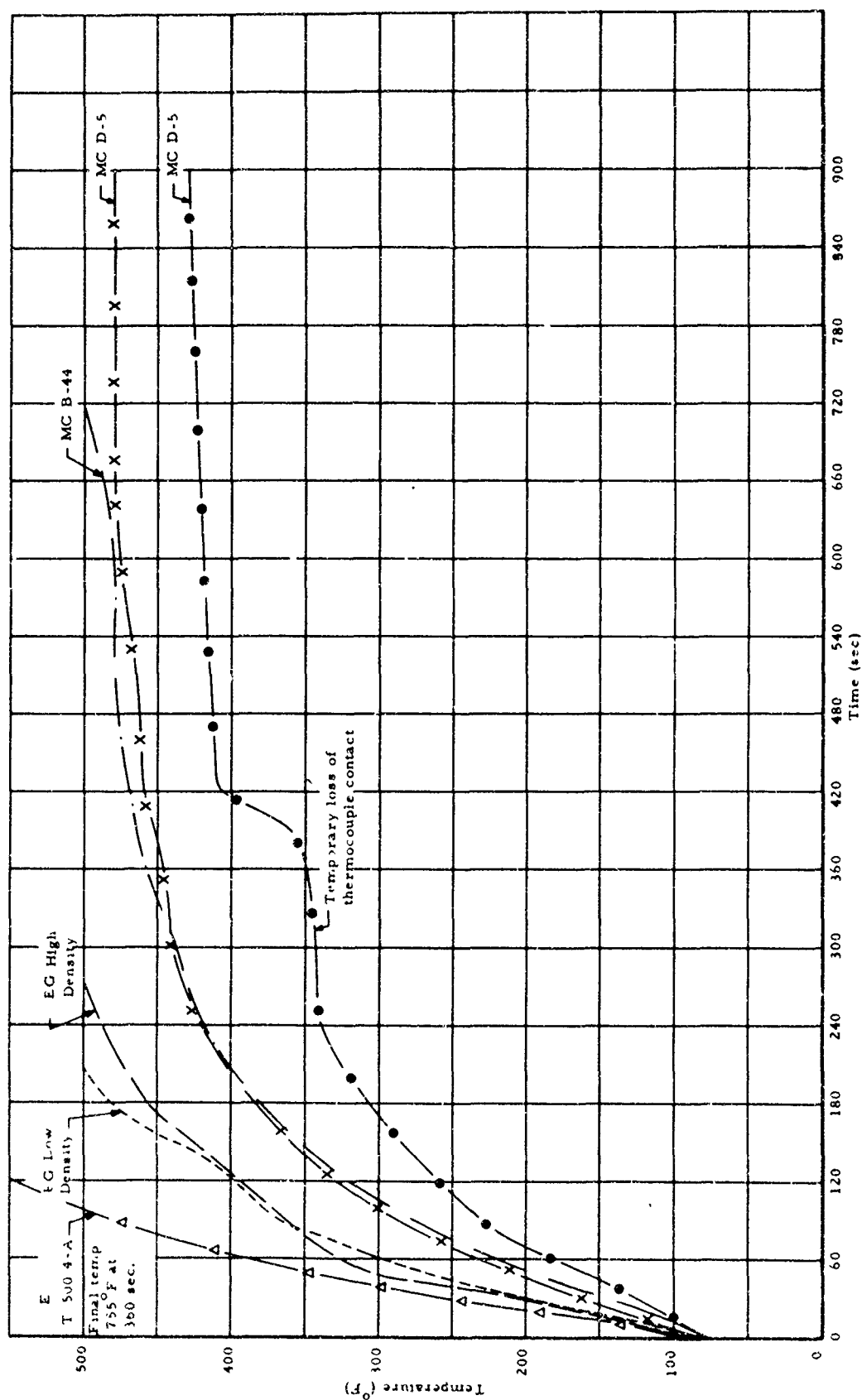


Figure 67. Substrate Temperature-Time History of Various Materials Exposed to 40 Btu/ft² sec Heat Flux Environment. Ablative Material Thickness Nominally 50 mils. Thermocouple Located Within Approximately 10 mils of Bondline

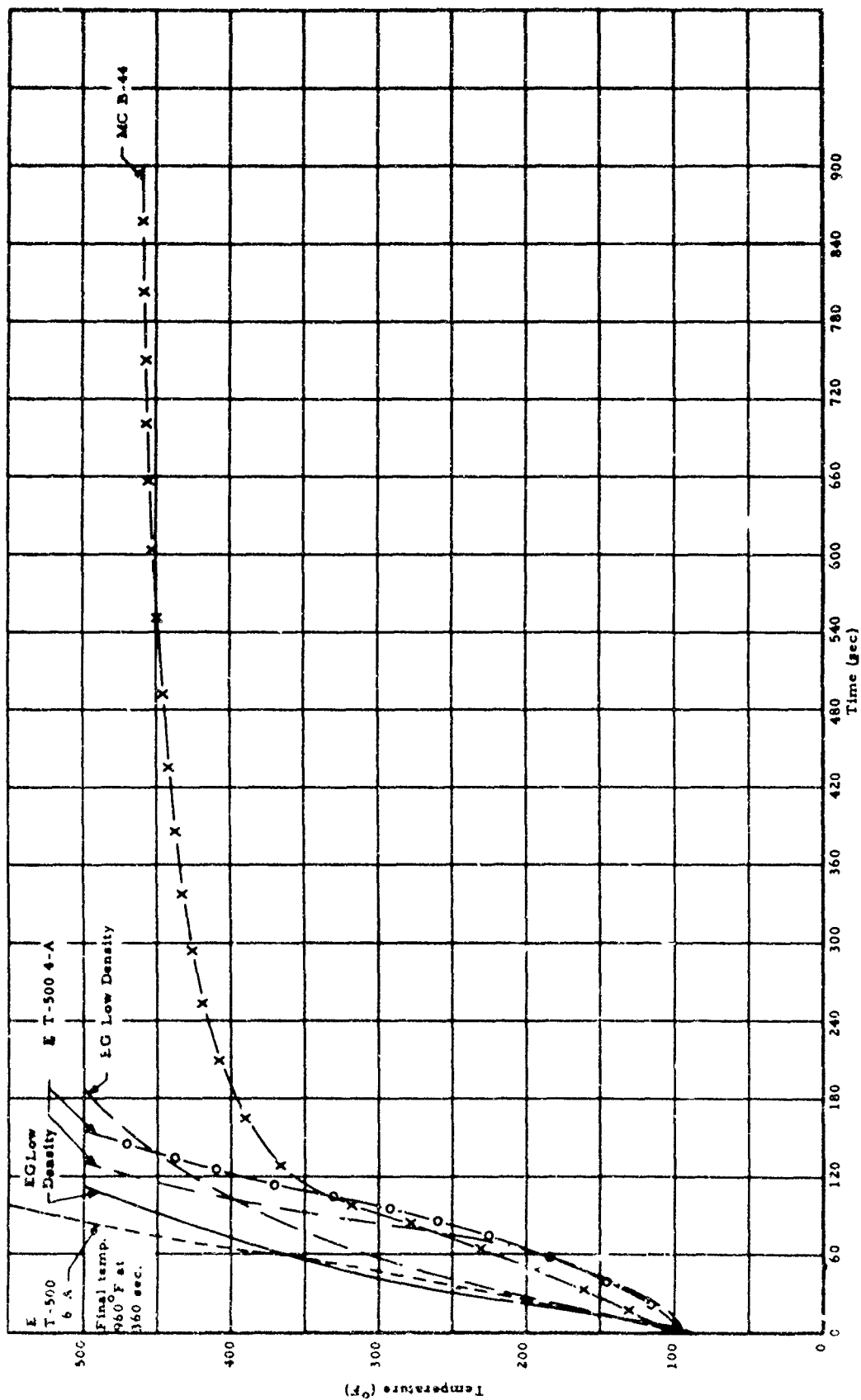


Figure 68. Substrate Temperature-Time History of Various Materials Exposed to 40 Btu/ft² sec Heat Flux Environment. Ablative Material Thickness Nominally 50 mils. Thermocouple Located Within Approximately 10 mil

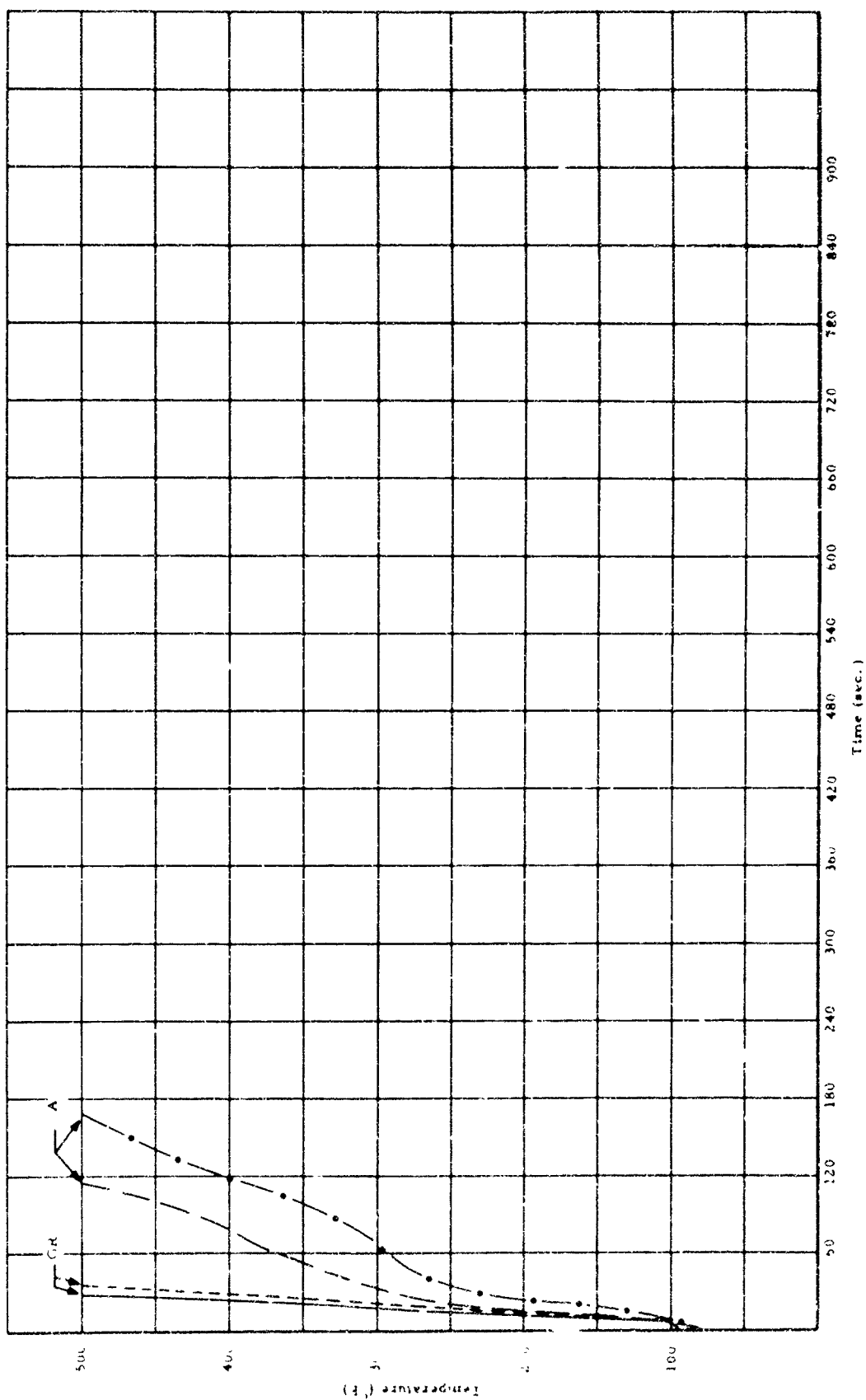


Figure 69. Substrate Temperature-Time History of Various Materials Exposed to 40 Btu/ft² sec Heat Flux Environment. Ablative Material Thickness Nominally 50 mil. Thermocouple Located Within Approximately 10 mils of Bondline, Unless Otherwise Noted

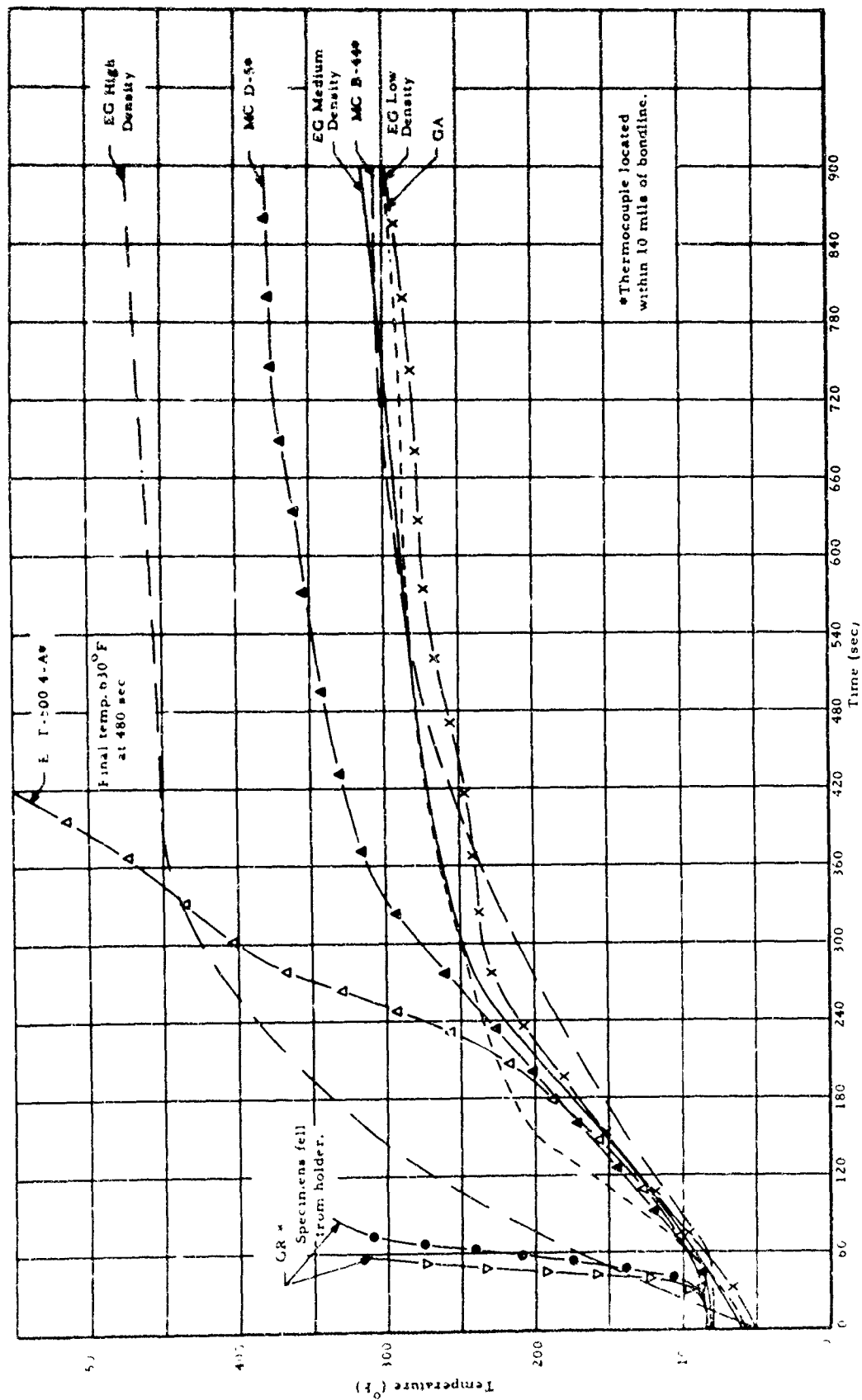


Figure 70. Substrate Temperature-Time History of Various Materials Exposed to 40 Btu/ft² sec Heat Flux Environment. Ablative Material Thickness Nominally 1/4 Inch. Thermocouple Located on Back Surface of Substrate, Unless Otherwise Noted

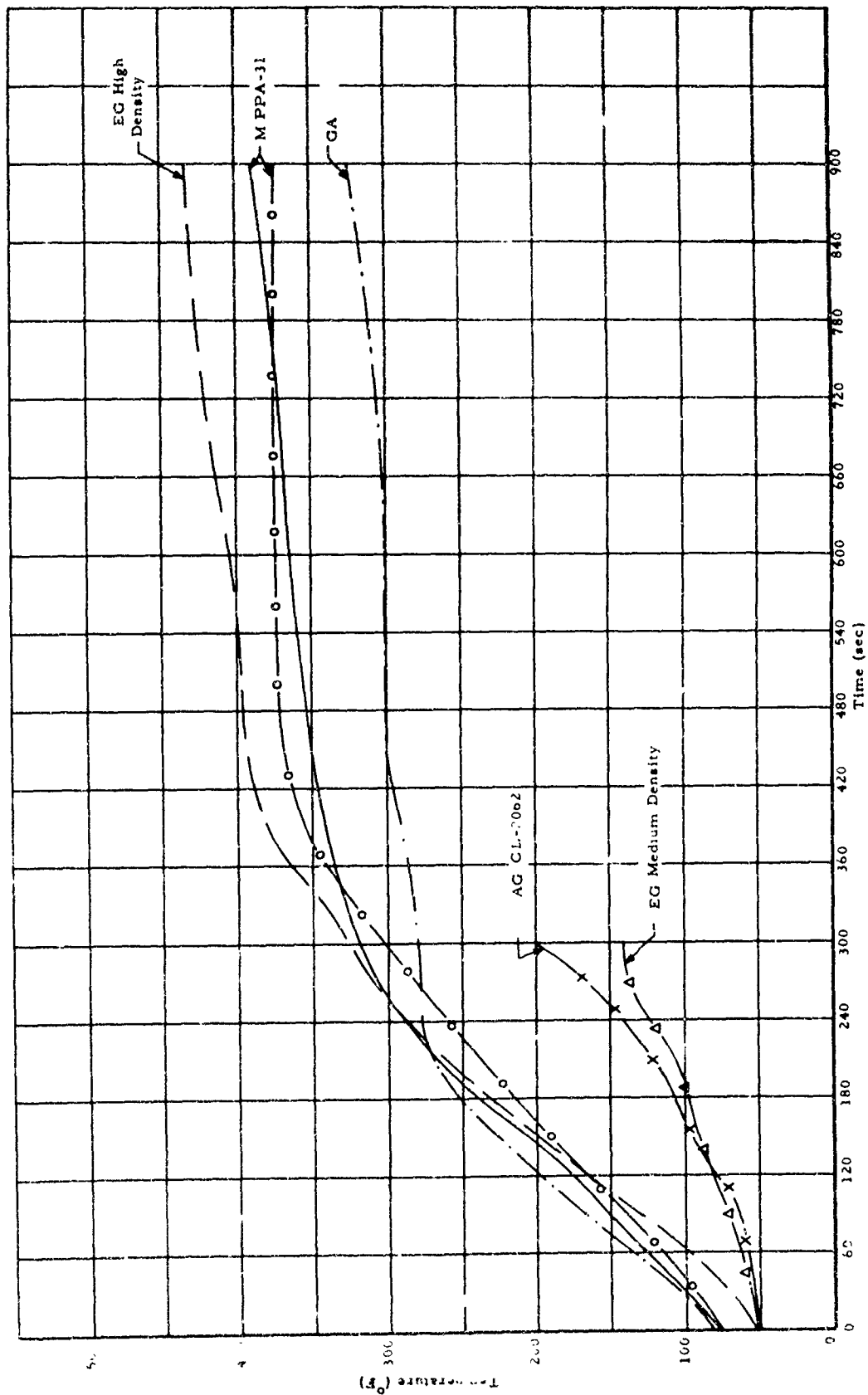


Figure 71. Substrate Temperature-Time History of Various Materials Exposed to 40 Btu/ft² sec Heat Flux Environment. Ablative Material Thickness Nominally 3/8 Inch. Thermocouple Located on Back Surface of Substrate

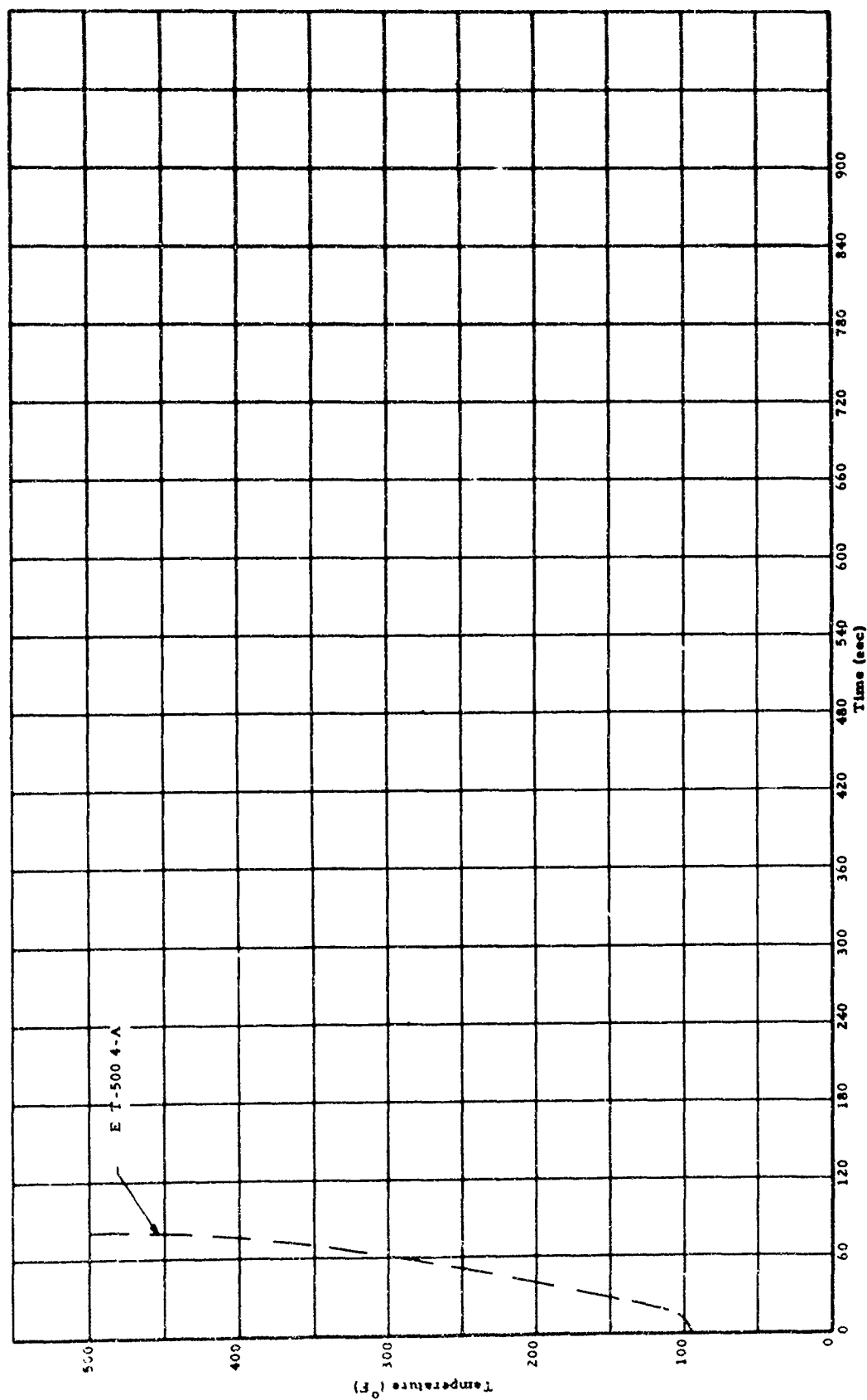


Figure 72. Substrate Temperature-Time History of Emerson Electric T-500 4-A Exposed to 150 Btu/ft² sec Heat Flux Environment. Ablative Material Thickness Nominally 50 mils. Thermocouple Located Within Approximately 10 mils of Bondline

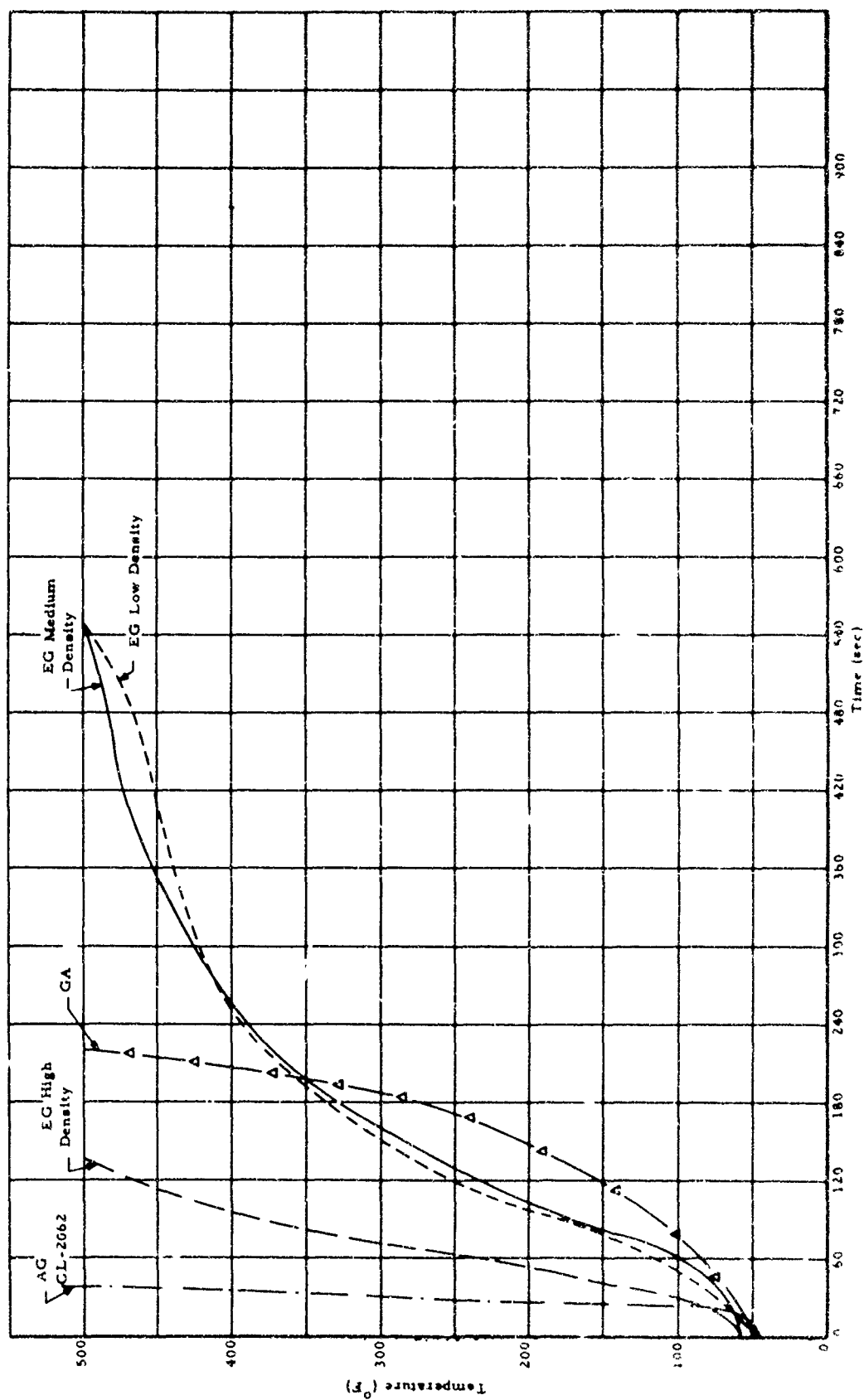


Figure 73. Substrate Temperature-Time History of Various Materials Exposed to 150 Btu/ft² sec Heat Flux Environment. Ablative Material Thickness Nominally 1/4 Inch. Thermocouple Located on Back Surface of Substrate

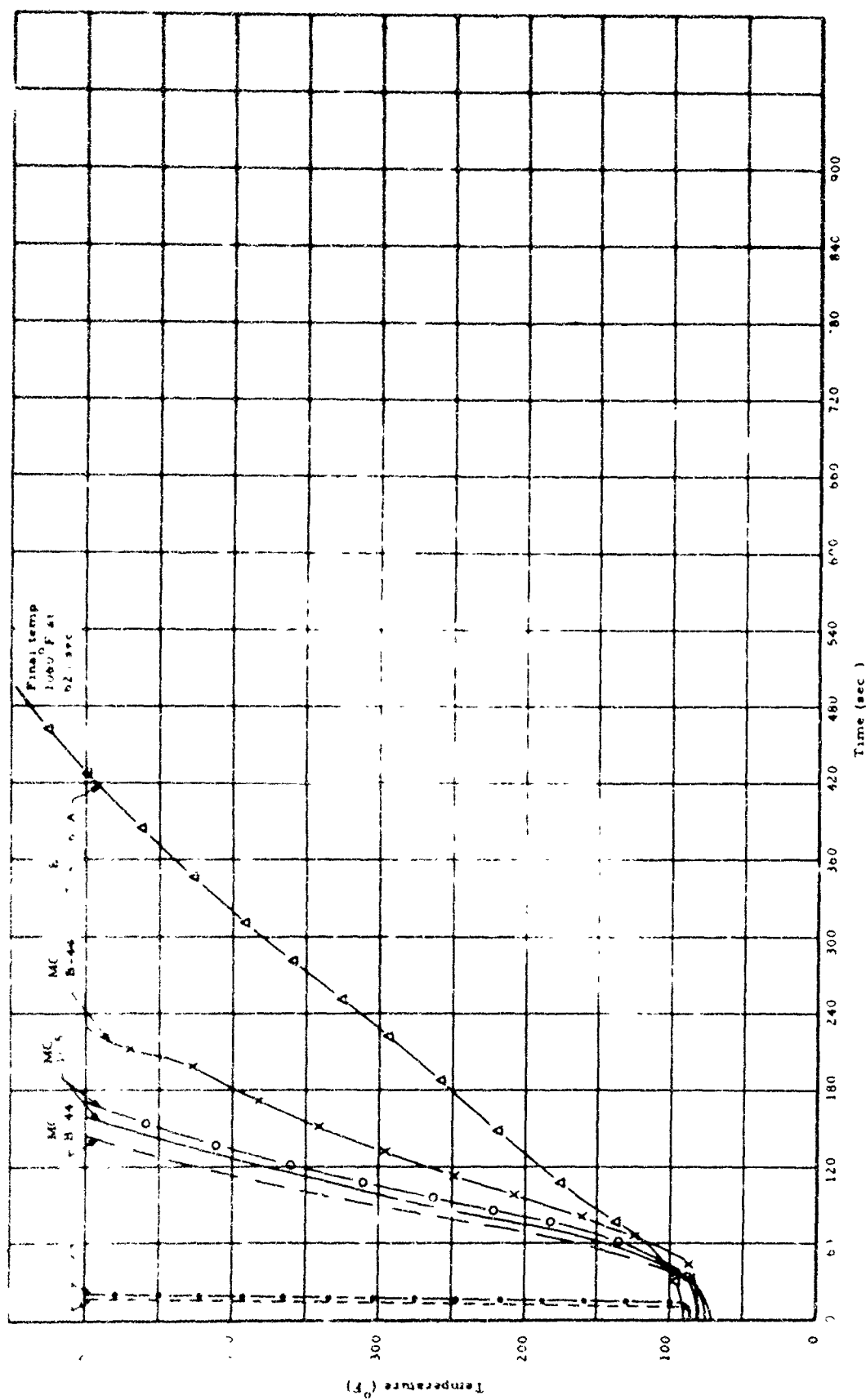


Figure 74. Substrate Temperature-Time History of Various Materials Exposed to 150 Btu/ft² sec Heat Flux Environment. Ablative Material Thickness Nominally 1/4 Inch. Thermocouple Located Within Approximately 10 mils of Bondline, Unless Otherwise Noted

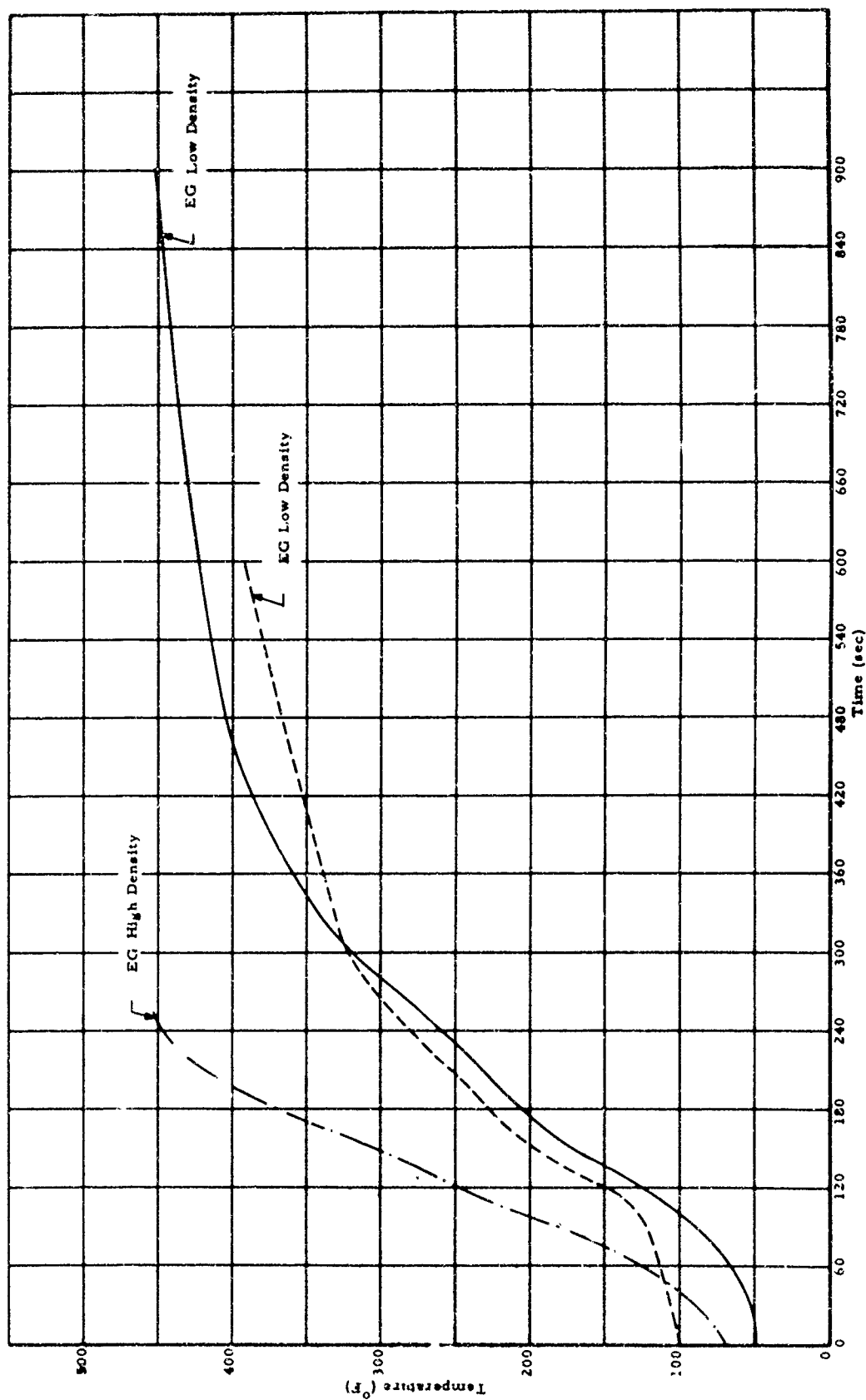


Figure 75. Substrate Temperature-Time History of Various Materials Exposed to 150 Btu/ft² sec Heat Flux Environment. Ablative Material Thickness Nominally 3/8 Inch. Thermocouple Located on Back of Substrate

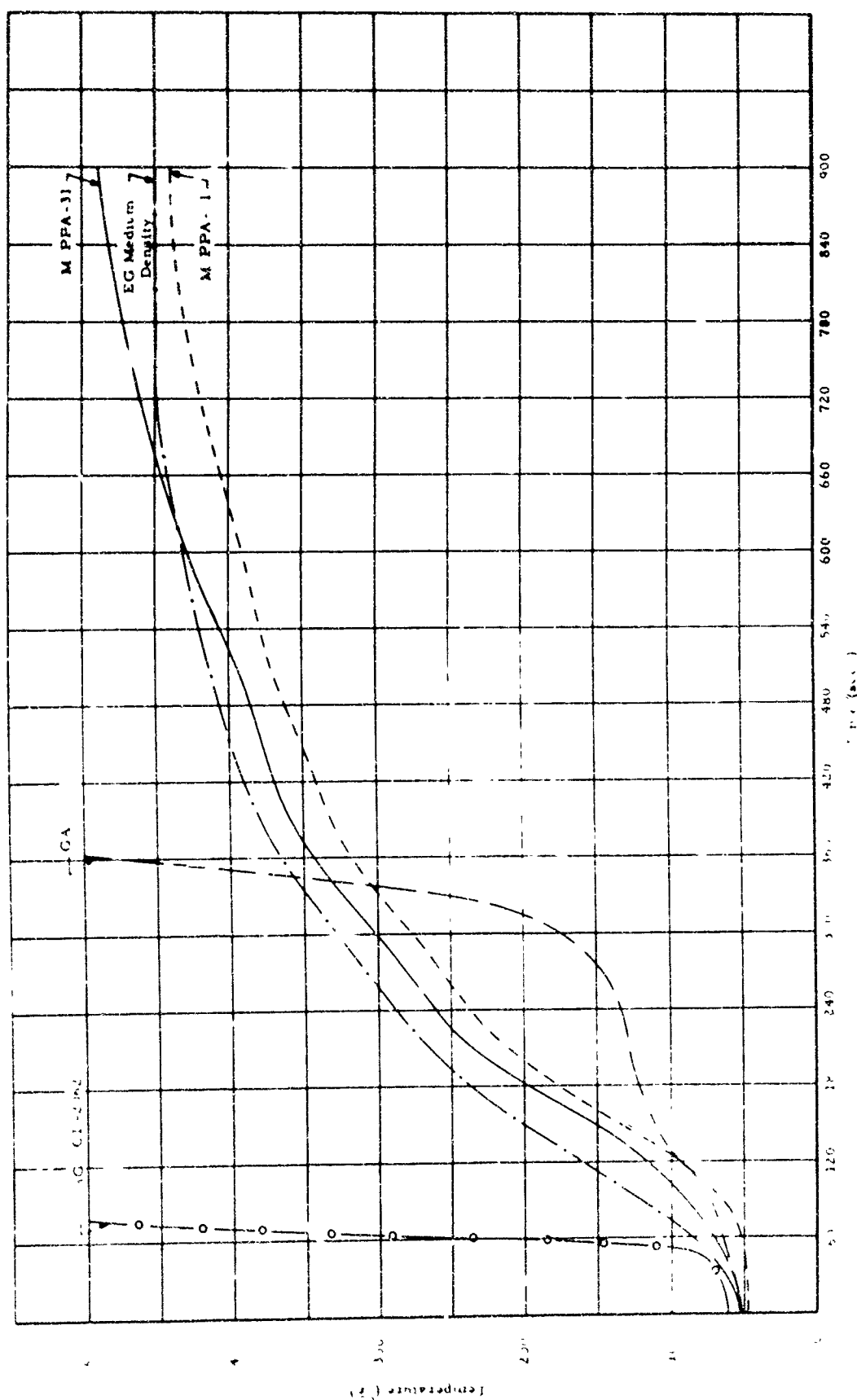


Figure 76. Substrate Temperature-Time History of Various Materials Exposed to 150 Btu/ft² sec Heat Flux Environment. Ablative Material Thickness Nominally 3/8 Inch. Thermocouple Located on Back Surface of Substrate, Unless Otherwise Noted

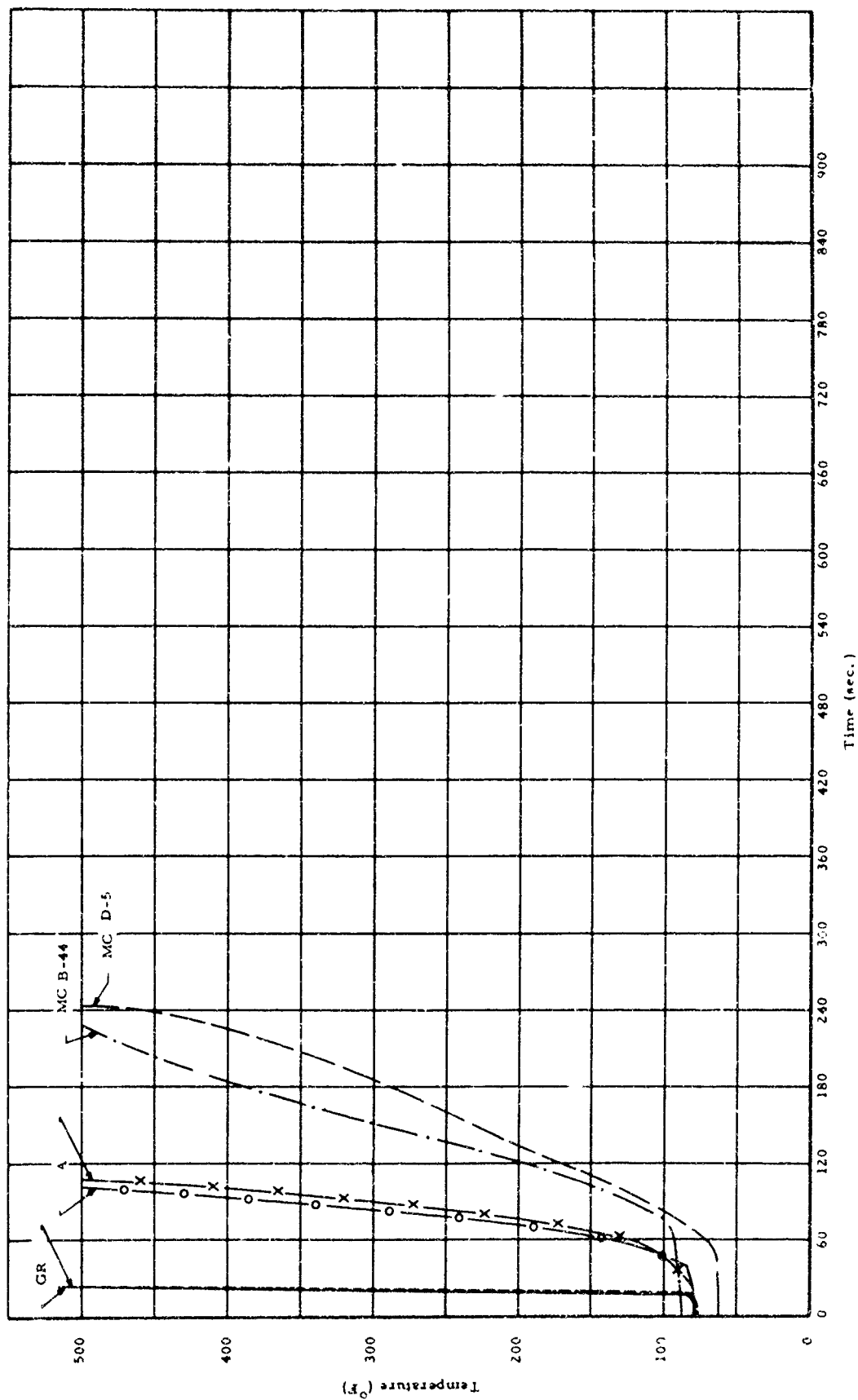


Figure 77. Substrate Temperature-Time History of Various Materials Exposed to 150 Btu/ft² sec Heat Flux Environment. Ablative Material Thickness Nominally 3/8 Inch. Thermocouple Located Within Approximately 10 mils of Bondline, Unless Otherwise Noted

Table 40. Results of Manufacturer AG Filled Epoxy Formulation Exposed to Arc-Plasma-Jet Effluent

Test Duration (sec)		300	39*	78**
Decrease in Weight	Gms	15.1	12.5	21.5
	%	62.1	86.7	87.4
Depth of Erosion (in.)		0.218	0.219	Burnthrough
Final Back Face Temp °F		200	520	500
Final Front Face Temp °F		2130	--	2860
Remarks		Heat Flux: 40 Btu/ft ² sec Sample Thickness: 3/8 in.		
Sample Appearance		Heat Flux: 150 Btu/ft ² sec Sample Thickness: #1/4 in. **3/8 in.		

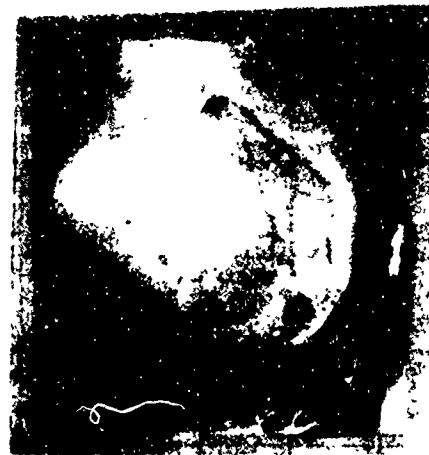


Table 41. Results of Manufacturer A Fibrous Ablative Composite Exposed to Arc-Plasma-Jet Effluent



Test Duration (sec)		900	176	113
Decrease in Weight	Gms	0.2	2.1	1.3
	%	6.7	70.0	44.4
Depth of Erosion (in.)		0.002	Burnthrough	0.035
Final Back Face Temp °F		490	500	500
Final Front Face Temp °F		1695	1920	1905
Remarks		Heat Flux: 15 Btu/ft ² sec Sample Thickness: 50 mil	Heat Flux: 40 Btu/ft ² sec Sample Thickness: 50 mil	
Sample Appearance				

Table 42. Results of Manufacturer A Fibrous Ablative Composite Exposed to Arc-Plasma-Jet Effluent

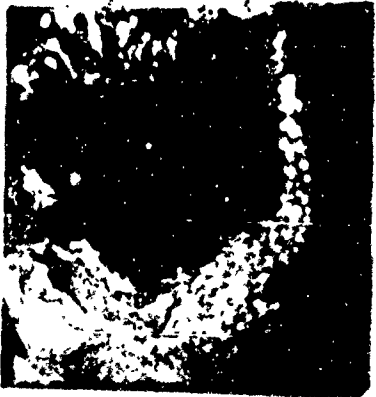

Test Duration (sec)	101		107
Decrease in Weight	Gms	7.4	7.7
	%	51.6	54.6
Depth of Erosion (in.)	0.369		0.377
Final Back Face Temp °F	500		500
Final Front Face Temp °F	2795		2830
Remarks	Heat Flux: 150 Btu/ft ² sec Sample Thickness: 3/8 in.		Heat Flux: 150 Btu/ft ² sec Sample Thickness: 3/8 in.
Sample Appearance			

Table 43. Results of Manufacturer E Subliming Epoxy Exposed to Arc-Plasma-Jet Effluent


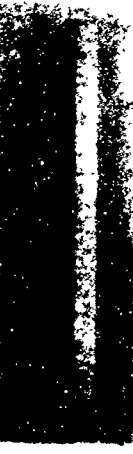

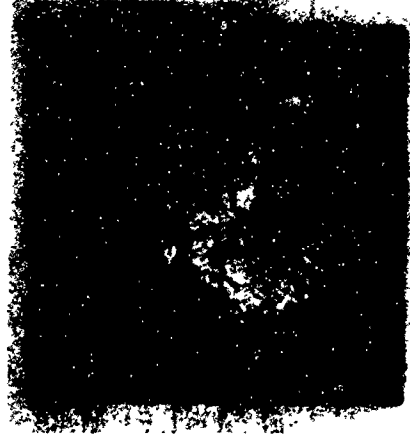
Test Duration (sec)		900	83
Decrease in Weight	Gms	0.5	4.3
	%	8.1	60.1
Depth of Erosion (in.)		0.006	0.013
Final Back Face Temp °F		400	500
Final Front Face Temp °F		1570	2785
Remarks	Heat Flux: 15 Btu/ft ² sec Sample Thickness: 50 mil		Heat Flux: 150 Btu/ft ² sec Sample Thickness: 50 mil
			
Sample Appearance			

Table 44. Results of Manufacturer E Subliming Epoxy Exposed to Arc-Plasma-Jet Effluent




Test Duration (sec)	132	156	360*	480**
Decrease in Weight	Gms 2.6	Gms 1.5	2.9	12.7
	% 31.8	% 20.8	53.9	68.9
Depth of Erosion (in.)	Burnthrough	Burnthrough	Burnthrough	Burnthrough
Final Back Face Temp °F	500	500	755	630
Final Front Face Temp °F	1715	1625	1690	1780
Remarks	Heat Flux: 40 Btu/ft ² /sec Sample Thickness: 50 mil 			
Sample Appearance				
				

Table 45. Results of Manufacturer E Subliming Epoxy Exposed to Arc-Plasma-Jet Effluent



Test Duration (sec)		360	620
Decrease in Weight	Gms	4.8	15.6
	%	79.2	59.9
Depth of Erosion (in.)		0.048	Burnthrough
Final Back Face Temp °F		960	1060
Final Front Face Temp °F		1740	2680
Remarks		Heat Flux: 40 Btu/ft ² sec Sample Thickness: 50 mil	Heat Flux: 150 Btu/ft ² sec Sample Thickness: 1/4 in.
Sample Appearance			

Table 46. Results of Manufacturer EG Low Density Silicone Elastomer in Honeycomb
Exposed to Arc-Plasma-Jet Effluent




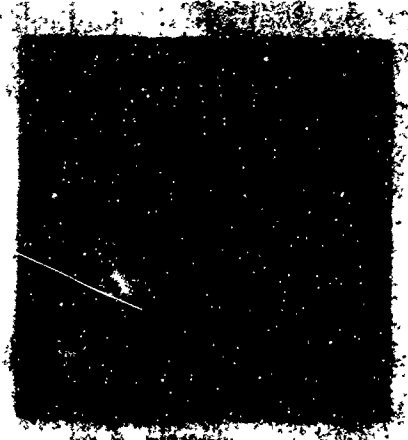
Test Duration (sec)		188	113
Decrease in Weight	Gms	0.5	0.5
	%	22.5	20.3
Depth of Erosion (in.)		0.035	0.027
Final Back Face Temp °F		500	500
Final Front Face Temp °F		1600	1785
Remarks		Heat Flux: 40 Btu/ft ² sec Sample Thickness: 50 mil	Heat Flux: 40 Btu/ft ² sec Sample Thickness: 50 mil
			
Sample Appearance			

Table 47. Results of Manufacturer EG Low Density Silicone Elastomer in Honeycomb
Exposed to Arc-Plasma-Jet Effluent





Test Duration (sec)		900	544
Decrease in Weight	Gms	2.9	2.9
	%	22.8	21.7
Depth of Erosion (in.)		0.008	Incr. 0.011
Final Back Face Temp °F		300	500
Final Front Face Temp °F		1760	2740
Remarks		Heat Flux: 40 Btu/ft ² sec Sample Thickness: 1/4 in.	Heat Flux: 150 Btu/ft ² sec Sample Thickness: 1/4 in.
			
Sample Appearance			

Table 4d. Results of Manufacturer EG Low Density Silicone Elastomer in Honeycomb
Exposed to A-c-Plasma-Jet Effluent




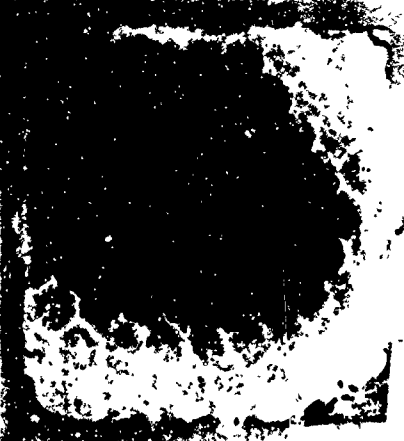
Test Duration (sec)		600	900
Decrease in Weight	Gms	4.0	4.0
	%	21.3	21.7
Depth of Erosion (in.)		Incr. 0.002	Incr. 0.004
Final Back Face Temp °F		395	455
Final Front Face Temp °F		2685	2805
Remarks	Heat Flux: 150 Btu/ft ² sec Sample Thickness: 3/8 in.		Heat Flux: 150 Btu/ft ² sec Sample Thickness: 3/8 in.
			
Sample Appearance			

Table 49. Results of Manufacturer EG Low Density Silicone Elastomer Without Honeycomb Exposed to Arc-Plasma-Jet Effluent


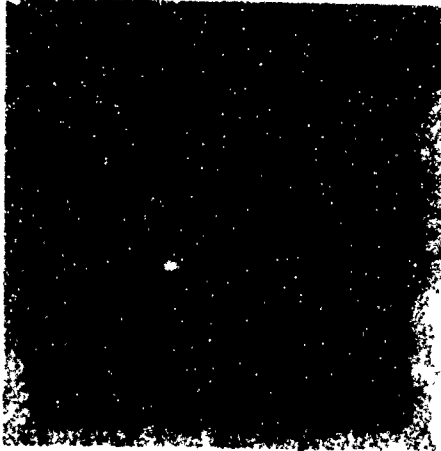
Test Duration (sec)		207
Decrease in Weight	Gms	0.5
	%	21.5
Depth of Erosion (in.)		0.019
Final Back Face Temp °F		500
Final Front Face Temp °F		1780
Remarks		Heat Flux: 40 Btu/ft ² sec Sample Thickness: 50 mil
		
Sample Appearance		

Table 50. Results of Manufacturer EG Medium Density Silicone Elastomer in Honeycomb
Exposed to Arc-Plasma-Jet Effluent





Test Duration (sec)		900	300
Decrease in Weight	Cms	2.9	2.7
	%	19.2	12.5
Depth of Erosion (in.)		Incr. 0.004	Incr. 0.015
Final Back Face Temp °F		315	140
Final Front Face Temp °F		1740	--
Remarks	Heat Flux: 40 Btu/ft ² sec Sample Thickness: 1/4 in.		Heat Flux: 40 Btu/ft ² sec Sample Thickness: 3/8 in.
			
Sample Appearance			

Table 51. Results of Manufacturer EG Medium Density Silicone Elastomer in Honeycomb
Exposed to Arc-Plasma-Jet Effluent



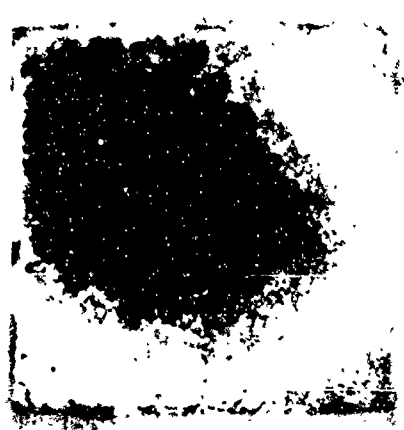

Test Duration (sec)		546	900
Decrease in Weight	Gms	3.0	3.5
	%	18.4	17.0
Depth of Erosion (in.)		Incr. 0.004	Incr. 0.009
Final Back Face Temp °F		500	450
Final Front Face Temp °F		2750	2820
Remarks	Heat Flux: 150 Btu/ft ² sec Sample Thickness: 1/4 in.		Heat Flux: 150 Btu/ft ² sec Sample Thickness: 3/8 in.
			
Sample Appearance			

Table 52. Results of Manufacturer EG High Density Silicone Elastomer in Honeycomb
Exposed to Arc-Plasma-Jet Effluent

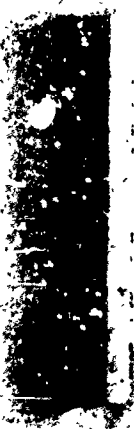
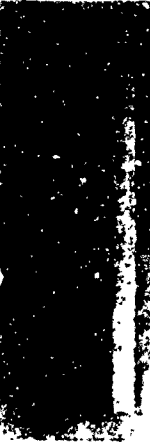

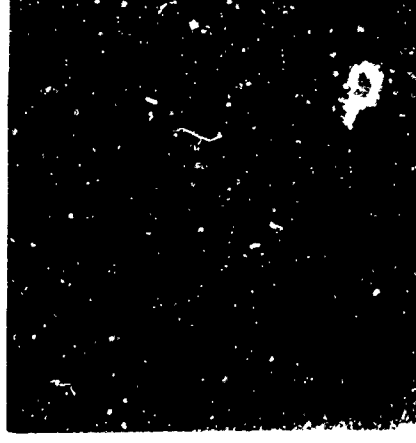
Test Duration (sec)		900	900
Decrease in Weight	Gms	6.1	7.4
	%	31.8	28.6
Depth of Erosion (in.)		Incr. 0.01E	Incr. 0.011
Final Back Face Temp °F		475	435
Final Front Face Temp °F		1785	1780
Remarks		Heat Flux: 40 Btu/ft ² sec Sample Thickness: 1/4 in.	Heat Flux: 40 Btu/ft ² sec Sample Thickness: 3/8 in.
			
Sample Appearance			

Table 53. Results of Manufacturer EG High Density Silicone Elastomer in Honeycomb
Exposed to Arc-Plasma-Jet Effluent

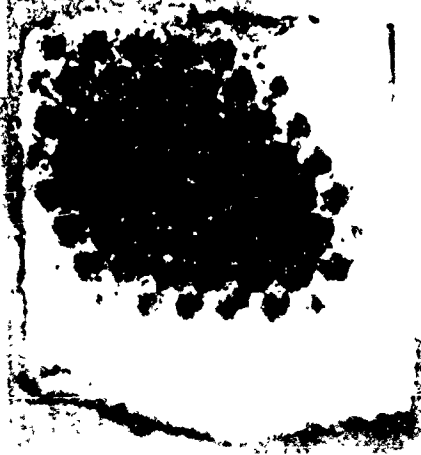

Test Duration (sec)		136	256
Decrease in Weight	Gms	3.7	6.5
	%	22.7	25.4
Depth of Erosion (in.)		Incr. 0.095	Incr. 0.113
Final Back Face Temp °F		500	455
Final Front Face Temp °F		2830	2870
Remarks		Heat Flux: 150 Btu/ft ² sec Sample Thickness: 1/4 in.	
			
Sample Appearance		Heat Flux: 150 Btu/ft ² sec Sample Thickness: 3/8 in.	
			

Table 54. Results of Manufacturer EG High Density Silicone Elastomer Without Honeycomb Exposed to Arc-Plasma-Jet Effluent


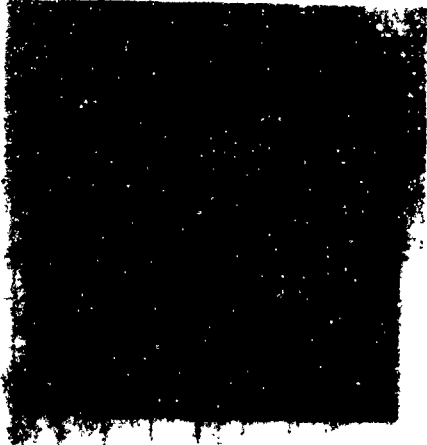
Test Duration (sec)		275
Decrease in Weight	Gms	0.8
	%	24.8
Depth of Erosion (in.)		0.014
Final Back Face Temp °F		500
Final Front Face Temp °F		1740
Remarks		Heat Flux: 40 Btu/ft ² sec Sample Thickness: 50 mil 
Sample Appearance		

Table 55. Results of Manufacturer GR Ablative Polymer Exposed to Arc-Plasma-Jet Effluent

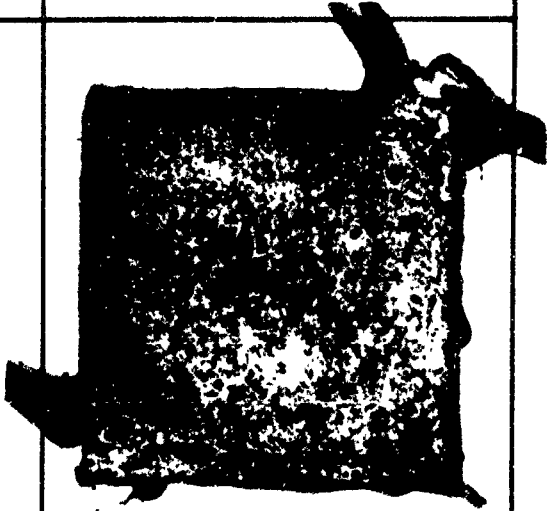

Test Duration (sec)		37	30	94	60
Decrease in Weight	Gms	1.9	2.8	18.0	16.9
	%	31.7	46.7	80.3	79.1
Depth of Erosion (in.)		Burnthrough	Burnthrough	0.232	0.231
Final Back Face Temp °F		500	500	345	320
Final Front Face Temp °F		1610	1600	1615	1635
Remarks		Heat Flux: 40 Btu/ft ² sec Sample Thickness: 50 mil		Heat Flux: 40 Btu/ft ² sec Sample Thickness: 1/4 in. NOTE: Both samples fell from holder during test.	
Sample Appearance					

Table 56. Results of Manufacturer GR Ablative Polymer Exposed to Arc-Plasma-Jet Effluent



Test Duration (sec)		20	18	24	23
Decrease in Weight	Gms	14.8	13.9	18.2	18.6
	%	68.5	62.5	61.8	61.4
Depth of Erosion (in.)		Burnthrough	Burnthrough	Burnthrough	Burnthrough
Final Back Face Temp °F		510	500	540	520
Final Front Face Temp °F		2145	2345	2705	2550
Remarks		Heat Flux: 150 Btu/ft ² sec Sample Thickness: 1/4 in.		Heat Flux: 150 Btu/ft ² sec Sample Thickness: 3/8 in.	
Sample Appearance					

Table 57. Results of Manufacturer GA Ablative Composite Exposed to Arc-Plasma-Jet Effluent

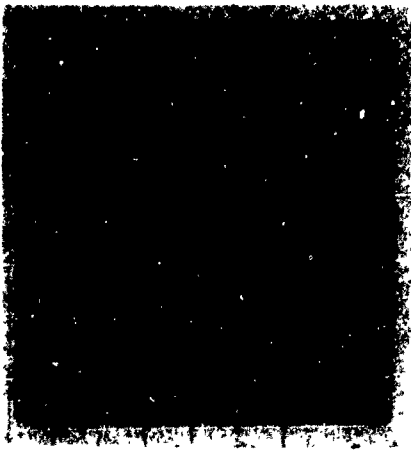
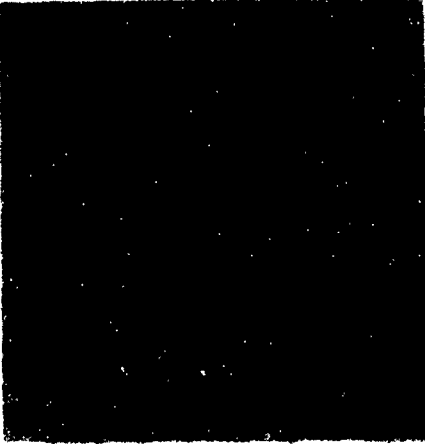
Test Duration (sec)		900	900
Decrease in Weight	Gms	9.1	11.0
	%	35.2	30.8
Depth of Erosion (in.)		Incr. 0.026	Incr. 0.042
Final Back Face Temp °F		300	325
Final Front Face Temp °F		1705	1735
Remarks		Heat Flux: 40 Btu/ft ² sec Sample Thickness: 1/4 in.	Heat Flux: 40 Btu/ft ² sec Sample Thickness: 3/8 in.
Sample Appearance			

Table 58. Results of Manufacturer GA Ablative Composite Exposed to Arc-Plasma-Jet Effluent



Test Duration (sec)		362	224
Decrease in Weight	Gms	13.6	20.9
	%	62.6	59.1
Depth of Erosion (in.)		Burnthrough	Burnthrough
Final Back Face Temp °F		500	500
Final Front Face Temp °F		2705	2860
Remarks		Heat Flux: 150 Btu/ft ² sec Sample Thickness: 1/4 in.	Heat Flux: 150 Btu/ft ² sec Sample Thickness: 3/8 in.
Sample Appearance			

Table 59. Results of Manufacturer M Microballoon Filled Silicone Elastomer in Honeycomb Exposed to Arc-Plasma-Jet Effluent

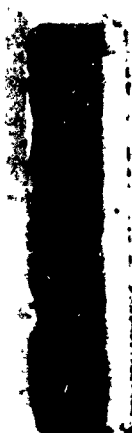

Test Duration (sec)		900	900	900
Decrease in Weight	Gms	4.6	4.6	5.6
	%	30.4	29.6	36.7
Depth of Erosion (in.)		0.014	Incr. 0.005	0.027
Final Back Face Temp °F		370	390	490
Final Front Face Temp °F		2030	2040	2770
Remarks		Heat Flux: 40 Btu/ft ² sec Sample Thickness: 3/8 in.		
				
Sample Appearance		Heat Flux: 150 Btu/ft ² sec Sample Thickness: 3/8 in.		
				

Table 60. Results of Manufacturer MC Silicone Elastomer in Honeycomb Exposed to Arc-Plasma-Jet Effluent



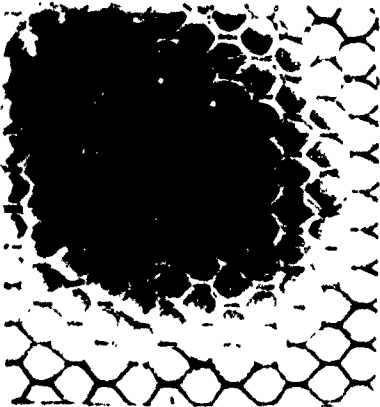
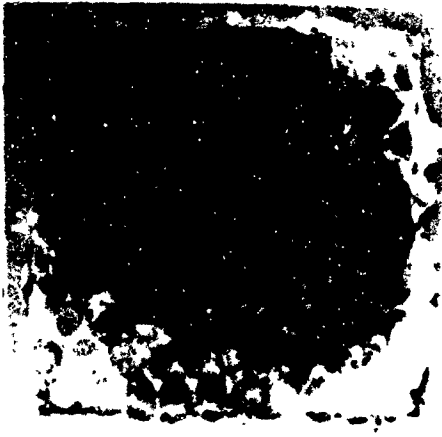


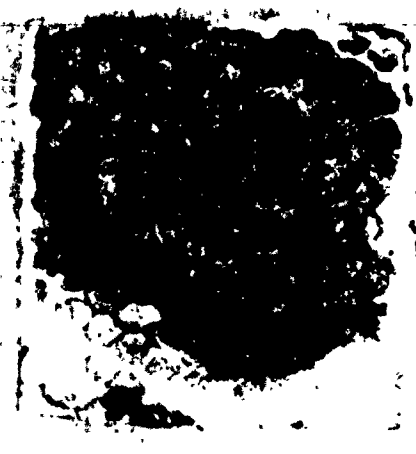
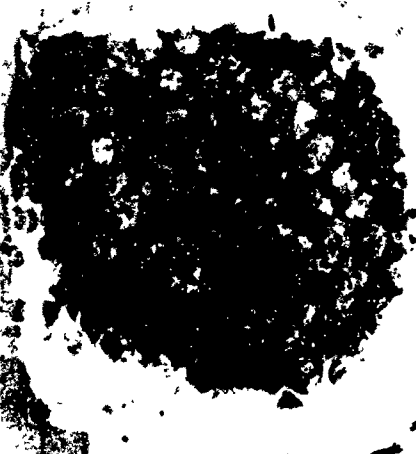
Test Duration (sec)		900	170
Decrease in Weight	Gms	3.6	2.8
	%	23.2	18.8
Depth of Erosion (in.)		Incr. 0.026	Incr. 0.016
Final Back Face Temp °F		380	500
Final Front Face Temp °F		1735	2860
Remarks		Heat Flux: 40 Btu/ft ² sec Sample Thickness: 1/4 in. 	Heat Flux: 150 Btu/ft ² sec Sample Thickness: 1/4 in. 
			
Sample Appearance			

Table 61. Results of Manufacturer MC Silicone Elastomer in Honeycomb Exposed to Arc-Plasma -Jet Effluent

Test Duration (sec)		158	244
Decrease in Weight	Gms	2.4	5.6
	%	16.2	25.1
Depth of Erosion (in.)		Incr. 0.026	Incr. 0.002
Final Back Face Temp °F		500	500
Final Front Face Temp °F		2895	2965
Remarks		Heat Flux: 150 Btu/ft ² sec Sample Thickness: 1/4 in. 	Heat Flux: 150 Btu/ft ² sec Sample Thickness: 3/8 in. 
Sample Appearance			

T. 52. Results of Manufacturer MC Silicone Elastomer Without Honeycomb
Exposed to Arc-Plasma-Jet Effluent


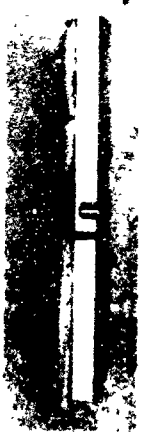
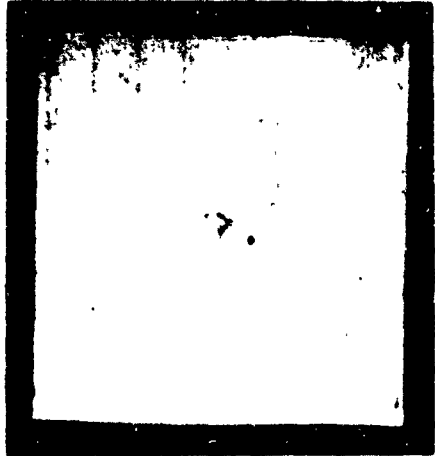

Test Duration (sec)		900	865*	900	900
Decrease in Weight	Gms	0.1	0.1	0.8	0.9
	%	4.0	3.1	27.1	29.7
Depth of Erosion (in.)		0.006	0.016	0.015	Incr. 0.003
Final Back Face Temp °F		370	500	430	489
Final Front Face Temp °F		1915	1915	1895	1875
Remarks		Heat Flux: 15 Btu/ft ² sec Sample Thickness: 50 mil *Thermocouple hole partially punctured sample.		Heat Flux: 40 Btu/ft ² sec Sample Thickness: 50 mil	
					
Sample Appearance					

Table 63. Results of Manufacturer MC Modified Silicone Elastomer in Honeycomb
Exposed to Arc-Plasma-Jet Effluent



Test Duration (sec)		900	143
Decrease in Weight	Gms	5.1	3.1
	%	36.7	22.4
Depth of Erosion (in.)		0.089	0.007
Final Back Face Temp °F		305	500
Final Front Face Temp °F		1715	2805
Remarks		Heat Flux: 40 Btu/ft ² sec Sample Thickness: 1/4 in.	
			
Sample Appearance		Heat Flux: 150 Btu/ft ² sec Sample Thickness: 1/4 in.	
			

Table 64. Results of Manufacturer MC Modified Silicone Elastomer Without Honeycomb
Exposed to Arc-Plasma-Jet Effluent



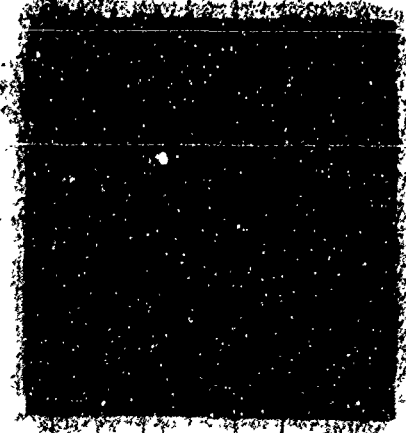




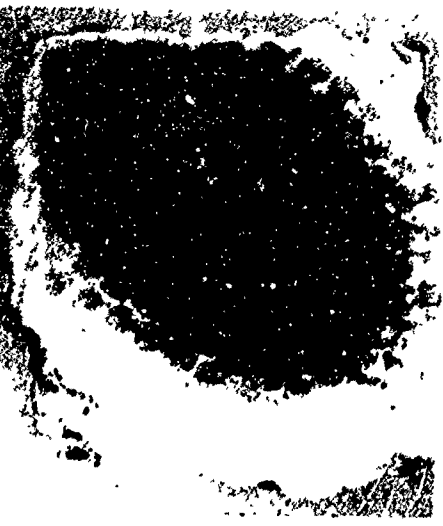
Test Duration (sec)		900	710
Decrease in Weight	Gms	1.2	1.3
	%	42.6	47.7
Depth of Erosion (in.)		0.023	0.017
Final Back Face Temp °F		460	500
Final Front Face Temp °F		1895	1740
		Heat Flux: 40 Btu/ft ² sec Sample Thickness: 50 mil	
			
Remarks		Heat Flux: 15 Btu/ft ² sec Sample Thickness: 50 mil	
			
Sample Appearance			
			

Table 65. Results of Manufacturer MC Modified Silicone Elastomer in Honeycomb
Exposed to Arc-Plasma-Jet Effluent

Test Duration (sec)		234	225
Decrease in Weight	Gms	3.6	6.3
	%	25.5	31.2
Depth of Erosion (in.)		0.019	Incr. 0.010
Final Back Face Temp °F		500	500
Final Front Face Temp °F		2525	2780
Remarks		Heat Flux: 150 Btu/ft ² sec Sample Thickness: 1/4 in. 	Heat Flux: 150 Btu/ft ² sec Sample Thickness: 3/8 in. 
Sample Appearance			

REFERENCES

1. "Procedures for Evaluating Coated Refractory Metal Sheet," MAB Report 201-M, Division of Engineering and Industrial Research, National Academy of Sciences, National Research Council, 3 August 1964.
2. J. C. Wurst and J. A. Cherry, "The Evaluation of High Temperature Materials," Final Report, Contract No. AF 33(616)-7838, ML-TDR-64-62, Vol. I, March 1964 and Vol. II, September 1964.
3. "Evaluation Procedures for Screening Coated Refractory Metal Sheet," MAB Report 189-M, Division of Engineering and Industrial Research, National Academy of Sciences, National Research Council, 15 February 1963.
4. L. G. Johnson, The Statistical Treatment of Fatigue Experiments (New York: Elsevier Publishing Company, 1964).
5. J. N. Berrettoni, "Practical Application of the Weibull Distribution," National Convention Transactions, American Society for Quality Control, 1962.
6. "Summary of Second High Temperature Inorganic Refractory Composites Coatings Working Group Meeting," ed. D. Roller, WADC-TR-59-415, June 1959.
7. J. W. Rosenbery, H. E. Smith, and J. C. Wurst, "Evaluation of Materials System for Use in Extreme Thermal Environments Utilizing an Arc Plasma Jet," AF 33(616)-6198, WADD-TR-60-926, June 1962.
8. J. C. Wurst and H. E. Smith, "The Evaluation of High Temperature Materials System with an Arc Plasma Jet," AF 33(616)-7838, ASD-TDR-62-655, July 1962.
9. J. C. Wurst, "The Development of a Standardized Screening Test for High Temperature Materials," paper presented at Sixth Refractory Composites Working Group Meeting, Dayton, Ohio 16, 17, 18 June 1962.
10. J. C. Wurst and J. A. Cherry, "The Evaluation of High Temperature Materials," Quarterly Progress Report, Contract No. AF 33(616)-7838, 13 December 1963.
11. Ibid., 10 June 1963.
12. "Chemical Reactions Between Propellant Gases and Nozzle Materials (U)," Atlantic Research Corporation, July 1963.

- *
13. J. Bodner, J. DePalma, and R. Keith, "A Scrubber Fume Disposal System for Arc-Plasma-Jet Testing, " Interim Progress Report, Contract No. AF 33(616)-7838, UDRI TR 64-111, September 1964.
 14. J. L. Engelke, "Heat Transfer to Particles in the Plasma Flame, " Stanford Research Institute, January 1962.
 15. G. D. Smith, "Heat Transfer Characteristics of Materials in Plasma Flames, " paper presented at Fourth Refractory Composites Working Group Meeting, Cincinnati, Ohio, November 1960.
 16. D. G. Moore, et al., "Studies of Particle-Impact Process for Applying Ceramic and Cermet Coatings, " National Bureau of Standards, ARL-59, August 1961.
 17. F. J. Dettrich, "Flame Spray Technique for Forming Nickel Aluminide-Ceramic Coating Systems, " paper presented at SAMPE National Symposium, Philadelphia, Pennsylvania, June 1963.

Unclassified

DOCUMENT CONTROL DATA - R&D		
<i>(Security classification of title, body of abstract and indexing classification must be entered when the overall report is classified)</i>		
1. ORIGINATING ACTIVITY (Corporate author)		2a. REPORT SECURITY CLASSIFICATION
University of Dayton Research Institute Dayton, Ohio 45409		Unclassified
2. REPORT TITLE		2b. GROUP
The Evaluation of Materials Systems for High Temperature Aerospace Applications Part I.		
3. DESCRIPTIVE NOTES (Type of report and inclusive dates)		
SUMMARY (January 1964 through January 1965)		
4. AUTHOR(S) (Last name, first name, initial)		
Wurst, John C. Cherry, John A. Gerdeman, Dennis A. and Hecht, Norman L.		
5. REPORT DATE	7a. TOTAL NO OF PAGES	7b. NO OF REFS
July 1966	176	17
8a. CONTRACT OR GRANT NO	8b. ORIGINATOR'S REPORT NUMBER(S)	
AF 33(615)-1312	AFML-TR-65-339 Part I	
a. PROJECT NO	8c. OTHER REPORT NO(S) (Any other numbers that may be assigned this report)	
7381	NONE	
c. Task No. 738102		
d.		
10. AVAILABILITY/LIMITATION NOTICES		
Not Releasable to OTS. Qualified requesters may obtain copies from DDC.		
11. SUPPLEMENTARY NOTES		12. SPONSORING MILITARY ACTIVITY
		Air Force Materials Laboratory Wright-Patterson AFB, Ohio 45433
13. ABSTRACT		
<p>(U) This report describes the evaluation of candidate materials systems for high temperature aerospace applications and is presented in three sections: the evaluation of refractory alloy coatings, the arc plasma jet evaluation of materials and the evaluation of plasma sprayed coatings.</p> <p>Section I describes the evaluation of two columbium base alloys, D-43 and C129Y, each with six different oxidation resistant coatings.</p> <p>In Section II the results of screening tests of several ablative materials by arc plasma jet, and the development of a plasma fired rocket exhaust simulator are discussed.</p> <p>Section III describes the evaluation of factors that affect the bond strength and thermal cycling endurance of plasma sprayed ceramic coatings modified with metal additions.</p>		

DD FORM 1473

Unclassified

Security Classification